Turbulent Coherent Structures in the Convective Boundary Layer Over Complex Terrain

by

Nevio Babić

Department of Environmental Sciences
University of Virginia

Date: _____

Approved:

_____
Stephan F.J. De Wekker, Supervisor

_____
Kevin M. Grise

_____
Todd M. Scanlon

_____
Haibo Dong

_____
Željko Večenaj

Dissertation submitted in partial fulfillment of the requirements for the degree of
Doctor of Philosophy in the Department of Environmental Sciences
to the Graduate Faculty of the University of Virginia
2018

Abstract

Coherent structures contribute significantly to turbulent exchange of heat, momentum and pollutants across the convective boundary layer (CBL). The typical taxonomy of CBL coherent structures includes horizontal convective rolls, open cells, alveolar polygonal structures, hairpin vortices, dust devils, near-surface streaks, and convective plumes. However, it is unknown how daytime coherent structures and complex terrain flows (such as thermally-induced and terrain-forced flows) interact and influence each other. Thermally-induced flows do not occur over flat terrain, so their possible impact on coherent structures requires elucidation. The goal of this dissertation is to investigate the coupling between spatiotemporal characteristics of coherent structures and thermally-driven flows in Owens Valley, California, the site of the T-REX experiment conducted in Spring 2006. The dissertation is organized into five chapters starting at the largest scales encompassing the entire Owens Valley and neighbouring mountain ranges, down to the smallest scales of a few tens of meters above the surface of the valley.

First, the influence of highly non-stationary macro-, meso-, and micro-scale phenomena on Monin-Obukhov similarity theory is assessed. This theory suffers from assumptions that are not valid over complex terrain. By contrasting five stationarity criteria common in boundary-layer meteorological research, we have found two criteria (one identifying the short-term signal variability, and the other identifying intermittency in the signal), to outperform the other three when determining the reduction in scatter around flux-variance similarity functions.

Next, emphasis is placed on the energy spectral gap, which often becomes elusive in complex terrain where different mesoscale phenomena may fill it completely. A better understanding of the spectral gap enables the determination of the ideal turbulence cut-off time scale necessary for the estimation of turbulence moments, which are the foundation of investigations in the remainder of the dissertation. A network of sixteen automatic weather stations is used to generate novel knowledge about the spatial variability of gap scales in a valley. Additionally, periodicity of upslope flows is observed and then validated against

a simple, analytic model. Three categories depicting the dominant along-valley variability are defined, which also represent the cornerstone of two more dissertation chapters.

Large eddy simulations are performed for three climatologically-representative case study days. These simulations aim to establish the mechanisms in which a valley environment modifies structural properties of horizontal convective rolls and open cells, two main modes of mixed layer convection. The principal finding here is the valley-induced narrowing of daytime convection, whose role is to ultimately increase the occurrence of rolls and transitional roll-like features in the valley CBL.

Next, the dissertation focuses on investigating the surface energy budget closure in Owens Valley. Here, the focus is on establishing how near-surface scalar similarity breaks down under the influence of entrainment-driven drawdown of drier and potentially warmer free-tropospheric air from above the CBL all the way down to the valley bottom. Resulting scalar dissimilarity violates Bowen ratio-based closures, by introducing non-local effects into sensible and latent heat fluxes, the key variables in the budget. The spectrally decomposed temperature-humidity correlation coefficient is used to quantify the impact of rolls and open cells on the surface energy balance (SEB) closure via entrainment. Once entrainment effects weaken, an improvement in the SEB closure is observed. The independence of this observation on the category and location in the valley, points to the ubiquity of entrainment degrading the SEB closure.

Finally, the dissertation focuses on the smallest scale of CBL convection, the near-surface coherent structures collectively referred to as ramp structures. Since these have not yet been studied over complex terrain, we move beyond the T-REX and Owens Valley, and include flux tower data from CASES-99 (gently rolling topography) and MATERHORN (playa, base of an isolated mountain), to establish the pertinent mechanisms in which complex terrain modifies ramp structural properties. The role of shear and buoyancy contribution to turbulence production is found to be essential in explaining the observed differences in ramp structural properties among the sites. Different generation mechanisms (bottom-up, top-down, turbulent kinetic energy (TKE)-based) are contrasted, by determining the degree of site-wide collapse of normalized ramp structural properties.

Contents

List of Tables

List of Figures

List of Abbreviations

ABL	Atmospheric Boundary Layer
ASL	Atmospheric Surface Layer
AWS	Automatic Weather Station
CASES-99	Cooperative Atmospheric Surface Exchange Study October 1999
C99	CASES-99 Tower
CBL	Convective Boundary Layer
CT	Central Tower
DNS	Direct Numerical Simulation
DPG	Dugway Proving Ground
DR	Double Rotation
DRI	Desert Research Institute
EBR	Energy Budget Ratio
EC	Eddy Covariance
ECMWF	European Centre for Medium-Range Weather Forecasts
EOP	Enhanced Observing Period
ES2	Eastern Slope 2 Tower
ESL	Eddy Surface Layer
FFT	Fast Fourier Transform
FW96	Foken and Wichura (1996) Stationarity Criterion
GMAST	Granite Mountain Atmospheric Sciences Testbed

HCR	Horizontal Convective Roll
IDM	Inertial Dissipation Method
IFC	Intermittency Fraction Criterion
IOP	Intensive Observing Period
ISFF	Integrated Surface Flux Facility
ISS-2	Integrated Sounding System 2
LAD	Least Absolute Deviations
LES	Large Eddy Simulation
LSQ	Least Squares
LST	Local Standard Time
M98	Mahrt (1998) Stationarity Criterion
MAD	Median Absolute Deviation
MM5	Fifth-Generation Penn State/NCAR Mesoscale Model
MSC	Mesoscale Secondary Circulation
MSE	Mean Squared Error
MAPR	Multiple Antenna Profiler Radar
MATERHORN	Mountain Terrain Atmospheric Modeling and Observations Program
MHAT	Mexican Hat
MOST	Monin-Obukhov Similarity Theory
MRFD	Multiresolution Flux Decomposition
NAM	North American Mesoscale Model
NCAR	National Center for Atmospheric Research
NLCD	National Land-Cover Dataset
NWP	Numerical Weather Prediction
PBL	Planetary Boundary Layer
PF	Planar-Fit

PL	Playa Tower
QC	Quality Control
RASS	Radio Acoustic Sounding System
RAT	Reverse Arrangement Test
RRTM	Rapid Radiative Transfer Model
RUT	Running Test
SEB	Surface Energy Balance
SD	Synoptic Downvalley
SEBAL	Surface Energy Balance Algorithm for Land
SFL	Surface Friction Layer
SGS	Subgrid-scale
SLTEST	Surface Layer Turbulence and Environmental Science Test
SRTM	Shuttle Radar Topography Mission
SSL	Shear Surface Layer
SU	Synoptic Upvalley
SVAT	Surface Vegetation-Atmosphere Transfer
TEAL	Theodorsen Ejection-Amplifier Like
TKE	Turbulent Kinetic Energy
TOS	Turbulent Organized Structure
T-REX	Terrain-Induced Rotor Experiment
USGS	United States Geological Survey
UTC	Coordinated Universal Time
YSU	Yonsei University
WRF	Weather Research and Forecasting
WS	Wind Shift

Acknowledgements

I would like to express my sincerest gratitude to my advisor Stephan F.J. De Wekker. Thank you for the kind support, guidance and encouragement you have provided over the years, as well as the opportunity to define and develop my own research topics. I am extremely grateful to my committee members Kevin Grise, Todd Scanlon, Željko Večenaj and Haibo Dong, for their feedback, suggestions, and support.

I will be forever grateful to all the excellent students and researchers formerly of the De Wekker lab group: Michael van den Bossche, Ross Palomaki, Temple Lee, Mark Sghiatti, Sandip Pal, Gert-Jan Duine, Nathan Rose, Ivana Marinović, Stephanie Phelps, and Mohamadou Diallo. Additionally, I thank graduate students Amélie Berger and Kelcy Kent, as well as undergraduate students Stephanie Durham and Dominique Ong, for accompanying me to the Shenandoah National Park when the lab members could not. You have all made the numerous field duties over the years both productive and fun, whether it was troubleshooting the Pinnacles instrumentation, visiting HOBOs along the Park trails, or human-corkscrewing weather stations across the Blue Ridge. Maintaining the extensive suite of measurements throughout the Blue Ridge would not have been possible without the support of the following people: Temple Lee (NOAA ATDD) for technical support; Jonathan Kofler and Phillip Handley (NOAA ESRL) for providing calibration cylinders; Alan Williams and Elizabeth Garcia (NPS) for being extremely responsive and helpful. I wish to acknowledge Sebastian Hoch (University of Utah) for helping me get started with the HALO Photonics Streamline, as well as Dave Emmitt (Simpsons Weather Associates) for many interesting discussions on Doppler wind lidars.

I am indebted to the Advanced Study Program, Vanda Grubišić, Steven Oncley and Bill Brown, for hosting my one-month visit to NCAR EOL. Many thanks to Jim Wilczak (NOAA ESRL), Ned Patton (NCAR MMM), and Julie Lundquist (University of Colorado Boulder), for numerous fruitful discussions. I am extremely grateful to Branko Kosović (NCAR RAL), for providing me with core hours on Cheyenne.

They say you are only as good as the company you keep around. I am greatly thankful

to: Kyle Davis, Shradda Dhungel, Aleksandra Babnis, Mark Sghiatti, Amélie Berger, Ross Palomaki, Nicole Bonino, Michael van den Bossche, Misty Boos, Mokganedi Tatlhego, and Gina Digiantonio, for being the most awesome friends one could wish for; to Karmen Babić, Branko Grisogono, Željko Večenaj, Temple Lee, Hrvoje Kozmar, Sandip Pal, and Ivana Stiperski, for all the stimulating discussions and generous academic support; to Joel Zimmerman (aka deadmau5), whose musical masterpieces made manuscript-editing and code-debugging more efficient; to Atilla, for always being a welcoming and supportive puppy.

I wish to thank the extensive support from everyone in the Department of Environmental Sciences administrative staff, in particular Debra Shifflett, Laurie Hammond, and Will Tomanek. I acknowledge the diligent and responsive support from the UVA Advanced Research Computing Services (ARCS), and the NCAR Computational and Information Systems Laboratory (CISL). I thank my numerous funding sources, including the Office of Naval Research, the National Science Foundation, and the NOAA-MOU. Finally, I acknowledge all the T-REX, CASES-99 and MATERHORN investigators for collecting the valuable data analyzed in this dissertation.

Last but not least, I am forever grateful to my mom Željka, dad Milan, and sister Iva, for their unwavering support, extreme generosity, and selfless love. You have always been my greatest inspiration, and I couldn't have made it without you.

1

Introduction

1.1 Motivation

Decoupled from the free troposphere aloft, the atmospheric boundary layer (ABL) constitutes the lowest layer of the Earth's atmosphere (Stull, 1988). As such, the ABL responds to surface-induced forcings with time scales equal to an hour or less. Despite the decoupling, a fixed sensor at the surface still experiences all the spatial and temporal scales of atmospheric motion. The weather at a certain location is under the influence of several dominant scales of motion (Van der Hoven, 1957), such as the seasonal cycle ($\approx$ 1-year cycle), passage of high and low pressure systems ($\approx$ 4-day cycle), diurnal cycle ($\approx$ 12-h cycle), as well as small-scale turbulence ($\approx$ 1-min to 10-min cycle), the main contributor to the weather directly experienced by the observer at the surface. The convectively driven ABL, known as the convective boundary layer (CBL), is characterized by strong turbulent mixing, driven primarily by surface heating and vertical wind shear. Of particular interest here is the CBL depth z_i, defined as the height above ground of the elevated temperature inversion. Being one of the main variables used to describe the evolution of the CBL, z_i is used in numerical weather prediction (NWP) as a key quantity in turbulence parameterization schemes (LeMone et al., 2013), scaling variable in theoretical models of CBL growth (Tennekes, 1973), as well as in air pollution models and associated numerical schemes. The spatiotemporal evolution of CBL-spanning eddies, for which z_i sets the upper size limit, is relatively well known over flat, horizontally homogeneous terrain. Complex, mountainous terrain, on the other hand, imposes a number of additional forcings and influences on CBL growth and evolution.

Mountains occupy up to 70% of the Earth's surface area (Strobach, 1991), and are inhabited by approximately a quarter of the global human population (Meybeck et al., 2001). This substantial portion of population, in turn, enjoys the myriad of ecosystem, social, agricultural, and information services that mountains provide (Meyers and Steenburgh, 2013; De Wekker et al., 2018). Compared to more timid terrain, however, mountains are far more sensitive to future projections of global climate warming (Gobiet et al., 2014). Specific only to ABL over mountains, high impact events such as ice and snow storms (Steenburgh et al., 1997), droughts (Vido et al., 2015), persistent cold air pools (Lareau et al., 2013), landslides (Kirschbaum et al., 2012), floods (Nuissier et al., 2008), local windstorms (Grisogono and Belušić, 2009), aviation hazards (Darby and Poulos, 2006), dust storms (Hahnenberger and Nicoll, 2012), wildfires (Yue et al., 2014), and air pollution episodes (Jirak and Cotton, 2006), may cause detrimental human, environmental and economic losses. The degree to which the frequency of these events becomes influenced by global warming, however, remains alarmingly uncertain (Nogués-Bravo et al., 2007; Gobiet et al., 2014). Furthermore, underestimations in global carbon budgets remain much larger over complex terrain (Rotach et al., 2014). Insufficiently resolved mountain topography and resulting ABL exchange processes, are held as the chief contributors to this uncertainty within the context of both operational and global NWP (Lehner and Rotach, 2018).

Over mountain topography, CBL evolution varies strongly in both time and space (Holzworth, 1964). Driven by radiative heating during the daytime, thermally-driven flows span several spatiotemporal scales of motion (Rotach et al., 2015). For a typical mountain range, these include the meso-α (200-2000 km), meso-β (20-200 km), meso-γ (2-20 km), and micro (< 2 km) scales. Resulting slope and valley flows exert a pronounced enhancement of turbulent transport processes. The underlying mechanisms of these flows are fairly well known (Whiteman, 2000; De Wekker and Kossmann, 2015). Thermally-driven flows complicate CBL structure over mountains, introducing multiple elevated temperature inversions (Wagner et al., 2014a), as well as mountain venting (Henne et al., 2005), cloud venting (Cotton et al., 1995), and advective venting (Adler and Kalthoff, 2014) of aerosols and pollutants into the free troposphere aloft. To reliably simulate the onset, intensity and spatial extent of such flows, the topography needs to be resolved with a resolution of at least 1 km (Wagner et al., 2014a). Despite the fact that operational, mesoscale NWP models are becoming capable of simulating complex terrain flows with adequate fidelity (Schmidli et al., 2018), they also require further improvements concerning static input fields, in particular land-use (Schicker et al., 2016) and soil moisture (Massey et al., 2016).

Increase in computing power, on the other hand, is resulting in progressively finer horizontal grid resolutions employed in operational NWP (Tang et al., 2013; Schalkwijk et al., 2015; Heinze et al., 2017). Hence, operational NWP over complex terrain is expected to become increasingly reliable in the near future. Ostensibly, such advances appear promising for the simulation of complex terrain flows, however it became progressively apparent in recent years that sub-kilometer horizontal grid spacings inevitably lead to disturbing numerical artifacts (Zhou et al., 2014; Rai et al., 2017a), ultimately detrimental for forecasting of thermally-driven flows (Cuxart, 2015). Known as the *grey zone* or *terra incognita* (Wyngaard, 2004), these subkilometer spacings are home to a broad class of CBL entities called coherent structures.

Coherent structures are defined as an organized three-dimensional region in turbulent shear flows, where some property (e.g. temperature) is correlated with itself at a time scale significantly longer than the smallest scale of the flow (Robinson, 1991). Unlike laboratory flows, coherent structures in the CBL assume many forms, depending on the ambient atmospheric stability and the scale considered (Young et al., 2002). From largest to smallest, coherent structures in the CBL take the form of horizontal convective rolls (Thurston et al. 2016), open cells (Salesky et al., 2017), closed cells (Wood, 2012), alveolar structures (Träumner et al. 2015), spoke-like patterns (Schmidt and Schumann 1989), dust-devils (Oncley et al., 2016), hairpin vortices and packets (Adrian 2007; Li and Bou-Zeid 2011), surface-layer streaks (Drobinski et al. 2004), and plume-like ramp structures (Wilczak and Tillman 1980). This richness in coherent structure taxa, however, has also led to alarming degree of ambiguity when determining impact of coherent structures on turbulent exchange in the CBL (Young et al., 2002). In turn, the current horizontal grid spacing employed in most LES and state-of-the-art operational NWP, ranging on average between 200 m and 2 km, falls into the *terra incognita*, thus fully resolving only the largest coherent structures. Meanwhile, the smaller coherent structures remain subgrid-scale (SGS), particularly near the surface. Hence, their effect on near-surface turbulent exchange has to be parameterized based on schemes that invoke universal scaling laws (Zhong and Chow, 2013, their Table 10.3). These laws assume flat terrain, local isotropy in the inertial subrange, and lack of any upscale energy cascade back towards resolved scales (Carper and Porté-Agel, 2004). The intermittency of near-surface coherent structures is well known to violate the latter two assumptions (Katul et al., 1995), however the critical lack of studies detailing coherent structures over complex terrain, leaves many open questions as to the applicability of such SGS closures to mountainous regions.

1.2 Dissertation Structure and Objectives

The main goal of this dissertation is to identify and investigate coherent structures in the CBL over mountainous terrain, and to determine their impact on turbulent exchange across a broad range of time and space scales. The research presented here combines rich, high frequency in situ data sets, remote sensing instrumentation, as well as LES in areas lacking necessary observations. The central study area is Owens Valley, California, the focal point of the Terrain-Induced Rotor Experiment (T-REX). The dissertation is organized in a top-down sense, wherein largest scales of motion, spanning entire Owens Valley and neighbouring tall mountain ranges, are analyzed first. From there, the scales of interest are progressively decreased, lastly focusing on the smallest motions near the surface of Owens Valley. This progression of dissertation chapters is illustrated in Figure 1.1 and outlined as follows:

- Chapter 2 first examines the applicability of the Monin-Obukhov similarity theory (MOST) in Owens Valley, by investigating the departure of the flux-variance similarity relationships from their flat-terrain counterparts. This type of analysis is traditionally performed to assess the suitability of MOST in areas where fundamental tenets upon which the theory relies, namely horizontal homogeneity, flux constancy with height, and stationarity, may be violated. The violation of these tenets results from either a single or multiple overlapping scales of motions;

- Chapter 3 isolates the largest and longest scales of motion. This is done by locating the time scale of the mesoscale spectral gap, often elusive and difficult to determine when multiple scales of motion overlap, as in complex terrain. The selection of an appropriate time scale to use in the mean trend removal ensures that statistical, higher-order turbulent moments used in the chapters to follow, do not suffer from longterm trends. Propeller-vane and sonic anemometry, wind profilers, and an analytic model of oscillating upslope flows, are used to describe the thermally-driven flows on the far end of the spectrum. This chapter categorizes synoptically calm and perturbed days, thus laying down the foundation for the next two chapters;

- Chapters 4 and 5 focus on the range of spatiotemporal scales directly after the mesoscale spectral gap, encompassing the major CBL-spanning, chief variance-producing coherent structures: horizontal convective rolls and open cells. As such, this range of scales directly corresponds to the *terra incognita*. Chapter 4 relies on real-world LES

to determine the characteristics of rolls and cells in Owens Valley for three case study days, representative of the categorization introduced in Chapter 3. Next, Chapter 5 examines the closure of the surface energy budget in Owens Valley, and determines the extent to which rolls and cells degrade the closure via non-local effects from the entrainment zone capping the CBL;

- Chapter 6 examines the smallest scales of coherent structures, collectively known as ramp structures, in the near-surface unstable atmospheric surface layer. Wavelet covariance technique is used to determine ramp structural properties. Focus is also placed on comparing different ramp structure generation mechanisms and conceptual scaling frameworks. This chapter incorporates, in addition to T-REX, experimental data collected from other major field campaigns (CASES-99, MATERHORN) with the aim of more objectively elucidating the effects of complex terrain on ramp structures;

- Chapter 7 summarizes the salient findings of the dissertation and proposes future research directions.

1.3 Novelty and Intellectual Merit

This dissertation proposes to bridge and close gaps in our knowledge of interactions that occur across a wide range of spatiotemporal scales of atmospheric flows over mountainous terrain. Specifically, through a synthesis of observations obtained using several different instruments deployed during T-REX, combined with high resolution LES, this dissertation aims to deliver a more complete, synergistic view of a coupled mountain meteorology/boundary-layer meteorology system in Owens Valley. Although some of the conclusions in this dissertation may be specific just to Owens Valley, the key physical principles and mechanisms will be extendable to other valleys worldwide. The results of this dissertation provide novel insights into the key couplings between stochastic, high-frequency turbulence, deterministic coherent structures, and thermally-driven flows. Ultimately, the goal is to propose improvements for existing turbulence parameterization schemes to account for these key couplings. Appropriate data analysis and interpretation of results will rectify the deficiencies of current NWP models when simulating complex terrain flows in the CBL.

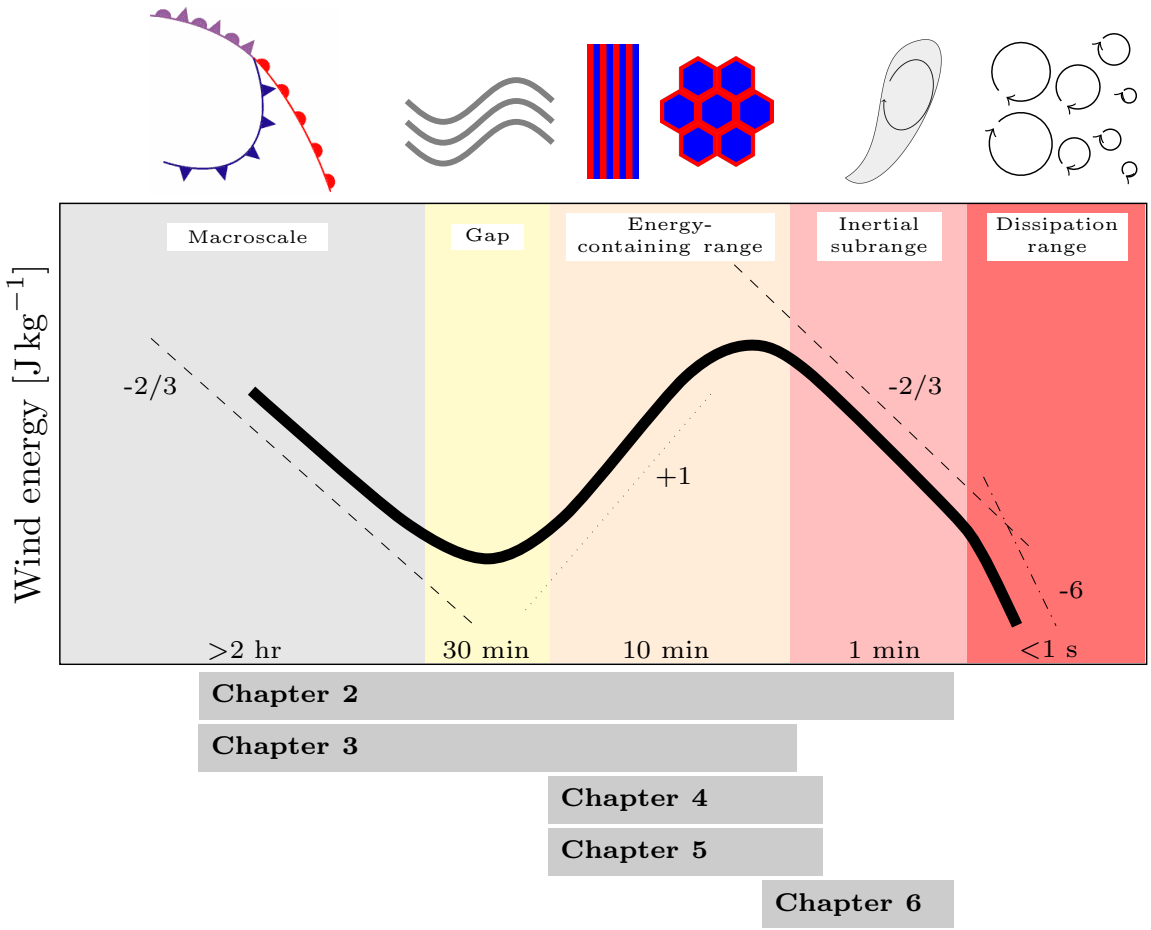

FIGURE 1.1: General outline showing the progression of the dissertation chapters across a typical near-surface wind energy spectrum in the CBL. Solid black line represents the reference, flat terrain near-surface spectrum for unstable conditions encountered in the CBL (Kaimal and Finnigan, 1994). Black dash-dotted, dashed, and dotted lines denote the -6, $-2/3$, and $+1$ spectral slopes, respectively. Time scales on the x-axis are organized in an approximate logarithmic fashion. Units on the y-axis are arbitrary and linear. Illustrations above the figure denote the main types of motion characteristic of each of the five spectral regions, from left to right: frontal systems, mountain waves, horizontal convective rolls, open cells, ramp structures, small eddies subject to viscous dissipation.

2

Flux-variance similarity in complex terrain and its sensitivity to different methods of treating non-stationarity

2.1 Introduction

[1] Continuous efforts and advances in micrometeorological measurement techniques during the last few decades have enabled a thorough and detailed observation of the atmospheric boundary layer (ABL) and the development of theories to describe turbulent processes in this layer. The main and most commonly accepted theoretical framework is the Monin-Obukhov similarity theory (MOST hereafter; Obukhov, 1946; Monin and Obukhov, 1954; see Foken, 2006 for a historical overview). Within this framework, similarity functions can be expressed through dimensionless ratios of turbulence variances and Monin-Obukhov surface layer velocity (u_*) and temperature (θ_*) scales. Initial experiments to evaluate MOST were conducted over flat, homogeneous terrain, where the major assumptions of MOST are presumably valid. These assumptions include stationary atmospheric conditions and the presence of a constant-flux layer, a synonym for the surface layer. The surface layer is traditionally defined as that part of the ABL in which kinematic turbulent fluxes of momentum and heat are nearly constant (not changing more than 10%) with height (Stull, 1988). The surface layer encompasses the lowest 10% of the ABL (Kaimal and Finnigan,

[1] Reprinted from Babić, N., Večenaj, Ž., and De Wekker, S. F. (2016): Flux-variance similarity in complex terrain and its sensitivity to different methods of treating non-stationarity. Boundary-Layer Meteorol., 159(1), 123-145.

1994).

Since the theory for describing MOST was developed for stationary conditions, serious departures from these conditions can result in errors in the fitted similarity functions, and MOST may not be successfully applied. Non-stationarity is most often introduced via a number of processes such as Kelvin-Helmholtz shear instabilities, horizontal meandering-like motions, internal gravity waves, and density currents (Cheng et al., 2005; Mahrt, 2007). On longer time scales, rapid forcing due to the advection of cloud layers (Andreas et al., 2008), the diurnal cycle (Metzger et al., 2007), as well as frontal passages (Lundquist, 2003; Piper and Lundquist, 2004) may all introduce further non-stationarity in the time series of meteorological variables. For example, integral turbulence characteristics, as well as dimensionless wind speed and temperature gradients, are affected by non-stationarity, which is reflected in increased scatter and less statistically significant goodness-of-fit measures. To exclude non-stationary data, numerous quality control procedures that include various criteria have been proposed (Bendat and Piersol, 1986, hereafter BP86; Foken and Wichura, 1996, hereafter FW96; Vickers and Mahrt, 1997; Mahrt, 1998, hereafter M98; Lee et al., 2006). In most studies, a single method is applied to treat non-stationarity, and it is rarely assessed how the method affects the similarity functions. Cava et al. (2008) compare two well known stationarity criteria (FW96; M98) in their calculations of the surface energy budget over flat terrain and found large differences in the covariances obtained from the two stationary data sets. Večenaj and De Wekker (2015) (hereafter VD15) applied four different criteria to remove 30-min non-stationary intervals from their dataset and observed that the resulting stationary data sets were vastly different. In fact, they show that it was unlikely that the different criteria simultaneously declared a particular 30-min interval stationary (their Fig. 4). They also show that intermittent turbulence, which is often argued to be a source of non-stationarity (Coulter and Doran, 2002; Cullen et al., 2007; Mahrt, 2007), is not thoroughly detected by any of the four criteria.

Recent efforts have tested MOST in urban, heavily populated areas with the aim to improve air pollution dispersion parameterizations. Following the detailed review of Roth (2000), Al-Jiboori et al. (2002), Quan and Hu (2009) and Wood et al. (2010) showed a successful application of local scaling (Nieuwstadt, 1984) from observations made on meteorological towers in urban areas. MOST has also been investigated above forest canopies (Nakamura and Mahrt, 2001; Burns et al., 2011), and over coastal (Shao and Hacker, 1990; Singha and Sadr, 2012; Kral et al., 2014; Zhao et al., 2013; Figueroa-Espinoza and Salles, 2014), offshore (Grachev and Fairall, 1997) and polar regions (Rodrigo and

Anderson, 2013). The majority of these studies are based on a single tower with few levels of measurements, making it difficult to investigate MOST at various levels in the surface layer and at different locations near the measurement site. Whereas MOST can hold at a specific location, spatial representativeness of the results may be questionable (Katul et al., 1999; Kanda et al., 2006) which has led to a growing number of investigations of intra-city MOST applicability (Fortuniak et al., 2013; Nordbo et al., 2013).

Only a few studies have addressed MOST in complex terrain. For instance, De Franceschi et al. (2009) observed a successful application of MOST across the entire stability range based on observations from a single ultrasonic anemometer installed 8 m above a valley floor in the European Alps. This successful aplication of MOST was confirmed for two data sets from which non-stationarity was removed beforehand using two different recursive digital filters. They showed that the flat terrain similarity relationships, initially proposed by Panofsky and Dutton (1984), can be extended and applied to surface layer measurements made over a valley floor. However, they emphasized the further need for measurements of turbulence quantities at several locations. Martins et al. (2009) investigated MOST over a steep slope for different classes of wind speed and wind direction, and found that MOST applicability changed for different stratifications. While their dimensionless standard deviations of the vertical wind speed component obeyed Monin-Obukhov similarity for all wind directions, dimensionless standard deviations of both longitudinal and lateral wind speed component supported a more limited applicability of the similarity theory. Furthermore, they found that the applicability of the similarity theory also depended on wind speed. Kral et al. (2014) in a similar study over a High-Arctic fjord found that the heterogeneous fetch in this complex terrain only has a minor impact on the form of the MOST functions. By comparing their analysis for data sets obtained using the double rotation and the planar fit techniques (Wilczak et al., 2001), they confirmed the necessity of proper rotation for measurements over complex terrain. Their study also demonstrated questionable validity of MOST during low wind speed conditions, contrary to Martins et al. (2009) and Moraes et al. (2005), who found the opposite to hold. Furthermore, their normalized standard deviations were shown not to obey the similarity rules for wind direction perpendicular to the valley axis. De Franceschi et al. (2009) found slightly better performance of the similarity theory for wind directions perpendicular to the valley axis, for all dimensionless standard deviations. Nadeau et al. (2013) found for a steep Alpine-type slope that the scaling was successful for the flux-variance similarity functions, but not for the flux-gradient similarity functions, especially during stable situations. Disparities such as those presented above

call for further measurement campaigns to be conducted over complex terrain, mainly to obtain a more definitive and conclusive range of the applicability of the similarity theory.

In this paper, we address the influence of non-stationarity on the flux-variance similarity functions over complex terrain. We investigate the effects of applying various stationarity criteria on the shape and goodness-of-fit measures of the similarity functions at three locations in the wide and deep Owens Valley during the Terrain-Induced Rotor Experiment (T-REX). We also investigate differences in the similarity functions between the three locations and between different heights at each of the locations. We focus on the similarity functions for standard deviations of the three wind speed components and the potential temperature. In addition to non-stationarity, there are other issues that need to be considered when investigating similarity functions. Self-correlation, for example, is an issue that may in some cases question the regression analysis used to evaluate MOST (M98; Klipp and Mahrt, 2004; Baas et al., 2006; Grachev et al., 2007a; Nadeau et al., 2013). Furthermore, some studies (e.g. Castelli and Falabino, 2013; Trini Castelli et al., 2014) have shown that low wind speed conditions, such as those occurring during very stable conditions, tend to complicate interpretation of similarity functions.

In Sect. 2.2, we describe the T-REX data set and some background behind the flux-variance similarity functions. For the investigation of turbulent quantities and similarity functions at specific locations in complex terrain, it is helpful to understand the characteristics of the mean wind and stability at these locations which we describe in Sect. 2.3.1. The use of surface fluxes in the expressions of the similarity functions above is justified only in the constant flux layer, a layer in which the vertical flux divergence is minimal. We therefore closely examine the divergence of the vertical fluxes in Sect. 2.3.2. To determine fitting parameters, we present an analysis based on the choice of the regression method in Sect. 2.3.3. The influences of treating non-stationarity on the fitting parameters is presented in Sect. 2.3.3, while the suitability of the scaling and regression approach is assessed through a self-correlation analysis in Sect. 2.3.4. Finally, the impact of applying stationarity criteria on the goodness-of-fit measures is discussed in Sect. 2.3.5, while concluding remarks of the study are given in Sect. 2.4.

2.2 Data and methods

2.2.1 Data processing

A detailed overview of T-REX can be found in Grubišić et al. (2008). A large number of measurements were conducted in Owens Valley, California, from 1 March to 30 April 2006, to investigate lee waves and rotors during synoptically forced conditions and to investigate thermally driven flows and their interaction with the structure and evolution of the ABL under weak synoptic forcing. Owens Valley is one of the deepest valleys in the contiguous United States. The valley has an average depth of 2.5 km, with the Sierra Nevada mountain range to the west and the White Mountains to the east. The average length of the valley is 150 km with an average width of 20 km at the T-REX investigation area (Fig. 2.1). The Owens Valley is characterized by a semiarid climate.

Three 34 m towers, managed and operated by the National Center for Atmospheric Research (NCAR) Integrated Surface Flux Facility (ISFF), were located along the Owens Valley and the adjacent slope. The central tower (CT) and the southern tower (ST) were located along the central axis of the valley floor, approximately 8 km apart. The third, western tower (WT) was located nearly perpendicular to the valley axis on a line passing through the CT, approximately 9 km to the west of the CT. The land cover in the vicinity of the towers was dominated by sandy soils with grass and shrubs. Geographical coordinates, height above mean sea level, surface slopes and displacement heights are given in Table 2.1. The displacement height d was assumed to be equal to 2/3 of the average canopy height H. To check the reliability of this relatively rough approximation of the displacement height d, we have also performed the technique proposed by De Bruin and Verhoef (1997), which is based on the free convection similarity relation between the standard deviation of the vertical wind speed σ_w and $\overline{w'\theta'}$. The difference between this newly obtained displacement height and the one obtained using the 2/3 rule was negligible at all three towers.

All ISFF towers were equipped with CSAT3 sonic anemometers (Campbell Scientific, Inc) at heights of 5, 10, 15, 20, 25 and 30 m above ground level (AGL). Measurements with the sonic anemometers were obtained with a sampling frequency of 60 Hz. To assess the degree of possible flux loss due to spectral attenuation by path averaging (Horst and Oncley, 2006), we used the analytical approach of Massman (2000, 2001), further developed by Lee et al. (2006), which resulted in a negligible difference between measured and corrected momentum and heat fluxes. The entire two month observational period was divided into a total of 2928 30-min intervals and the statistical first and second order moments were

calculated using 30-min block averaging. For each 30-min interval, a coordinate rotation was applied to obtain the along-wind u and cross-wind v wind speed component. A rotation which does not affect the vertical wind speed component was applied, since it is known that such a rotation may also act as a high pass filter. Because our aim in this study is to address non-stationarity exclusively using the five stationarity criteria, our intention is to avoid any inadvertent removal of non-stationarity (aside from already performing block averaging). However, we have also performed a section-wise planar fit (Wilczak et al., 2001; Nadeau et al., 2013), since we are dealing with measurements over sloping complex terrain. For this purpose, the entire two month observational period was used to obtain the coefficients in the multiple linear regression needed to find the plane parallel to the long-term streamlines. For all four wind direction sectors (upvalley, downvalley, upslope, downslope), no significant differences between the resulting covariances were observed (not shown). Similar to De Franceschi et al. (2009), Tampieri et al. (2009), and Večenaj et al. (2011), we assume the sonic temperature T_s to be a good approximation of the virtual potential temperature θ_v. Data completeness for the two-month period at all towers and all levels was greater than 90% (see VD15, their Table 1). A complete and detailed description of the stationarity criteria used in this study is provided in VD15, though for completness we briefly summarize each of the criteria in Appendix A. Finally, we do not remove cases of low wind speed conditions nor perform the *total* approach (VD15), due to a relatively short measurement period.

2.2.2 Theoretical background

For measurements made inside the surface layer, the following scaling group, composed of the friction velocity u_*, characteristic temperature scale θ_* and the Obukhov length L, forms the basis of MOST:

$$u_* = \left(\overline{u'w'}^2 + \overline{v'w'}^2\right)^{1/4}, \tag{2.1}$$

$$\theta_* = -\frac{\overline{w'\theta'}}{u_*}, \tag{2.2}$$

$$L = -\frac{u_*^3\overline{\theta}}{\kappa g\overline{w'\theta'}}, \tag{2.3}$$

where $\overline{u'w'}$ and $\overline{v'w'}$ are the vertical kinematic momentum fluxes of the along-wind u and cross-wind v wind speed components, respectively; $\overline{w'\theta'}$ is the surface value of the vertical

kinematic heat flux, $\overline{\theta}$ is potential temperature, κ (= 0.4) is the von Kármán constant (Högström, 1996), g (= 9.81 m s^{-2}) is the acceleration due to gravity, [$^-$] denotes averaging with respect to time while [$'$] denotes turbulent perturbations around the mean.

According to MOST, quantities made dimensionless by these scaling parameters are universal functions of the non-dimensional stability parameter ζ, defined as:

$$\zeta = \frac{z-d}{L}, \tag{2.4}$$

where z is the measurement height above the ground and d is the zero-plane displacement height.

The dimensionless standard deviations of wind velocity components and temperature can be written as (Panofsky and Dutton, 1984):

$$\frac{\sigma_i}{u_*} = \begin{cases} \alpha_i \left(1-\beta_i\zeta\right)^{1/3} & \text{for} \quad \zeta < 0, \\ \alpha_i \left(1+\beta_i\zeta\right)^{1/3} & \text{for} \quad \zeta > 0, \end{cases} \tag{2.5}$$

$$\frac{\sigma_\theta}{|\theta_*|} = \begin{cases} \alpha_\theta \left(1-\beta_\theta\zeta\right)^{-1/3} & \text{for} \quad \zeta < 0, \\ \alpha_\theta \left(1+\beta_\theta\zeta\right)^{-1} & \text{for} \quad \zeta > 0, \end{cases} \tag{2.6}$$

where $i = u, v$ and w denotes the longitudinal, lateral and vertical wind velocity components, respectively. The above set of equations is also referred to as the flux-variance similarity relationships or as integral turbulence characteristics (e.g. FW96).

For the calculation of the dimensionless standard deviations of potential temperature (2.6), data obtained during near-neutral stratification were discarded given the large scatter of these data as has also been reported in other studies and attributed to low values of the sensible heat flux H. For example, De Franceschi et al. (2009), Nadeau et al. (2013) and Wang et al. (2014) apply the criterion $|H| < 10\,\mathrm{W\,m^{-2}}$ to remove those data, while Li et al. (2012) apply the criterion $|H| < 5\,\mathrm{W\,m^{-2}}$. In our case, we reject all the dimensionless standard deviations of potential temperature corresponding to $|H| < 10\,\mathrm{W\,m^{-2}}$ and $|\zeta| < 0.05$. Finally, we exclude all data corresponding to $|u_*| < 0.02\,\mathrm{m\,s^{-1}}$ to avoid unusually large values of the dimensionless standard deviations in the strongly unstable and stable situations, respectively.

2.3 Results and discussion

2.3.1 Owens Valley spring climatology

The flows at CT and ST are predominantly aligned along the valley floor and show a distinct diurnal pattern with southeasterly upvalley winds during unstable and northwesterly downvalley winds during stable conditions (Fig. 2.1). Strongest flows are southeasterly and somewhat weaker at CT compared to ST. Contrary to the flows at the valley sites, the general flow at WT is characterized by both valley and slope flows. Most pronounced are the consistent downslope flows during stable conditions (Fig. 2.1), while the upslope wind component is weak and overpowered by the upvalley flows during unstable conditions. While upvalley and downvalley winds at CT and ST generally occur during unstable and stable stratification, respectively, both upvalley and downvalley flows also occur during a significant portion of the opposite stability (not shown). This indicates that synoptic-scale forcing occasionally dominates the relatively weaker thermally-driven circulation, as is the case, for example, during pressure-driven or forced channeling (Whiteman, 2000).

2.3.2 Turbulent flux divergence with height

To examine the divergence of vertical fluxes, we adopt the approach of Grachev et al. (2005). We calculate absolute differences of all three vertical fluxes ($\overline{u'w'}$, $\overline{v'w'}$ and $\overline{w'\theta'}$) on five mid-levels between two adjacent tower levels, normalized by the appropriate flux on the lower level of measurement, according to:

$$K = \left| \frac{\{\overline{u'w'},\, \overline{v'w'},\, \overline{w'\theta'}\}_{\text{upper}} - \{\overline{u'w'},\, \overline{v'w'},\, \overline{w'\theta'}\}_{\text{lower}}}{\{\overline{u'w'},\, \overline{v'w'},\, \overline{w'\theta'}\}_{\text{lower}}} \right| \leqslant 10\,\%, \tag{2.7}$$

where the typical "textbook-suggested" variability limit of 10% is used for the change of vertical flux with height in the constant flux layer. Although K might implicitly depend on the separation between the measurement levels, defining it as in (2.7) such a dependency is avoided.

Figure 2.2 shows the dependence of vertical momentum and heat flux divergences on the stability parameter ζ. Although the vertical flux divergence is shown only for CT, similar qualitative results hold for the other two towers (not shown). The longitudinal momentum flux (Fig. 2.2a) could be considered constant with height ($K_{\overline{u'w'}} < 20\,\%$) for $\zeta < 0.2$ and $\zeta > -0.4$ for stable and unstable stratification, respectively. While the shape of $K_{\overline{u'w'}}$ is similar for both stratifications, there is more scatter in the stable than

in the unstable situation. Even though both the longitudinal and lateral momentum flux divergences are quite comparable in magnitude ($0 < K < 120\%$, Fig. 2.2a,b), the latter ones are shifted toward larger values on all mid-levels. Consequently, only the lateral momentum fluxes at the lowermost two tower levels could be considered part of a constant flux layer, within similar stability ranges presented above for $\overline{u'w'}$. Based on our analysis of the vertical momentum flux divergence, surface layer scaling might be justified during weakly unstable and weakly stable stratification, but not for the free convection conditions ($\zeta < -1$) and very stable stratification ($\zeta > 1$), in agreement with M98. On the other hand, the vertical divergence of the heat flux exhibits different behavior compared to the momentum flux divergence (Fig. 2.2c). Vertical heat flux divergence is minimal for the strongly and moderately unstable stratification ($\zeta < -0.2$), with $K_{\overline{w'\theta'}}$ rarely exceeding 10%. Approaching near-neutral stratification from both stability sides ($|\zeta| < 0.05$), there is an abrupt increase in $K_{\overline{w'\theta'}}$, due to low values of the vertical heat flux in the denominator in (2.7). For the moderately and strongly stable stratification, there is an increased heat flux divergence across all mid-levels ($5 < K_{\overline{w'\theta'}} < 60\%$), and the constant-flux layer is almost non-existent.

Based on the above analysis we conclude that the absence of a constant flux layer in the majority of stability ranges makes the use of surface layer scaling inadequate for the Owens Valley. Only for a narrow range of ζ during weakly stable and the weakly unstable stratification, both the momentum and heat flux divergences are smaller than 10%. Alternative scaling approaches to surface layer scaling are local scaling, mixed-layer scaling and the local free convection scaling (Stull, 1988). During convective conditions, we exclude the possibility of using the mixed-layer scaling, since our measurements are well below the interface of the surface and mixed layers (approximately taken to be $0.1\, z_i$). Wyngaard et al. (1971) explored the idea of local free convection scaling based on the data obtained during the 1968 Kansas experiment. They concluded that, even though L is no longer a significant length in the local free convection region, it might nevertheless be convenient to write local free convection predictions in terms of the usual surface layer scales and z/L. We decide to investigate local similarity scaling rather than the more specific surface layer scaling, following other studies where the concept of constant flux layer was not justified (e.g. Nadeau et al., 2013). Local similarity scaling provides us with an alternate version of the dimensionless groups in the similarity functions, composed of the local friction velocity u_{*l}, local temperature scale θ_{*l}, and local Obukhov length Λ. For the subsequent analysis of the flux-variance functions, all three parameters (2.1)-(2.3) are

calculated with the local values of the momentum and heat fluxes.

2.3.3 Influence of stationarity on the form of the similarity functions

The similarity functions (2.5) and (2.6) include the free parameters $\alpha_{i,\theta}$ and $\beta_{i,\theta}$. The α parameter represents the value of a particular normalized standard deviation in the near-neutral limit and can be interpreted as a measure of the isotropy of the flow (Panofsky and Dutton, 1984; Nadeau et al., 2013). The β parameter determines the deviation of the best-fit curve from the near-neutral value of α. To enforce stationarity, we require simultaneous stationarity of all 30-min second order statistical moments ($\sigma_{i,\theta}$, $\overline{u'w'}$, $\overline{v'w'}$ and $\overline{w'\theta'}$) on the left-hand side of the flux-variance similarity expressions (2.5) and (2.6), with respect to all five stationarity criteria. The fitting parameters $\alpha_{i,\theta}$ and $\beta_{i,\theta}$ can then be determined using a suitable regression method, as discussed below.

Regression approach

Traditionally, the fitting parameters $\alpha_{i,\theta}$ and $\beta_{i,\theta}$ have been estimated using least squares (hereafter LSQ) regression (Detto et al., 2008; Marques Filho et al., 2008; Vesala et al., 2008; Wilson, 2008; Fortuniak et al., 2013; Nadeau et al., 2013; Pegahfar and Bidokhti, 2013; Yusup and Lim, 2014). The fitting parameters are estimated by minimizing the sum of squared residuals. The suitability of such a regression procedure becomes questionable, by giving excessive weight to outliers due to squareing of the residuals. This is because the assumption of a normal, Gaussian distribution of the residuals, is most often violated for surface layer turbulence data. For example, Liu et al. (2011) have shown that, at least for unstable stratification, the probability density functions of vertical velocity w' and temperature θ' fluctuations are non-Gaussian. Here, we perform a regression in a least absolute deviations (hereafter LAD) sense, which minimizes absolute values of the deviations without squareing them. By doing so, LAD is more robust to outliers compared to LSQ. Gray et al. (1993) have shown successful performance of LAD in estimating global and regional predictors in their analysis of seasonal tropical cyclone activities. More recently, Schüttemeyer et al. (2006) have used LAD to relate sensible heat fluxes calculated using eddy covariance instrumentation and a large aperture scintillometer. To our knowledge, there exist no other studies which apply LAD in ABL-based studies, especially to more complex formulations (such as (2.5) and (2.6)). The potential reason for this is that LAD, unlike LSQ, does not have an analytical solving method.

By reducing (2.5) and (2.6) to a linear form $y = ax + b$ to enable computation, we are

able to apply LAD to each of our stationary data sets. The procedure is shown in Appendix B, along with a comparison of the α parameters obtained using LSQ and LAD (Fig. B.1). In the remainder of the study all the fitting parameters $\alpha_{i,\theta}$ and $\beta_{i,\theta}$ are calculated using this more robust regression method, given the better overall treatment of outliers.

Analysis of fitting parameters

The results for the α parameters on all three towers are plotted in Figs. 2.3 and 2.4 for unstable and stable stratification, respectively. Vertical profiles of the β parameters for all towers are shown in Figs. 2.5 and 2.6 for unstable and stable stratification, respectively. Where applicable, we also include values of the free parameters from several other studies that use the same form of the flux-variance relationships (2.5) and (2.6) and that are also based on local scaling. The flat terrain values found in Panofsky and Dutton (1984) are also added for comparison. We note that this comparison with previous studies needs to be taken with a degree of caution. In addition to different types of underlying topography, every study is specific in terms of the used data processing tools, the means of treating non-stationarity, the influences of various surface roughness elements on the flow in the close proximity of the measurement location, and the nature of the flow itself.

Independent of stability and of the stationarity criterion applied (Figs. 2.3 and 2.4), α_u and α_v are consistently larger and α_w is lower compared to the well established flat terrain near-neutral values (2.39, 1.92, 1.25 for α_u, α_v, α_w, respectively). This behavior is consistent for all three locations and does not seem to change with height, although offsets from the flat terrain values tend to be larger for WT than for CT and ST. Even though surface layer turbulence over flat terrain is already anisotropic ($\alpha_u > \alpha_v > \alpha_w$), the latter observation suggests that this anisotropy can be further enchanced in a valley. As explained by Panofsky and Dutton (1984), the longitudinal and lateral wind speed components are primarily governed by large quasi-horizontal eddies while the vertical wind speed component is under the influence of eddies whose size is comparable with the measurement height. Furthermore, Panofsky and Dutton (1984) argue that values of dimensionless $\sigma_{u,v}$ in complex terrain tend to be larger compared to those measured at a flat site due to larger eddies having good memory of the rougher conditions of the upstream fetch. This explanation is also plausible for our results. We hypothesize that α_u and α_v parameters at CT and ST are on average lower compared to those at WT because the fetch at CT and ST is primarily bimodal (Fig. 2.1), with relatively constant surface roughness across the entire valley floor. WT, on the other hand, experiences a larger variety of upwind

roughness conditions (Fig. 2.1). As a result, the largest eddies adapt more slowly to this transition between internal boundary layers over areas of varying roughness (Beljaars, 1987). De Franceschi et al. (2009) argue that α_u and α_v may additionally be affected by the variations in the geometry of the valley. However, α parameters for both cross- and along-valley directions in their case, show the opposite relation to the flat terrain values compared to our results. This might be due to the fact that the Owens Valley is much wider (20 km versus 2 km) and deeper (2500 m versus 1500 m) than the Adige Valley, so the largest, most energetic eddies that encompass the depth of the boundary layer, are unlikely to be constrained by the valley dimensions in our case. Castelli and Falabino (2013) note also that data which correspond to low wind speeds may contribute to the relative increase of α for the wind speed components. Low wind speed conditions most often result in weak turbulent mixing, and standard deviations of wind speed components are normalized by small values of the friction velocity in those circumstances, which overestimates α parameters. Previous studies suggest that the similarity scaling of σ_w might not only be affected by non-stationarity, but also by the choice of the averaging time scale (Wilson, 2008; Mahrt et al., 1998), and by the definition of the friction velocity u_{*l} (Wilson, 2008). In this study we use a 30-min averaging window which is well within the limits proposed by Wilson (2008) but non-turbulent motions may be inadvertently included in the analysis (Vickers and Mahrt, 1997; Mahrt, 2007).

α parameters for stationary data sets, for all wind speed components and both stabilities, exhibit consistent grouping up between the flat terrain parameters and the parameters obtained using the non-filtered data sets. This suggests that non-stationarity increases the turbulence intensity associated with the horizontal wind speed components, while it decreases the intensity of vertical mixing. In other words, it enhances the anisotropic nature of dimensionless standard deviations of wind speed components. Furthermore, the α parameters obtained from the FW96 and IFC data sets seem to always be the closest ones to the corresponding flat terrain values, which might suggest that they might share some common, univocal properties when addressing non-stationarity. On the other hand, during unstable stratification (Fig. 2.3), the α_θ parameters obtained from the stationary data sets do not show any consistent remoteness from the parameters based on non-filtered data sets. During stable stratification (Fig. 2.4) they do exhibit this, again with α_θ for FW96 and IFC data sets showing the largest offset from the α_θ for the non-filtered data set.

Closer examination of the β parameters (Figs. 2.5 and 2.6) shows how the integral turbulence characteristics tend to change their dependence on ζ for different locations in the

valley and for different variables. Contrary to Figs. 2.3 and 2.4 where flat terrain values of the $\alpha_{u,v,w}$ parameters are reported (Panofsky and Dutton, 1984), corresponding "textbook-suggested" flat terrain values for $\beta_{u,v,\theta}$ for unstable and $\beta_{u,v,w,\theta}$ for stable stratification, respectively, do not exist to our knowledge. The most notable feature is a quasi-exponential decrease with height of the $\beta_{u,v}$ parameters at all three towers during unstable stratification (Fig. 2.5), indicating strongest dependence on ζ closest to the surface. This behavior is valid for both the original and stationary data sets and across all three towers. On the other hand, β_w has an erratic behavior with height, often with less agreement between stationary data sets compared to $\beta_{u,v}$. Despite the use of several quality control criteria (Section 2.2) on the standard deviations of potential temperature, both LSQ and LAD (not shown) are still unable to resolve several data sets and their dependency on ζ, resulting in unusually large β_θ parameters. This is also the case for the $\beta_{u,v}$ during stable stratification (Fig. 2.6). De Franceschi et al. (2009) also report some of their β_θ parameters to be ambiguous and difficult to interpret. β_θ values for some of the stationary data sets (especially RUT, FW96 and IFC) tend to be negative, indicating possible inappropriateness of (2.6) for expressing the stability dependence of dimensionless standard deviations of potential temperature (Pahlow et al., 2001). This inappropriateness does not seem to be a result of the choice of the regression method, since both LSQ and LAD-based β_θ for stable stratification are mostly negative. Detailed examination of stationary data sets (not shown) revealed that, due to their stringent treatment of non-stationarity, these data sets do not extend far into the strongly stable limit. As a consequence, the fitting procedure fails in estimating β_θ, even though α_θ parameters (Fig. 2.4) for stable stratification are well within the limits found in the literature (Marques Filho et al., 2008; Nadeau et al., 2013).

2.3.4 Quantification of self-correlation

Self-correlation occurs when a common variable (in our case the local friction velocity u_{*l}) appears on both sides of the equality sign in (2.5) and (2.6). The degree to which it occurs mainly depends on the choice of the scaling variables used to non-dimensionalize standard deviations of wind speed components and potential temperature, as well as on the choice of the regression method used to evaluate the similarity functions. To address this concern, we use the method initially proposed by Klipp and Mahrt (2004). This method is based on randomizing and resampling time series of every variable found in our flux-variance relationships (2.5) and (2.6). These include the local heat flux $\overline{w'\theta'}_l$, local friction velocity $u_{*\,l}$, potential temperature $\overline{\theta}$ and the standard deviation $\sigma_{i,\theta}$. This

randomization with replacement is then repeated 1000 times for all stationary data sets, after which all 1000 coefficients of determination are calculated, then averaged, and a single value of $\langle R^2_{rand} \rangle$ is obtained. This value is a measure of self-correlation due to the common variable. Before this step, the original data sets' coefficient of determination R^2_{data} is computed for each stationary data set. Finally, the difference between these two coefficients $R^2_{data} - \langle R^2_{rand} \rangle = R^2_{diff}$ is interpreted as a measure of the actual fraction of variance attributed to physical processes: as it approaches unity, the effect of self-correlation is less pronounced. If it approaches negative unity, self-correlation has a significant impact on the total variance. Results for both stabilities are shown in Fig. 2.7.

For unstable stratification (Fig. 2.7a), self-correlation has a significant contribution in the case of horizontal velocity components ($R^2_{diff} < 0$). This is an indication that u_{*l} and Λ might be inappropriate scaling variables. Instead, the vertical convective scale w_* and the boundary layer depth z_i might be a more reliable set of variables for scaling σ_u and σ_v during convective conditions (Lumley and Panofsky, 1964; Wilson, 2008). Also, on average, self-correlation has less impact at WT than at CT and ST, and for the vertical wind speed dimensionless standard deviations than for the other three variables. This indicates that local scaling with u_{*l} and Λ is suitable for σ_w. There does not seem to be a preference of any stationarity criterion over the other, since they all share roughly the same range of fraction of actual variance attributable to the governing processes. For $\sigma_{u,v}$, these ranges correspond to $-0.6 < R^2_{diff} < 0.2$, while for σ_w this range is narrower, $-0.1 < R^2_{diff} < 0.5$. The unusually large positive values of R^2_{diff} for FW96 stationary data sets at CT and ST are due to large R^2_{data}, since this stationarity criterion seems to most efficiently remove non-stationary outliers (compared to other four criteria).

During stable, nocturnal conditions, locally scaling standard deviations of wind speed components and potential temperature should be adequate (e.g. Nieuwstadt, 1984). However, Fig. 2.7b seems to suggest that, for nearly all stationary data sets, towers and variables, scaling with u_{*l} and Λ severely suffers from self-correlation. Specifically, with the exception of some R^2_{diff} values at WT for the vertical wind speed component, all other fractions of variances due to physical processes are negative. Unfortunately, this is a limitation of the method suggested by Klipp and Mahrt (2004), since it heavily relies on the coefficient of determination R^2 (see Appendix C for further explanation of this deficiency). This renders drawing any reliable conclusions about self-correlation during stable stratification invalid.

2.3.5 *Influence of stationarity on the goodness-of-fit measures*

Here, we assess the effect of stationarity criteria on the goodness-of-fit measures of the flux-variance similarity functions (2.5) and (2.6). We determine the goodness-of-fit by calculating the amount of scatter for each of the stationarity criterion, relative to the amount of scatter in the original data set, based on the fitting parameters α and β obtained from the original data set. By doing so, the contribution of non-stationarity to the total scatter around the similarity functions is reflected within these parameters. To quantify a potential increase or decrease in the scatter around the similarity functions, we use the median absolute deviation (MAD) with respect to particular stationary data set, normalized by the MAD with respect to the original data set:

$$S = \frac{\text{median}\,|x - \text{median}(x)|}{\text{median}\,|X - \text{median}(X)|} \tag{2.8}$$

In (2.8), x represents the data set after applying each of the stationarity criteria, while X represents the original data set. A MAD ratio S smaller (larger) than unity indicates a decrease (increase) in scatter relative to the original data set. MAD is a more reliable measure of scatter compared to e.g. the mean squared error (MSE), since it is more robust against outliers. Results indicating these ratios are shown in Fig. 2.8.

For unstable stratification (Fig. 2.8a), applying any of the stationarity criteria, in almost all cases results in a decrease in scatter for all standard deviations across all towers. Even so, slightly better reduction in the scatter is noticed at CT and ST compared to WT, especially for the case of dimensionless standard deviations of wind speed components. Generally, FW96 shows the best overall improvement for all four dimensionless standard deviations($0.3 < S < 0.6$). IFC follows as the next best criterion in this sense ($0.3 < S < 0.9$), while RAT, RUT and M98-resulting stationary data sets show relatively common degree of improvement ($0.5 < S < 1.1$). For the latter three criteria, some levels report an increase in scatter, relative to the original data set.

For stable stratification (Fig. 2.8b), there is a much broader range of MAD ratios S, exceeding unity more often than was case for the unstable stratification. Excluding some of these high MAD ratios, there is still an improvement over the original data set when RAT, RUT and M98 are considered, although it is not as large as for the unstable stratification. Occasional poorer performance during stable conditions could also be attributed to the inability of the stationarity criteria to properly detect non-stationarity caused by phenomena such as gravity waves, density currents, and meandering motions. The FW96

and IFC criteria still show more improvement than the other three criteria ($0.1 < S < 0.8$), even more than during unstable stratification.

2.4 Conclusion

In this study, we investigated the effects of the treatment of non-stationarity on the flux-variance similarity functions at two valley locations and one slope location in the Owens Valley, California, during the T-REX field campaign. Stationary data sets were obtained from a previous study (VD15) that applied five different stationarity criteria to the first and second order statistical moments from the two-month data set. To determine if the use of surface layer scaling in these similarity functions is justified for our data set, the underlying assumption of a constant flux layer for surface layer scaling was investigated. A constant-flux layer was found only for a narrow range of stability, making it necessary to use local scaling instead of the more specific surface layer scaling in the similarity functions. We introduce a novel approach for estimating fitting parameters for the similarity functions. Specifically, we apply a regression method (least absolute deviations) which is more robust against outliers, compared to a usually adopted variant (least squares regression).

Our investigation of the local flux-variance similarity functions in Owens Valley can be summarized as follows:

- non-stationarity tends to increase the dimensionless standard deviations with more pronounced anisotropy, that is, more variance in the horizontal than in the vertical direction. Partial removal of non-stationarity by any of the five criteria tends to bring the values of the near-neutral dimensionless standard deviations (α parameters) of all three wind speed components closer to their corresponding flat terrain values. However, the values remain larger over all three sites (especially over the slope site), indicating more anisotropy of the flow than over flat terrain;

- the $\alpha_{u,v,w,\theta}$ parameters behave similarly with height across all three towers, with values deviating more from the reference flat-terrain values at the slope compared to the valley locations. The β parameters show generally the same patterns with height, although more consistently for $\beta_{u,v,w}$ during unstable stratification than for stable stratification. On the other hand, β_θ increases slightly with height for unstable, while it is nearly constant with height for stable stratification;

- assessment of the degree to which self-correlation might impact proper evaluation

of the similarity functions, has revealed that, during convective conditions, dimensionless standard deviations of horizontal wind speed should be scaled with some other scaling variables (e.g. w_* and z_i), rather than locally with u_{*l} and Λ. On the other hand, the same method is not applicable for stable stratification, due to weaker dependence of the dimensionless standard deviations on the stability parameter ζ;

- overall, stationary data resulting from the FW96 and IFC criteria show the most prominent reduction of scatter in the dimensionless variances of wind speed components and potential temperature. Moreover, these two criteria show similar behaviour in most cases (e.g. vertical profiles of α parameters), suggesting that they might share some common favorable properties when treating non-stationarity. Reduction of the scatter is consistent for all three wind speed components and potential temperature and is larger for the stable than for the unstable stratification.

Increasing demands for more accurate weather predictions in complex terrain require the use of improved parameterization schemes which need to properly resolve atmospheric flows on all scales and during all possible stratifications. We can make steps towards improving these paramaterizations by investigating fundamental and implicit properties of the turbulent flow over complex terrain, including effects of non-stationarity as we did in the current study. Flux-profile similarity relationships, rather than flux-variance similarity relationships, are most commonly used in turbulence paramaterization schemes and an investigation of these relationships for the three complex terrain locations in this study, including their sensitivity to the treatment of non-stationarity, will be the next step in our investigations. To gain a better understanding of why non-stationarity enhances anisotropy, for both stationary and non-stationary 30-min intervals suitable spectral analysis should be performed. Finally, more attention will be given to the alternative types of scaling, such as mixed-layer scaling, to properly describe the stability dependence of the integral turbulence characteristics of the horizontal wind speed components during unstable stratification in complex terrain.

Table 2.1: Characteristics of the NCAR ISFF towers in Owens Valley: latitude, longitude, height above mean sea level, average slope inclination, estimated canopy height and zero plane displacement, respectively.

tower	latitude [°]	longitude [°]	h [m]	α [°]	H [m]	d [m]
CT	36°48.091'N	118°09.601'W	1155	0.20	0.8	0.53
ST	36°44.015'N	118°07.376'W	1141	0.20	0.8	0.53
WT	36°45.595'N	118°14.842'W	1529	3.25	0.1	0.07

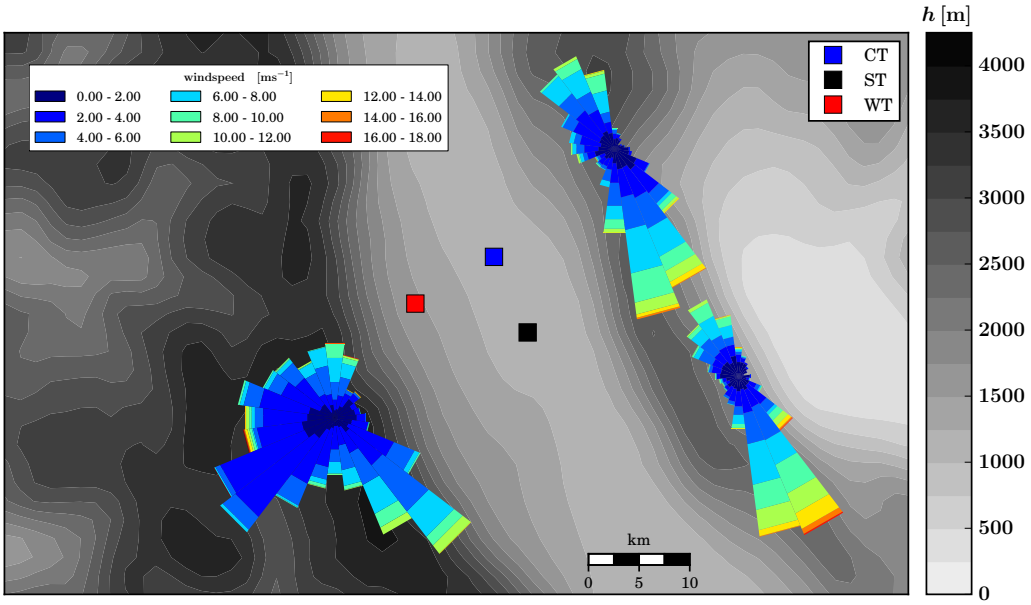

FIGURE 2.1: Topographical representation of the Owens Valley. Blue, black and red circles denote the CT, ST and WT, respectively. Each wind rose is constructed based on data collected at 10m for the two-month period. The position of wind roses are corresponding to the tower locations (top - CT, right - ST, left - WT). The color bar on the right denotes height above mean sea level in meters.

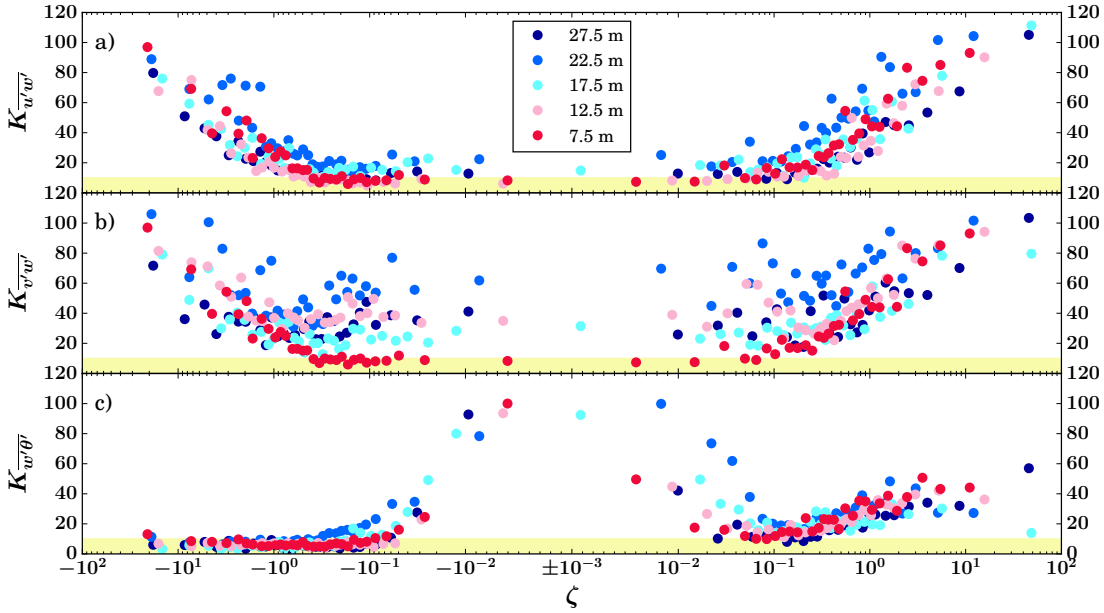

FIGURE 2.2: Composited bin averages (medians shown) of **a** vertical momentum flux $\overline{u'w'}$,**b** vertical momentum flux $\overline{v'w'}$ and **c** vertical heat flux $\overline{w'\theta'}$ divergence coefficients at CT. Color representing each of the five mid-levels is given in the legend. Yellow shaded area indicates the constant-flux layer with a maximum flux divergence of 10%.

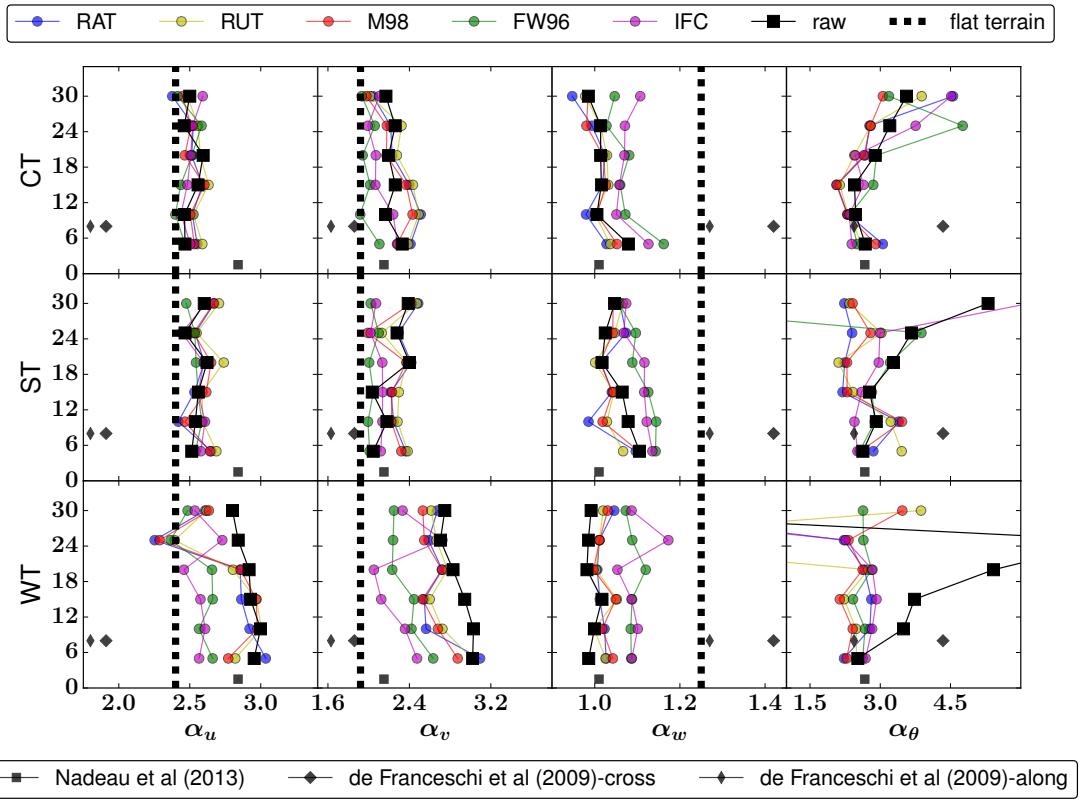

FIGURE 2.3: Fitting coefficients α for the unstable regime ($\zeta < 0$) as a function of height (in meters) at all three towers. First row is for CT, second for ST and third for WT. Color associated with each of the stationarity method is given in the upper legend, together with black dashed lines, which denote the flat terrain values given in Panofsky and Dutton (1984). The α values found in Nadeau et al. (2013) at 1.5 m height AGL are shown as squares, while cross-valley and along-valley α parameters from De Franceschi et al. (2009) are represented by big and small diamonds, respectively. The α_θ parameters are shown on a logarithmic scale for demonstration purpose, due to their exceedingly large values found by the least squares procedure.

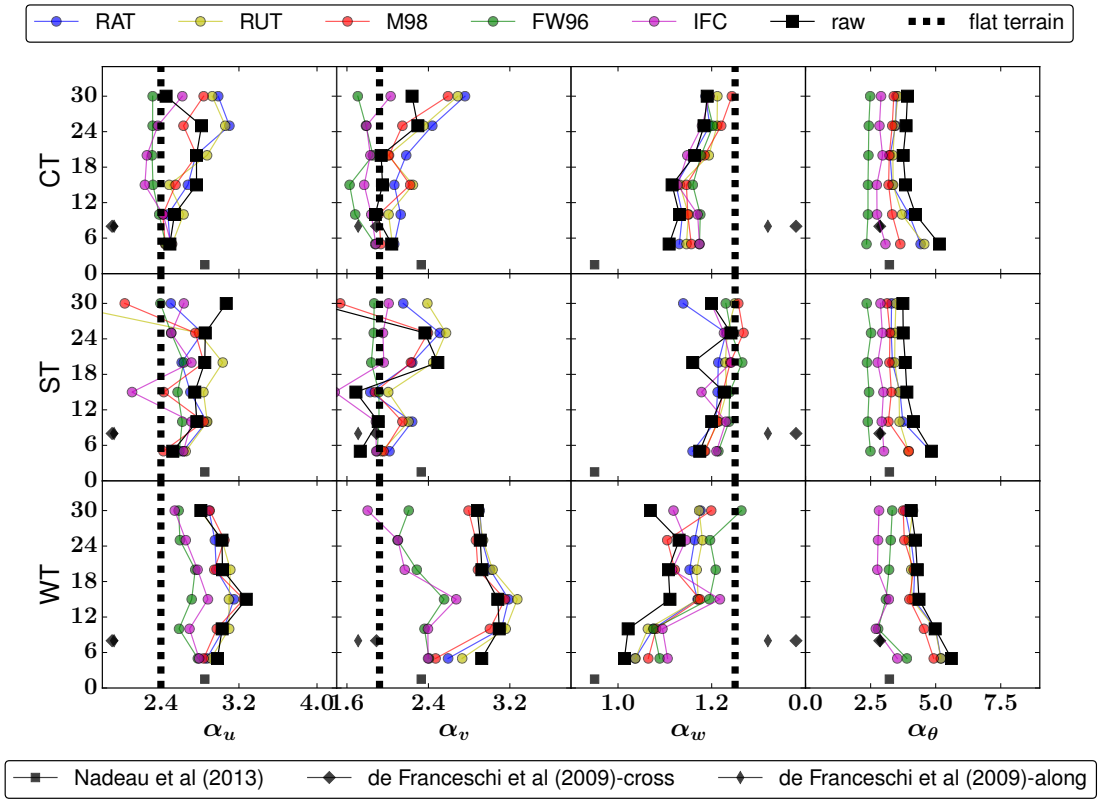

FIGURE 2.4: Same as Fig. 2.3 but for the stable regime ($\zeta > 0$).

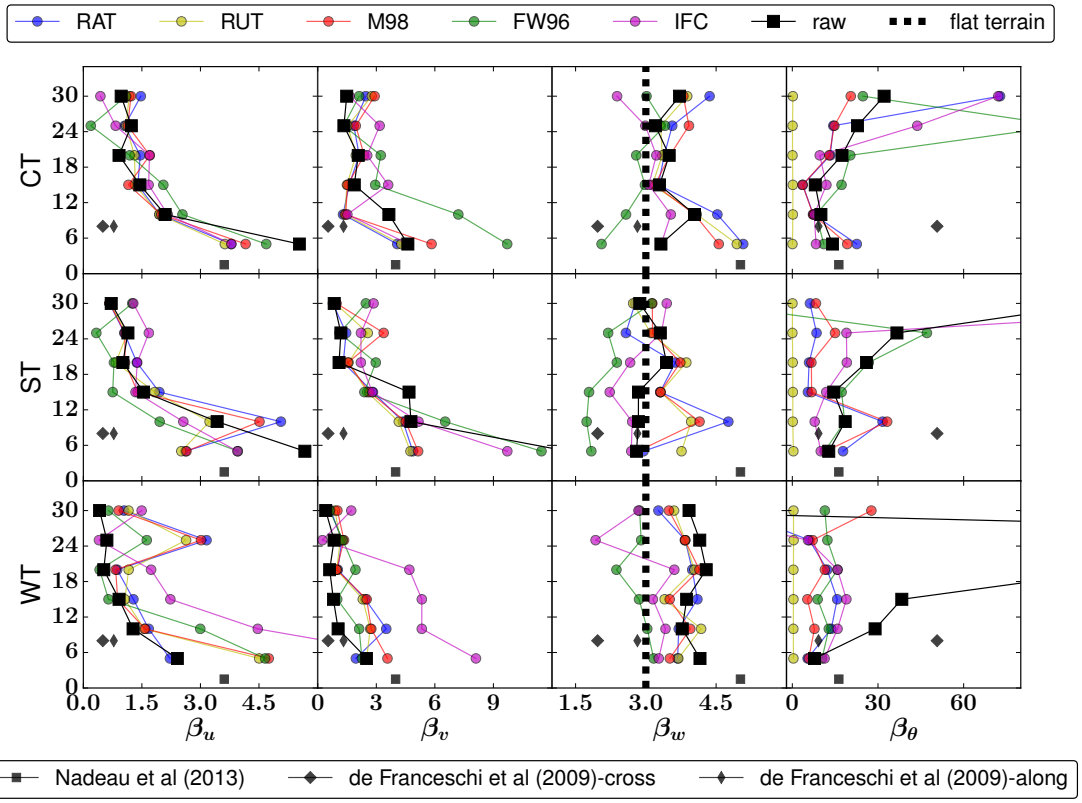

FIGURE 2.5: Fitting coefficients β for the unstable regime ($\zeta < 0$) as a function of height at all three towers. First row is for CT, second for ST and third for WT. Legends are the same as in Fig. 2.3, however only the corresponding flat terrain value for β_w (Panofsky and Dutton (1984)) is shown.

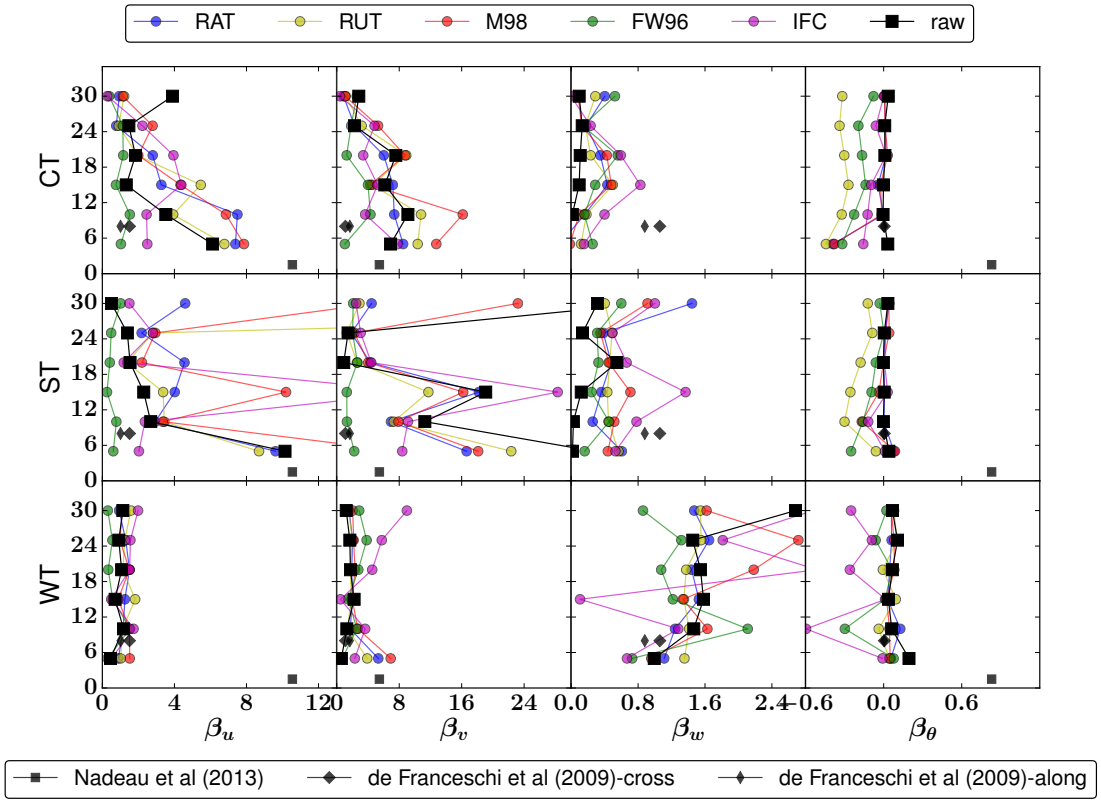

FIGURE 2.6: Same as Fig. 2.5 but for the stable regime ($\zeta > 0$).

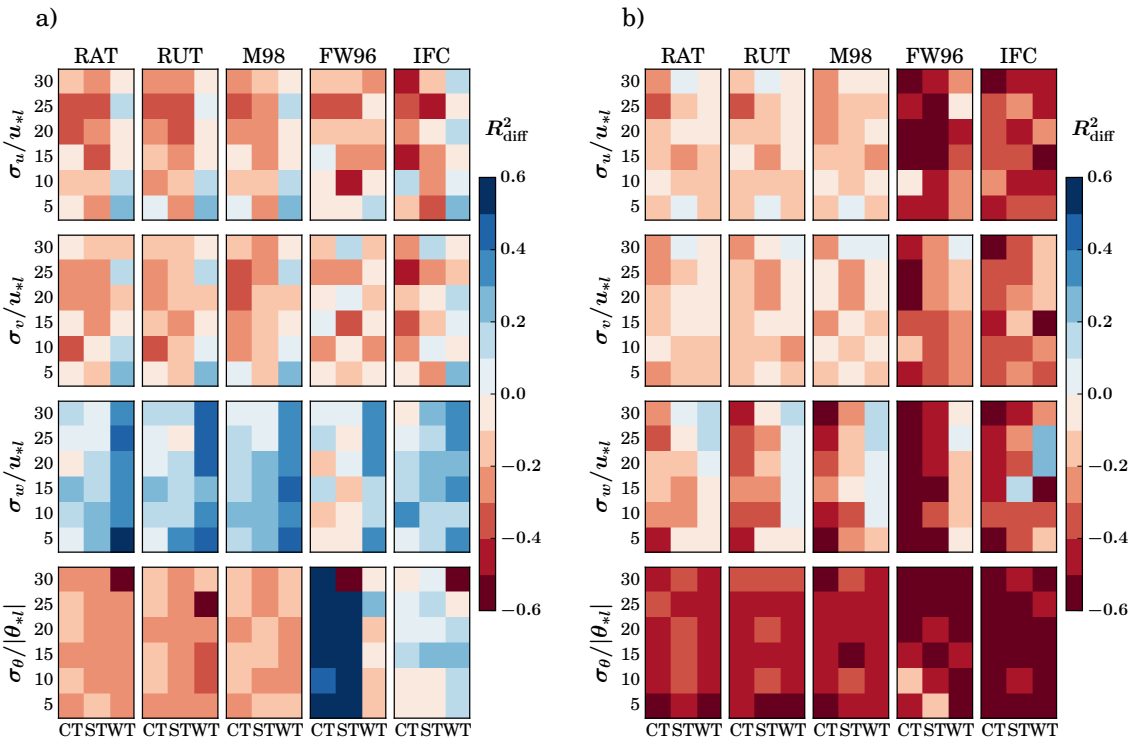

FIGURE 2.7: Values of the difference $R^2_{data} - \langle R^2_{rand} \rangle = R^2_{diff}$ indicating the influence of self-correlation for all five stationarity criteria and for all heights during **a** unstable and **b** stable stratification. First row is for u, second for v, third for w and fourth row for θ.

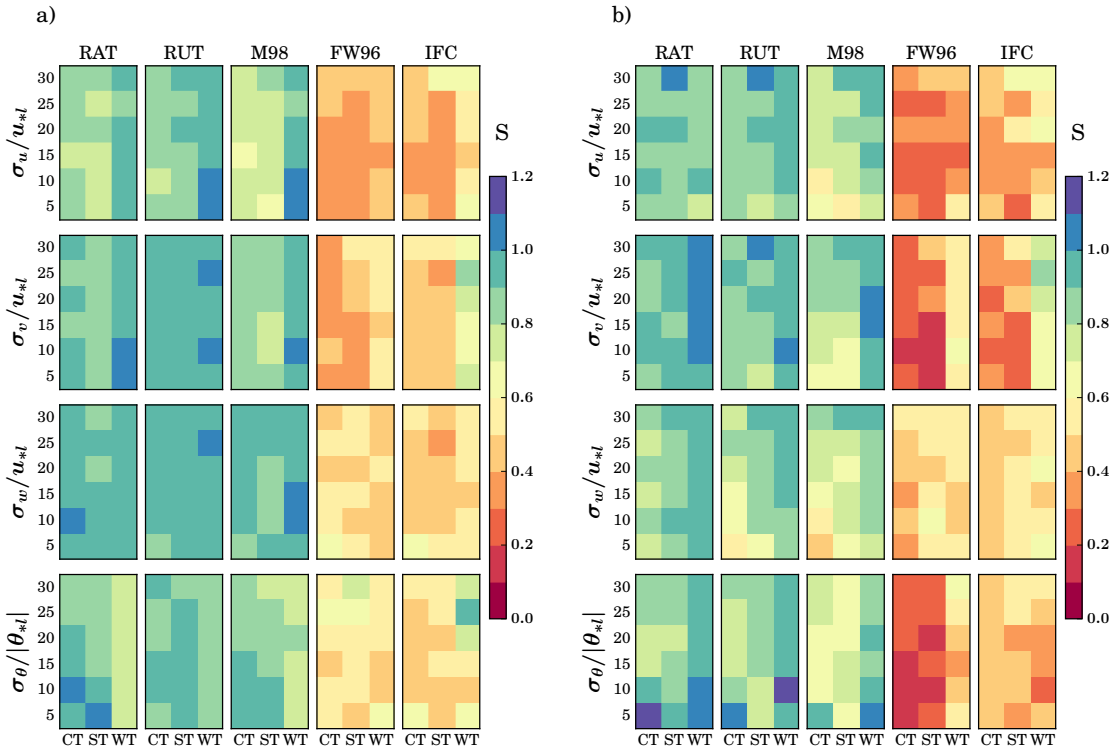

FIGURE 2.8: Values of MAD ratios S indicating an increase/decrease in scatter relative to the original dataset for all five stationarity criteria and for all heights during **a** unstable and **b** stable stratification. First row is for u, second for v, third for w and fourth row for θ.

3

Spectral gap characteristics in a daytime valley boundary layer

3.1 Introduction

[1] The notion of decomposing time series of winds and scalars into a mean and a fluctuating component, represents the cornerstone of the eddy covariance technique. Assuming that the turbulent, microscale motions of interest are separated from macroscale and mesoscale motions by a so-called spectral gap, one can readily apply such a decomposition (Reynolds, 1894). Knowledge of the spectral gap and associated gap time scales (referred to simply as gap scales) is essential for determining the turbulent fluxes of momentum, heat and other scalars within the atmospheric boundary layer (ABL). Proper estimates of these fluxes are crucial for a number of applications, including the calculation of the net ecosystem exchange and the development of new turbulence closure parameterization schemes. Gap scales that are chosen too long or too short can lead to an over- and under estimation of the fluxes, respectively. Therefore, knowledge of gap scales for defining turbulent perturbations is important in ABL meteorology.

The daytime convective boundary layer (CBL) is characterized by intense turbulent mixing on time scales ranging from minutes up to an hour (Stull, 1988). The typical near-surface power spectrum of wind speed is represented by three distinct regions (Kaimal and

[1] Reprinted from Babić, N., Večenaj, Ž., and De Wekker, S. F. (2017). Spectral gap characteristics in a daytime valley boundary layer. Q. J. R. Meteorol. Soc., 143(707), 2509-2523.

Finnigan, 1994): the dissipation region, in which the smallest turbulent eddies eventually dissipate into heat by the action of viscosity; the inertial subrange, in which the turbulent flux is zero and the eddies simply cascade the energy from large towards small scales; and the energy-containing region, in which the largest turbulent eddies are convective thermals spanning the whole CBL depth. These thermals correspond to the major variance-containing time and space scales in the CBL. In the frequency domain, all frequencies lower than those corresponding to the energy-containing region are assumed to belong to the mesoscale and macroscale and do not contribute to the turbulent flux.

By plotting frequency-weighted power spectral density of the longitudinal wind speed component in an energy-preserving log-linear fashion, one can expect to observe a spectral gap (Kaimal and Finnigan, 1994). Despite being a first-order approach with significant subjectivity, this approach yields reasonable gap scale estimates (Van der Hoven, 1957; Metzger and Holmes, 2008; Večenaj et al., 2012; Babić et al., 2016b). A more objective approach is the ogive function analysis (Oncley et al., 1996), which relies on the cumulative integral of a turbulent cospectrum of momentum and scalars. This approach is useful not just for gap scale determination, but also for assessing the influence of gap scales on the surface energy budget closure (Foken, 2008; Charuchittipan et al., 2014) and for investigating the impact of secondary circulations on sensible and latent heat fluxes (Gao et al., 2016). Two more recent approaches that result in the most objective gap scales for both unstable and stable stratification are the multiresolution flux decomposition (MRFD; Vickers and Mahrt, 2003; Voronovich and Kiely, 2007 - VK07; Viana et al., 2010) and the Hilbert-Huang transform (Huang et al., 1998; Barnhart et al., 2012) approach. Unlike earlier approaches, they both have the favourable property of satisfying Reynold's decomposition rules and they both provide the (co)variance decomposition at sufficiently fine resolution for objective gap scale determination.

Micrometeorologists have investigated the spectral gap and its properties since the mid 20th century (see e.g. Larsén et al., 2016, for a historical overview). Van der Hoven (1957) was among the first to prove the existence of a spectral gap. Vinnichenko (1970) corroborated the existence of a spectral gap in the free atmosphere based on a 5-year long data set. Fiedler and Panofsky (1970) postulated the existence of such a gap by using a vorticity cascading model from small towards large wavenumbers (Lumley and Panofsky, 1964). Even these early pioneering studies were well aware of the fact that the spectral gap may not be fully present, depending on the height of the measurement above ground (Caughey, 1977) and on the ubiquitous nature of mesoscale motions, including mountain

and gravity waves, Kelvin-Helmholtz instabilities, meandering motions, downslope windstorms, atmospheric rotors and valley-slope wind systems (Whiteman, 2000). If intense enough, the energy associated with these phenomena may become comparable with the microscale, turbulent energy, thus resulting in a smoothing of the gap.

A number of recent studies have investigated the spectral gap and related gap scales over more complex terrain when synoptic forcing is moderate to strong. Večenaj et al. (2010) were able to successfully determine the gap scale during a Bora downslope windstorm event in the lee of the Dinaric Alps along the eastern Adriatic Coast. At a location further inland, Babić et al. (2016b) were also able to locate the spectral gap for several Bora episodes of varying intensities. Liang et al. (2014) have successfully applied MRFD to data collected at their complex terrain site over the Loess Plateau in China. Sievers et al. (2015) recently conducted a more extensive investigation of gap scales for several sites, including a fjord in NE Greenland where the complex topography influenced the low-frequency, energy-containing region of the turbulent spectrum, hence directly affecting the gap scales. Despite the above efforts, it is still unclear to what extent thermally-driven and terrain-forced flows influence gap scales.

The choice of the study site over complex terrain is essential for the choice of post-processing algorithms (Stiperski and Rotach, 2016). Double rotation, triple rotation and the planar fit rotation act as high-pass filters, thus also detrending the data to a certain extent (Wilczak et al., 2001; Finnigan et al., 2003; Shimizu, 2015; Oldroyd et al., 2016). Stiperski and Rotach (2016) attempted to objectify the optimal post-processing routines for studying turbulence in complex terrain, but it remains unclear whether block-averaging, linear detrending or running mean filtering would be the preferred choice for data collected in a typical CBL over complex terrain. Inappropriate filtering may underestimate both the variances and fluxes during unstable conditions (Stiperski and Rotach, 2016), again calling for a much needed elaborate investigation of the variability of CBL gap scales in complex terrain.

The goal of this study is to provide a comprehensive overview of the daytime gap scales and spectral gap characteristics in Owens Valley, CA, by analyzing data from a suite of in-situ and remote sensing instruments. To achieve this, we will build upon the analysis of Stiperski and Rotach (2016), with the added emphasis on the horizontal velocity variances. Unlike the vertical velocity variance, the horizontal one memorizes the upstream configuration of the topography (Panofsky and Dutton, 1984; De Franceschi et al., 2009; Babić et al., 2016a). Hence, underlying topography may modulate the wind energy spectrum. We

will investigate the relationship between spectral gap characteristics and synoptic forcing, the valley-slope wind system and the potential influence of the "topographic memory". Finally, we will make qualitative inferences about the connection between the spectral gap and mesoscale phenomena such as atmospheric rotors, convective rolls and secondary circulations.

3.2 Data and Methodology

3.2.1 Terrain-Induced Rotor Experiment (T-REX)

We use data from the T-REX field campaign conducted in Owens Valley, CA, during March and April 2006 (Grubišić et al., 2008). The overarching goal of T-REX was the investigation of atmospheric rotors and mountain waves, as well as their interactions with the valley ABL. With an average depth of 2.5 kilometers at the T-REX study site (Fig. 3.1a), Owens Valley represents one of the deepest valleys in the contiguous United States. Its crest-to-crest width is equal to approximately 30 kilometers, while the valley floor is roughly 15 kilometers wide. The valley is bounded by the Sierra Nevada mountain range ("Sierras") to the west and by the Inyo Mountains ("Inyos") to the east. Due to primarily arid conditions persisting throughout the year, the valley surface is covered with low grasses and shrubs, up to one meter tall.

In-situ instrumentation

Three 34-meter National Center for Atmospheric Research (NCAR) Integrated Surface Flux Facility (ISFF) towers were deployed in Owens Valley throughout the entire observational period. We use data from two of these towers in the current study. The first tower, marked as the central tower (CT), was located at the valley floor and separated roughly 9 kilometers from the western tower (WT), which was located at the eastern slopes of the Sierras (Fig. 3.1b). Both towers were equipped with CSAT-3 sonic anemometers (Campbell Scientific, Inc.) at 5, 10, 15, 20, 25 and 30 meters above ground level (a.g.l.). The sonic anemometer measurements were sampled at 60 Hz and then downsampled to 10 Hz to decrease computational time and to mitigate aliasing effects (Kaimal and Finnigan, 1994). Data coverage for the entire campaign and all twelve anemometers is greater than 90% (Večenaj and De Wekker, 2015). Initial screening of the raw data included despiking and outlier removal following well-adopted guidelines (Vickers and Mahrt, 1997). After quality control and assurance, we applied a correction to take into account transducer

shadowing by the sensor probes (Horst et al., 2015). Raw 10 Hz data were then organized into temporal segments of various durations depending on the type of the analysis, ranging from 27.3 min to 1 h 49 min. Following recent recommendations by Stiperski and Rotach (2016), we have also performed a planar fit rotation to align the coordinate system with the mean wind for each temporal segment (Wilczak et al., 2001). For this purpose, the entire 2-month observational period was used to determine the long-term streamline flow plane. A correction for flux loss due to spectral attenuation by path averaging (Lee et al., 2006) is negligible in our case since the measurements were conducted well above the ground.

The high cost of sonic anemometers has restricted their deployment to only a limited number of locations in field experiments. This limits the amount of spatial information about the flow and, consequently, the gap scales. To overcome this, we introduce more robust anemometers into our analysis. Sixteen 10-meter towers were deployed throughout Owens Valley during the entire 2-month observational period, which were part of the Desert Research Institute (DRI) Automatic Weather Station (AWS) network (Grubišić et al., 2008). The location of each AWS, labeled sequentially starting from the northwest corner of the network, is indicated in Fig. 3.1b. Wind speed and direction were measured with propeller-vane anemometers (RM Young 05103-L Wind Monitor) on each AWS at a height of 10 meters a.g.l. Air temperature was also measured at a height of 2 meters a.g.l. with HMP-45C sensors inside a radiation shield. The temporal resolution of the AWS data is 30 s. All sensors were calibrated prior to deployment. The data coverage of all AWS is excellent, with only a single missing 30-s value during the entire observational period. These 30-s data are organized into segments of various durations, ranging from 1 h 4 min to 8 h 32 min, depending on the type of the analysis. For each temporal segment, the coordinate system is rotated into the mean wind. Following rotation, the wind speed is decomposed into the longitudinal u and lateral v wind speed components. Propeller, as well as cup anemometers, have been reported to be well suited for the study of turbulence, in particular the estimation of horizontal velocity variances (Kristensen, 2000; Yahaya and Frangi, 2004), where they can be equally useful as sonic anemometers. This makes them ideal for the study of the spectral gap and the determination of gap scales (Kaimal et al., 1982).

Remote sensing instrumentation

We analyze data from a boundary layer wind profiler, the NCAR Integrated Sounding System 2 (ISS2), located on the western slope close to AWS-2 (Fig. 3.1b). ISS2 is a ver-

tically pointing 915 MHz UHF radar that relies on the Doppler Beam Swinging technique to detect backscatter from clear-air turbulence and precipitation and to derive horizontal and vertical wind speed and direction every 30 min (Parsons et al., 1994). During T-REX, ISS2 was deployed in the low altitude mode, providing a range gate resolution of 100 m starting from 120 m a.g.l.

To complement the vertical profiles of horizontal wind speed and direction obtained with the ISS2, we also analyze the vertical profiles of virtual temperature measured with the NCAR Multiple Antenna Profiler Radar (MAPR) Radio Acoustic Sounding System (RASS), located approximately 2 km southwest of AWS-4 (Fig. 3.1b). The time resolution of RASS data is 30 min, with a range gate resolution of 60 m starting from 120 m a.g.l.

3.2.2 Categorizing synoptically forced and non-forced days

When synoptic forcing aloft is weak to nonexistent, the valley CBL grows along with a non-disturbed evolution of the valley and slope flows (De Wekker and Kossmann, 2015). Wind direction reversal of upslope and upvalley flows is expected to occur during both the morning and evening transitions due to reversal of horizontal temperature and corresponding pressure gradients (Whiteman, 2000). As pointed out by Zhong et al. (2008), mechanisms such as forced channeling, pressure-driven channeling and downward momentum transfer, may all disturb the quiescent CBL evolution. This disturbance of the CBL evolution was recently found to be dependent on the location in the valley and time of day, specifically tied to the occurrence of intense westerly windstorms (Serafin et al., 2017). Hence, to isolate synoptically driven days from those that experienced a thermally-driven wind shift associated with weak to no synoptic forcing, we define three categories (see also Appendix D): "Wind Shift" (WS): weak to no synoptic forcing during daytime, favoring a diurnal wind direction shift; "Synoptic Upvalley" (SU): strong synoptic forcing, favoring consistent daytime upvalley flows with a single or no wind direction shift during the transition periods and "Synoptic Downvalley" (SD): strong synoptic forcing, favoring consistent daytime downvalley flows with a single or no wind direction shift during the transition periods. This classification emphasizes the importance of wind direction steadiness which is a prerequisite for sufficiently stationary time series intended for (co)spectral analyses that we perform later in the study. Large daytime wind direction variability increases the risk of (co)spectral analysis falsely recognizing this variability and adding artificial energy into the spectral gap (Kaimal et al., 1982). Such import of energy is related to a violation of the Wiener-Khintchine theorem for a random, stationary process, which is evidenced in

a plot of wind energy vs. frequency as a +1 spectral slope at the low-frequency lobe of the energy-containing region (Lumley and Panofsky, 1964). This approach to wind direction classification prevents us from investigating the gap scale variability during the transition periods, which remains an open question.

The wind climatology of the three categories is shown in Fig. 3.2. Only AWS-1 through AWS-6 are shown here, as a representation of flow variability across the valley. As expected, both of the upvalley categories (WS and SU) show consistent south-southeasterly, upvalley flow throughout the day (Fig. 3.2d,e). The main difference between these two categories lies in the transitional periods: nighttime north-northwesterly downvalley flows indeed occurred on WS days but not on SU days. WS days experience weaker winds compared to the SU days, a result of weaker downward momentum mixing and weaker synoptic influence. Winds are the weakest during the morning of WS days (Fig. 3.2a) and show a weak signature of upslope flows until 11 LST, particularly for the western slope locations (AWS-1,2,3). As already pointed out by Babić et al. (2016a), these upslope flows are gradually overpowered by more intense upvalley flows as morning progresses. Surprisingly, the upslope wind also occurs on SU days except at AWS-6 (Fig. 3.2e). Slight veering of winds towards downslope flows occurs at all six locations around 15:00 LST on WS days, accompanied by weakening of winds across the valley. This occurs first at AWS-1 and lastly at AWS-6, a result of the eastward propagation of the shadow front cast by the Sierras. On the other hand, the winds remain upvalley throughout the late evening and following night of SU days. During early afternoon (after 13:00 LST) on WS days, the CBL deepens sufficiently so that downward momentum mixing becomes pronounced, resulting in a cross-valley gradient of along-valley wind speed similar to that of the SU category (where upvalley flows already start around 10:00 LST). We conclude that the synoptic influence results in an earlier onset of downward momentum mixing. Unlike WS and SU days, SD days show steady north-northwesterly, downvalley flow across the entire valley which persists on those days (Fig. 3.2f) and decreasing wind speed during daytime (Fig. 3.2c).

3.3 Results

In this section, we first obtain gap scale estimates using data from propeller-vane anemometers (AWS) and then from sonic anemometers (NCAR-ISFF). We will relate these gap scales to synoptic forcing, wind speed, and location in the valley.

3.3.1 Propeller-vane-based gap scales

For obtaining objective gap scale estimates using data from the propeller-vane anemometers, we apply two approaches to the u wind speed component.

Fourier spectral analysis

A simple, straightforward first-order approach to estimate gap scales and examine the bulk properties of the spectral gap is the fast Fourier transform (FFT). We apply FFT to each day from all three categories, from 08:00 LST to 16:32 LST, i.e. an 8 h 32 min period, similar to Kaimal et al. (1982). Such long periods are required to ensure that the spectral gap is not influenced by the low-frequency end of the spectrum. Once calculated, an average frequency-weighted power spectral density is obtained for each AWS and for each category. To increase statistical robustness further, pairs of AWS in the along valley direction are averaged.

Figure 3.3 shows the final result after these steps. The spectral gap is evident at all six cross-valley AWS combinations and independent of synoptic forcing. The gap is approximately between 10 and 100 min for the AWS on the western slope, and between 10 and 50 min for the AWS closer to the valley floor. The gap shows a cross-valley gradient, becoming deeper and wider from the westernmost AWS (1+7) and the easternmost AWS (6+12) towards the AWS on the valley floor (4+10, 5+11). The FFT-based approach reveals that a gap scale in the range 10-50 min should capture the full extent of the daytime turbulent spectrum, particularly at the valley floor.

MRFD

The MRFD (Appendix E) is more robust than the FFT in determining the most suitable gap scales for variance and flux calculations (Vickers and Mahrt, 2003). However, the approach has so far only been applied to high-frequency data from sonic anemometers. Here, we extend this approach to the coarser AWS data. We apply MRFD to segments 2 h 8 min in duration. To increase statistical robustness and take into account changing atmospheric conditions, we overlap each of these windows by shifting them 1 hour forward in time, which results in a total of 7 windows for each day. The gap scales are then estimated for each temporal segment using the algorithm of VK07 (Appendix F), through identification of local extremes, zero crossings and inflection points in the (co)variances in question.

An example of the application of the algorithm is presented in Fig. 3.4a. As expected, the MRFD u variance from a subset of AWS data does not exhibit a zero crossing (Fig. 3.4a), since variances are positive-definite. Even so, the algorithm successfully estimates the gap scale at 25 min, owing to the presence of a local minimum in energy, indicative of a spectral gap. The increase in energy at longer periods is a manifestation of mesoscale and macroscale influences. We note that the small number of points in the MRFD u variances from the propeller-vane data increases the sensitivity of the fitting algorithm to outliers. In the following analyses we will perform several averaging steps for each AWS to further mitigate this sensitivity.

In the remainder of the paper, we will refer to the gap scale for a particular variable using its mathematical notation τ_{xx}, where x is the variable of interest. We present the dependence of τ_{uu} on wind speed and on elevation of each AWS for the three categories in Fig. 3.5. At first glance, it is obvious that the range of gap scales shown in Fig. 3.5 is well within the range proposed earlier based on Fig. 3.3, i.e. 10-50 min. WS days exhibit the largest spread of gap scales valley-wide, ranging from 17 to 30 min (Fig. 3.5a). On the other hand, SU days exhibit the most limited range out of all three categories, placing the ideal gap scale between 20 and 27 min (Fig. 3.5b). The average valley-wide gap scale increases from quiescent conditions (WS) to synoptically-driven upvalley conditions (SU) to synoptically-driven downvalley conditions (SD). This is in accordance with Fig. 3.3, and may be explained by the high susceptibility of the low-frequency end of the energy-containing region to mesoscale phenomena, such as mountain waves and atmospheric rotors.

Color-coding the data points in Fig. 3.5 as a function of AWS elevation reveals that gap scales generally tend to increase towards the valley sidewalls, particularly on SU and SD days. For WS days this is less clear, as the smallest gap scales occur at mid-slope stations. However, the spread of the gap scale values is larger for the WS days and hence the influence of position across the valley is stronger for the WS days than for the SU and SD days. The increase of energy in the gap towards the western slope (Fig. 3.3a-c) could be related to stronger coupling between the CBL and the mesoscale at those elevations. Finally, regardless of the synoptic category, τ_{uu} tends to decrease with increasing wind speed. VK07 explain this behavior from the tendency of the main variance carrying eddies, i.e. convective thermals, to break up with an increase in shear associated with strong winds. This mechanism narrows the energy-containing region, shifting the gap toward smaller scales (i.e. higher frequencies).

Based on Fig. 3.5, we propose a simple valley-wide parameterization of τ_{uu} for each of the three categories, which only depends on the wind speed U:

$$\tau_{uu,\mathrm{WS}} = -3.25\,U + 38.72, \quad r^2 = 0.33 \tag{3.1}$$

$$\tau_{uu,\mathrm{SU}} = -2.00\,U + 37.64, \quad r^2 = 0.66 \tag{3.2}$$

$$\tau_{uu,\mathrm{SDa}} = -2.73\,U + 43.71, \quad r^2 = 0.25 \tag{3.3}$$

$$\tau_{uu,\mathrm{SDb}} = -3.14\,U + 48.39, \quad r^2 = 0.67 \tag{3.4}$$

The second parameterization for SD (Eq. 3.4) is introduced to improve the goodness of fit after removal of the four AWS with the smallest gap scales that deviate from the apparent dependency (dashed line in Fig. 3.5c). We note that this very robust type of a parameterization disregards the stability dependence of gap scales (VK07) and may seem unsuitable for low wind speed conditions, as the gap scales on the order of more than 30 min would require averaging times of one hour or more, not the 30 min typically adopted within the eddy covariance framework. The longer averaging times are not entirely surprising, since the time scales of motions in the low-wind, free convection regime (Wyngaard et al., 1971) are much longer than in their stable counterparts, and longer T is required for sufficient convergence of ensemble turbulent statistics (Lenschow et al., 1994; Foken, 2008; Metzger and Holmes, 2008). Stiperski and Rotach (2016) also suggest that averaging times longer than 30 min are preferred when studying turbulence statistics in complex terrain. Parameterizations such as Eqs. 3.1-3.4 are useful since they rely on easily measurable quantities and facilitate the comparison with gap scales in other valleys.

The regular mesh configuration of 16 AWS analyzed in this study enables us to construct a contoured map of daytime gap scales in Owens Valley (Fig. 3.6). A minimum τ_{uu} equal to 17 min is observed at the valley floor, while a maximum of 29 min is characteristic of the western slope. τ_{uu} exhibits along-valley homogeneity and appears to increase at a slower rate at the eastern slope compared to the western slope.

3.3.2 Sonic-based gap scales

VK07 have shown that, depending on the dominant carrying eddy motion, each (co)variance may have its own respective gap scale. In other words, setting a fixed gap scale running mean length instead of a (co)variance-dependent one might introduce serious under- or overestimations, particularly in turbulent fluxes. To investigate how the gap scale varies as a function of the (co)variance, we use sonic anemometer data.

The twelve sonics on CT and WT also allow for an investigation of the dependency of gap scales on height. We do this for the three synoptic categories and for u, w and θ variances and uw and $w\theta$ covariances. We apply MRFD to temporal segments 1h 49 min in duration, followed by the application of the VK07 algorithm to determine the gap scales for each of the five (co)variances. An example of gap scale retrieval using sonic anemometer data is presented in Fig. 3.4b. The VK07 algorithm detects a root (i.e. a zero crossing) in the case of the MRFD $w\theta$ covariance (Fig. 3.4b), with a corresponding gap scale of 14 min. Beyond this period, the MRFD covariance begins to increase again with sporadic zero crossings, a manifestation of mesoscale heat fluxes that are poorly sampled and not scalable with similarity theories. As was done with AWS data in the previous sections, we overlap these temporal segments by shifting them approximately 54 min forward in time, resulting in a total of 8 segments for each day. An average gap scale is then obtained for each height by averaging all retrieved gap scales for each category. Figure 3.7 shows the variation with height of the obtained gap scales. Note that data from CT and WT are representative for the valley floor and the western slope, respectively. All five gap scales show similar range of values across the entire flux tower height, within the limits observed in Figs. 3.5 and 3.6, i.e. 17-29 min. τ_{uu} estimates are larger at the western slope than at the valley floor and are larger for the SU and SD days than for the WS days, in agreement with the results for the propeller-vane-based estimates presented earlier in Figs. 3.5 and 3.6. However, compared to their propeller-vane-based counterparts, sonic-based τ_{uu} are larger by about 2 min at the valley floor and by about 5 min at the western slope.We have found the coarser sampling rate of the propeller-vanes to be mainly responsible for this discrepancy, since the major features of interest in the spectra are found to be shifted toward smaller gap scales when the spectra based on 10-Hz sonic data are compared with spectra obtained using sub-sampled (block averaged) sonic data (not shown). Nevertheless, the similarity of the cross-valley gradient observed in τ_{uu} estimates from sonics and propeller vanes shows promise for the use of propeller-vane data to estimate gap scales.

Among all five gap scales, the ones associated with the temperature variance $\tau_{\theta\theta}$ are generally the smallest. τ_{uu} and $\tau_{\theta\theta}$ show negligible height variability, while τ_{ww}, τ_{uw} and $\tau_{w\theta}$ generally increase with height, converging towards a value of 30 min at 30 m regardless of synoptic forcing. This increase with height is mainly due to decreasing eddy sizes toward the surface, shifting the gap scales toward shorter periods (Vickers and Mahrt, 2003). The τ_{uu} exhibit overall the largest spread, while the spread is smallest for $\tau_{\theta\theta}$. Finally, the gap scales associated with the covariances seem to be less sensitive to synoptic forcing compared

to those associated with the variances. In other words, variables such as turbulent kinetic energy (which is comprised of variances) are more affected by synoptic influence than turbulent fluxes (i.e. covariances) of momentum and of scalars.

3.4 Discussion

To explain possible physical mechanisms that control the variability in the spectral gap and the gap scales obtained earlier, we investigate in more detail the possible influence of the topography on the wind spectrum, as well as the significant energy peaks around 80-200 min (Fig. 3.3). We also make qualitative inferences pertaining to possible influences of mesoscale phenomena over complex terrain on the spectral gap and the gap scales determined earlier. Finally, the findings from this study are summarized into a conceptual diagram of the daytime valley spectral gap.

3.4.1 Influence of the "topographic memory" on the spectral gap

Panofsky et al. (1982) have investigated how velocity spectra respond to sudden changes in surface roughness and different topographic features. They have shown that the u and v spectra are particularly sensitive to terrain, contrary to the w spectrum. The terrain effects became evident through an addition of energy at the low-frequency end of the horizontal velocity spectra. This, in turn, may influence the gap scales as well. We now analyze the data from the propeller-vanes to investigate possible terrain influences on the horizontal velocity spectra in Owens Valley.

For AWS-1 through AWS-6 and for all three synoptic categories, we organize time series of u and v wind speed components into temporal segments 1 h 4 min in duration starting at 08:00 LST, which we shift 16 min forward in time to increase sample sizes. This results in a total of 28 temporal segments for each day. We linearly detrend each temporal segment and apply the FFT, similar to previous work (e.g. Kaimal et al., 1972). The obtained power spectral densities are then frequency weighted and normalized by the square of the variance of the respective wind speed component. Temporal segments for which the turbulent intensity $\sigma_u/U > 0.5$ (U being the segment mean wind speed), i.e. segments that do not satisfy the Taylor's frozen turbulence hypothesis (Stull, 1988), are discarded. To obtain a station-representative spectrum, we average the spectra for each synoptic category. These averaged spectra are plotted in Fig. 3.8 as a function of the non-dimensional frequency $f = nz/U$. We note here that any direct comparison with the Kaimal near-neutral spectra is not possible due to normalization with the variance instead

of the friction velocity u_* and dimensionless dissipation rate ϕ_ϵ which are not measured at the AWS. Despite such normalization, we report relatively good collapse of the spectra at the high-frequency end ($f = 0.005 - 0.03$) which closely follow the $-2/3$ slope, indicative in our case of the mixed layer inertial subrange (McNaughton, 2004b).

Although some variability is present between $f = 0.0007 - 0.002$, both u and v spectra collapse well at the low-frequency end for all AWS and all three categories. The valley spectra shown here agree reasonably well with earlier observations. For example, Van Gorsel et al. (2003) report minimal spectral disturbances at the low-frequency end in and above their forested slope of the Riviera valley. They reasoned that large scale eddies (i.e. convective thermals) that are stationary with respect to the topography, are represented by spectral peaks. Our study shows that these spectral peaks vary across the Owens Valley and as a function of synoptic forcing. This, in turn, may be related to spatial variability in CBL depths (De Wekker and Kossmann, 2015). We conclude that valley dimensions generally do not modulate the high-frequency end of the spectral gap. Magnago et al. (2009) also showed that the spectra for the along-valley footprint in a narrow valley in southern Brazil compared reasonably well with the Kaimal near-neutral spectra.

To conclude, spectra for the entire cross-valley section show similar behavior at the high-frequency end of the gap with some cross-valley variability in the spectral peaks. Differences are very subtle and do not offer plausible evidence that valley geometry affects gap scale variability.

3.4.2 Valley-slope flow system

The spectra shown in Fig. 3.3 were characterized by broad spectral peaks with periodicities between approximately 80 and 200 min, thus adding significant energy into the spectral gap. We discuss here how these peaks may have been caused by the daytime valley-slope flow system. To this end, we first investigate how we can detect upslope flows and examine some of their characteristics.

Detection of upslope flows

Detection of upslope flows in Owens Valley is complicated by a number of factors, in particular by their masking by the much stronger upvalley flow early in the day (Fig. 3.2d,e). Given the difficulty of detecting these flows in mean wind speed and direction, we consider their turbulent aspect. As pointed out by Rotach et al. (2008) (R08), the momentum flux is fundamentally different in a valley compared to flat terrain (Kaimal

and Finnigan, 1994). Namely, the friction velocity u_* should be defined as a combination of the so-called frictional shear $\overline{u'w'}$ and directional shear $\overline{v'w'}$. Central to testing our hypothesis that the spectral peak at 80-200 min is caused by upslope flows, is Fig. 10 from R08. According to that figure, the directional shear signature caused by upslope flows is due to a vertical offset between the near-surface upslope flow and the mid-valley flow, being largest for a $\pm 90^\circ$ offset. Near the surface, the sign of directional shear is expected to be negative at the slope to the right of the upvalley flow (cf. Fig. 15f in Weigel and Rotach, 2004) and positive at the slope to the left of the upvalley flow (cf. Fig. 15d in Weigel and Rotach, 2004). Catalano and Moeng (2010) and Schmidli (2013) report these cross-valley shear stresses in high-resolution idealized numerical simulations. For the western slope of Owens Valley where turbulence measurements were made, the sign of directional shear is then expected to be positive on WS and SU days, and negative on SD days. It is this directional shear which we will use as a signature for the presence of upslope flows.

We observed directional shear values (not shown) that were one to two orders of magnitude smaller than in the Riviera valley (Van Gorsel et al., 2003, Weigel and Rotach, 2004; R08), resulting from the gentler sloping sidewalls of Owens Valley. Given the very small values and since different scales of motion may contribute substantially but with opposite signs, we now turn to the decompositioning of the directional shear, i.e. the lateral momentum flux $v'w'$, into scales of different eddy sizes. To this end, we apply MRFD to sonic data at the 10 m level at CT and WT for all three synoptic categories (we do not apply the FFT for this purpose since it does not satisfy Reynolds' decomposition at each decomposed scale of motion). Temporal segments of v and w 27.3 min in duration are subject to MRFD. To increase statistical robustness, we advance each segment 13.6 min forward in time, resulting in 38 segments per day. Since MRFD satisfies Reynold's decomposition at all scales, we calculate a cumulative MRFD vw covariance ($\sum D_{vw}$) by summation from small toward larger periods. An identical philosophy is used in the ogive approach (Oncley et al., 1996). Intepretation in terms of length scales is more intuitive compared to frequency scales. Hence we apply Taylor's frozen turbulence hypothesis and filter out all temporal segments for which $\sigma_u/U > 0.5$. We sort all $\sum D_{vw}$ covariances with respect to wind direction, and average them together into bins. To obtain the same number of curves in the resulting figure, we average together 20 (WS), 50 (SU) and 20 (SD) individual $\sum D_{vw}$ covariances. We prefer equal bin sizes over equal bin spacings within each category, to achieve consistent weighting of events among bins and to decrease the influence of random errors. The final step involves invoking Taylor's frozen turbulence

hypothesis, by multiplying temporal scales with the bin-averaged wind speed U to obtain the desired length scales. Only qualitative assessments are meaningful when interpreting resulting length scales larger than approximately 5 km, since Taylor's hypothesis is not applicable to the mesoscale (Klipp, 2014).

Figure 3.9 shows the resulting decomposition of directional shear as a function of eddy scales at CT and WT. The rightmost point of each curve denotes the value of the total directional shear. On WS days, $\sum D_{vw}$ is positive at WT (Fig. 3.9d), in agreement with the conceptual framework of R08. However, eddy sizes less than roughly 100 m first contribute to negative directional shear, indicating that the smaller eddies most likely exhibit downward transport of $v'w'$ momentum, similar to $u'w'$. Eddies larger than 100-200 m then add positive directional shear, all the way to the mesoscale. These positive contributions to $\sum D_{vw}$ from larger eddies are attributed to upslope flows. A surprising, perhaps even contradicting, finding is the qualitatively identical evolution of directional shear in the case of SU days compared to the WS category (Fig. 3.9b,e). Synoptic disturbance is usually expected to weaken or even completely inhibit the evolution of the conceptual valley-slope flow system. The directional shear decompositioning as presented here has enabled us to show the existence of weak upslope flows, even in the presence of downward mixing of synoptic-scale flows which usually negates their existence (De Wekker and Kossmann, 2015).

Similar results are obtained for the SD category (Fig. 3.9c,f), but now the sign of directional shear is negative at the slope across all scales. As with WS and SU, we do not observe leveling off of the $\sum D_{vw}$ covariance at WT, but rather an increasing contribution from eddies larger than 200 m. A leveling off is again observed at CT (Fig. 3.9c), indicating the absence of upslope flows at the valley floor. R08 indicate that the slope wind system may be evident even after the thermally-driven valley wind system has fully developed. Our results show that this statement is also valid for the synoptically influenced valley wind system.

Periodicity of observed upslope flows

While the previous analysis has shown that upslope flows are present over the sidewalls of the Owens Valley, the 80-200 min spectral peaks in Fig. 3.3 are yet to be explained. We hypothesize that the interplay of near-surface and mid-valley flow is the underlying cause of this periodicity. To investigate this, information about the vertical flow structure is needed which we obtain from the ISS2 wind profiler measurements over the western slope (Fig.

3.1b). Figure 3.10 shows time-height Howmöller diagrams of wind direction, resulting from circular averaging across all days for each category. Direct comparison of the lowest range gate (120 m a.g.l.) and winds measured at AWS-2, the closest in-situ station (Fig. 3.2), reveals very good correspondence for all three categories. To define the mid-level valley flow, we average (in a circular sense) the wind direction for the four range gates confined by the Sierras and Inyos ridgetops. From this value we subtract the wind direction from the lowest range gate, which is sufficiently representative of the near-surface flow. This methodology follows the concept of the aforementioned schematic figure from R08, where any non-zero difference in wind direction between the near-surface and mid-valley flow is expected to generate non-zero directional shear, our signature for the presence of upslope flows.

The calculated wind direction differences shown in Fig. 3.11 directly reinforce conclusions drawn from Fig. 3.9. For the case of WS days, the wind direction difference is equal to nearly $+90^{\circ}$, resulting in the positive directional shear observed earlier in Fig. 3.9d. In the course of a WS day, this difference decreases, pointing to upslope flows becoming gradually overpowered by upvalley flows. On SU days, the difference settles around $+45^{\circ}$. This smaller difference between mid-valley and near-surface flow partly explains the smaller values of $\sum D_{vw}$ covariances compared to the WS case (Fig. 3.9d,e). Finally, SD days show a -45° difference in the morning approaching zero by mid-afternoon. The opposite sign of the difference here is a confirmation of the earlier observed negative $\sum D_{vw}$ covariances (Fig. 3.9f).

Figure 3.11 supports our hypothesis that upslope flows are causing the 80-200 min spectral peak (Fig. 3.3). Periodical jumps of the wind direction difference to $+90^{\circ}$ are observed to take place on WS days approximately every 90 min prior to 13:00 LST (indicated by black arrows), and then less frequent (every 120-150 min) until late afternoon (18:00 LST). Similar behavior occurs on SD days, where the jumps are closer to -45° of difference and take place every 90-120 min throughout the day (indicated by light gray arrows). This explains the spectral peaks for WS and SD days. However, the twice daily occurrence of such jumps on SU days, at 09:00 LST and 15:00 LST (indicated by two dark gray arrows), is not observed in Fig. 3.3 as a separate peak at a period of roughly 360 min. The temporal segments which were previously used to generate Fig. 3.3 are 8 h 32 min in duration, and not sufficiently long to detect such cycles.

To further quantify the observed periodicity of upslope flows in Owens Valley and confirm the apparent evolution of this periodicity over time, we apply the theoretical

prediction of oscillating anabatic and katabatic flows, derived by Bastin and Drobinski (2005) for a sea breeze over a gentle slope. Essential to the model is the presence of a horizontal mesoscale temperature gradient, caused by cold air advection by the sea breeze. In a valley, the cold air advection is tied to upslope flows, hence allowing us to extend the model of Bastin and Drobinski (2005) to a valley. The pulsation frequency of anabatic, upslope flows reads as:

$$\omega = \sqrt{\frac{g}{\theta_0} \sin\alpha \left(\frac{\partial(\overline{\theta} + \theta^*)}{\partial x} \cos\alpha + \Gamma \sin\alpha \right)}, \tag{3.5}$$

where g is gravitational acceleration, θ_0 is surface potential temperature, α is slope inclination, $\frac{\partial\overline{\theta}}{\partial x}$ is the horizontal mesoscale temperature gradient, $\frac{\partial\theta^*}{\partial x}$ is the horizontal temperature perturbation gradient and Γ is the vertical lapse rate. According to Bastin and Drobinski (2005), the $\frac{\partial\theta^*}{\partial x}$ term is progressively smaller during the day due to convection and may be neglected. $\frac{\partial\overline{\theta}}{\partial x}$ is estimated as the central difference between air temperature measurements at AWS-2 and AWS-14 for WS and SU, and for AWS-13 and AWS-3 for SD (Fig. 3.1b). Different gradients are used to accommodate the different prevailing along-valley directions for 1) WS and SU and 2) SD days (Fig. 3.2d,e,f). AWS-8 is closest to the mid-point of the two central differencing schemes from which $\frac{\partial\overline{\theta}}{\partial x}$ is calculated, so air temperature from AWS-8 is taken as θ_0 for all three categories. The lapse rate is estimated as a daytime average of the lowest four range gates of virtual potential temperature remotely sensed by the RASS (Fig. 3.1b). Only the first four range gates up to 300 m are considered since they are expected to encompass the full depth of the upslope flow layer, in the range of 20-200 m (Prandtl, 1942; Whiteman, 2000). Our calculations showed that the lapse rate does not change much throughout the day during dry, convective conditions. Figure 3.12 shows the time series of the final pulsation period T_p for all three categories. Despite the model's simplicity, the level of correspondence between calculated pulsation periods and the periodicities estimated quantitatively from ISS2, is striking. The period T_p is contained within the range 120-250 min for WS days, somewhat larger than the estimate based on Fig. 3.11. The period T_p for the SU category, especially after noon, compares well with the 360 min period estimated from Fig. 3.11. The periods T_p for WS and SU days are similar prior to 10:00 LST, and diverge afterwards. This implies that downward momentum mixing, which occurs at 10:00 LST on SU days but does not occur on WS days (Fig. 3.2a,b), might cause the large increase in T_p for SU days. Finally, T_p for SD days remains relatively constant at approximately 120 min throughout the day. This is another confirmation of the

conclusion from Fig. 3.11 earlier which showed that the pulsations occurred at consistent intervals. The increase of T_p during WS and SU days is consistent with observations by Bastin and Drobinski (2005) and Drobinski et al. (2007b). Finally, the increase in T_p may be a consequence of an increase of the effective fetch along the western slope, since wind direction gradually converges toward the along-valley axis ($150^\circ - 330^\circ$ degrees of azimuth) by late afternoon (Fig. 3.2d,e). This fetch extension may be thought of as a decrease of the effective slope angle. Ye et al. (1987) and Schumann (1990) have shown that steady state upslope flows are seldom achieved and oscillations occur at longer periods (on the order of several hours) with decreasing slope angle.

3.4.3 Atmospheric rotors, subrotors and mountain waves

The frequent occurrence of atmospheric rotors, downslope windstorms and mountain waves in Owens Valley (Strauss et al., 2016; Serafin et al., 2017) motivates a discussion of potential influences these phenomena might have on the spectral gap (Fig. 3.3). The dynamics of both the lee-wave-type and hydraulic-jump-type rotors (Hertenstein and Kuettner, 2005) are now relatively well known. However, the spectral response due to rotors has been studied in less detail. Small-scale subrotor vortices, imposed onto the bigger rotor structure, occur with periods on the order of 5 to 10 min (Doyle et al., 2009). Given the larger frequency of occurrence of these structures on SU and SD days (Table 3.1), we argue that for these days, the largest turbulence levels between 5 and 20 min (Fig. 3.3) are driven primarily by these rotors. The WS days experienced fewer rotor occurrences than the two synoptically dominated categories (SU and SD), which explains the smaller amount of energy in the energy-containing region (Fig. 3.3). Interesting to note is that quasi-periodic pulsations observed in the case of the bora downslope windstorm (Belušić et al., 2007) occur with a similar 3 to 11 min period. This might point to a dynamically similar contribution of such intense mesoscale phenomena to the spectral gap.

The influence of mountain waves on the daytime spectral gap is less clear (Worthington and Thomas, 1998) as this influence is often masked by the influence of convection gravity waves which are initiated when the CBL itself acts as an effective mountain (Worthington, 2006). Jiang et al. (2006) report that the developing CBL, below a mountain wave train, acts as a sponge layer absorbing the downward propagating wave energy. However, the specific details of this interaction are difficult to determine using the data sets analyzed in this paper.

3.4.4 Horizontal convective rolls

Horizontal convective rolls (HCR) are nearly linearly organized, 2D horizontal roll vortices that appear during conditions of strong winds and moderate surface heating (Lemone, 1973). HCRs experience lifetimes on the order of 5 to 20 min, starting from their generation, strenghtening, gradual decay, and final re-emergence. This qualifies them as potential contributors to the energy at the high-frequency end of the gap. However, it is uncertain if HCRs occur in Owens Valley. Only few observations (Tian et al., 2003; Belušić et al., 2015) and numerical simulations (Tian and Parker, 2002; Rai et al., 2017a) of HCRs over complex terrain exist, and further research, detailing the capacity of valleys to initiate and/or maintain their structure, is required.

3.4.5 Mesoscale secondary circulations

Mesoscale secondary circulations (MSCs) other than the slope and valley winds, occur in the presence of heterogeneous sensible and latent heat fluxes (Foken, 2008), and induce a low-frequency, local coherent structure that is spatially fixed to the heterogeneity. Tower observations in situations when MSCs occur, often report poor closure of the surface energy budget due to typical sampling times of 30 min not capturing the total flux induced by MSCs (Sakai et al., 2001). MSCs tend to persist with cycles of 30 min up to several hours, thus placing them directly inside the spectral gap (Fig. 3.3). Franssen et al. (2010) report that sufficiently strong turbulent mixing, and generally strong winds, tend to reduce the negative impacts of MSCs on budgeting and energy partitioning. Patton et al. (2005) have determined that the size of the heterogeneity necessary to induce an MSC needs to be 4-9 times that of the CBL depth z_i. Presence of MSCs typically increases the low-frequency energy in the spectra (Eder et al., 2015b). The lack of such energy added at the lowest frequencies plotted in Fig. 3.8 implies absence of MSCs in Owens Valley. Furthermore, the presence of such coherent structures most likely would result in the complete smoothing of the spectral gap (Kang, 2009), which is not evident in Fig. 3.3.

We conclude that MSCs are not significant contributors to energy inside the gap, due to lack of large-scale surface heterogeneities in Owens Valley, as well as due to frequent occurrence of moderate to strong winds (Fig. 3.2) and resulting turbulent mixing.

3.4.6 Conceptual picture of the daytime valley spectral gap

Insights gained from the preceding analyses about the properties of the daytime valley spectral gap enable us to provide a schematic diagram for a typical case (Fig. 3.13). The

conceptual picture of the daytime valley spectral gap covers the range of scales considered in this study, i.e. from 1 min to roughly 8 hours.

The coloring of the spectral curves (from yellow to red to black) depicts the effect of an evolving CBL in a valley, with increasing energy at the high-frequency end of the gap as the day progresses. This corresponds to the shifting of the spectral peak frequency (on the order of 10 min) towards longer periods, signifying the growth of convective thermals and deepening of the CBL. Superpositioned on top of this turbulent peak (blue line) is the potential contribution to the spectrum from (sub)rotor activity and from HCRs. At the low-frequency side of the gap, the addition of energy at periods ranging from approximately 80 to 200 min results from the presence of upslope flows. These spectral peaks are more pronounced at the slope compared to the valley floor. The shifting of the peaks towards longer periods is equivalent to an increase in the upslope flow pulsation period T_p as the day progresses. The gray shaded area denotes the region of periods at which a potential contribution to the spectrum from mountain wave activity occurs. The conceptual diagram presented here would be equivalent for both the valley floor and the slope, with the largest difference evident in the width and depth of the gap: according to Fig. 3.3, slope locations are expected to be associated with shallower and narrower spectral gaps.

3.5 Conclusion

We used a two-month long data set, comprised of 16 automatic weather stations, 2 flux towers and a remote sensing system to determine the most suitable range of gap scales and to investigate the characteristics of the daytime valley spectral gap in Owens Valley. We attributed different peaks in the spectra to common encountered mesoscale phenomena.

We have shown that reliable gap scales τ_{uu} can be obtained by extending the MRFD approach to propeller-vane anemometers. We depict for the first time the spatial distribution of gap scales in a valley and show that gap scales vary across the valley with larger scales over the sidewalls than over the valley floor. The application of the MRFD approach to the flux towers revealed that gap scales change with height above the surface, particularly below 15 m. While τ_{uu} and $\tau_{\theta\theta}$ were relatively constant with height and equal to approximately 30 min and 15 min respectively, the gap scales for the vertical velocity variances and the momentum and heat covariance increased with height. Above 15 m, all gap scales converge and τ_{uu} may be taken as the upper limit for all (co)variances to apply a single running mean length. We proposed simple, valley-wide parameterizations of τ_{uu} as a function of wind speed and of synoptic forcing but further research is needed to confirm

whether such parameterizations can be extended to other valleys.

Our analysis shows that the geometry of Owens Valley and mesoscale secondary circulations do not affect the estimated gap scales since there is no modulation of the horizontal wind velocity spectra at the high-frequency end of the gap. Instead, we found spectral peaks at period of 5-20 min and argued that these are primarily a superposition of strong turbulent CBL mixing and (sub)rotor activity during synoptically perturbed days. We also hypothesized a potential contribution of horizontal convective rolls to the spectral peak at these periods, but the presence of horizontal convective rolls could not be confirmed.

Finally, we have gained insight into the dominant thermodynamical processes occurring at the low-frequency end of the spectral gap. The innovative use of the MRFD approach in this study was extended to gain a deeper insight into the characteristics of this side of the spectral gap. In particular, we showed the effect of upslope flows that we were able to detect by tracking the evolution of the directional shear as a function of dominant eddy length scales. Furthermore, this study for the first time quantified the pulsating nature of upslope flows in a valley with periodicities ranging from approximately 80 to 200 minutes, which were affected by synoptic influence and by time of day. As a result, we were able to construct a conceptual picture of the spatiotemporal behavior of the daytime valley spectral gap.

Table 3.1: Summary of the categorization algorithm, showing the day of each category, its clearness index CI (Whiteman and Allwine, 1986), the T-REX designation and prevailing mesoscale phenomena as summarized by Grubišić et al. (2008).

Category	Date	CI	Designation	Phenomena
WS	Mar 11	0.66	/	/
	Mar 16	0.59	/	/
	Mar 17	0.60	/	/
	Mar 20	0.62	/	/
	Apr 9	0.68	IOP-11	Rotor
	Apr 10	0.68	/	/
	Apr 14	0.37	/	/
	Apr 15	0.77	/	/
	Apr 23	0.57	/	/
SU	Mar 2	0.79	IOP-1	Mountain wave
	Mar 5	0.63	IOP-2	Hydraulic jump
	Mar 6	0.32	IOP-2	Rotor
	Mar 13	0.79	IOP-4	Mountain wave
	Mar 15	0.77	/	/
	Mar 23	0.69	EOP-1	/
	Mar 24	0.65	IOP-6	Mountain wave
	Mar 27	0.55	/	/
	Mar 28	0.28	IOP-7	/
	Mar 30	0.75	EOP-2	/
	Mar 31	0.61	IOP-8	Mountain wave
	Apr 2	0.73	IOP-9	Mountain wave
	Apr 3	0.41	IOP-9	Mountain wave
	Apr 4	0.55	/	/
	Apr 7	0.79	/	/
	Apr 8	0.78	IOP-10	Mountain waves
	Apr 11	0.62	IOP-12	Gravity waves
	Apr 12	0.79	IOP-12	/
	Apr 13	0.69	/	/
	Apr 20	0.76	/	/
	Apr 21	0.65	IOP-14	Gravity waves
	Apr 25	0.73	/	/
SD	Mar 8	0.80	/	/
	Mar 10	0.79	IOP-3	Rotors
	Mar 18	0.68	/	/
	Mar 19	0.68	/	/
	Mar 21	0.76	IOP-5	Mountain waves
	Apr 17	0.80	/	/
	Apr 28	0.79	EOP-4	/

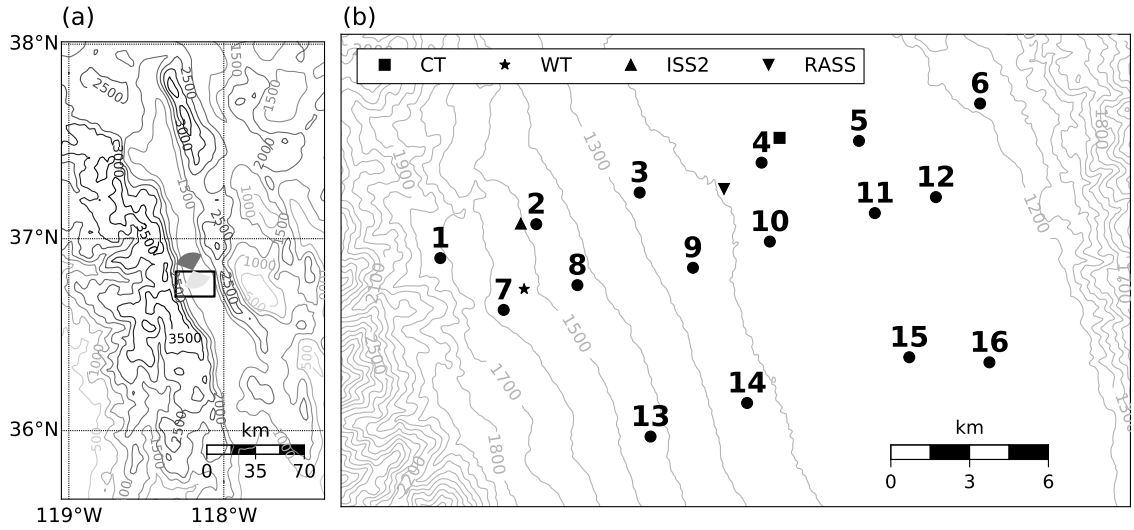

FIGURE 3.1: **(a)** 1 arc-minute topographical representation of Owens Valley, contoured every 500 meters. Dark and light gray shadings denote the main upvalley and downvalley wind direction sectors, while the black rectangle denotes the T-REX area of interest to this study; **(b)** 1 arc-second SRTM (Farr et al., 2007) topographical representation of the area of interest contoured every 100 meters, with the labels and corresponding markers showing the location of the two NCAR-ISFF flux towers (CT, WT), 16 DRI-AWS, ISS2 wind profiler and RASS.

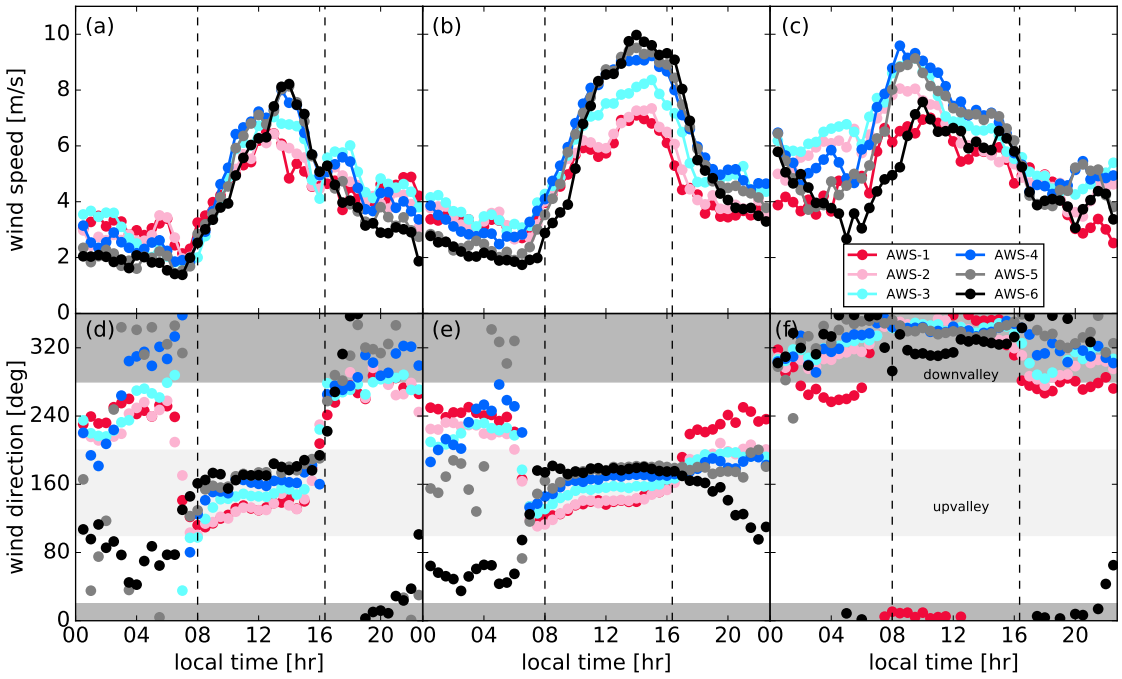

FIGURE 3.2: Composite means of wind speed for **(a)** WS, **(b)** SU and **(c)** SD, and composite circular means of wind direction for **(d)** WS, **(e)** SU and **(f)** SD, for DRI-AWS 1-6. The vertical dashed lines denote the daytime range analyzed with the Fourier and MRFD methods.

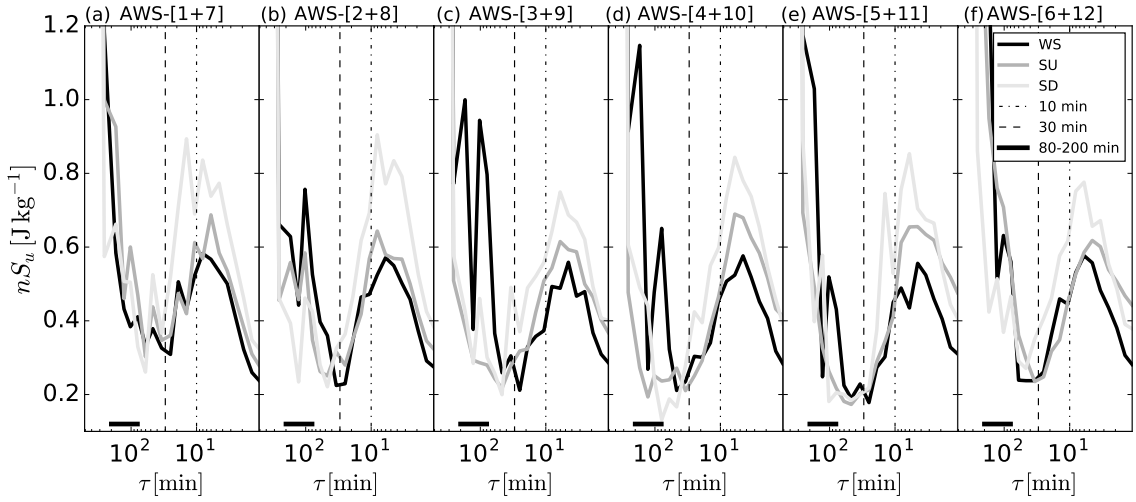

FIGURE 3.3: Log-linear representation of mean frequency-weighted power spectral densities of the longitudinal wind speed component nS_u as a function of the gap scale τ, for **(a)** AWS-[1+7], **(b)** AWS-[2+8], **(c)** AWS-[3+9], **(d)** AWS-[4+10], **(e)** AWS-[5+11] and **(f)** AWS-[6+12]. Vertical dashed-dotted and dashed lines denote gap scales equal to 10 min and 30 min, respectively. Horizontal black lines at the bottom denote the 80-200 min period.

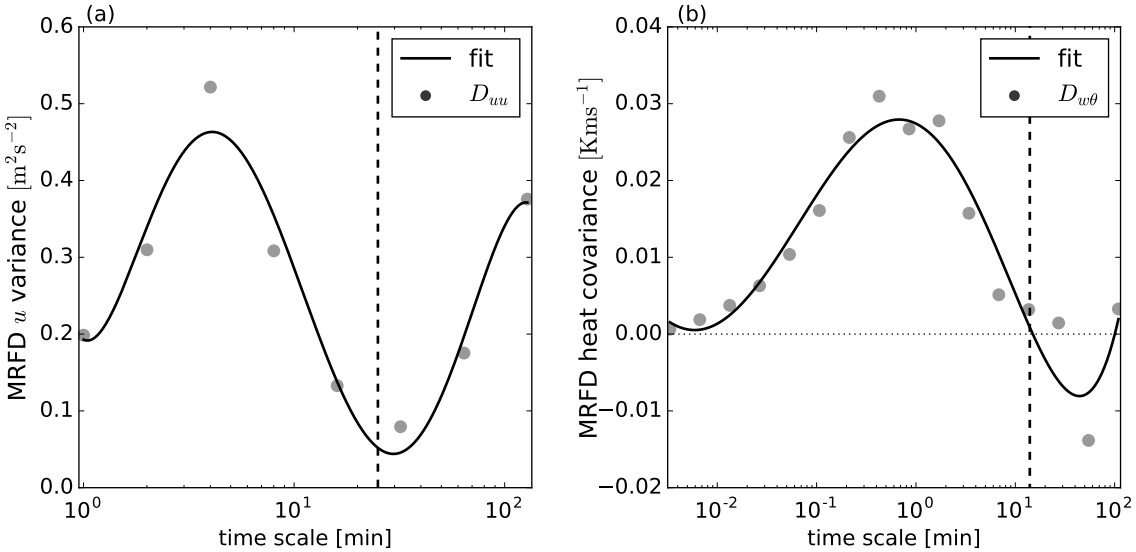

FIGURE 3.4: Examples of the VK07 algorithm. **(a)** Application of the VK07 algorithm to the D_{uu} MRFD variance obtained from a sample 2 h 8 min period at AWS-4: calculated gap scale is equal to 25 min (dashed line); **(b)** Application of the VK07 algorithm to the $D_{w\theta}$ MRFD covariance obtained from a sample 1 h 49 min period from WT: calculated gap scale is equal to 14 min (dashed line).

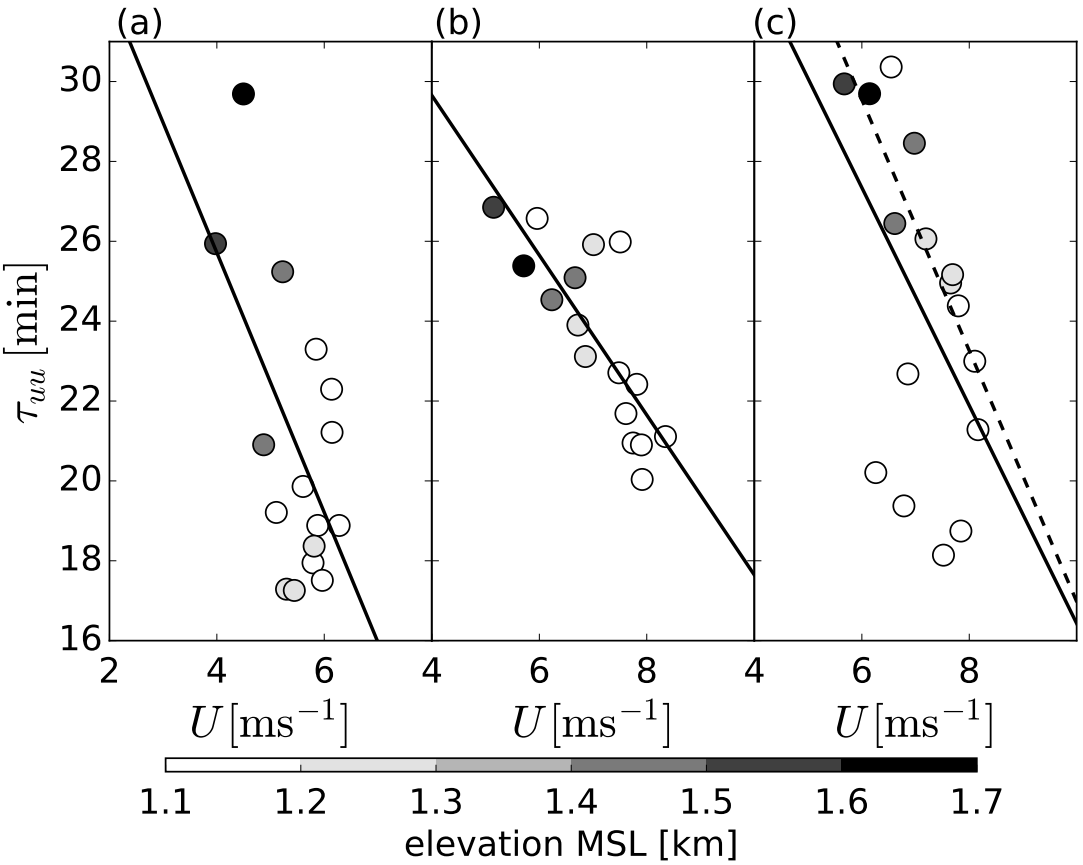

FIGURE 3.5: Average gap scales τ_{uu} based on D_{uu} MRFD variances plotted as a function of station-averaged wind speed, obtained by applying the VK07 algorithm to the 16 DRI-AWS for **(a)** WS, **(b)** SU and **(c)** SD. Each dot is the mean average of all gap scales obtained for a particular AWS (16 points in each subplot). Each dot is greyscale-coded with respect to the elevation of the station it represents. Solid and dashed black lines represent least square fits (Eqs. 3.1-3.4).

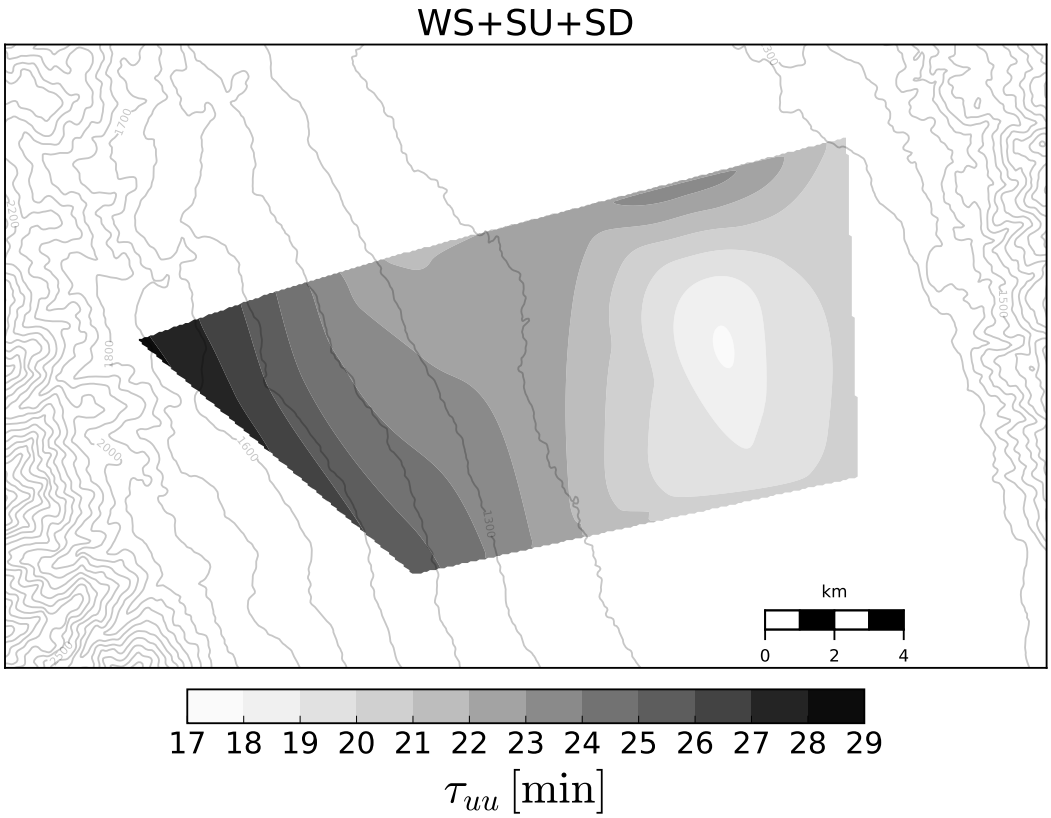

FIGURE 3.6: Same data from Fig. 3.5, here averaged together. Linear interpolation of the final 16 gap scale averages onto a regular grid is used to produce the map. Gray contour lines denote 1 arc-second SRTM topography, contoured every 100 meters.

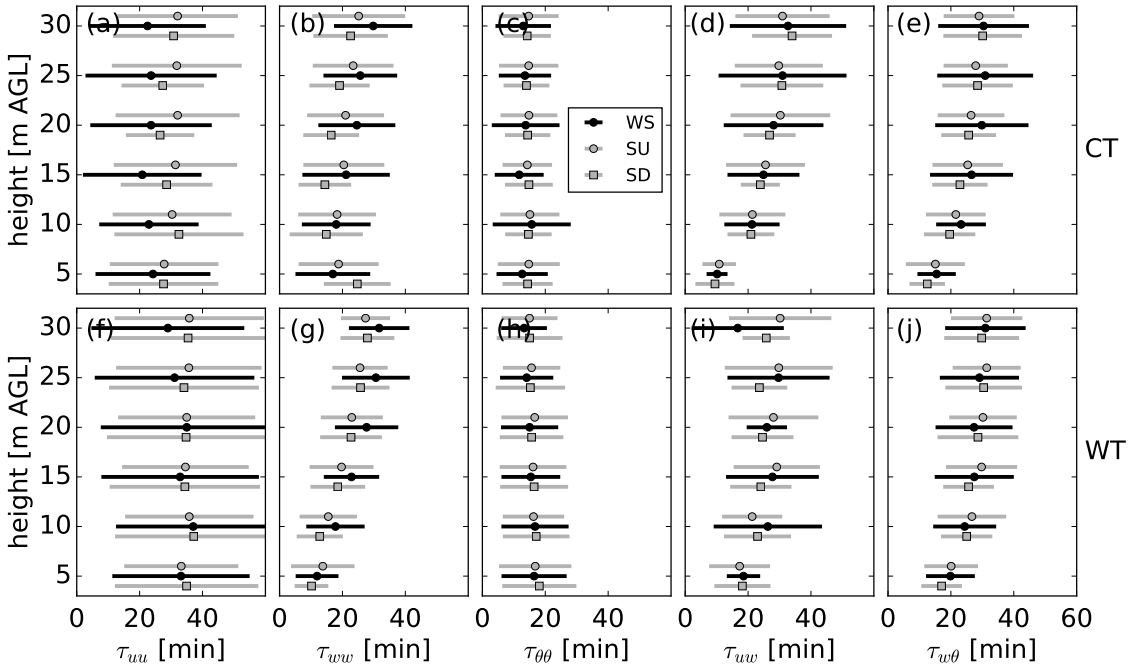

FIGURE 3.7: Average gap scales τ based on MRFD covariances: **(a)** τ_{uu} at CT, **(b)** τ_{ww} at CT, **(c)** $\tau_{\theta\theta}$ at CT, **(d)** τ_{uw} at CT, **(e)** $\tau_{w\theta}$ at CT, **(f)** τ_{uu} at WT, **(g)** τ_{ww} at WT, **(h)** $\tau_{\theta\theta}$ at WT, **(i)** τ_{uw} at WT and **(j)** $\tau_{w\theta}$ at CT, obtained by applying the VK07 algorithm to CSAT-3 data. The horizontal bars denote $\pm$ one standard deviation.

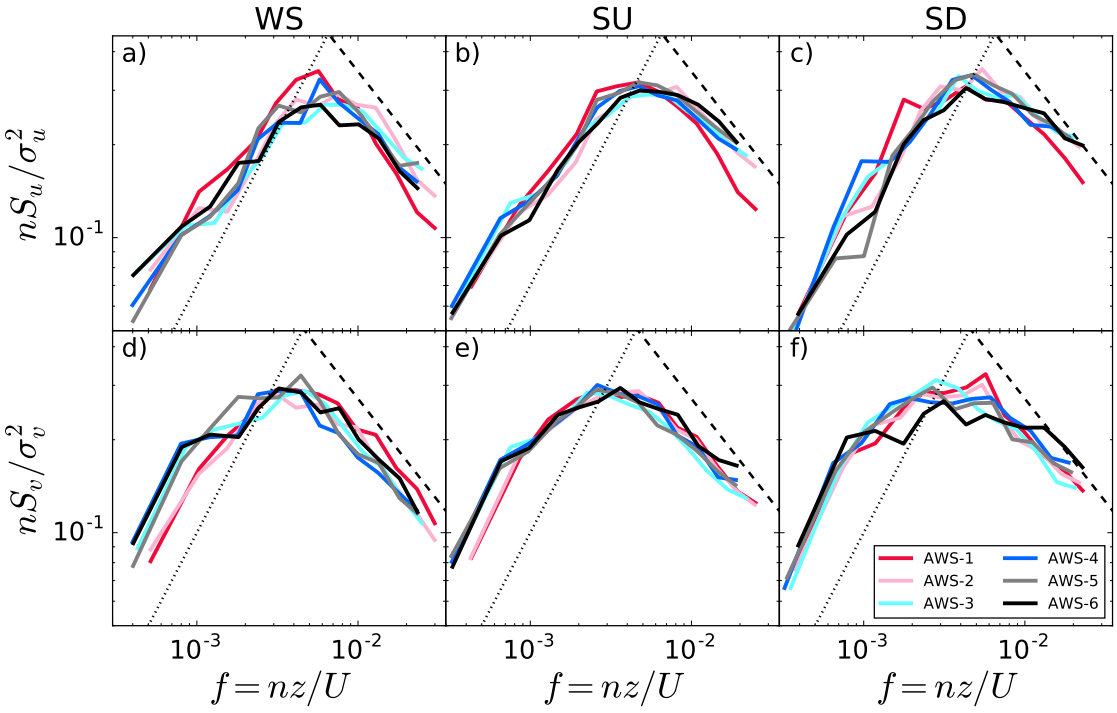

FIGURE 3.8: Composite variance-normalized and frequency-weighted power spectral densities, plotted against the non-dimensional frequency $f = nz/U$, for **(a)** u during WS days, **(b)** u during SU days, **(c)** u during SD days, **(d)** v during WS days, **(e)** v during SU days, and **(f)** v during SD days, for AWS 1-6. Dashed and dotted lines denote the $-2/3$ and $+1$ spectral slopes, respectively.

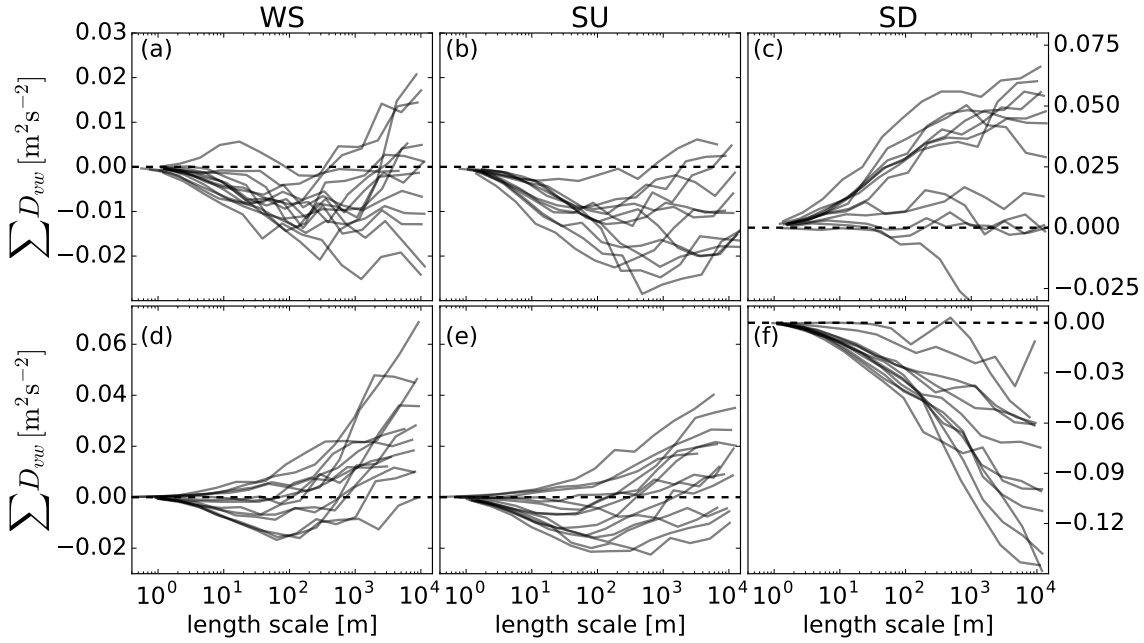

FIGURE 3.9: Composite cumulative MRFD covariances of directional shear vw for **(a)** CT during WS days, **(b)** CT during SU days, **(c)** CT during SU days, **(d)** WT during WS days, **(e)** WT during SU days and **(f)** WT during SD days. Dashed lines denote zero flux.

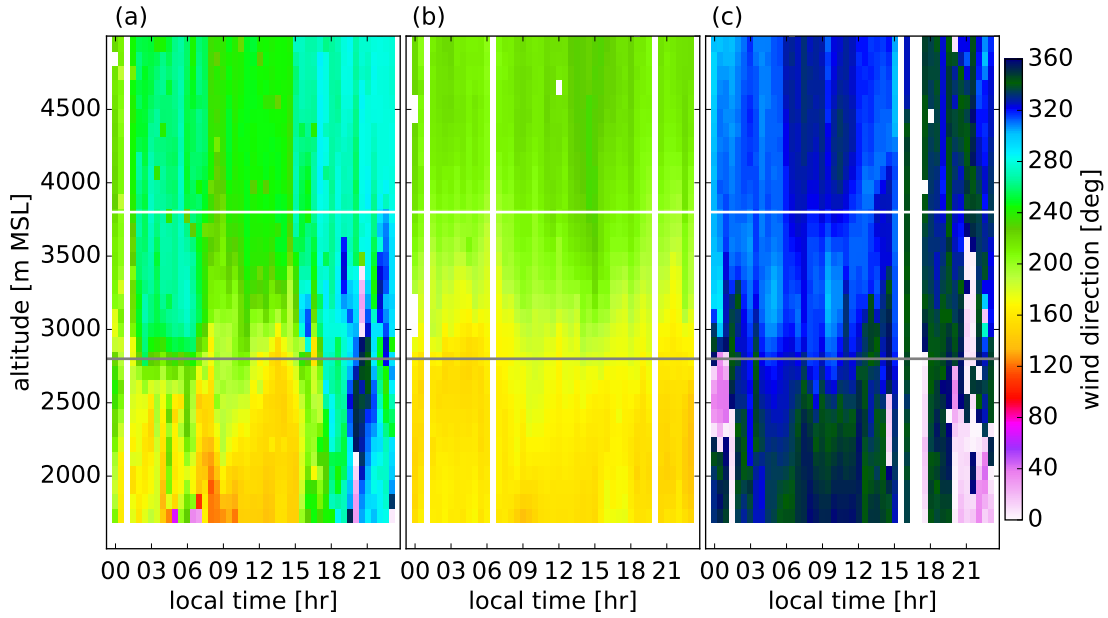

FIGURE 3.10: Time-height Hovmöller diagrams of composite circular mean wind direction for **(a)** WS, **(b)** SU and **(c)** SD, obtained with the ISS2 wind profiler. Solid black and white lines denote the approximate ridgetop heights of the Inyos and the Sierras, respectively. White patches denote either missing data or northerly winds.

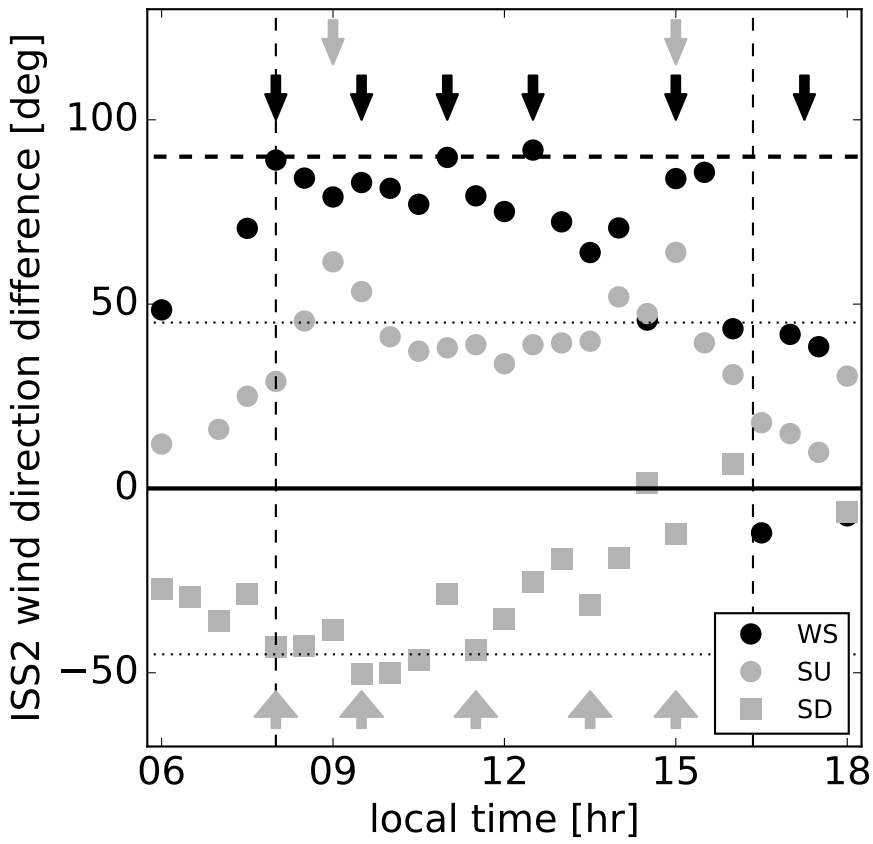

FIGURE 3.11: Time series of circular mean wind direction difference obtained from the ISS2 wind profiler. Vertical dashed lines denote the daytime period analyzed in this study, solid black line denotes no wind direction difference, horizontal dotted lines denote $\pm 45^{\circ}$ difference, while horizontal dashed line denotes $+90^{\circ}$ difference. Vertical arrows denote the occurence of an amplitude in the upslope flow periodicity pattern, shaded to correspond with their respective category (the thin gray arrows denote the SU, while the thick gray arrows denote the SD category).

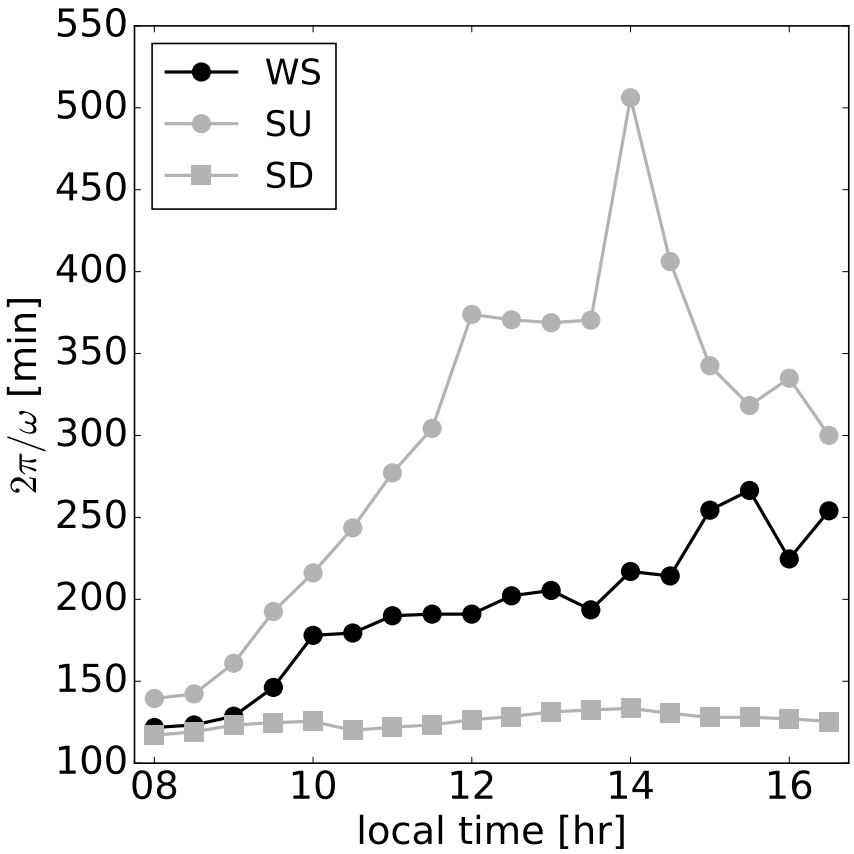

FIGURE 3.12: Time series of the upslope flow pulsation period $T_p = 2\pi/\omega$, for all three categories.

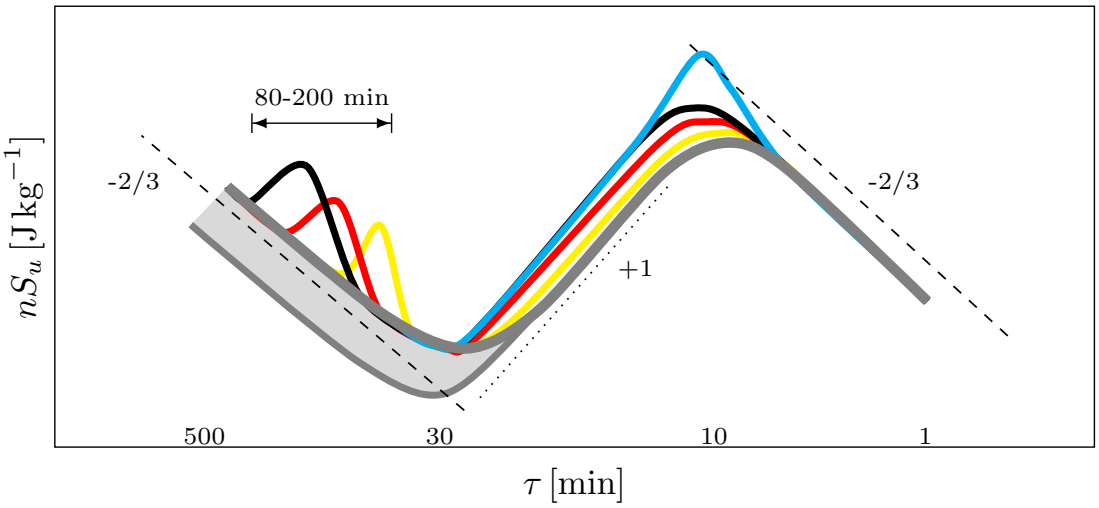

FIGURE 3.13: Schematic diagram depicting the temporal evolution of the daytime valley spectral gap. Solid gray line denotes the flat terrain near-neutral spectrum (Kaimal et al., 1972), solid yellow line denotes the mid-morning, solid red line the early afternoon, and solid black line the late afternoon situation. Solid parabolic curves at the low-frequency end of the gap denote the upslope flow periodicity for the same three situations. Blue line denotes contribution to the energy-containing region from (sub)rotor activity. The gray shaded area denotes the contribution to the spectral gap from mountain wave activity. Black dashed and dotted lines denote the $-2/3$ and $+1$ spectral slopes, respectively. Magnitudes on the y-axis are arbitrary.

4

Characteristics of roll and cellular convection in a deep and wide semiarid valley: A large-eddy simulation study

4.1 Introduction

[1] Rolls and cells are CBL phenomena that have attracted interest from the research community for many years. In fair-weather free-convective conditions during low winds, convection in the CBL organizes into a seemingly infinite number of polygons that form open cells (Moeng and Sullivan, 1994). When the convection is additionally forced due to strong winds and vertical shear, open cells transform into linearly elongated structures, known as horizontal convective rolls (Young et al., 2002). Cells can be either of the open (updrafts surrounding a center downdraft core) or closed (downdrafts surrounding a center updraft core) type. Here, we focus exclusively on open cells over land, as closed cells are almost entirely limited to stratocumulus-topped CBL over oceans (Atkinson and Zhang, 1996; Wood, 2012). Consistent increase in computing power over the past six decades has made it possible to nearly resolve several CBL features, including rolls and cells, in numerical weather prediction (NWP). Recent subkilometer (LES) performed for the Netherlands (Schalkwijk et al., 2015) and Germany (Heinze et al., 2017), are clear examples that globally operational LES, while promising, is not yet achievable: current predictions range from one (Schalkwijk et al., 2015) to five decades (Lehner and Rotach, 2018).

[1] Reprinted from Babić, N., and De Wekker, S. F. (2018), currently pending revisions in Atmos. Res.

As a result, modern NWP currently faces a challenge of bridging the range of grid spacings spanning rolls and cells, known as the *terra incognita* (Wyngaard, 2004). This range, typically on the order of several hundred meters, has been used in several LES-based studies of rolls and cells (Tian and Parker, 2003; Miao and Chen, 2008; Huang et al., 2009; Ryu et al., 2013; Thurston et al., 2016). In the *terra incognita*, use of both a planetary boundary layer (PBL) scheme and LES is poorly justified. This explains the oftentimes simulated artificial dependency of roll characteristics on grid spacing (LeMone et al., 2010; Ching et al., 2014; Thurston et al., 2016). Specifically, decreasing the grid spacing triggers rolls more rapidly, while also decreasing their wavelength and linearity. As LES becomes utilized as both a research and forecasting tool with increasing computing power, such grid spacing dependency warrants attention.

Improved NWP model resolution has also led to a better representation of topographic features and their effects (Schmidli et al., 2018). Such effects include the impact of valleys on the overlying free troposphere (Wagner et al., 2014b; Duine and De Wekker, 2017) and mountain induced exchange of mass and energy between the CBL and the free troposphere that is amplified due to mechanisms such as mountain venting and advective venting (De Wekker and Kossmann, 2015). Valley atmospheres are characterized by the presence of transient thermally and dynamically driven flows (Serafin et al., 2018) with scales that are similar to those of rolls and cells *terra incognita*. Specifically, the role of sloping terrain, such as valley sidewalls, in modifying convection organization within the CBL, is still not fully understood (Serafin et al., 2018). Sloping terrain generates local breezes that may in turn affect the turbulent exchange within the CBL. While these breezes are relatively well understood and simulated, their relationship with rolls and cells has received no attention thus far.

To investigate rolls and cells in a valley atmosphere, we use the nested LES approach (Talbot et al., 2012). Such a modeling setup avoids the *terra incognita* and is capable of simulating complex terrain flows using real-world topography and land-use, with real-time forcing driven by the mesoscale parent domain. Our study area is Owens Valley, a deep and wide semiarid valley. We address the following questions:

- Do structural parameters of rolls and cells (wavelength, orientation, aspect ratio, roll organization factor) in Owens Valley, fall within the range of previously observed and simulated flat terrain values?
- Within the valley atmosphere, are these parameters different over the floor and the adjacent slope?

- Do the characteristics of rolls and cells depend on the presence of upslope flows on the valley sidewalls?

4.2 Background

Rolls and cells have important impacts on atmospheric processes. For example, they impact turbulent exchange mechanisms differently with rolls being significantly more efficient than cells in transporting momentum (Salesky et al., 2017, S17). Rolls also affect pollutant dispersion and wildfire spreading differently than cells because of differences in vertical velocity distributions (Thurston et al., 2016; S17). Both rolls and cells may aid deep convection initiation (Weckwerth, 2000) and generate gravity waves above the CBL (Melfi and Palm, 2012). Contrary to cells, rolls may also serve as the dominant transport mechanism for momentum in the hurricane boundary layer (Zhang et al., 2008). Furthermore, prevalence of rolls or cells is partly responsible for the surface energy budget underclosure in the atmospheric surface layer (Foken et al., 2011).

The bulk CBL stability parameter $-z_i/L$ is most often used to define regimes characterized by either open cells, rolls or a transition between the two. Here, z_i is the CBL depth and L the Obukhov length (Stull, 1988). $-z_i/L$ is a dimensionless parameter reflecting relative contributions of buoyancy and shear to convection organization in the CBL. Many observational and numerical studies have concluded that rolls prevail for small $-z_i/L$ while cells prevail for large $-z_i/L$. Early studies based on LES, concluded that the transition from rolls to cells occurs for $15 < -z_i/L < 25$ over flat, horizontally homogeneous terrain (Deardorff, 1972; Etling and Brown, 1993; Khanna and Brasseur, 1998). Application of these criteria relies on the presence of spatially uniform surface fluxes and CBL height. These conditions do not not occur in complex terrain where shear and buoyancy are modulated by terrain-induced effects (Serafin et al., 2018). Such effects include z_i depressions along mountain bases (De Wekker, 2008), slope circulations embedded within the CBL (Reuten et al., 2005), and presence of multiple elevated layers and ill-defined z_i (Schmidli, 2013; De Wekker and Kossmann, 2015).

The characteristics of cells and rolls in the CBL can be described with a few basic parameters. The wavelength λ quantifies the spacing between two successive roll updraft branches or the diameter of a single cellular polygon (Eymard and Weill, 1982; Atkinson and Zhang, 1996). Young et al. (2002) make the distinction between wide and narrow rolls, concluding that wide rolls are typical for open sea while narrow rolls are more common over flat terrain. This narrowing of overland rolls has been ascribed to the absence of

latent heat release during fair weather conditions over land (Müller and Chlond, 1996).

Rolls are aligned within $\Theta \approx \pm 20^{\circ}$ of either the bulk CBL or surface wind direction vectors (Etling and Brown, 1993). However, there is large variability from study to study and from case to case (see Fig. 5 in Kelly, 1984). This variability is due to differences in the used reference wind vectors, and the varying contribution of thermal and shear instabilities to roll formation. As pointed out by Kelly (1984), most discrepancies between analytical model implementations of these two instability mechanisms lead to inconsistent conclusions for roll orientation.

Given the importance of the CBL depth z_i in limiting the vertical extent of convection, it is common practice to define the aspect ratio as $AR = \lambda / z_i$. The majority of experimental and numerical estimates of AR (Young et al., 2002) agree with predictions from linear theories (Kuettner, 1971), which suggest $AR = 2.8$. For a number of flat terrain case studies, Young et al. (2002) reported an $AR = 3.15 \pm 0.77$.

Complex terrain and heterogeneous land-use tend to disrupt the subtle structure of convection over land. In the lee of the Dinaric Alps, Belušić et al. (2015) reported a possible occurrence of rolls induced by the Bora downslope windstorm. They estimated a wavelength $\lambda \approx 1$ km and an AR of 1.5 using aircraft measurements. Weston (1980) observed cloud streets from satellite imagery over the hilly British Isles with an $AR \approx 3.2$ and an alignment of these streets to within 25 degrees of the mean wind direction. By coupling radar and satellite imagery with simulations, Tian et al. (2003) were able to elucidate rolls over undulating hills. Both their observed ($\lambda \approx 2 - 4$ km; $AR \approx 1.6 - 3.3$) and simulated ($\lambda \approx 2 - 3$ km; $AR \approx 2.5 - 3.8$) roll properties were similar to those over flat terrain (Young et al., 2002). Additionally, they found rolls oriented slightly off the dominant surface wind direction. Using LES, Rai et al. (2017a) simulated roll initiation downhill of a shallow ridge, associated with an $AR \approx 3$ and a $-z_i/L \approx 2$. At the same time, they observed the roll orientation to be a function of the mean wind speed. Despite the above efforts, a consistent picture of the extent to which complex terrain impacts properties of rolls and cells (λ, orientation, AR, roll organization factor), is yet to emerge.

The parameters defining cells and rolls are traditionally derived using satellite imagery (Atkinson and Zhang, 1996), aircraft (Lemone, 1976), clear-air radars (Weckwerth et al., 1997), dual-Doppler lidars (Träumner et al., 2015) and tall towers (Lemone, 1973). When such measurements are sparse or unavailable, LES has served as a reliable substitute. For instance, S17 introduced a measure of roll organization $\mathcal{R}$ that relies solely on horizontal LES fields of resolved vertical velocity, enabling them to better quantify the transition

from cells to rolls.

Nested LES over both flat (Talbot et al., 2012) and various complex terrain areas have been conducted, including gentle slopes (Muñoz-Esparza et al., 2017; Rai et al., 2017b), isolated mountains (Michioka and Chow, 2008; Xue et al., 2014) and basins (Crosman and Horel, 2017). Previous attempts at nested LES in valleys exist as well. However, grid spacings in the *terra incognita* (e.g. 150 m in Chow et al., 2006) precluded any objective analysis of convection organization. According to Cuxart (2015), grid spacings on the order of 50 m or finer are necessary to ascertain explicitly resolved convection over complex terrain. To our knowledge a nested LES satisfying this condition does not currently exist for a mountain valley. A number of idealized studies satisfying this criterion exists for valleys (e.g. Schmidli, 2013; Brötz et al., 2014; Wagner et al., 2014b; Leukauf et al., 2016). However, initiation from an atmosphere at rest generated cellular convection and no rolls in such studies. Although a background wind in the study of Catalano and Moeng (2010) generated roll-like structures in their idealized shallow valley, little attention was given to simulated roll properties. To our knowledge, Schumann (1990) is the only study to provide an estimate of aspect ratio for rolls simulated with LES for a 10° slope ($AR \approx 2.5$).

A wide mountain valley is a suitable environment for studying rolls and cells, since the channeled along-valley flow has a bimodal character (Zardi and Whiteman, 2013). This reduces the degrees of freedom concerning the fetch from which convection is initiated and advected. Wider valleys may contain a greater number of rolls and cells between the sidewalls, thus increasing statistical robustness. During daytime, rolls within the valley CBL are expected to be parallel with the adjacent sidewalls, especially if the sidewalls are tall. Previously, most studies have focused on banded orographic convection induced by relatively shallow hills (Tian and Parker, 2003; Tian et al., 2003; Fuhrer and Schär, 2007), leaving open questions regarding convection organization in valleys bounded by tall sidewalls. Therefore, a deep and wide valley, such as Owens Valley, serves as a suitable environment for establishing a relationship between rolls and cells and valley/slope flows.

4.3 Data and Methods

4.3.1 T-REX observations

T-REX took place during March and April 2006, in Owens Valley, CA, to study atmospheric rotors and their interaction with the valley boundary layer (Grubišić et al., 2008). In this study, we use data from two flux towers: the central tower (CT) located at the

valley floor near Independence, and the western tower (WT) located roughly 9 kilometers to the southwest, at the western slope of the valley (Fig. 4.1b). We used CSAT3 (Campbell Scientific, Inc.) sonic anemometer measurements collected at 5 and 10 meters above ground level (AGL). The post-processing of these measurements is explained in more detail in Babić et al. (2016a) and Babić et al. (2017) (B17). Data from the sonic anemometers are also used to obtain the Obukhov length L at 5 m, necessary for the calculation of the bulk CBL stability parameter $-z_i/L$. To obtain the CBL depth z_i, we use data from the National Center for Atmospheric Research (NCAR) Integrated Sounding System 2 (ISS-2), a 915 MHz wind profiler located roughly 3 kilometers north of WT. Although a similar wind profiler was located near CT, it is inadequate for retrieving z_i due to poor data quality. Hence, we only report z_i for ISS-2 in this study.

With the Sierra Nevada to the west and the Inyo and White Mountains to the east, the semiarid Owens Valley runs in a northwest-southeast direction for approximately 150 km. The valley is roughly 3 km deep and roughly 30 km wide around the area of interest for this study (Fig. 4.1a). Gentle western and relatively steeper eastern sidewalls characterize the valley. The average inclination of the western slope is approximately 3.25°, while the valley floor slopes towards the north at an angle of 0.2°. The western slope of the valley has little along-slope variability for several tens of kilometers.

4.3.2 Model configuration

The WRF model is a fully compressible, non-hydrostatic atmospheric model developed to simulate atmospheric phenomena across a wide range of spatio-temporal scales, for both research and operational purposes (Powers et al., 2017). In this study, we used version 3.8.1 of the model. To investigate the characteristics of rolls and cells in Owens Valley, we performed three simulations. Each simulation represents one day from the three main climatological categories defined in B17: the Wind Shift (WS) category, comprised of quiescent days where a diurnal reversal of wind direction occurred; the Synoptic Upvalley (SU) category, where a single or no wind direction reversal occurred and winds were mainly upvalley; the Synoptic Downvalley (SD) category, where a single or no wind direction reversal occurred and winds were mainly downvalley. The three case study days were April 15 2006 (WS), March 27 2006 (SU), and April 28 2006 (SD). In the remainder of the paper, the three simulations will be referred to as WS, SU, and SD, respectively.

The regional setting for the WS case (Fig. 4.2a) was characterized by an upper-level trough occupying the majority of the region. This trough provided sustained westerly-

southwesterly flows above Owens Valley with speeds of about 5 ms^{-1} at 700-hPa. The strong low pressure center located off the coast of the Olympic Peninsula lacked a high pressure counterpart in the region, thus providing a weak to nonexistent large-scale horizontal pressure gradient. The lack of such a gradient implies lack of pressure-driven channeled flows (Zhong et al., 2008; Zardi and Whiteman, 2013), thus enabling the thermally-driven flows in the valley to remain decoupled from those aloft. A similar upper-level trough was coupled with a corresponding ridge to the east of Owens Valley during the SU case (Fig. 4.2b). Such a setting favors pressure-driven channeling, which resulted in strong south-southeasterly, upvalley flows in the valley. The predominance of southerly winds immediately above the valley's ridgetops with speeds at 700-hPa of approximately 5 ms^{-1} also suggests that these upvalley flows were partly channeled by the valley topography. During the SD case (Fig. 4.2c), the upper-level ridge located off the coast of California sustained north-northwesterly winds (about 3 ms^{-1} at the 700-hPa level) at the ridgetop level above the valley, resulting in forced channeling. The valley flows were enhanced by an approaching cold front (Zhong et al., 2008) and by pressure-driven channeling due to the presence of a strong trough over the southern Rockies.

Domain setup

The main setup was the same for all three simulations (Table 4.1). Five one-way nested domains were employed. The outermost three domains (d01, d02 and d03) were run with a PBL scheme while the innermost two domains (d04 and d05) were run in LES mode (Figure 4.1). Hence, the outer three domains will be referred to as WRF-MESO domains, and the inner two domains as WRF-LES domains. The outermost two WRF-MESO domains (not shown) encompassed part of the eastern Pacific and the majority of the Rockies, respectively. For all three simulations, WRF-MESO domains were initialized at 00 UTC and run for 24 hours. The WRF-LES domains were initiated at 12 UTC and spun up for 3 additional hours to allow sufficient time for the development of turbulent fields. Heterogeneous land-use causes turbulence to develop rapidly in the WRF-LES domains, similar to triggering random temperature perturbations in idealized LES. All five domains were run concurrently as in Rai et al. (2017a). All simulations and domains used the Dudhia shortwave radiation scheme (Dudhia, 1989), the Rapid Radiative Transfer Model longwave radiation scheme (Mlawer et al., 1997), the revised MM5 Monin-Obukhov surface-layer similarity scheme (Jiménez et al., 2012), the Noah land-surface model (Chen and Dudhia, 2001), while only the outermost (d01) WRF-MESO domain used a cumulus parameter-

ization scheme (Kain, 2004). Topographic shading was enabled for all simulations and domains. North American Mesoscale Model (NAM) 12-km forecast analyses were used as initial and boundary conditions at a 6-hr interval, similar to Daniels (2010), Schmidli et al. (2009) and Zhou and Chow (2013). The model top was located at 100 hPa, with a 5-km deep Rayleigh damping layer regulating reflection of gravity waves off the model top.

The three WRF-MESO domains were run with horizontal grid spacings of 12.15, 4.05 and 1.35 km. A similar setup has been successfully used by a number of authors (Talbot et al., 2012; Heath et al., 2017; Rai et al., 2017a,b). The grid spacing in these domains is coarser than the spacings occupying the *terra incognita*, thus justifying the use of a PBL scheme (Zhou et al., 2014). The United States Geological Survey (USGS) topography data set at 2-arc-min (d01) and 30-arc-sec (d02, d03) resolution was used, while the National Land Cover Dataset (NLCD-2006) at 30-arc-second resolution was used for all WRF-MESO domains. All WRF-MESO domains had 60 vertically stretching levels, with 11 levels below 1 km and the lowest level located at 37 m AGL. The PBL scheme in the WRF-MESO domains was the Yonsei University scheme (Hong et al., 2006), a common first-order non-local scheme known to perform well, even over complex terrain where horizontal advection terms may be important (Schmidli et al., 2011; Lee and De Wekker, 2016).

The two WRF-LES domains were run with horizontal grid spacings of 270 and 54 m. A parent-to-child nesting ratio of five between d03 and d04 served to circumvent the *terra incognita* as quickly as possible, thus mitigating the undesirable effect of grid spacing on turbulent kinetic energy (TKE), particularly the horizontal velocity variances (Wyngaard, 2004; Zhou et al., 2014; Rai et al., 2017a). The location of the WRF-LES domains is shown in Fig. 4.1a. To take into account the fetch needed to develop turbulence in Owens Valley, the inner WRF-LES domain (d05) was shifted towards the downwind end of its parent (d04) domain in all three simulations. Furthermore, within d05 for SU and SD cases, the T-REX region of interest was located near the farthest downwind boundary, thus ensuring sufficient fetch for development of resolved convection. For the WS case, the T-REX region of interest was centered within the inner WRF-LES domain (Fig. 4.1b). Different domain positions were required due to strong winds, especially for the SU and SD cases. Slow turbulence development downwind of the inflow boundary is a known issue with the nested LES framework (Mazzaro et al., 2017; Rai et al., 2017a). The large area of d05 in our simulations served an important purpose of encompassing the entire valley range between the Sierras and the Inyos, thus capturing the full extent of the valley wind system (Zardi and Whiteman, 2013). Methods to alleviate such large domains and

targeted positioning are currently being developed, such as the cell perturbation method (Muñoz-Esparza et al., 2014, 2017).

The outer WRF-LES domain d04 used the same vertical levels as the WRF-MESO domains. The same setup was inadequate for d05 due to excessively large grid aspect ratios over the steep slopes of the Sierras and the Inyos. Instead, we adopted the vertical grid refinement feature recently developed by Daniels et al. (2016), which implements custom vertical levels irrespective of the parent domains. The domain d05 thus had 113 vertically stretching levels, with 33 levels below 1000 m and the lowest level located 13 m AGL. As a result, the average vertical spacing was 40 m within the first 3000 m. However, numerical instabilities still prevailed, particularly over the Sierras. To avoid this without excessively smoothing the topography, the WRF parameter "epssm", which serves as a sound wave damper (Dudhia, 1995), was modified for both WRF-LES domains, similar to Crosman and Horel (2017). For both WRF-LES domains, we used the Shuttle Radar Topography Mission (SRTM) 1-arc-sec topography data and the NLCD-2006, 1-arc-sec land-use data. Finally, both WRF-LES domains modelled the subgrid-scale (SGS) TKE using the 1.5-order TKE closure (Moeng, 1984), which uses the prognostic TKE equation for the estimation of both horizontal and vertical eddy diffusivities.

The SU run required more attention than the other two case studies. In contrast to WS and SD, initial SU simulations revealed a very late onset of the upvalley wind system both at the valley floor and the slope, even in the innermost WRF-LES domain (not shown). This issue is related to improper initialization of soil moisture in the model as was also found by Daniels (2010). They found the NAM soil moisture values to be three times those observed using a network of gravimetric soil moisture probes deployed during T-REX. Such sensitivity of complex terrain wind dynamics on adequate initialization of soil moisture has long been recognized (De Wekker et al., 2005; Chow et al., 2006; Schmidli et al., 2009; Angevine et al., 2014; Massey et al., 2014; Kalverla et al., 2016). To improve the simulation of the valley wind system for SU, we nudged the NAM soil moisture fields towards observed values. For the entire Owens Valley and for altitudes below 2000 m MSL we divided the NAM fields by a factor of three, while for all higher altitudes we used a factor of 1.5 to relax the values back towards the original NAM values. This nudging was applied to all five domains and all four soil layers coupled with the Noah land-surface model (Peter Kalverla, 2016, personal communication). Finally, because the SU case featured non-negligible cloud cover (see the clearness index values in Table 3.1), we adopted the Morrison 2-moment microphysics scheme (Morrison et al., 2009). We

note that this cloud cover was associated with mountain wave activity aloft, and did not manifest as CBL-generated cloud streets.

4.3.3 Methods

Post-processing of LES fields

From 15 UTC until completion of each simulation at 00 UTC, the output from the inner WRF-LES domain was saved every 30 seconds. To contrast convection organization over the valley floor and over the western slope, two subdomains were defined: the CT and WT subdomains, as each of them includes a flux tower (CT or WT). The subdomains consisted of 128^2 horizontal grid points. At each output time and for each subdomain, horizontal slices of turbulent perturbation fields of the three velocity components u', v', w', potential temperature θ' and specific humidity q' were calculated as deviations from their spatial means. For brevity, the primes will be omitted in the remainder of the paper. An overline $\overline{\ }$ denotes a temporal average over a 15-min period and angle brackets $\langle\,\rangle$ denote a spatial average across the whole subdomain.

For obtaining ensemble averages representative of a large number of thermals within a domain, larger domains (Agee and Gluhovsky, 1999; de Roode et al., 2004) and longer averaging times (Lenschow et al., 1994; de Roode et al., 2004) are preferred. The relatively small size of the two subdomains (6.91 km^2) was a compromise between maintaining relatively small spatial heterogeneity in elevation and land-use, and sufficient domain size for ensemble average calculation. Even so, their size was still greater than domain sizes typically encountered in idealized LES (Sullivan and Patton, 2011) and recent nested LES (Rai et al., 2017a). On the other hand, the spatially and temporally unsteady boundary layer top limited the use of longer time averages, especially during morning and early afternoon hours.

In idealized LES, analyses are traditionally performed once the CBL reaches an equilibrium state, typically in the last few hours of a simulation or after multiple large-eddy overturning timescales (Sullivan and Patton, 2011; Gibbs and Fedorovich, 2014). However, nesting LES inside a mesoscale model means that an equilibrium state is rarely, if ever, achieved. The constantly evolving regional weather patterns modify the parent domains driving the flow inside the child LES domains. These evolving patterns were used to achieve different convection modes (via $-z_i/L$), similar to prescribing a constant geostrophic forcing or surface sensible heat flux in idealized LES.

Unlike idealized LES where the geostrophic flow is set along either x or y axis, the

orientation of Owens Valley constrains the direction of the valley flow mainly in the upvalley (WS, SU) or downvalley (SD) directions. Hence, the output horizontal velocity components u and v had to be rotated into the mean wind for a meaningful interpretation of derived statistics (Chow et al., 2006). This rotation was performed for each output time. In doing so, the mean flow was contained within the $\langle u \rangle$ velocity component, while $\langle v \rangle$ was zero.

Roll organization factor $\mathcal{R}$, aspect ratio AR, wavelength/diameter λ, roll orientation Θ

To quantify the structural organization of the CBL in the subdomain, we adopted the method recently introduced by S17. This approach relies on transforming the vertical velocity w field in the horizontal plane, from the Cartesian coordinate system (x, y) into a cylindrical frame of reference (ρ, θ), where ρ is the radial and θ the angular coordinate. Upon transformation, two-point spatial autocorrelation R_{ww} equals:

$$R_{ww}(r_\rho, r_\theta) = \frac{\langle w(\rho, \theta)\, w(\rho + r_\rho, \theta + r_\theta) \rangle}{\langle w^2 \rangle}, \tag{4.1}$$

where r_ρ and r_θ denote radial and angular lags, respectively. If the w field exhibits roll-like appearance, R_{ww} will be large; if it exhibits cellular appearance, R_{ww} will decrease and lack orientation preference, a property known as axisymmetry. This property of R_{ww} can be used to define a roll organization factor $\mathcal{R}$ (S17). A large $\mathcal{R}$ indicates the presence of rolls and a small $\mathcal{R}$ the presence of cells:

$$R(r_\rho) = \max_{r_\theta} \left[R_{ww}(r_\rho, r_\theta) \right] - \min_{r_\theta} \left[R_{ww}(r_\rho, r_\theta) \right] \tag{4.2}$$

$$\mathcal{R} = \max_{r_\rho} \left[R(r_\rho) \,|\, r_\rho / z_i \geqslant 0.5 \right] \tag{4.3}$$

For each subdomain, $\mathcal{R}$ was calculated at each output time, and an ensemble average $\overline{\mathcal{R}}$ was obtained by averaging all thirty $\mathcal{R}$ values within each 15-min period.

To obtain the aspect ratio AR and wavelength λ, we extended the approach of Eymard and Weill (1982) and Lohou et al. (1998) to R_{ww}, by considering the distance from minimum autocorrelation to the origin. We obtained AR as:

$$AR = 2 \left[r_\rho / z_i \,|\, R_{ww} = \min \left(R_{ww} \right) \right] \tag{4.4}$$

Then, $\lambda = z_i\, AR$. Finally, analogous to $\overline{\mathcal{R}}$, we obtained ensemble average $\overline{\mathbf{AR}}$ and $\overline{\lambda}$. Additionally, we emphasize that for WS, $\overline{\mathbf{AR}}$ refers to the aspect ratio of cells (diameter λ normalized by z_i), and for SU and SD it refers mainly to the aspect ratio of rolls (wavelength λ normalized by z_i).

Although R_{ww} could be extended to provide the roll orientation Θ (associated with the angular lag r_θ at largest autocorrelation, following S17), such an approach would yield ambiguous values for cells and transitional structures due to their greater axisymmetry. Instead, we turned to a simpler approach introduced by Thurston et al. (2016), which considers frequency distributions of Θ'_{10}, wind direction anomalies from the subdomain-wide circular average 10-m wind direction. Since rolls are known to be aligned slightly off the average wind direction vector (Lemone, 1973), the distribution of Θ'_{10} is expected to reflect this offset.

Multiresolution flux decomposition (MRFD)

MRFD partitions data sets of any two variables x and y (each of length $2^M = 128$, $M = 7$ grid points) into segments containing 1, 2, 4, ..., 2^M points. At every scale, the segment mean is subtracted and the MR cospectrum for that segment is obtained. The resulting variables and MR cospectrum at each scale are:

$$\hat{x}_n(m) = \frac{1}{2^m} \sum_{i=1}^{n2^m} x_{r_i}(m), \tag{4.5}$$

$$\hat{y}_n(m) = \frac{1}{2^m} \sum_{i=1}^{n2^m} y_{r_i}(m), \tag{4.6}$$

$$D_{xy}(m+1) = \frac{1}{2^{M-m}} \sum_{n=1}^{2^{M-m}} \hat{x}_n(m)\hat{y}_n(m), \tag{4.7}$$

where $x_{r_i}(m)$ and $y_{r_i}(m)$ denote the residual series (following successive removal of segment means on windows with preceding widths greater than 2^m points). The $\hat{}$ notation denotes the average at the local scale n. Finally, the cumulative MR cospectrum, analogous to an ogive (Oncley et al., 1996), is obtained by summing over all averaging scales 1, ..., $S = 7$:

$$\sum_{m=1}^{S} D_{xy}(m) = \left[\left(x - \hat{x}^S\right)\left(y - \hat{y}^S\right)\right]. \tag{4.8}$$

MRFD cospectra were calculated in the north-south (y) direction, and then averaged (for each scale) along the 128 columns in the east-west direction (x). The final MRFD cospectrum was obtained by averaging all 128 spatial and 30 temporal cospectra, similar to Gibbs and Fedorovich (2014). The y direction was chosen in the first step since it more closely corresponds to the along-valley axis (150°-330° azimuth). The advantage of

MRFD compared to Fast Fourier Transform (FFT) is the independence of MRFD on any periodicity in a data set, omitting the need for tapering the data due to heterogeneous inflow and outflow at the subdomain boundaries. Furthermore, interpretation of peaks in the MRFD cospectra is less ambiguous compared to the FFT, due to the local nature of the former (Howell and Mahrt, 1997).

When decomposed with MRFD, the directional shear vw exhibits trends in the low-frequency part of cumulative MRFD $\sum D_{vw}/w_m^2$, indicating presence of upslope flow (B17). To facilitate easier comparison, we normalized each directional shear curve with its corresponding mixed-layer velocity scale $w_m = (w_*^3 + 5u_*^3)^{1/3}$ (Moeng and Sullivan, 1994; Catalano and Moeng, 2010), where w_* and u_* are the convection and friction velocities, respectively.

CBL depth determination

For the estimation of z_i from LES output, we used the standard flux method following Sullivan et al. (1998). At each output time, a three-dimensional sensible heat flux array $w\theta$ was obtained at each grid point within the subdomain, and all 128^2 profiles were averaged into a single vertical flux profile $\langle w\theta(z)\rangle$. The height above ground at which $\langle w\theta(z)\rangle$ reached a local minimum was defined as $\langle z_i\rangle$. The final 15-min estimate $\overline{\langle z_i\rangle}$ was obtained by averaging all thirty $\langle z_i\rangle$ values for each subdomain, and will be written simply as z_i in the remainder of the paper. To ensure we were considering only conditions when the daytime turbulence in d05 was resolved, we discarded all 15-min ensemble statistics for which z_i was less than 400 m. This threshold depth was chosen to be greater than WRF's effective vertical resolution of $(6-8)\,\Delta z$.

To obtain the CBL depth z_i from ISS-2, we used the method proposed by Heo et al. (2003). This method relies on an elevated maximum in the refractive index structure parameter (Angevine et al., 1994) and on changes of the Doppler spectral width with height. This latter criterion is required in our case, since the elevated maximum was difficult to observe in most cases during T-REX. The temporal resolution of z_i and associated $-z_i/L$ was equal to 30 min.

4.4 Results

We first determine whether the three simulations reproduced the observed flow thermodynamics by validating the d05 output against pertinent T-REX observations. Then, we

dedicate each subsection to answering the three questions posted at the end of the Introduction: 1) Are structural parameters of rolls and cells ($\overline{\mathbf{AR}}$, $\overline{\lambda}$, $\overline{\mathcal{R}}$, Θ) in Owens Valley, different from those found over flat terrain? 2) Within the valley itself, are these parameters different over the floor and the adjacent slope? 3) Does a relationship exist between different convection modes (rolls, cells) and upslope flows?

4.4.1 Time series validation

The overall trend of wind speed evolution was well captured in all three cases except for some underestimated wind speed during mid-afternoon at the valley floor for WS and SU and at the slope for SU (Fig. 4.3a, b, c, and Fig. 4.4a, b, c),

Wind direction was also well simulated in all three cases, especially at the valley floor (Fig. 4.3d, e, f and Fig. 4.4d, e, f). Slight counter-clockwise (WS, SU) and clockwise (SD) turning of the surface winds was evident at the western slope (Fig. 4.4d, e, f) due to an interaction of valley and slope flows. The evolution of winds closely followed the long-term (2 month) trends previously observed for the three categories (B17, Fig. 3.2).

The time evolution of $-z_i/L$ (Weckwerth et al., 1999; Gibbs et al., 2011; Thurston et al., 2016) provides an indication of the presence of either rolls, cells or transitional structures. On WS, conditions for the presence of transitional structures were present until early afternoon across the valley (Figs. 4.3g, 4.4g). Afterwards, the CBL deepened and upvalley winds weakened, resulting in conditions for cell prevalence until the end of the simulation. On SU (Figs. 4.3h, 4.4h), conditions for the presence of rolls prevailed in the afternoon both at the valley floor and slope due to intensifying upvalley flows. On SD, strong downvalley flows during morning and early afternoon hours (Figs. 4.3i, 4.4i) supported conditions for rolls, transitioning into cells nearing the end of the simulation. With the exception of a delay in conditions favorable for rolls at the valley floor on SU (Fig. 4.3h), the evolution of $-z_i/L$ was sufficiently captured by LES for all cases and subdomains. This agreement is encouraging, considering the potential uncertainties associated with calculating the observed $-z_i/L$ (large distance between ISS-2 and WT) and simulated $-z_i/L$ (subdomain-average, in an area of horizontally heterogeneous complex terrain).

The favorable comparison between simulated and observed evolution of variables and parameters relevant to convection organization reported above, allows us to study simulated properties of rolls and cells.

4.4.2 Properties of rolls and cells

We focus specifically on each of the four structural parameters ($\overline{\mathbf{AR}}$, $\overline{\lambda}$, $\overline{\mathcal{R}}$, Θ) with an emphasis on 1) establishing the bulk differences between Owens Valley and flat terrain (and linear theory), and 2) determining valley-slope contrasts for each parameter. Details on obtaining these parameters are outlined in Section 4.3.3. We limited our investigation to the height $z/z_i = 0.25$. This height is well above the surface layer where the influence of SGS motions on resolved convection is non-negligible.

Aspect ratio $\overline{\mathbf{AR}}$

In all three case studies, simulated aspect ratios (Fig. 4.5a) ranged between 2.3 and 2.6, which is smaller than observed $\overline{\mathbf{AR}}$ for several overland roll cases (Young et al., 2002) and the theoretical prediction derived using linear theory (Kuettner, 1971). Our simulated $\overline{\mathbf{AR}}$ agree well with the only reported occurrence of roll aspect ratios from idealized LES conducted over a heated slope by Schumann (1990). This result confirms that valleys tend to narrow the already narrow overland rolls even further. The same narrowing mechanism seems to apply for cells that were simulated on WS, given that cellular aspect ratios in this case were smaller, by an order of magnitude, than their flat terrain and open sea counterparts (Miura, 1986).

The advection of cells and rolls onto the western slope did not alter their aspect ratio: differences between $\overline{\mathbf{AR}}$ over the valley floor and the slope were not statistically significant ($p > 0.05$).

Wavelength/diameter $\overline{\lambda}$

We next compare cell diameters (WS) and roll wavelengths (SU, SD) (Figure 4.5b). The cell diameters on WS were generally larger than the roll wavelengths on SU and SD. On the other hand, rolls were spaced closer together on SD than on SU. Here, the only statistically significant difference between the valley and slope subdomains was found for SD ($p = 0.03$). We hypothesize that the contrast between SU and SD stems from variations in upstream topography: while the downvalley flow is mostly uninterrupted for several tens of kilometers to the north and northwest, the presence of an approximately 500 m tall hill roughly 15 kilometers south of the CT subdomain (Fig. 4.1b) may have disrupted the roll linearity on SU. This is also confirmed by a more perpendicular flow to the western slope on SD (Fig. 4.4f) than on SU (Fig. 4.4e), implying that advection of flow over the hill on SU disrupted roll linearity downstream of it.

The dependency of z_i on the wavelength/diameter λ has previously been examined through linear theory (Kuettner, 1971) and flat terrain observations (Weckwerth et al., 1997). We now investigate how this dependency varied between the WS, SU, and SD cases in Figure 4.6. Details of the linear regression parameters are shown in Table 4.2. In all three cases and for both subdomains, the linear regression yielded best fits close to the linear theory prediction (Kuettner, 1971). An exception was again the CT subdomain on SD (Fig. 4.6c). Compared to the cell case (Fig. 4.6a), the slope of best fits for the roll cases (Fig. 4.6b, c) converged slightly towards the relationship established by Weckwerth et al. (1997) for flat terrain. Similar to the cell $\overline{\mathbf{AR}}$, the agreement between the corresponding cell diameters (Fig. 4.6a) and the linear theory prediction for banded convection, was striking. In addition to making cells narrower (as was shown in Fig. 4.5a), a valley also tends to make cells behave more like rolls, by imposing a certain amount of linearity into cellular axisymmetry.

Roll organization factor $\overline{\mathcal{R}}$

On average, the pattern of increasing $\overline{\mathcal{R}}$ (Fig. 4.5c) with more pronounced linearity in convection agrees well with inferences made previously for $\overline{\mathbf{AR}}$ (Fig. 4.5a) and $\overline{\lambda}$ (Fig 4.5b). The difference between the valley and slope $\overline{\mathcal{R}}$ is statistically significant ($p = 0.002$) only on WS. Additionally, there was a tendency for greater $\overline{\mathcal{R}}$ at CT for all three case studies. The SD case had slightly weaker winds but larger $\overline{\mathcal{R}}$ values than the SU during roll-prevalent conditions. This indicates a dependency of $\overline{\mathcal{R}}$ on the direction of the along-valley wind with subsequent variations in the upstream topography.

$\overline{\mathcal{R}}$ depicts the transition regime well (Fig. 4.7), unlike $\overline{\lambda}$ or $\overline{\mathbf{AR}}$ which do not scale with $-z_i/L$ over land (Young et al., 2002). The convection transitioned from quasi-cellular to fully cellular during the afternoon on WS (Figs. 4.7a). This was reflected in the relatively low values of $\overline{\mathcal{R}}$, particularly near the transitional region ($15 < -z_i/L < 25$) where our values were comparable to those of S17. Interestingly, with $-z_i/L$ increasing beyond 30, $\overline{\mathcal{R}}$ increased over the valley floor and slope, but decreased over flat terrain. This suggests that flow channeling by the valley sidewalls tended to impose linearity onto the prevailing cells during free-convective conditions, further corroborating the findings based on $\overline{\mathbf{AR}}$ (Fig. 4.5a) and $\overline{\lambda}$ (Figs. 4.5b, 4.6a).

With increasing winds during SU, $-z_i/L$ decreased sufficiently to allow development of rolls (Figs. 4.3h, 4.4h). As a result, a broader range of $-z_i/L$ enabled both rolls and cells (Fig. 4.7b). The $\overline{\mathcal{R}}$ increase with decreasing $-z_i/L$ was less pronounced over the valley

floor and slope than over flat terrain. In other words, cells were more linear and rolls were less linear compared to flat terrain. On the other hand, the SD case sustained conditions most favourable for rolls and the transitional roll-like structures, while there were almost no cellular structures (Figs. 4.3i, 4.4i and 4.7c). The increase of $\overline{\mathcal{R}}$ with decreasing $-z_i/L$ agreed with flat terrain simulations, although there was a tendency for greater linearity below $-z_i/L = 7$ (Fig. 4.7c) compared to the idealized LES results in S17.

In conclusion, the transitional regime in $-z_i/L$ was found to be broader in Owens Valley compared to flat terrain, resulting in enhanced occurrence of transitional structures with overall reduced cellular axisymmetry.

Roll orientation Θ

To investigate the alignment of cells and rolls relative to the dominant along-valley flow, we calculated probability frequency distributions of 10-m wind direction anomalies Θ'_{10}. We show these frequency distributions for both subdomains and all three case studies in Fig. 4.8. Similar figures for the frequency distributions of Θ'_{10} were shown previously by Thurston et al. (2016), and for radar reflectivity by Heath et al. (2017). For all three case studies and both the valley floor and slope, instantaneous wind direction anomalies from the average 10-m wind direction fell within range of previously observed (Kelly, 1984) and simulated (Thurston et al., 2016) flat terrain values ($\Theta'_{10} \approx \pm 20^\circ$).

On WS (Fig. 4.8a, d), the peak distribution of anomalies did not deviate from the dominant upvalley flow direction until 21 UTC. Until that time, Θ'_{10} rarely exceeded $\pm 20^\circ$. After 21 UTC and following the weakening of upvalley flow (Figs. 4.3a, 4.4a), convection transitioned into a near free-convection state, as indicated by a broader frequency distribution, now spanning $\pm 40^\circ$. However, at this time the peak frequency distribution became more negative, indicating that cells were oriented to the left of the upvalley flow.

Prevalence of rolls on SU and SD (Fig. 4.8b, c, e, f) resulted in narrower distributions than on WS, rarely exceeding $\pm 20^\circ$. Rolls were oriented parallel to the mean wind for Owens Valley, contrary to Thurston et al. (2016) who found a steady positive offset of rolls from the mean wind in their flat terrain simulations. This suggests that a valley environment tends to lock rolls into a fixed alignment with the dominant upvalley or downvalley flow, irrespective of along-valley flow direction or location in the valley.

4.4.3 Coupling of convection modes with upslope flows

The previous section showed certain differences among simulated cell and roll parameters between the valley floor and slope. Since slope sites are typically influenced by upslope flows, the valley floor-slope contrasts that we found previously (Section 4.4.2) may be related to the upslope flows. To investigate this, we analyze upslope flow presence and strength. Unfortunately, pure upslope flows are often masked by upvalley flows and difficult to observe with traditional tools such as time series inspection and flow visualization. As a surrogate for upslope flow, we study the lateral momentum flux vw, also known as directional shear (Van Gorsel et al., 2003; Rotach et al., 2008) using multiresolution flux decomposition (Section 4.3.3).

To make our results directly comparable to results from a 2-month analysis in B17 (Fig. 3.9), we report $\sum D_{vw}/w_m^2$ for each case study and both subdomains (Fig. 4.9). To investigate the dependency on convection organization, we color-coded each curve with its respective $\overline{\mathcal{R}}$ value (Fig. 4.7). In this manner, cold colors represent cells, near-gray colors represent the transitional regime, while warm colors represent rolls.

For scales greater than approximately 900 m, the majority of $\sum D_{vw}/w_m^2$ at CT does not show obvious increasing or decreasing trends with increasing length scale, regardless of the case study (Fig. 4.9a, b, c). This indicates that there were minimal signatures of an upslope flow component at the valley floor. At the slope, the superposition of along-valley and an upslope flow component resulted in either increasing (Fig. 4.9d) or decreasing (Fig. 4.9f) trends in $\sum D_{vw}/w_m^2$. These trends coincide with trends from a 2-month analysis in B17 and with the sign convention proposed by Rotach et al. (2008). An exception is the absence of positive $\sum D_{vw}/w_m^2$ on SU days, (Fig. 4.9e) contrary to what was found in B17.

To test the hypothesis of upslope flow strength influencing convection organization (via $\overline{\mathcal{R}}$), we considered the difference in $\sum D_{vw}/w_m^2$ between 864 m and the largest scale, equal to 6.91 km (dimension of the subdomain). This difference was taken as a proxy for the strength. We focus only on WT, since upslope flows were not present at the valley floor. The correlation between these differences and $\overline{\mathcal{R}}$ were negligible (Pearson correlation coefficient $r = 0.08, -0.09, -0.06$ for WS, SU and SD, respectively), suggesting that the strength of upslope flow did not affect convection organization over the gentle western slope of Owens Valley.

4.5 Summary and Conclusions

We investigated cells and rolls in Owens Valley, a deep and wide semiarid valley, by performing high-resolution simulations for three case studies that were representative of a certain synoptic regime. The simulations were performed by nesting LES inside mesoscale WRF. The fine horizontal grid spacing, equal to 54 m, along with an average vertical spacing of 40 m below the surrounding ridgetops, ensured that daytime convection was explicitly resolved. Evaluation of model output against observations collected during T-REX, revealed that LES adequately reproduced the valley-slope flow, as well as the onset of horizontal convective rolls and open cells. The near-ideal topography of Owens Valley, including small variability in ridgeline elevations (relative to the valley CBL depths) and the steady western slope angle, add value to the generality of the results reported here.

We can summarize the main findings of the present study as follows:

- Both rolls and cells behave differently in Owens Valley compared to flat terrain.

  Roll aspect ratios $\overline{\mathbf{AR}}$ were smaller than values traditionally found over level terrain, and smaller than values obtained from linear theory of banded convection. In other words, the role of a valley environment was to narrow banded convection. When winds were downvalley, rolls were spaced slightly closer together compared to upvalley case, as indicated by statistically significant differences of the simulated roll wavelengths. Unlike flat terrain, rolls were aligned with the main (along-valley) wind. Differences in upstream topography between the upvalley and downvalley flow cases was considered the root cause of these differences in roll properties.

  Cellular aspect ratios $\overline{\mathbf{AR}}$ were an order of magnitude smaller than over flat terrain and open sea. Therefore, valleys tend to introduce linearity into cellular axisymmetry. Cells lacked orientation preference similar to rolls, but the distribution of wind direction anomalies Θ'_{10} was larger for cells than for rolls, in agreement with past studies.

  The transition from rolls to cells occurred over a broader $-z_i/L$ range compared to flat terrain. Inspection of the roll organization factor $\overline{\mathcal{R}}$ further supported the notion that valleys introduce certain linearity into convection organization.

- In most cases, structural parameters of cells and rolls exhibited statistically insignificant differences between the valley floor and the adjacent slope. Only on two occasions were these differences statistically significant: roll organization factor $\overline{\mathcal{R}}$ was

larger over the floor than the slope on WS, and roll wavelength was larger over the slope than over the floor on SD. This points to the importance of simultaneously considering multiple convection-related metrics, as they may provide a more objective viewpoint of contrasts in convection organization.

- Extension of MRFD to LES output enabled the investigation of quantitative aspects of upslope flows in Owens Valley, in agreement with a previously established observational climatology. Our results indicate that upslope flows did not modify convection organization. For instance, the strength of the upslope flow was poorly correlated with the roll organization factor $\overline{\mathcal{R}}$. Although our conclusions are limited to a particular cross-section of Owens Valley, we argue that similar conclusions hold in general for the valley due to negligible differences in the along-valley slope angle.

The principal finding of our study is the valley-induced narrowing of daytime convection, whose role is to ultimately increase the occurrence of rolls and transitional roll-like features in the valley CBL. The increased linearity may modify turbulent exchange of momentum and scalars as well, in a manner more typical for horizontal convective rolls. Properly representing this added linearity over complex terrain in operational NWP, as subkilometer grid spacings become more viable, will be of critical importance, given the subtle interplay between the *terra incognita* and resolving the topography with sufficient accuracy.

Our study provided useful case studies for the investigation of rolls and cells in a wide and deep valley. Arguably, the two main limitations of the present study are the use of unusually large innermost LES domains and the inability of exploring in more detail the dependency of convection properties on upstream topography. The former limitation could be alleviated with achieving resolved turbulence more rapidly by means of, for instance, the cell perturbation method (Muñoz-Esparza and Kosović, 2018). Idealized LES possesses potential to mitigate the latter limitation, where varying the strength and direction of the background flow could be utilized to generate different convective features. Similarly, varying the slope angle and along-valley terrain variability with such idealized simulations can help generalize our findings. Thereby, equilibrium states may be more easily attained as well, resulting in more reliable ensemble averaged statistics. Developing suitable parameterizations of such topographical effects on convection organization in complex terrain is highly relevant for operational NWP, where subkilometer LES is still not entirely achievable. However, idealized LES studies should take special care when differentiating between

mountain waves aloft and rolls beneath, as both may leave a similar signature when applying spatial autocorrelation detection algorithms. From an observational point of view, future field experiments conducted in complex terrain should focus on resolving both the vertical and horizontal structure of convection, for instance, by utilizing high-resolution single and dual Doppler lidar systems.

Table 4.1: Details of the domain configurations and model setup.

	d01	d02	d03	d04	d05
Horizontal resolution (m)	12150	4050	1350	270	54
Parent-to-child ratio	1:3	1:3	1:3	1:5	1:5
# of grid points	150×120	178×175	220×223	241×281	901×901
# of vertical levels	60	60	60	60	113
Time step (s)	30	10	3.33	0.22	0.04
epssm	0.1	0.1	0.1	0.4	0.5
Nesting	one-way				
Topography	2 arc-min	30 arc-sec		SRTM 1 arc-sec	
Land-use	NLCD-2006 30 arc-sec			NLCD-2006 1 arc-sec	
Simulation runtime	00 UTC - 00+ UTC			12 UTC - 00+ UTC	
Turbulence closure	Horizontal Smagorinsky 1st order			1.5-order SGS TKE	
PBL scheme	YSU			none	
Cumulus scheme	Kain-Fritsch	none			
Land surface scheme	Noah				
Surface layer scheme	Revised MM5 Monin-Obukhov				
Radiation scheme	RRTM + Dudhia				
Microphysics scheme	Morrison 2-mom (March 27 only)				
Initial conditions	NAM				

Table 4.2: Linear regression statistics for the relationships of the form $\lambda = az_i + b$.

		slope a	intercept b [km]	r^2
WS	CT	2.7 ± 0.3	-0.2 ± 0.3	0.77
	WT	2.1 ± 0.2	0.5 ± 0.3	0.71
SU	CT	3.4 ± 0.4	-0.9 ± 0.4	0.79
	WT	3.4 ± 0.4	-0.7 ± 0.4	0.80
SD	CT	1.0 ± 0.4	1.1 ± 0.3	0.21
	WT	3.6 ± 0.4	-1.1 ± 0.4	0.73

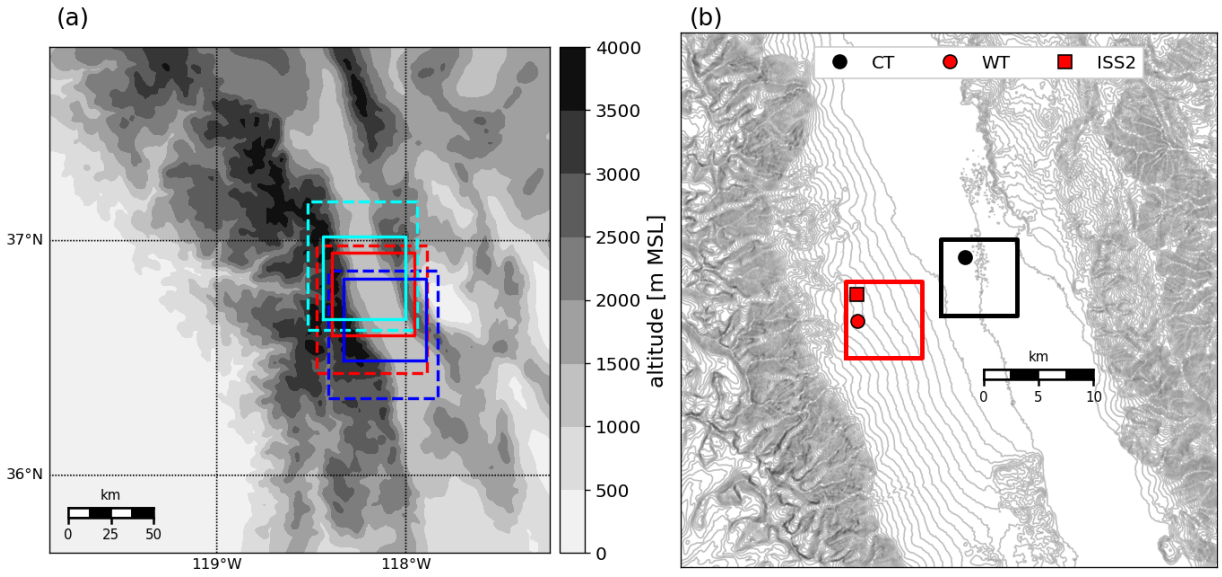

FIGURE 4.1: **(a)** 1-arc-minute topographical representation of the innermost WRF-MESO domain d03. The topography is contoured every 500 m. The dashed and solid rectangles denote the borders of the outermost (d04) and innermost (d05) WRF-LES domains, for WS (red), SU (blue) and SD (cyan); **(b)** 1-arc-second SRTM topographical representation of the innermost (d05) LES domain for the WS case, contoured every 50 meters. The large black and red squares represent the outlines of the 6.91×6.91 km^2 CT and WT subdomains, respectively.

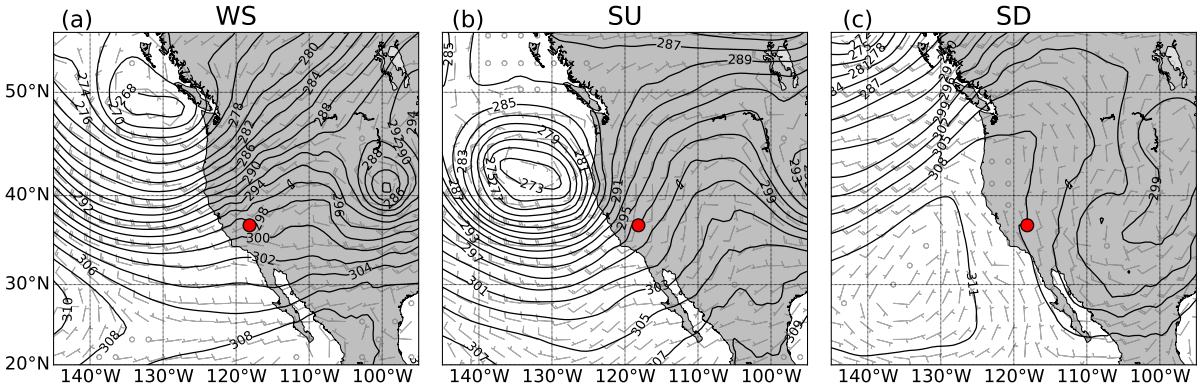

FIGURE 4.2: ECMWF 700-mb reanalysis products for 00 UTC on **(a)** April 16, **(b)** March 28 and **(c)** April 29. Black contour lines denote isoheights in increments of 2 geopotential decameters, while the red dot marks the location of CT.

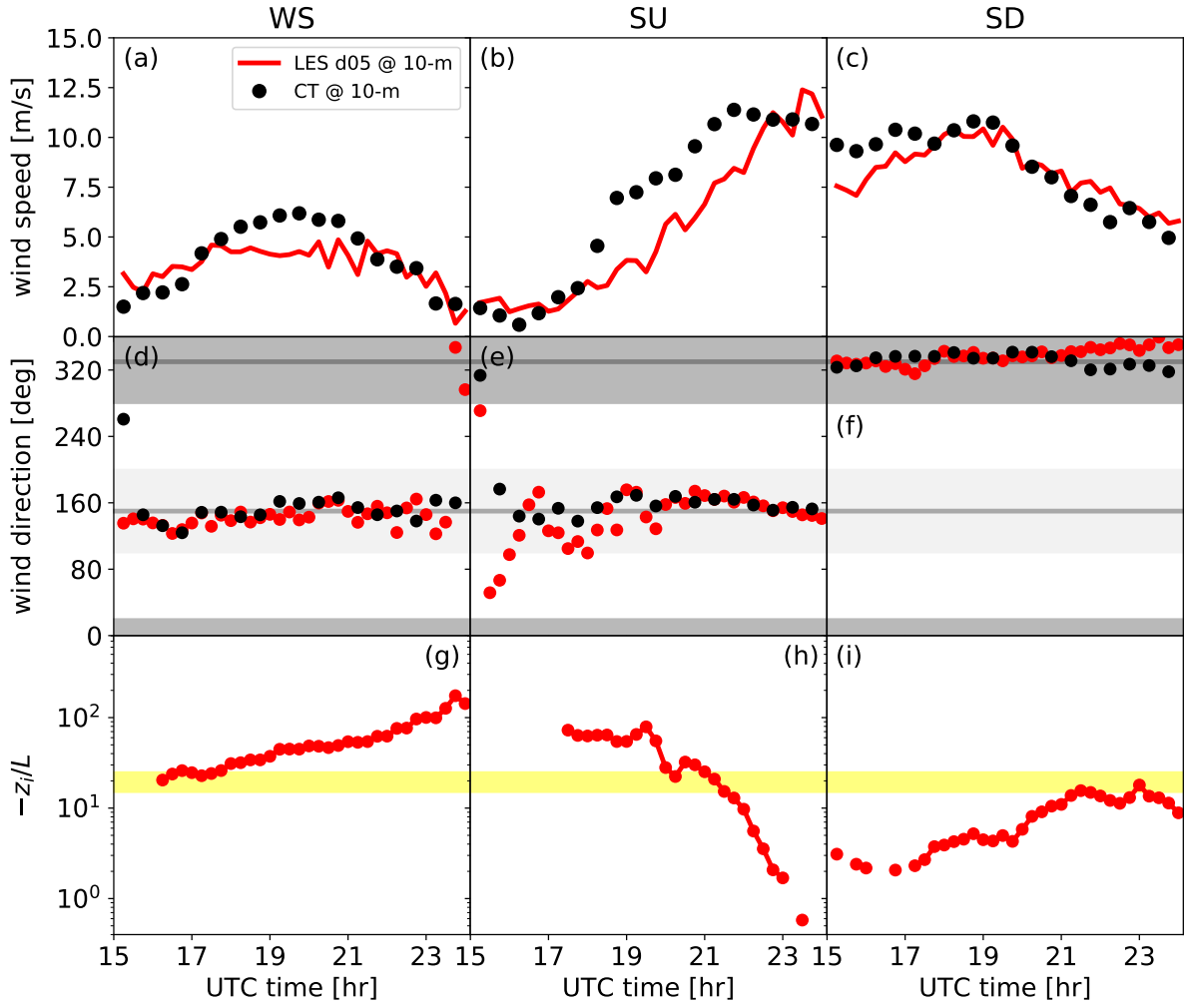

FIGURE 4.3: Time series comparison of **(a)**, **(b)**, **(c)** wind speed, **(d)**, **(e)**, **(f)** wind direction and **(g)**, **(h)**, **(i)** bulk CBL stability parameter $-z_i/L$ for the three case study simulations at the valley floor. Red markers denote 15-min averages at the grid point closest to CT, while black markers denote 30-min observations. The $-z_i/L$ values in **(g)**, **(h)**, **(i)** represent spatiotemporal averages over the entire 6.91x6.91 km^2 CT subdomain. Dark and light grey shaded areas in **(d)**, **(e)**, **(f)** denote the downvalley and upvalley sectors, respectively. Solid gray lines in **(d)**, **(e)**, **(f)** denote the along-valley axis (150°-330° azimuth). Yellow shaded region denotes the commonly accepted range in which transitional convection structures occur. Gaps in **(g)**, **(h)**, **(i)** are associated with data rejected due to insufficiently large z_i (Section 4.3.3).

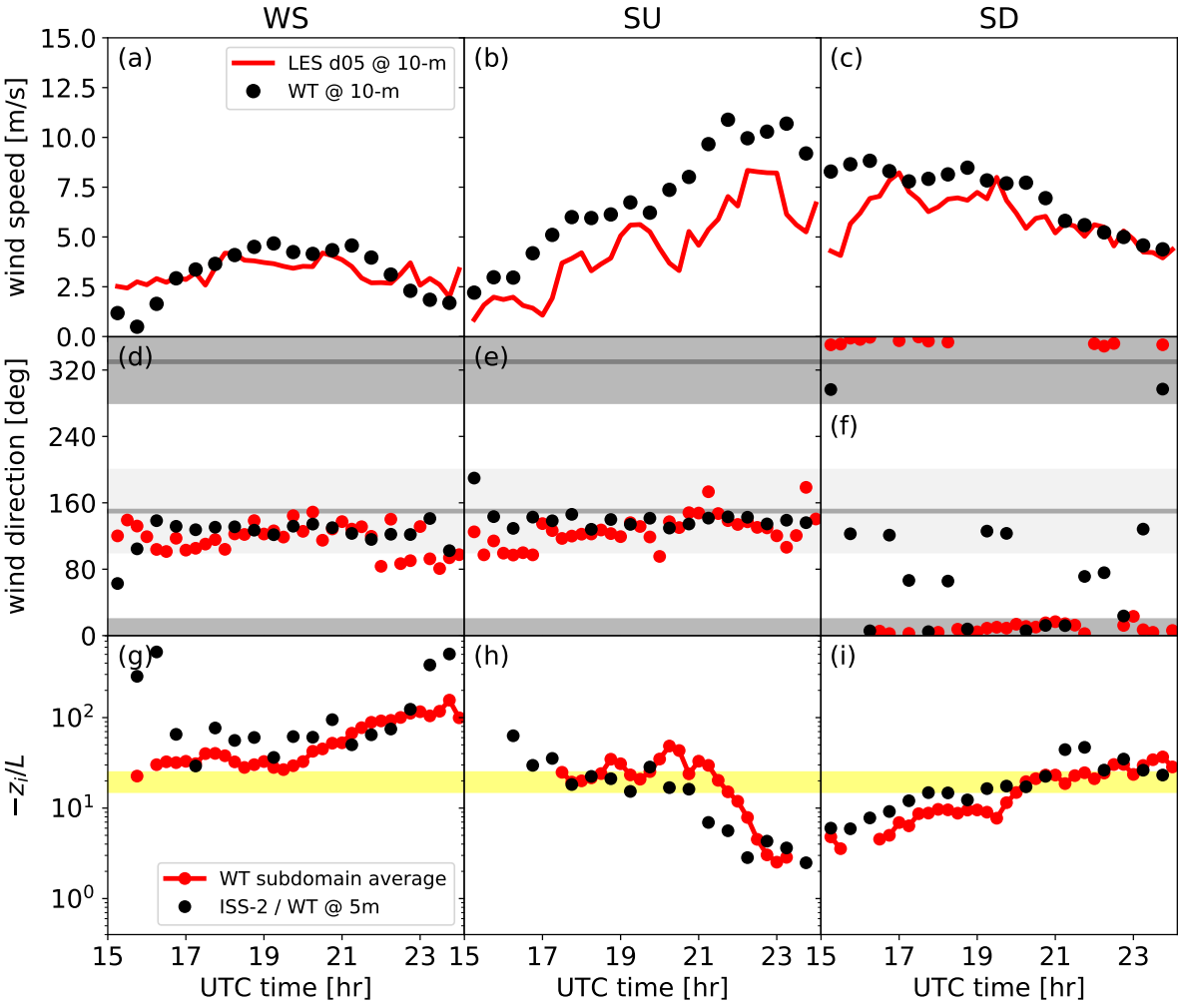

FIGURE 4.4: Same as in Fig. 4.3 but for WT and the WT subdomain.

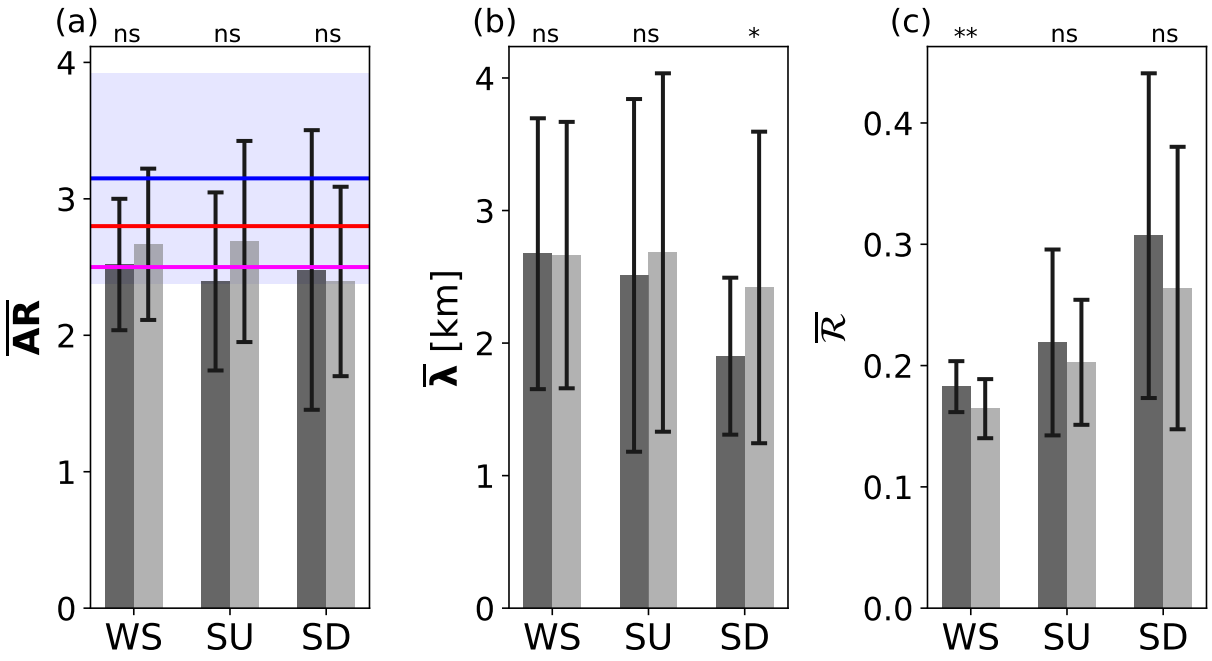

FIGURE 4.5: Statistical comparison of **(a)** aspect ratio $\overline{\mathbf{AR}}$, **(b)** wavelength (in case of rolls) or diameter (in case of cells) $\overline{\lambda}$ and **(c)** roll organization factor $\overline{\mathcal{R}}$, at $z/z_i = 0.25$. Vertical bars represent means of all available 15-min ensemble averages from each simulation. Dark gray bars denote the CT subdomain, while light gray bars denote the WT subdomain. Error bars represent $\pm$ one standard deviation. Markers above each subplot represent results of the Student t-tests at 95% significance level (ns stands for 'not significant', * denotes $p \leqslant 0.05$ and ** denotes $p \leqslant 0.01$), where the test was applied to test differences between the CT and WT subdomains. Magenta line in **(a)** denotes AR of rolls simulated over a 10° slope by Schumann (1990), red line denotes the theoretical value by Kuettner (1971), while blue line and blue shading denote mean and standard deviation of AR for overland rolls (Young et al., 2002), respectively.

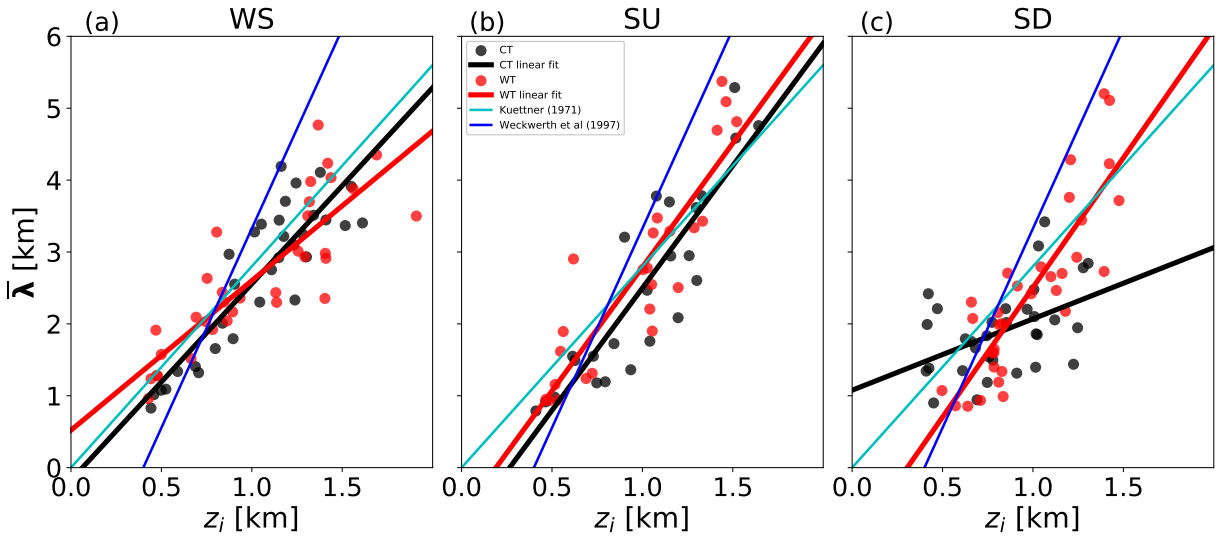

FIGURE 4.6: Wavelength (in case of rolls) or diameter (in case of cells) $\overline{\lambda}$ at $z/z_i = 0.25$ as a function of the CBL depth z_i, for **(a)** WS, **(b)** SU and **(c)** SD. Each dot represents a spatial average over the entire subdomain and a temporal average over a 15-min period. Black and red dots are for the CT and WT subdomains, respectively, while solid black and red lines are their respective best fits obtained with linear regression (details given in the text). Blue and cyan solid lines are the best fits obtained by Weckwerth et al. (1997) and Kuettner (1971), respectively.

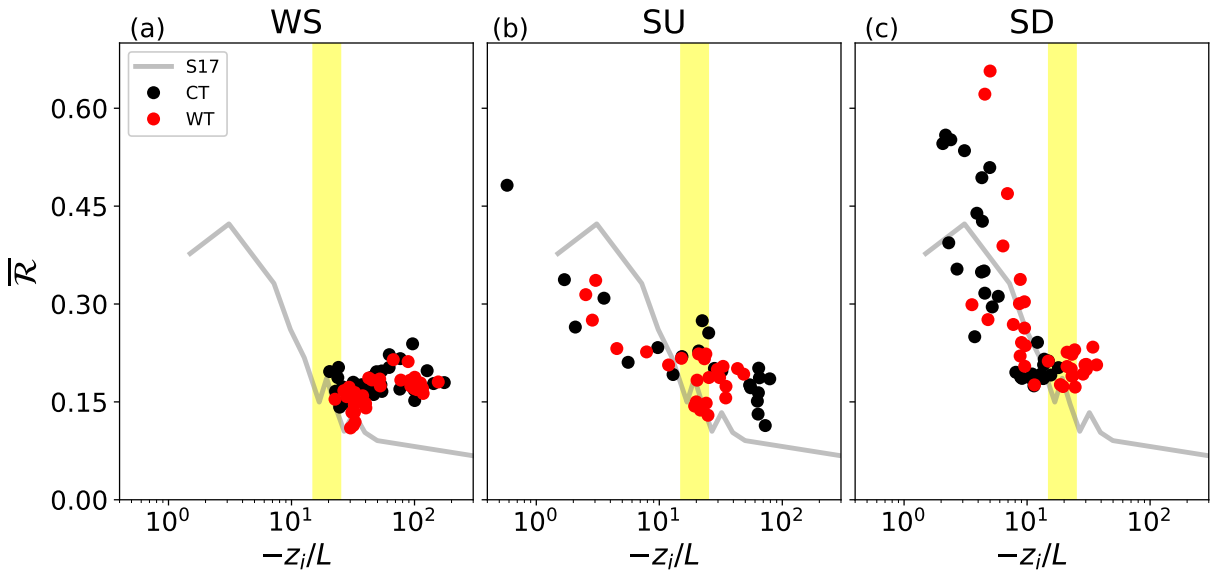

FIGURE 4.7: Roll organization factor $\overline{\mathcal{R}}$ at $z/z_i = 0.25$ for **(a)** WS, **(b)** SU and **(c)** SD. Each dot represents a spatial average over the entire subdomain and a temporal average over a 15-min period. Yellow shaded region denotes the commonly accepted range in which the transition from rolls to cells is expected to occur. Grey line in **(a)**, **(b)** and **(c)** denotes roll organization factors at $z/z_i = 0.25$ reported by S17 for their suite of idealized, flat terrain LES.

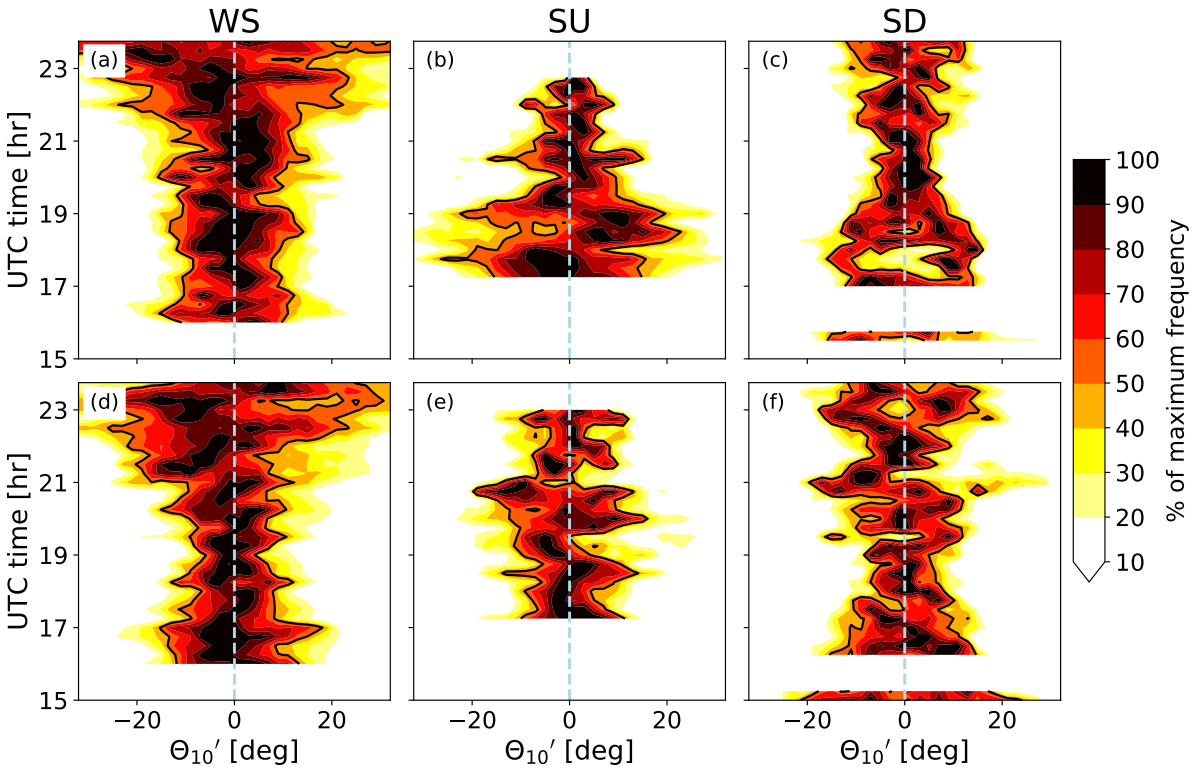

FIGURE 4.8: Contoured frequency by time diagram of the 10-m wind direction anomalies Θ'_{10}, for **(a)**, **(d)** WS, **(b)**, **(e)** SU and **(c)**, **(f)** SD. Top row of panels is for the CT subdomain and the bottom row of panels for the WT subdomain. The shading represents the percentage of maximum frequency of anomalies for the entire subdomain and for each 15-min averaging period. The solid black contour line represents 50% of the maximum frequency. The dashed gray line denotes zero wind direction anomaly.

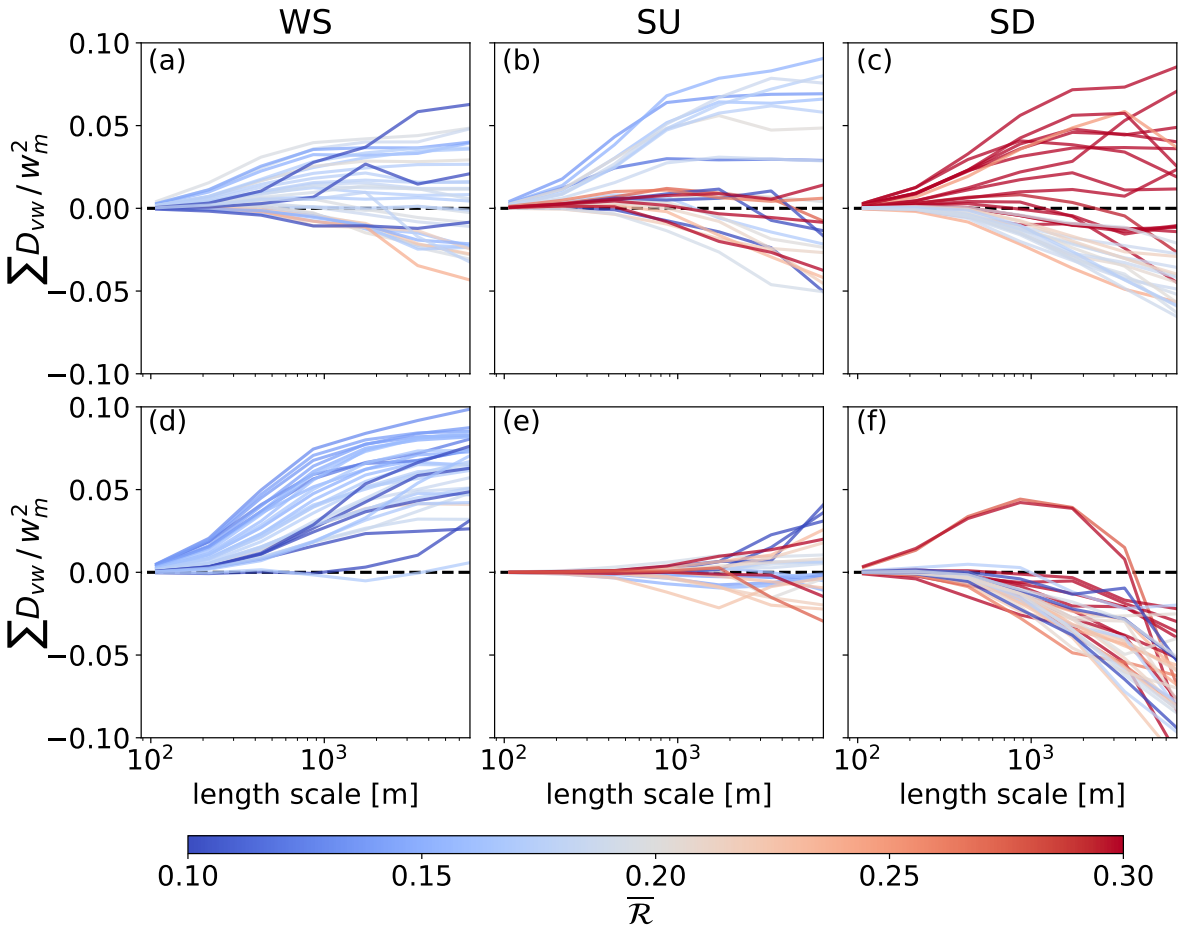

FIGURE 4.9: Cumulative normalized MRFD covariances of directional shear $\sum D_{vw}/w_m^2$ for **(a)**, **(d)** WS, **(b)**, **(e)** SU and **(c)**, **(f)** SD, at $z/z_i = 0.25$. Top row of panels is for the CT subdomain and the bottom row of panels for the WT subdomain. Each curve is color-coded with its corresponding roll organization factor $\overline{\mathcal{R}}$. Dashed line denotes zero flux.

5

Multiscale investigation into causes of the surface energy balance underclosure in a semiarid valley

5.1 Introduction

Governed by the first law of thermodynamics, the provided energy input (composed of the net radiation R_{net} and ground heat flux G_0) should balance the energy output (composed of the sensible H and latent LE heat fluxes) in the atmospheric surface layer (ASL). Hence, the energy balance ratio (EBR) should be unity:

$$EBR = \frac{H + LE}{R_{net} - G_0} \tag{5.1}$$

A number of applications invoke the assumption of a fully closed surface energy balance (SEB), i.e. $EBR = 1$. For instance, land-surface models (LSM) are constrained by measured heat fluxes to properly model land-atmosphere interactions (Williams et al., 2009). Majority of surface vegetation-atmosphere transfer (SVAT) models are used to model the SEB that is fully closed, however their validation heavily depends on the quality of measured SEB components (Foken et al., 2011). To estimate evapotranspiration at the surface using satellite remote sensing, the Surface Energy Balance Algorithm for Land (SEBAL) framework (Long and Singh, 2010) invokes perfect SEB closure by attributing the SEB residual to the latent heat flux LE. However, as evidenced by multitudinous experimental endeavours and review studies (Wilson et al., 2002; Foken, 2008; Leuning et al., 2012), perfect SEB closure is seldomly achieved in the daytime ASL. Specifically for the FLUXNET network (Baldocchi et al., 2001; Wilson et al., 2002), the average EBR has been shown to

range between 0.7 and 0.9. A myriad of potential reasons and physical mechanisms have been proposed to be the culprit of such underclosure (Foken, 2008; Leuning et al., 2012). A consensus has recently been reached (Foken et al., 2011), dismissing instrumental errors and sensor deficincies as crucial causes of the SEB underclosure. Instead the traditional eddy covariance (EC) methodology (Swinbank, 1951), with its customary 30-min temporal averaging, may miss a substantial portion of the heat fluxes H and LE. These flux portions are carried by low-frequency motions, commonly referred to as turbulent organized structures (TOS, Kanda et al., 2004), circulations assuming a series of overturning updrafts and downdrafts.

TOS may be classified into two distinct forms of convection organization in the CBL: low-wind speed cellular convection and high-wind speed horizontal convective rolls (Atkinson and Zhang, 1996). In low-wind speed situations, the low-frequency component of ASL fluxes will be biased since either a quasi-stationary updraft or downdraft will preferentially be sampled (Sakai et al., 2001). During high-wind speed conditions, this is not the case as a number of SEB related studies have reported better or even complete SEB closure (Wilson et al., 2002; Kanda et al., 2004; Franssen et al., 2010; Anderson and Wang, 2014). Improved SEB closure in these studies has been ascribed to pronounced mechanical mixing and a larger number of eddies sampled within 30 min. TOS have also been recognized by De Bruin et al. (2005), Lamaud and Irvine (2006) and Gao et al. (2017, 2018) to affect SEB via entrainment of warmer and drier free tropospheric air. This is quantified with the temperature-humidity correlation coefficient $r_{\theta q} = \overline{\theta' q'}/(\sigma_\theta \sigma_q)$, which exhibits negative values in the entrainment zone and positive values in the daytime ASL (Detto et al., 2008). Since perfect scalar similarity ($r_{\theta q} = 1$) is expected to hold in the ASL, violations from $r_{\theta q} = 1$ denote influence from non-local sources, such as the entrainment zone. Such scalar dissimilarity invalidates approaches to close SEB with traditional Bowen ratio-based methods (Twine et al., 2000), and is known to violate the Monin-Obukhov similarity theory (Andreas et al., 1998; Van de Boer et al., 2014). However, a detailed quantification of the relationship between $r_{\theta q}$ and EBR does not exist. Since the two forms of TOS are both CBL-spanning eddy entities, they are capable of bringing freshly entrained, scalar-dissimilar air from the entrainment zone down into the ASL. However, it is unknown which of the two forms of TOS are more efficient in this non-local violation of near-surface scalar similarity, and ultimately, the SEB underclosure as well.

With the increasing effects of climate change worldwide through aridification, processes such as desertification become increasingly pronounced and widespread (DOdorico et al.,

2013). One might argue that the feedbacks between desertification and other global change drivers (Maestre et al., 2016) are even more emphasized in mountainous regions which are also affected by elevation dependent warming (Gobiet et al., 2014; Pepin et al., 2015). As a result, for reliable future climate projections over mountains, proper validation and calibration of land-surface models with EC variables is paramount (Williams et al., 2009). Provided that half of the FLUXNET stations are sited in complex terrain (Rotach et al., 2014), the need to better our understanding of SEB in such environments is obvious. Unlike flat and horizontally homogeneous terrain, several factors require special care whenever examining SEB underclosure in complex terrain. Over sloping terrain, the orientation (gravity-parallel versus slope-normal) of the radiation measuring system has been found to affect R_{net} (Matzinger et al., 2003; Hiller et al., 2008; Serrano-Ortiz et al., 2016; Georg et al., 2016). The choice of the optimal post-processing treatment of EC-derived heat fluxes is essential (Večenaj and De Wekker, 2015; Stiperski and Rotach, 2016), particularly concerning coordinate rotation. Most SEB studies in complex terrain have been conducted over hilly terrain (Serrano-Ortiz et al., 2016; McGloin et al., 2018) and in mountain valleys (Hammerle et al., 2007; Hiller et al., 2008; Rotach et al., 2008; Nadeau et al., 2018), arriving to a general conclusion that the observed SEB underclosure, being typically poorer compared to the average FLUXNET underclosure, should be subject to great scrutiny when minimizing the numerous sources of uncertainties.

The goal of the present study is twofold: (1) to quantify the relationship between EBR and scalar similarity (expressed via $r_{\theta q}$), and (2) to determine whether scalar similarity violation due to entrainment depends on the prevalent form of TOS. We propose that a semi-arid valley represents a suitable environment for addressing our goal. As pointed out by Mahrt (1991) and Lamaud and Irvine (2006), a drier environment, characterized by low rates of evapotranspiration and a Bowen ratio ($Bo = H/LE$) exceeding unity, is subject to more pronounced entrainment impacts on scalar similarity. We expect this feature to facilitate an easier quantification of TOS effects on EBR. Valley flows experience significant channeling by the neighbouring sidewalls (Zhong et al., 2008), resulting in bimodality of the along-valley channeled flow which minimizes the degrees of freedom concerning the upwind fetch conditions. This is essential for reducing uncertainties when investigating the impact of complex terrain on the SEB underclosure. Owens Valley, CA, where the Terrain-Induced Rotor Experiment took place in Spring 2006, satisfies the above requirements.

5.2 Data and Methods

5.2.1 Terrain-Induced Rotor Experiment

Owens Valley

We analyze data from the Terrain-Induced Rotor Experiment (T-REX, Grubišić et al., 2008), conducted from March 1 to April 30 2006 in Owens Valley, CA (Fig. 5.1a). Owens Valley runs in a northwest-southeast direction for approximately 150 km, with the Sierra Nevada to the west and the Inyo and White Mountains to the east. Gentle western and relatively steeper eastern sidewalls characterize the approximately 3 km deep and roughly 30 km wide valley. Sloping with an angle of 3.25°, the western aluvial slope is characterized by little along-slope variability for several tens of kilometers. On the other hand, the valley floor slopes towards the north at an angle of 0.2°. The valley climate is mainly semiarid.

While the western slope is characterized by nearly homogeneous land-use (composed of steppe-dominant shrubs and grasses), the valley floor is less homogeneous (Fig. 5.1b). The majority of the valley around the T-REX region of interest is characterized by moderately permeable sandy loam and loamy sand soils. Land-use to the north of the town of Independence located nearby CT, is dominated by alkali meadows, wetlands and patchy irrigation fields, facilitating relatively large soil moisture throughout T-REX (Fig. 5.2a). Towards the south and the town of Lone Pine (bottom of Fig. 5.1b), land-use becomes more homogeneous and dominated by the Owens River watershed. As a result, the southern end of the valley is associated with greater aridity and relatively lower soil moisture (Fig. 5.2a). Despite the soil temperature being elevation-dependent (Fig. 5.2b), the low and high soil temperatures to the north of Independence and near Lone Pine, respectively, reflect these soil moisture contrasts. This northwest-southeast variability in land-use and soil properties governs a contrasting partitioning of input energy ($R_{net} - G_0$), producing an along-valley gradient in temperature and humidity that persisted throughout the 2-month research campaign.

To answer the two questions posted at the end of the Introduction, we split the 2-month data set into three categories (Babić et al., 2017, hereafter B17) to obtain days with targeted fetch conditions: Wind Shift (WS), comprised of quiescent days on which a twice diurnal reversal of wind direction occurred; Synoptic Upvalley (SU), for which a single or no wind direction reversal occurred and winds were upvalley during the day; Synoptic Downvalley (SD), for which a single or no wind direction reversal occurred and winds were downvalley during the day.

SEB instrumentation

To determine EBR, we use data from three 34-m National Center for Atmospheric Research (NCAR) Integrated Surface Flux Facility (ISFF) flux towers. These towers are designated as the central tower (CT), southern tower (ST) and western tower (WT), as depicted in Fig. 5.1b. CT and ST were deployed along the valley's central axis, with a separation of approximately 8 km. WT was located at the western slope approximately 9 km to the southwest of CT, perpendicularly to the along-valley axis. Each tower was equipped with EC instrumentation at 5 m above ground level (AGL), with the exception of CT, where the 5-m EC setup was operated on a separate 5-m tower located 9 m to the northwest of CT. To supplement the EC variables with the information about the CBL depth z_i, we used data of remotely sensed winds from the National Center for Atmospheric Research (NCAR) Integrated Sounding System 2 (ISS-2) wind profiler deployed approximately 3 kilometers north of WT.

The EC instrumentation consisted of a CSAT3 sonic anemometer (Campbell Scientific, Inc., CSI) and a Campbell KH2O krypton hygrometer (CSI) displaced 25 cm behind the CSAT3. Both sensors were facing towards west to minimize flow distortion with respect to the climatologically prevalent along-valley and westerly winds (Babić et al., 2016a, hereafter B16). The CSAT3 measurements of three wind speed components u, v, w and sonic temperature T_s were collected at 60 Hz, while water vapor mixing ratios q from the KH2O were sampled at 10 Hz. To achieve synchronous time series, the raw CSAT3 data were down-sampled to 10 Hz by block-averaging six consecutive values. We split the 2-month data set into 2928 30-min averaging periods.

A 1 m tall darkhorse stand was located in the vicinity of each flux tower to measure R_{net}. At CT, a CM21 pyranometer and a CG4 pyrgeometer (Kipp & Zonen) were used to obtain shortwave and longwave radiation flux densities, respectively. At ST and WT, a PSP pyranometer and a PIR pyrgeometer (Eppley) were used instead. All of the above were installed in a gravity-vertical configuration. R_{net} was obtained at a temporal resolution of 30 min, as the sum of the four shortwave and longwave, incoming and outgoing flux densities. Initial data obtained at a 5-min temporal resolution were block-averaged into 30-min averages.

Ground heat flux G_0 and additional soil thermal properties were collected in the vicinity of each flux tower. REBS HFT-3 heat flux plates (CSI) buried 5 cm below surface were used to obtain soil heat flux G, while volumetric heat capacities c_{soil} and soil temperatures T_{soil} were collected with Hukseflux TP01 thermal properties sensors 1 cm and 4 cm below

the surface. Due to wiring problems at WT, G values are not available from March 31 to April 18. By accounting for heat storage by the soil between the surface and the REBS heat flux plates, we follow Oncley et al. (2007), Gao et al. (2017) and Liang et al. (2017) to obtain the ground heat flux G_0. Raw 5-min data were block-averaged to obtain 30-min averages.

Valley-wide soil properties

To obtain information of soil moisture and temperature properties beyond the flux towers, we use the network of 23 gravimetric soil moisture probes (ECH2O EC-20, Decagon Devices). Each probe was buried 5 cm below the surface. The location of the probes is shown in Fig. 5.1a. Raw data were calibrated independently for each site to obtain volumetric water content and soil temperature at a 5-min temporal resolution (Daniels, 2010). To obtain information about spatial gradients shown in Fig. 5.2, we consider the full temporal range for which each sensor was operating during T-REX.

Post-processing

To ensure reliable EBR estimates, a number of corrections are necessary. Initial preprocessing of the CSAT3 and KH2O data sets included despiking and removal of questionable data (Vickers and Mahrt, 1997). Flow shadowing by the CSAT3 transducers may result in a heat flux underestimation, hence a correction is applied to the raw wind speed components, following Horst et al. (2015). Despite semiarid conditions, we correct T_s for moisture effects (Schotanus et al., 1983). Other corrections include correcting LE for density effects (Webb et al., 1980), accounting for flux attenuation due to a displacement between the CSAT3 and KH2O (Oncley et al., 2007), as well as accounting for oxygen ultraviolet light absorption by the KH2O (Tanner et al., 1993). Given sufficiently arid conditions, we can assume that the sonic temperature T_s is a reasonable approximation of both the potential θ and virtual potential θ_v temperatures, which we denote as θ in the rest of the analyses. Turbulent perturbations necessary to obtain H and LE were derived by detrending 10 Hz time series within each 30-min record with a location-dependent running mean length (B17). Specifically, we used a running mean of length 22, 18 and 26 min at CT, ST, and WT, respectively. Finally, sensible $H = \rho c_p \overline{w'\theta'}$ and latent $LE = \rho L_v \overline{w'q'}$ heat fluxes were obtained, where ρ denotes air density, $c_p = 1005\,\mathrm{Jkg^{-1}K^{-1}}$ is the specific heat of air at constant pressure, and $L_v = 2500\,\mathrm{Jg^{-1}}$ is the latent heat of vaporization of water.

Since measurements were collected during late winter and early spring in a semiarid valley well above low, sparse vegetation, several corrections are not necessary. High-frequency covariance losses due to path-averaging may occur when the CSAT3 is close to the ground (Lee et al., 2006; Grachev et al., 2007b). Appropriate corrections were found to be negligible for the 5-m CSAT3 (not shown), and are not applied in our case. Encouraged by Liang et al. (2017) who investigated SEB in another semiarid valley, we can neglect the vertical moisture movement in the soil, air heat storage between the surface and the EC setup, as well as flux densities associated with plant photosynthesis. To filter out values associated with the morning and evening transitional periods, each 30-min record satisfy $H > 10$ Wm^{-2} and $0 < EBR < 3$. Given that CT and ST were sited over an essentially flat valley floor (Fig. 5.1b), it is useful to consider how EBR differed between the two sites. At the 5-m level, the 2-month average daytime EBR was found to be statistically insignificantly different between CT and ST ($p = 0.80$) and statistically significantly different between CT and WT ($p = 0.01$), allowing us to omit ST in favor of minimizing redundant analyses. Finally, there are two additional considerations demanding greater attention. Specifically, we determine which rotation procedure is more suitable for Owens Valley (Appendix G) and to what extent angle of the western slope impacted R_{net} (Appendix H).

While it is customary to filter out 30-min records not satisfying some form of stationarity (Foken, 2008), we do not apply such a procedure. Provided that we already subset the data by splitting the 2-month period into three climatological categories (WS, SU, SD), further filtering out non-stationary records would result in critically less robust statistics. Although this may leave a certain degree of scatter in our results, we will use the longterm stationarity of wind direction, on which WS, SU and SD are founded (B17), as a proxy for flow stationarity.

5.3 Results and discussion

5.3.1 Climatological overview of SEB in Owens Valley

The semiarid nature of Owens Valley becomes immediately apparent from the large difference between H and LE (Fig. 5.3). During T-REX, the average Bowen ratio B_o ranged between 6 and 9 at the floor, and between 3 and 7 over the slope. Relatively smaller B_o over the slope coincided with reduced R_{net}, resulting from larger average albedo over the slope (0.22) compared to the floor (0.18). Largest R_{net} and H occurred on SD days, the least cloudy category (B17). The ground heat flux G_0 is comparable to the small magnitude

of LE, both over the floor and slope. Small G_0 is typical for sandy and permeable soils (Liang et al., 2017), while larger G_0 prevails for less permeable, clay-dominant playa soils (Heusinkveld et al., 2004; Hang et al., 2016). The main reason for better closure on SU and SD days (Fig. 5.3b,c,e,f) is due to high-speed pressure-driven and forced-channeled flows, resulting from the synoptic pressure distribution over the western Pacific and Rockies (Zhong et al., 2008). These flows did not occur on WS days (Fig. 5.3a,d), for which the weaker thermally-driven flows help explain degraded closure and lower EBR.

EBR steadily increased from early morning (15 UTC) until early evening (01 UTC, Fig. 5.3). This trend has been reported in previous studies, marking a ubiqutous feature of the daytime SEB (Wilson et al., 2002; Franssen et al., 2010; Liang et al., 2017; Xu et al., 2017). In the late afternoon and early evening, slight SEB overclosure ($EBR > 1$) occurred as a result of all four flux densities achieving small values. This overclosure occurred regardless of category and location. Independent of the category, SEB closure was better at the floor (Fig. 5.3a,b,c) than the slope (Fig. 5.3d,e,f). Interestingly, EBR did not exhibit a steady increase throughout the day on SD days, when the flow was downvalley as opposed to the upvalley-type WS and SU days. Rather, it remained constant during the day. This dependency of SEB on flow fetch has not been reported so far for valleys. Greatest wind speed in the morning hours on SD days (B17) help explain the better SEB closure in this case, particularly the overall smaller change in EBR on SD than on WS and SU days. On a side note, we point out that nighttime SEB closure was also much better on SD than on WS and SU days, improving as the night progressed (Fig. 5.3c,f). According to B17, nighttime flows on WS and SU were mainly downslope flows from the Sierras, while on SD days they were strictly downvalley over both the floor and slope. This further highlights the importance of considering fetch and flux footprints when studying SEB in horizontally heterogeneous complex terrain.

To quantify EBR in a more objective way than simple time series visualization, we display the traditional scatterplots of input energy $R_{net} - G_0$ versus energy fluxes $H + LE$ in Fig. 5.4, for both the floor and slope as well as all three categories. Details of the linear regression statistics are given in Table 5.1. This representation corroborates the time series of Fig. 5.3, thus agreeing with the conclusion that SEB closure was best on SD days and worst on WS days, and overall better over the floor. The slopes of the observed linear relationships fall inside the range of previously reported values (Wilson et al., 2002). In summary, this brief climatological overview confirms that SEB underclosure highly depends on the location in Owens Valley, as well as on the fetch and magnitude of the prevailing

along-valley flow.

5.3.2 Effects of TOS entrainment on EBR

Dependency of EBR on friction velocity u_* and $r_{\theta q}$

We present side-to-side comparisons of EBR, $r_{\theta q}$ and friction velocity $u_* = \left(\overline{u'w'}^2 + \overline{v'w'}^2\right)^{1/4}$ in Fig. 5.5. u_* is known to be highly correlated with EBR due to greater turbulent mixing (Wilson et al., 2002; Franssen et al., 2010; Anderson and Wang, 2014), hence we aim to establish whether the same holds for Owens Valley. For upvalley flows (Fig. 5.5a,b,d,e), EBR and u_* were positively correlated, in line with past studies, suggesting that greater turbulent mixing promotes better SEB closure. However, for downvalley flows (Fig. 5.5c,f), EBR and u_* were negatively correlated. Although larger u_* aided improved closure during morning hours on SD days, the fact that EBR continued to gently increase while u_* decreased until evening, points to phase differences among the constituting SEB flux densities playing a more critical role than the intensity of turbulent mixing alone. Furthermore, it is likely that this unusual negative correlation is specific to daytime downvalley flows in Owens Valley. In a traditional, textbook view of valley flows (Zhong and Chow, 2013), daytime downvalley flows are more anomalous and generally less understood and studied (Zhong et al., 2008).

We now investigate the temporal and spatial evolution of scalar similarity via $r_{\theta q}$. At the valley floor (Fig. 5.5a,b,c), $r_{\theta q}$ ranged between 0.2 and 0.6. On WS and SU, $r_{\theta q}$ exhibited a steady decrease over the course of these days, while it remained more or less steady on SD days. Over the slope (Fig. 5.5d,e,f) $r_{\theta q}$ remained steadier than over the floor. Furthermore, scalar similarity over the slope was overall larger than over the floor, with values ranging between 0.4 and 0.8. The contrasting temporal $r_{\theta q}$ tendencies between the floor (continuously decreasing) and the slope (nearly steady), suggest the importance of measurement location in Owens Valley when examining scalar similarity.

Inspection of EBR and $r_{\theta q}$ time series (Fig. 5.5) above, gave rise to several alarming conclusions. Why was SEB closure better over the floor than the slope of Owens Valley, despite scalar similarity being more violated over the floor? Why has EBR converged to unity along with progressively degraded scalar similarity on WS and SU days? Since scalar similarity in Owens Valley was always violated ($r_{\theta q} < 1$), why does SEB get closed at all? These questions challenge the expected behavior of SEB becoming closed once perfect scalar similarity is attained. The reason for the emergence of these questions is rather

simple: integrated 30-min turbulence statistics, such as those reported in Fig. 5.5, mask signature of discrete eddy motions. To avoid this masking, we turn to examining scale contributions to $r_{\theta q}$. We hypothesize that isolating only that scale range characterized by TOS, will clarify these counter-intuitive questions. Such a scale-aware approach of studying $r_{\theta q}$ is not novel (e.g. Wyngaard et al., 1978; Asanuma et al., 2007; Williams et al., 2007; Scanlon and Sahu, 2008; Li et al., 2012; Cancelli et al., 2014; Gao et al., 2018), however it has not yet been used to isolate contributions to $r_{\theta q}$ just from the principal violators of scalar similarity, the TOS. This crucial step will help us clarify these dubious new questions and, more importantly, enable us to answer the two initial questions that have motivated this study.

Scale-aware analysis of $r_{\theta q}$ and EBR

We define a scale-dependent, cumulative spectral temperature-humidity correlation coefficient using MRFD (Appendix E):

$$\sum D_{r_{\theta q}} = \frac{\sum D_{\theta q}}{\left(\sum D_{\theta\theta} \sum D_{qq}\right)^{1/2}} \tag{5.2}$$

Fig. 5.6 illustrates $\sum D_{r_{\theta q}}$ for each category, both towers and each 30-min record (individual gray lines). There are three frequency bands of importance: 1) the high-frequency band ($\tau < 0.05$ min), where $\sum D_{r_{\theta q}}$ converges to zero as the smallest resolvable scale (i.e. the Nyquist frequency) is reached. This low correlation results from the spatial separation between the CSAT3 and KH2O and has no physical meaning; 2) the mid-frequency band (between $\tau \approx 0.05$ min and the time scale at which the peak spectral value is attained), associated with scalar similarity due to local (up to ≈ 1 km) land use distribution; 3) the low-frequency band (between the time scale at which the peak spectral value is achieved and $\tau = 27.3$ min), corresponding to TOS. As a result, in this band $\sum D_{r_{\theta q}}$ nearly always decreases, signifying the drawdown of entrainment air by TOS overturning. This last band is of greatest importance here, as it contains the signature of TOS. We chose the peak in $\sum D_{r_{\theta q}}$ to delineate the limit of this low-frequency band, since it shifts to longer time scales as the CBL deepens. In other words, TOS effects on $r_{\theta q}$ are due to larger eddies as CBL grows in depth. Since we will focus on isolating certain frequency bands, the following two benefits of MRFD compared to traditional Fourier spectra will prove essential (Howell and Mahrt, 1997): 1) the local nature of MRFD (as opposed to global nature of Fourier spectra) makes distinguishing between spectral peaks less ambiguous, and 2) given our interest in

the low-frequency contribution due to TOS, tapering may bias the results, however no tapering is required in the case of MRFD.

Inspection of individual $\sum D_{r_{\theta q}}$ (Fig. 5.6) reveals that the degraded scalar similarity in the low-frequency band occurred over both the floor (Fig. 5.6a,b,c) and slope (Fig. 5.6d,e,f), confirming the conclusion from Fig. 5.5 that scalar similarity was nearly always violated in Owens Valley. In other words, $\sum D_{r_{\theta q}}$ did not attain unity within any of the three frequency bands. A major difference between the floor and slope, are the generally larger $\sum D_{r_{\theta q}}$ over the slope in the mid-frequency band, which we attribute to greater land-use homogeneity surrounding WT (Fig. 5.1b). Homogeneous land-use is not capable of degrading scalar similarity as much as a more heterogeneous land-use distribution, such as the one along the valley floor.

To incorporate the information pertaining to EBR into Fig. 5.6, we sort individual $\sum D_{r_{\theta q}}$ with respect to increasing EBR and define discrete bins. A similar step was made by Gao et al. (2018) but with u_* instead of EBR. Sorting in this manner is equivalent to time progression, given that EBR steadily increased throughout the day (Fig. 5.3). Since each subset of data contains different sized populations (Table 5.1), each bin is weighted differently, similar to B17. In other words, over the floor bins are composed of 20 (WS), 40 (SU) and 16 (SD) individual $\sum D_{r_{\theta q}}$, while over the slope these numbers are 10 (WS), 15 (SU) and 7 (SD). Finally, we show the median average of each bin in Fig. 5.6, color-coded with its respective EBR. In this fashion, darker colors represent large SEB underclosure and morning hours, while lighter colors denote closed SEB and afternoon hours. At the valley floor during upvalley flow (Fig. 5.6a,b), the shifting of the peak $\sum D_{r_{\theta q}}$ towards longer periods coincides with deepening of the CBL, lightening of the curve coloring (increase in EBR) and hence improved SEB closure, in line with Fig. 5.5a,b. A novel finding here is that in the low-frequency band (which narrows as time progresses), the decrease in scalar similarity reduces as EBR reaches and slightly exceeds unity. This implies that the effect of TOS entrainment on SEB is large in the morning and steadily weakens until late afternoon. In other words, SEB gets closed once entrainment can no longer violate scalar similarity. This finding holds for SD days as well, albeit to a lesser extent (Fig. 5.6c). Over the slope (Fig. 5.6d,e,f), binning of $\sum D_{r_{\theta q}}$ would suggest that the $\sum D_{r_{\theta q}}$ reduction in the low-frequency band does not exhibit a clear ordering with increasing EBR as it does at the floor.

A scale-aware analysis of $r_{\theta q}$ revealed that TOS entrainment indeed degraded scalar similarity in Owens Valley during T-REX. Ordering of spectral $r_{\theta q}$ curves with respect to

EBR, has also indicated that our initial question may have an affirmative answer. In other words, entrainment effects induced by TOS in the low-frequency range were apparently correlated with EBR.

Impact of TOS-induced entrainment on EBR

These encouraging results motivate us to perform the final step required to answer our initial question: Does a relationship exist between EBR and TOS-induced scalar similarity violations? We quantify this TOS effect on EBR by extracting the amplitude of $\sum D_{r_{\theta q}}$ in the low-frequency band:

$$\Delta = \sum D_{r_{\theta q}}(\tau_{max}) - \sum D_{r_{\theta q}}(\tau_{27.3\,\mathrm{min}}) \tag{5.3}$$

Fig. 5.7 displays individual Δ versus EBR over both the floor and slope, and for all three categories. This illustration corroborates the finding from the previous section, that TOS entrainment was responsible for the SEB underclosure. As Δ tends to zero, i.e. as TOS entrainment ceases affecting ASL fluxes, EBR tends to unity, over both the floor and slope. We note that the same relationship was observed at ST as well (not shown), indicating that these conclusions are representative for a much larger portion of Owens Valley, not just the limited cross-section through CT and WT. Even so, the convergence to unity is slightly less pronounced at the slope, which we hypothesize to be due to $\sum D_{r_{\theta q}}$ remaining close to unity in the mid-frequency band (Fig. 5.6d,e,f). This would make a distinction of a clear peak in $\sum D_{r_{\theta q}}$ less obvious, thus pointing to a potential weakness of the way in which we separate the mid-frequency from the low-frequency portion. Nonetheless, it is now clear that the extent to which TOS degraded SEB closure, did not depend on the fetch of the along-valley flow, given similar range of Δ in all six cases shown in Fig. 5.7.

In conclusion, we have confirmed the first of our two initial questions, wherein a definitive relationship between EBR and $r_{\theta q}$ has been confirmed. However, this relationship holds only if the effect of TOS on $r_{\theta q}$ is isolated, as 30-min statistics have been proven to lead to faulty conclusions.

Dependence of scalar dissimilarity on prevalent form of TOS

On low-speed WS days, TOS manifested as open cells, while on high-speed SU and SD days, TOS were mostly organized as horizontal convective rolls (Salesky et al., 2017). Fig. 5.7 suggests that violation of SEB closure and scalar similarity, ultimately did not depend on which form of convection organization prevailed either, given the qualitatively similar

dependence of EBR on Δ in all cases. We can reinforce this statement by examining the relationship between Δ and the bulk CBL stability parameter $-z_i/L$, where L is the Obukhov length (Kaimal and Finnigan, 1994). This relationship is illustrated in Fig. 5.8 for the western slope, given z_i was obtained from the ISS-2 wind profiler. While open cells prevail for $-z_i/L$ greater than 25, rolls are dominant when $-z_i/L$ is smaller than approximately 15, with the intermediate values marking the gradual transition between the two forms of TOS (Salesky et al., 2017). By calculating the Pearson correlation coefficient between Δ and $-z_i/L$, we found r = 0.26, 0.01 and -0.18 for WS, SU and SD, respectively. We can assume the same held for the valley floor too, given qualitatively similar dependence between EBR and Δ at the floor and slope sites (Fig. 5.7). This weak correlation in all three cases, signifies that entrainment-driven violation of scalar similarity and EBR, was a ubiquitous feature of the CBL. In other words, it was not influenced by the prevalence of these two types of TOS motions, thus directly answering our second question.

Influence of land-use heterogeneity on scalar similarity

In addition to ASL flux contamination by entrainment effects induced by TOS, SEB is also highly sensitive to horizontal gradients of temperature and humidity (Oncley et al., 2007; Leuning et al., 2012; Cuxart et al., 2016; Roo and Mauder, 2018). Such gradients result from horizontally inhomogeneous terrain, heterogeneous land-use, or contrasting soil thermal properties. A pronounced horizontal along-valley gradient in temperature and humidity persisted in Owens Valley during the entire T-REX (Fig. 5.2), calling into question its potential impact on SEB. SEB, in its traditional form given by (5.1), neglects flux densities associated with such horizontal advection. However, by utilizing a network of automatic weather stations deployed in Owens Valley during T-REX (B17) to determine these flux densities (not shown), we found values one to two orders of magnitude smaller than the SEB residual $\overline{Q_R}$ (Table 5.1), insufficient to close SEB. To our knowledge, the study of SEB in the Riviera Valley in the Swiss Alps by Rotach et al. (2008), is the only other study to have evaluated flux densities due to horizontal advection in a valley. Similar to our findings, they also observed values one-to-two orders of magnitude smaller than $\overline{Q_R}$. Considering the recent investigation of spatial scales contributing to horizontal advection by Cuxart et al. (2016), our small values are not surprising. Cuxart et al. (2016) observed that advection terms of this order of magnitude are associated with heterogeneities and scalar gradients on the order of 1 km and larger, in agreement with the separation between AWS during T-REX (roughly 3 km). In other words, such coarse separation is not able to

capture the finer-scale advection on a land-use basis (decametre-to-hectometre scale), for which Cuxart et al. (2016) observed flux densities comparable to $\overline{Q_R}$.

5.4 Conclusions and Summary

We investigated the impact of TOS and associated entrainment effects on ASL heat fluxes and hence on SEB. Additionally, we examined which of the two main TOS eddy motions, horizontal convective rolls and open cells, are more efficient in degrading scalar similarity near the surface, and hence SEB as well. By focusing on both synoptically unperturbed and perturbed flows in Owens Valley, we have for the first time examined the impact of different along-valley flow regimes on SEB.

We can summarize the results as follows:

- During daytime, SEB in Owens Valley exhibited an underclosure comparable to previously reported range of values, with EBR ranging on average between 0.6 and 0.9. EBR exhibited a strong dependency on location in the valley (valley floor and western slope) and on the fetch of the along-valley wind (upvalley and downvalley). SEB closure was overall better at the valley floor on synoptically perturbed days (EBR = 0.81 for SU, EBR = 0.89 for SD). Closure was worst (EBR = 0.67) over the western slope on synoptically quiescent days (WS) in the presence of well-developed thermally-driven valley and slope flows;

- We used violation of near-surface temperature-humidity similarity $r_{\theta q}$ to investigate TOS-induced entrainment effects and their impact on EBR. $r_{\theta q}$ on average ranged between 0.2 and 0.6 over the floor and between 0.4 and 0.8 over the slope, indicating location-dependent scalar dissimilarity. Inspection of $r_{\theta q}$ time series indicated improved SEB closure with increasingly violated scalar similarity over the floor, and little change in this violation over time at the slope. This counterintuitive result was rebuted after spectrally decomposing $r_{\theta q}$ using MRFD. By extracting the change Δ in $\sum D_{r_{\theta q}}$ only in the low-frequency band where TOS are the dominant eddy motions, we showed that TOS-induced entrainment did occur over both the floor and slope. Once entrainment zone ceased contaminating ASL fluxes ($\Delta \to 0$), EBR converged to unity and SEB closure was attained;

- The two main classes of TOS, horizontal convective rolls and open cells, were quantified using the bulk CBL stability parameter $-z_i/L$. We found a weak correlation

of $-z_i/L$ with the strength of entrainment effects Δ, indicating that entrainment violates scalar similarity in the ASL regardless of which TOS motion is present at any moment in the CBL.

Our study motivates further investigation of SEB in complex terrrain. The unanimous correlation of TOS-induced violation of scalar similarity with EBR (Fig. 5.7), lends itself as a candidate for developing a parameterization of entrainment effects on SEB. Such a parameterization should focus on scale-dependence of near-surface scalar similarity and Bowen ratio on the CBL depth z_i and entrainment zone evolution, quantified through e.g. the entrainment zone thickness, ratio of entrainment heat flux to the surface heat flux, and the entrainment velocity. These quantities can be readily obtained with the use of remote sensing instruments (Träumner et al., 2011), unmanned aerial systems (Dias et al., 2012), and routine radiosoundings (Van de Boer et al., 2014). The negative correlation between u_* and EBR we found for daytime downvalley flows on SD days, deviates from the traditional view of stronger turbulent mixing promoting SEB closure. Future studies should focus on other valley environments to determine whether this finding is always a function of synoptic forcing or specific just to Owens Valley.

Table 5.1: SEB closure linear regression statistics, for the three categories (WS, SU, SD) and both flux towers (CT, WT). Also shown are the category-averaged SEB residuals $\overline{Q_R} = (R_{net} - G_0) - (H + LE)$, as well as the total number of 30-min records available for further analyses.

category	site	slope	intercept [$\mathrm{Wm^{-2}}$]	r^2	$\overline{Q_R}$ [$\mathrm{Wm^{-2}}$]	# of 30-min records
WS	CT	0.75 ± 0.02	13 ± 8	0.87	60	138
	WT	0.67 ± 0.04	20 ± 9	0.86	58	57
SU	CT	0.81 ± 0.02	10 ± 7	0.85	52	339
	WT	0.72 ± 0.02	17 ± 6	0.89	58	168
SD	CT	0.89 ± 0.02	10 ± 8	0.95	27	102
	WT	0.80 ± 0.02	26 ± 7	0.95	31	78

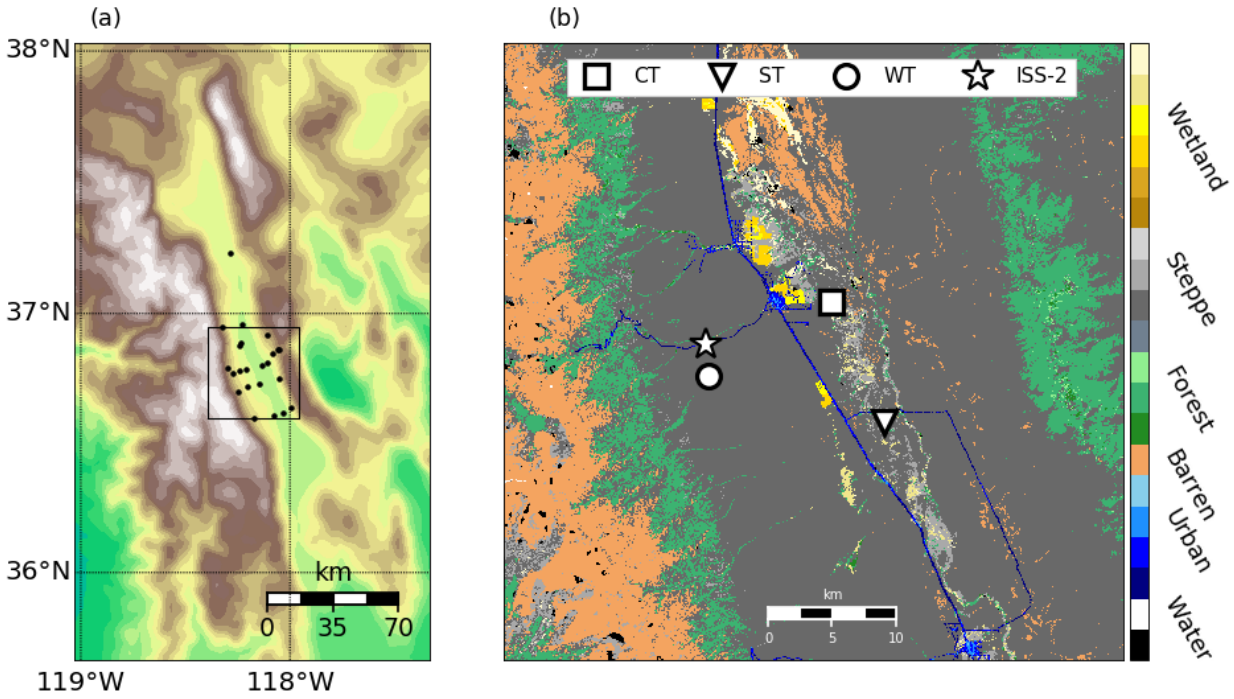

FIGURE 5.1: **(a)** 1-arc-minute topographical representation of Owens Valley. The 23 black dots represent the Decagon gravimetric soil moisture probes (ECH2O). The topography is contoured every 500 m. The solid square denotes the T-REX region of interest; **(b)** 1-arc-second National Land Cover Dataset (NLCD-2006) land-use representation of the T-REX region of interest. The colorbar denotes the dominant land-use type.

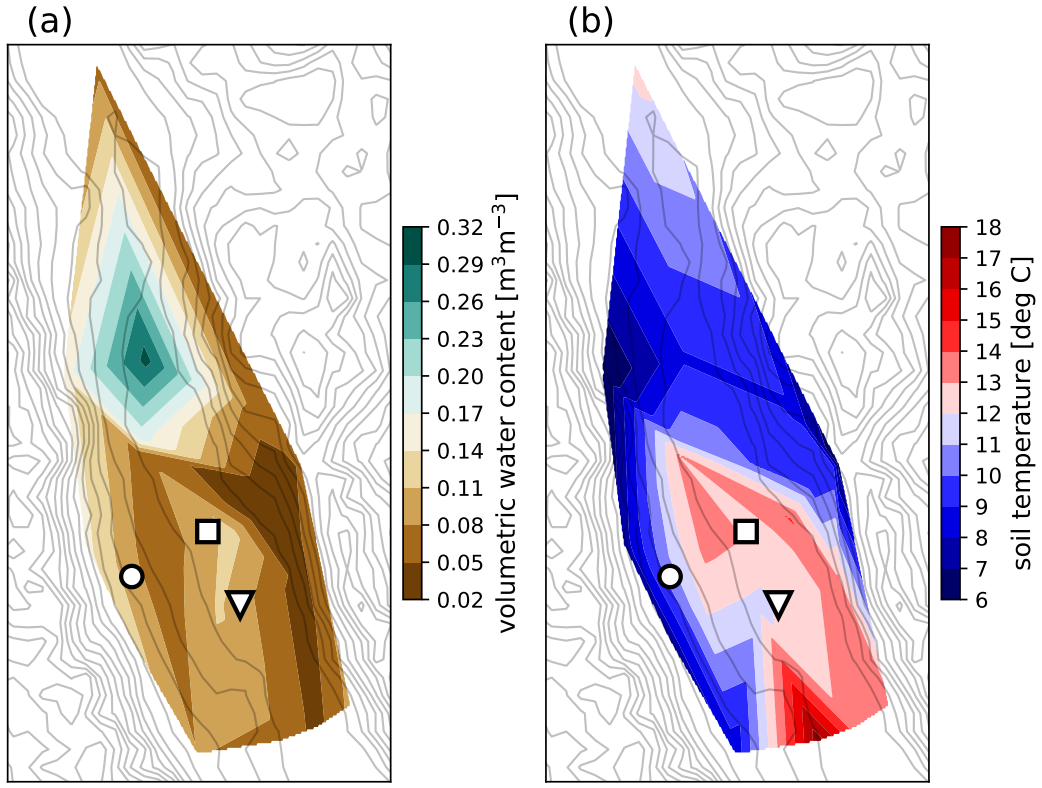

FIGURE 5.2: **(a)** Volumetric water content (=volume of water in the soil / total volume of soil), linearly interpolated from the 23 Decagon soil moisture probes. The contour is a median average for the entire 2-month period. **(b)** Same as for (a) but for soil temperature. Large markers are the same as in Fig. 5.1b.

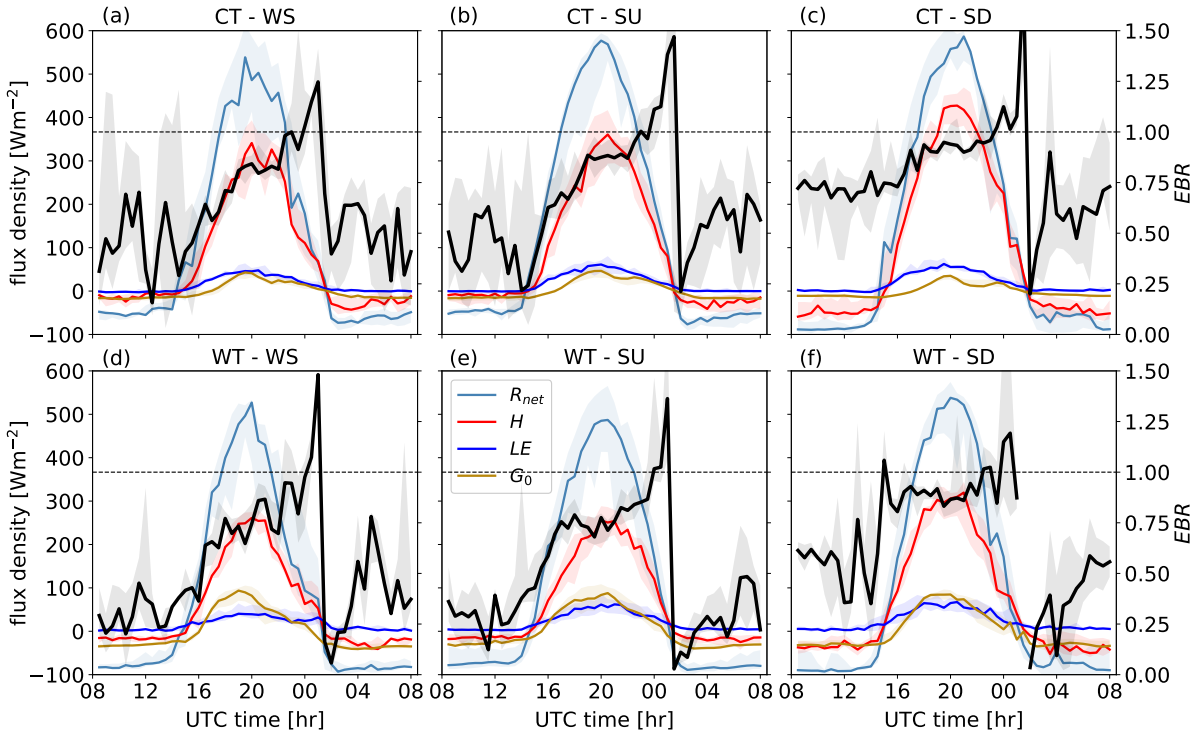

FIGURE 5.3: Median composite time series of the SEB components for **(a)** CT and WS, **(b)** CT and SU, **(c)** CT and SD, **(d)** WT and WS, **(e)** WT and SU and **(f)** WT and SD. Shadings represent the interquartile range for each flux density. EBR is shown as a solid black line. Horizontal dashed line denotes perfect SEB closure ($EBR = 1$).

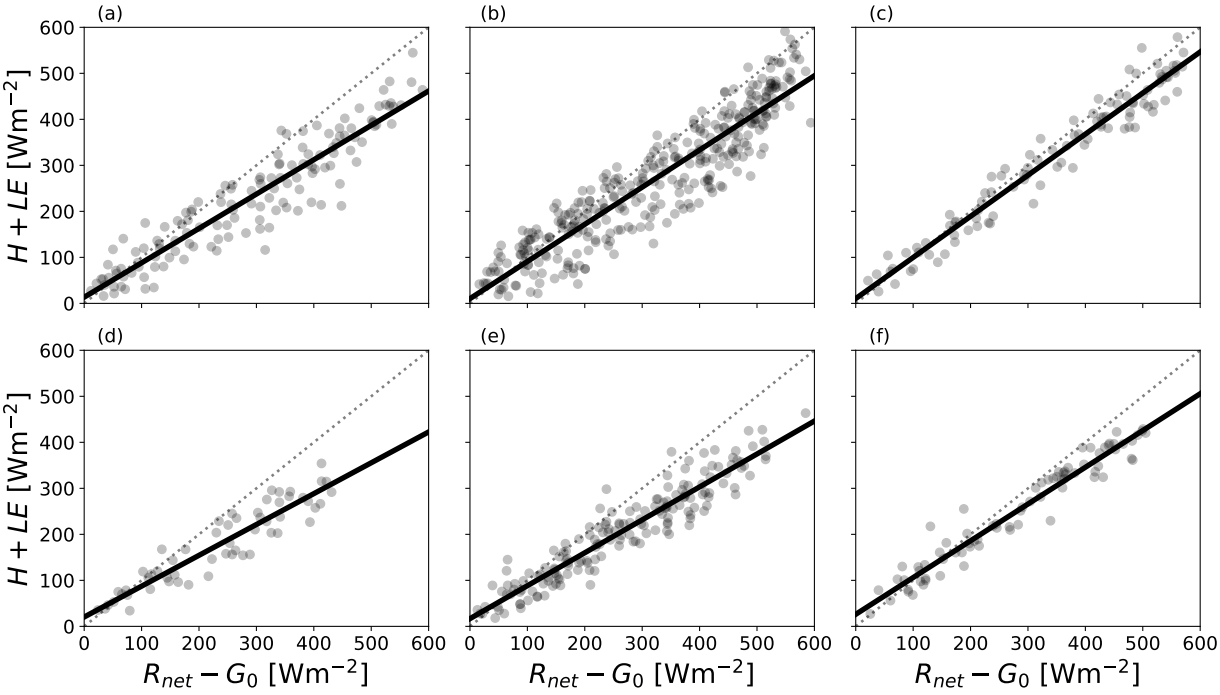

FIGURE 5.4: Scatterplot of the energy fluxes ($H + LE$) versus input energy ($R_{net} - G_0$), for **(a)** CT and WS, **(b)** CT and SU, **(c)** CT and SD, **(d)** WT and WS, **(e)** WT and SU and **(f)** WT and SD. Dotted line denotes perfect SEB closure, while the solid black lines denote best-fit linear regression relationships. The statistics of the linear regression for each case are given in Table 5.1.

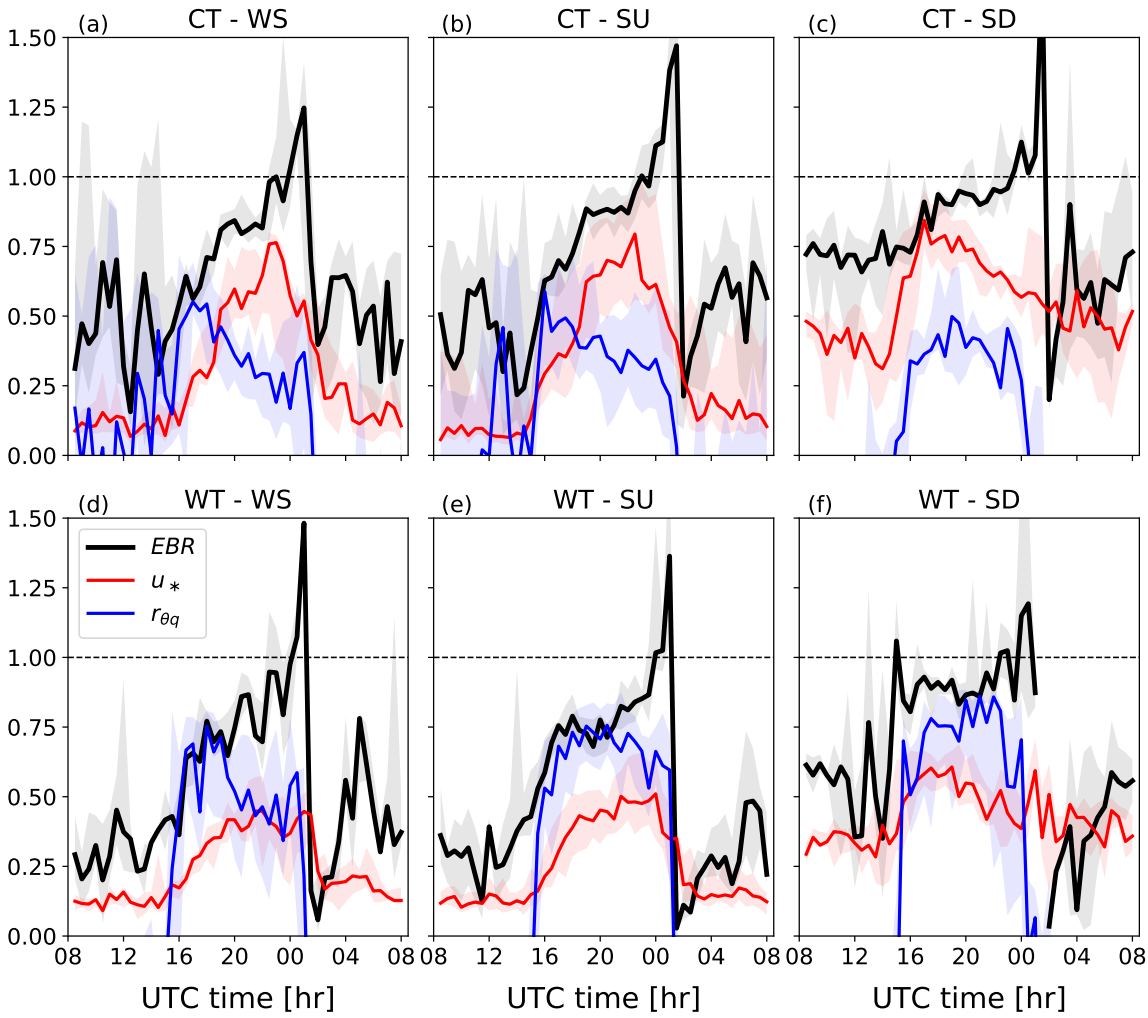

FIGURE 5.5: Median composite time series of the EBR, friction velocity u_* and $r_{\theta q}$ correlation coefficient, for **(a)** CT and WS, **(b)** CT and SU, **(c)** CT and SD, **(d)** WT and WS, **(e)** WT and SU and **(f)** WT and SD. Shadings represent the interquartile range for each variable. Horizontal dashed line denotes perfect SEB closure ($EBR = 1$).

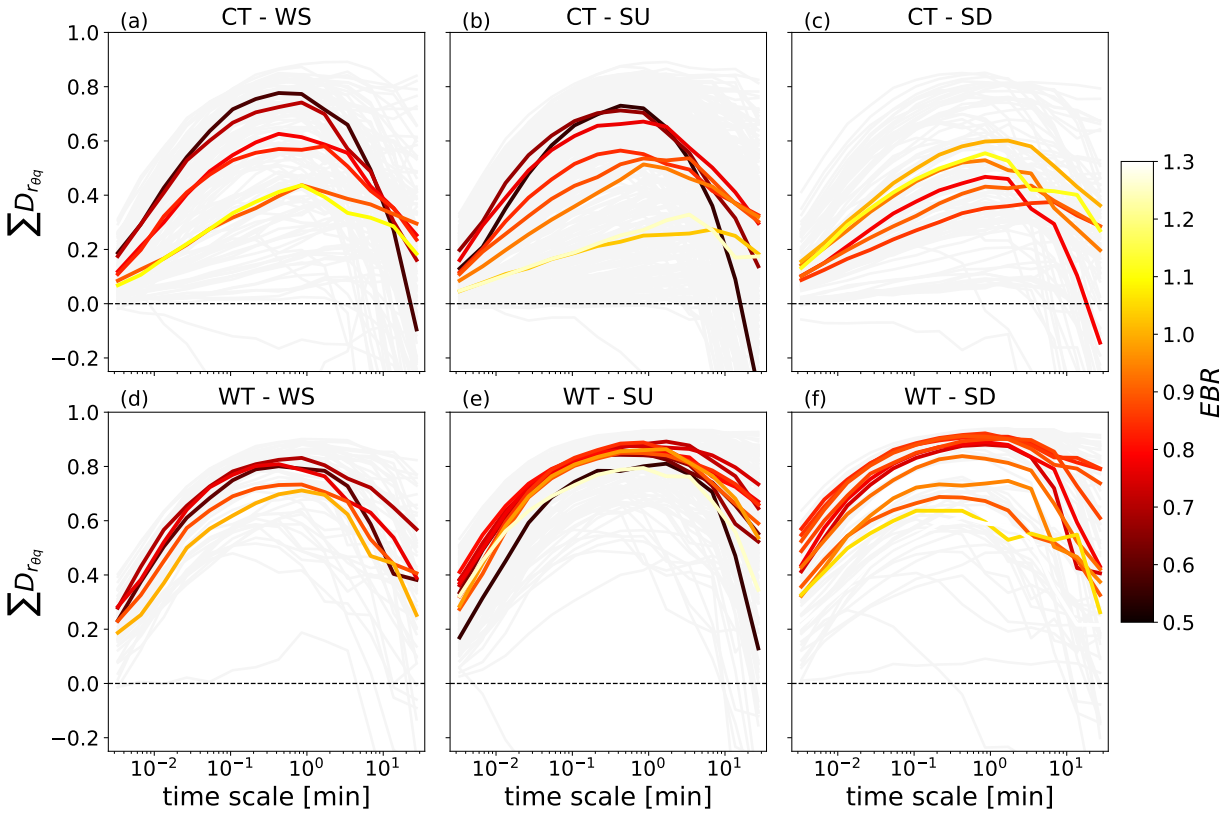

FIGURE 5.6: MRFD ogives of the temperature-humidity correlation coefficient $\sum D_{r_{\theta q}}$, shown in light gray for **(a)** CT and WS, **(b)** CT and SU, **(c)** CT and SD, **(d)** WT and WS, **(e)** WT and SU and **(f)** WT and SD. Shown in color are bin-averages (median composites) of $\sum D_{r_{\theta q}}$, color-coded with the median EBR for each respective bin.

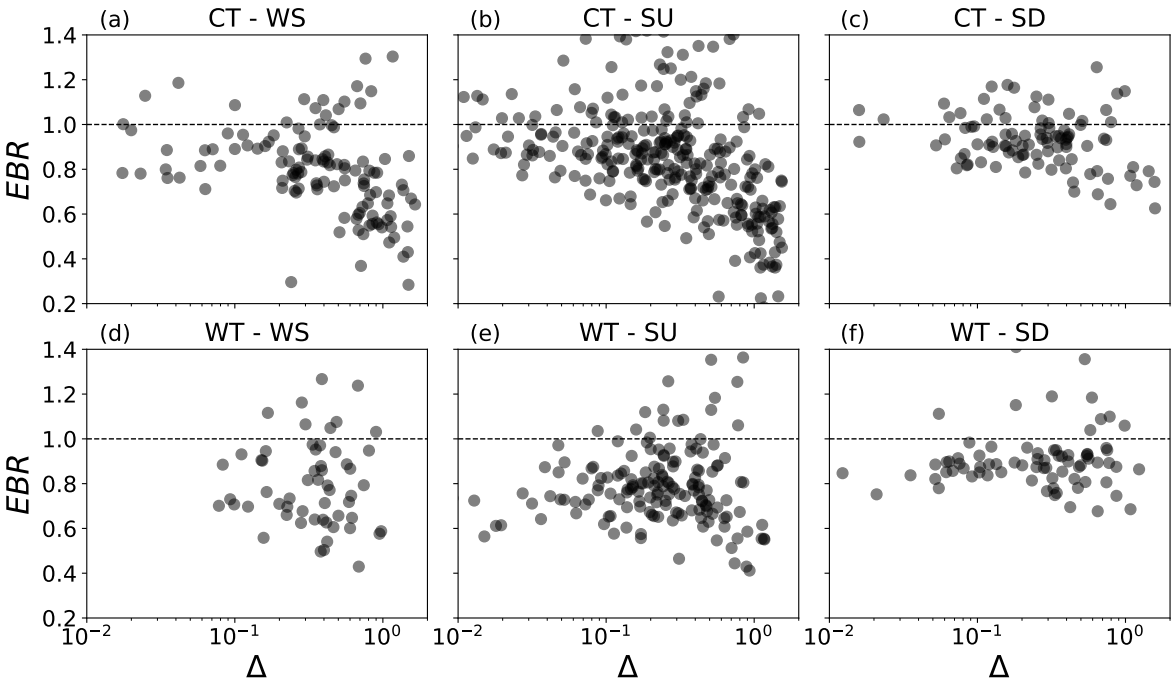

FIGURE 5.7: Scatterplot of the low-frequency amplitude Δ in $D_{r_{\theta q}}$, for **(a)** CT and WS, **(b)** CT and SU, **(c)** CT and SD, **(d)** WT and WS, **(e)** WT and SU and **(f)** WT and SD. Horizontal solid line denotes perfect SEB closure ($EBR = 1$).

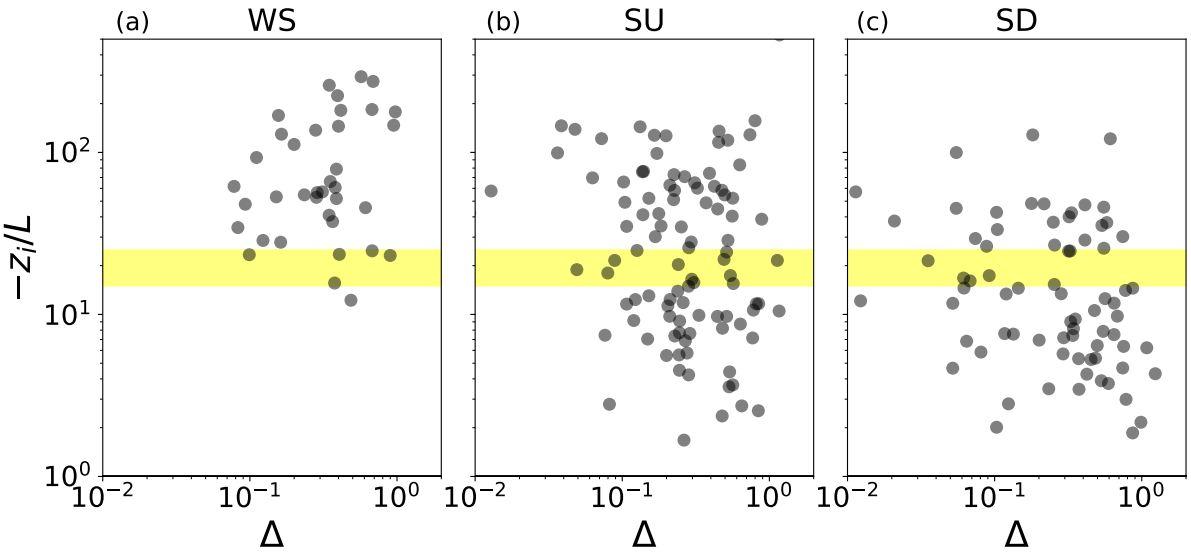

FIGURE 5.8: Scatterplot of the bulk CBL stability parameter $-z_i/L$ as a function of the low-frequency amplitude Δ in $D_{r_{\theta q}}$, for **(a)** WS, **(b)** SU, and **(c)** SD, at the western slope of Owens Valley. Yellow shaded region denotes the commonly accepted range in which the transition from rolls to cells is expected to occur.

6

Ramp structures in the unstable atmospheric surface layer over flat and complex terrain

6.1 Introduction

The stochastic nature of both canonical laboratory and atmospheric turbulent shear flows historically led to statistically-based approaches of describing such flows (Monin and Yaglom, 1975). However, with the advent of instrumentation capable of resolving ever smaller turbulent motions, it became clear that turbulent flow is far from purely stochastic. Taylor (1958) and Kaimal and Businger (1970) were among the first to provide evidence of the presence of deterministic, highly ubiquitous, intermittent structures in the atmospheric surface layer (ASL). These structures, called coherent structures, have also been observed in water channel flows (Kline et al., 1967) and wind tunnel experiments (Head and Bandyopadhyay, 1981). Taxonomy of coherent structures in the neutral and unstable ASL includes hairpin vortices (Adrian, 2007), surface-layer streaks (Drobinski et al., 2004) and plume-like temperature ramps (Wilczak, 1984). We will collectively refer to these as ramp structures, given the universality of their geometrical signatures in velocity and temperature time series (Belušić and Mahrt, 2012).

By modifying the turbulent transport of momentum, heat and other scalars in the ASL, ramp structures are responsible for as much as 40% to 60% of the total transport (Barthlott et al., 2007). Ramp structures are largely responsible for driving surface temperature fluctuations (Katul et al., 1998; Garai et al., 2013), thus introducing errors in applications relying on remote sensing of the land-atmosphere interface (Garai and Kleissl,

2011). Furthermore, ramp structures govern the pressure redistribution and pressure-gradient interaction terms in the budgets of turbulent kinetic energy (TKE) and other higher order moments (Wilczak and Businger, 1984; Schols and Wartena, 1986; Zhuang, 1995). By parameterizing these budget terms with the ensemble ramp structural properties, Wilczak and Businger (1984) were able to close these budgets and circumvent the need for static pressure perturbations, otherwise known to be notoriously difficult to obtain in the ASL.

The most striking effect of ramp structures on ASL thermodynamics is the breakdown of inertial subrange local isotropy (Sreenivasan et al., 1979; Katul et al., 1995). Local isotropy violations become problematic in modelling subgrid-scale (SGS) motions in large-eddy simulation (LES) of turbulent shear flows. Namely, SGS parameterizations have difficulty properly representing the forward and backward cascade of energy between the resolved and SGS motions (Carper and Porté-Agel, 2004). In turn, the intermittent velocity and scalar microfronts induced by ramp structures modulate higher-order turbulent statistics (Antonia et al., 1982; Mahrt and Howell, 1994). As horizontal resolution on the order of 20 m and finer is required for sufficient convergence of such statistics in LES (Sullivan and Patton, 2011), it becomes clear that better knowledge of ramp structures is necessary for improving SGS models, given that such fine LES is not yet plausible in the context of operational numerical weather prediction (Schalkwijk et al., 2015). Furthermore, although a clear picture of ramp structure dynamics exists, a unified theoretical framework describing generation of ramp structures does not. Currently, the bottom-up (McNaughton, 2004b) and top-down (Hunt and Morrison, 2000) mechanisms, are suggested to explain ramp structure evolution in the ASL. However, there is considerable dispute as to which mechanism is correct (Adrian et al., 2000). More experimental efforts targeted at reconciling this dispute are expected to improve the aforementioned SGS parameterizations.

Owing to ramp structure ubiquity in the ASL, the variety of land-use types over which ramp structures have been studied is not surprising. For instance, ramp structures have been investigated within and above forest canopies (Baldocchi and Meyers, 1988; Scanlon and Albertson, 2001; Serafimovich et al., 2011), over mountain glaciers (Litt et al., 2015), snow-covered slopes (Aksamit and Pomeroy, 2018), open sea (Mason et al., 2002), irrigated agriculture (Zhang et al., 2011), vineyards (Li and Bou-Zeid, 2011), dried lakebeds (Katul et al., 1995), playa deserts (Chauhan et al., 2013), urban canopies (Christen et al., 2007; Yagi et al., 2017), football fields (Garai and Kleissl, 2011), and along marine (Lotfy and

Harun, 2018) and lake (Calaf et al., 2013) shorelines. All of the above studies, however, suffer from two perilous drawbacks. First, analyses are usually based only on single flux tower measurements, thus limiting comparison with other studies of similar design, given that conditional sampling methods used for ramp structure detection greatly differ among them. Second, very little is known about ramps in horizontally heterogeneous complex terrain. Although a few studies of ramp structures in complex terrain do exist (e.g. Krusche and De Oliveira, 2004; Potužníková et al., 2015; Träumner et al., 2015; Babić et al., 2016b), none of them have focused on systematically disseminating potential impacts that slope-induced physical mechanisms may have on ramp structure properties and generation mechanisms.

The specific goals of the present study are threefold:

- to determine and contrast ramp structural properties (number N, duration D, length ℓ, intensity R, flux contributions F_{uw}, $F_{w\theta}$, inclination angle γ) over flat terrain and complex terrain, including gently rolling terrain, at the base of an isolated mountain, and in a deep and wide mountain valley;
- to examine the impact of sloping terrain on ramp structural properties;
- to contrast the main ramp structure generation mechanisms across several sites, by scaling ramp structural properties with pertinent length, temperature, and stability scales.

6.2 Ramp structure generation mechanisms

6.2.1 Bottom-up framework

Introduced by McNaughton (2004a,b) and further developed by Laubach and McNaughton (2009), the bottom-up ramp structure generation mechanism relies on the tenet that the CBL is a complex thermodynamical system composed of self-organizing, self-similar coherent structures (Fig. 6.1a). In this framework, such coherent structures are known as Theodorsen Ejection-Amplifier-Like (TEAL) structures. TEALs can be viewed as another instance of ramp structures, as their fundamental dynamics closely resemble those of other structures that we refer to as ramp structures. Initiated near the surface by a hydrodynamic inflectional instability in the wind speed profile, an initial sequence of an ejection/sweep cycle continuously repeats itself in the presence of mean shear (gray eddies in Fig. 6.1a). Here, ejections denote upward movement of low-momentum fluid, while

sweeps signify downward movement of high-momentum fluid. The resulting TEAL cascade grows up to z_s, the depth of the inner, surface friction layer (SFL). At this height, only those TEALs that have retained their structural similarity over the course of the cascade, will encounter eddies of comparable size and energy from the outer layer. Such eddies, originally detached but now attached once interacting with the TEAL, originated due to Richardson cascade of z_i-scale eddies in the outer layer. The interaction of two such eddies (blue eddies in Fig. 6.1a) results in their mutual cancellation at z_s. Here, we use Townsend's hypothesis of active, attached and inactive, detached eddies (Townsend, 1961). Respectively, these delineate eddies that actively contribute to turbulent shear stress, and those disconnected from the ground which do not contribute to the shear stress.

Three scaling variables are sufficient to conceptualize the onset, evolution and final destruction of TEALs (Laubach and McNaughton, 2009): the SFL depth z_s, taken as the relevant length scale:

$$z_s = \frac{u_\epsilon^3}{\kappa\epsilon_0} = (z-d)\left[\left(\frac{1}{a(\epsilon/\epsilon_0 - 1)} + \frac{1}{(2a)^2}\right)^{1/2} - \frac{1}{2a}\right]^{-1}, \tag{6.1}$$

the dissipation velocity scale u_ϵ:

$$u_\epsilon = (\kappa\epsilon_0 z_s)^{1/3} = \left[\frac{\kappa\epsilon\,(z-d)}{(1+a(z-d)/z_s)^{-1} + (z-d)/z_s}\right]^{1/3}, \tag{6.2}$$

and the dissipation temperature scale θ_ϵ (von Randow et al., 2006):

$$\theta_\epsilon = -\frac{\overline{w'\theta'}}{u_\epsilon}, \tag{6.3}$$

where z is the measurement height above ground, d the displacement height, $a = 5$ a constant necessary to construct a satisfactory TKE dissipation profile in the SFL, ϵ the viscous dissipation of TKE, ϵ_0 the TKE dissipation rate in the outer layer, $\kappa = 0.4$ the von Karman constant (Högström, 1996), and $\overline{w'\theta'}$ the ensemble-averaged sensible heat flux. From this set of variables, we can define the SFL stability parameter $(z-d)/z_s$. From a fluid mechanics viewpoint, the bottom-up mechanism is more common in low-to-moderate Reynolds number Re (ratio of inertial to viscous forces) turbulent flows (Hunt and Morrison, 2000).

6.2.2 Top-down framework

According to Hunt and Morrison (2000) and Hunt and Carlotti (2001), the generation of attached *small eddies* in the ASL is driven primarily by top-down impingement of detached

large eddies from the ML (Fig. 6.1b). Following Drobinski et al. (2004), the *small eddies* fit in our ramp structure definition, while *large eddies* would constitute streaky structures, and superstructures or very large scale motions (Hutchins and Marusic, 2007). Here the ASL is split into two layers (Drobinski et al., 2004, 2007a): the eddy surface layer (ESL), where blocking by the surface drives turbulent exchange, and the shear surface layer (SSL), where shear is the dominant mechanism. By sweeping onto the ground, the detached *large eddies* become distorted by shear (in the SSL) and finally by blocking (in the ESL). This impingement occurs between low-momentum regions of *large eddies*, which organizes *small eddies* in lines parallel with the mean wind (Inagaki et al., 2017). Impinging and distortion effects are often evidenced as a -1 slope in the spectra of the longitudinal velocity component or, equivalently, as a $\ln(r)$ behavior in second-order longitudinal structure functions (Chamecki et al., 2017). Such evidence, along with the high Re of atmospheric flows, serve as the strongest arguments in favor of the top-down mechanism for ramp structure generation.

We adopt $z-d$, the friction velocity $u_* = \left(\overline{u'w'}^2 + \overline{v'w'}^2\right)^{1/4}$ ($\overline{u'w'}$ and $\overline{v'w'}$ being the ensemble-averaged longitudinal and lateral momentum fluxes, respectively), and the Monin-Obukhov (MO) temperature scale $\theta_* = -\overline{w'\theta'}/u_*$, as the scaling set for the top-down mechanism. Furthermore, we will consider Obukhov length L, defined traditionally to be the top of the ASL and a crucial variable within the MO similarity theory (Kaimal and Finnigan, 1994), as an additional length scale:

$$L = -\frac{u_*^3 \overline{\theta}}{\kappa g \overline{w'\theta'}}, \tag{6.4}$$

where $\overline{\theta}$ is the potential temperature and g the acceleration due to gravity. The MO stability parameter can then be defined as $-(z-d)/L$.

6.2.3 TKE-based framework

Both shear and buoyancy produce turbulence in the ASL. In the unstable ASL investigated here, the extent of their superposition in producing TKE serves as another, more general, point of view for studying ramp structures (Fig. 6.1c). To this end, we examine the reduced TKE budget equation introduced recently by Chamecki et al. (2018):

$$\frac{P}{\epsilon} + \frac{B}{\epsilon} - 1 = \frac{R}{\epsilon}, \tag{6.5}$$

where $P = -\overline{u'w'}/(dU/dz)$ is the mechanical production of turbulence, dU/dz vertical wind shear, $B = (g/\overline{\theta})\overline{w'\theta'}$ buoyant production of turbulence, and R the residual budget term (Stull, 1988). Division by ϵ serves to define two dimensionless parameters, P/ϵ and B/ϵ. These parameters describe the character of turbulence in the unstable ASL. More importantly, we can define three corresponding length scales, each characterizing the production or destruction of TKE. These are the shear length scale $\ell_P = u_*^3/P$, the buoyancy length scale $\ell_B = u_*^3/B$, and the dissipation-based length scale $\ell_\epsilon = u_*^3/\epsilon$ (Chamecki et al., 2017; Ghannam et al., 2018). Note the qualitative similarity between z_s (Eq. 6.1) and ℓ_ϵ, but keep in mind that z_s takes into account the TKE dissipation rate of the outer/mixed layer, not that of the ASL.

6.3 Data and methods

6.3.1 Experimental data

The data sets analyzed in this study were collected during three field campaigns: the Cooperative Atmospheric Surface Exchange Study October 1999 (CASES-99), the Mountain Terrain Atmospheric Modeling and Observations (MATERHORN) Program, and the Terrain-Induced Rotor Experiment (T-REX). Characteristics of each campaign are presented in Table 6.1, while the experimental areas and overview of pertinent sonic anemometers are presented in Figs. 6.2 and 6.3, respectively. Next, we introduce the specific measurements from each campaign in more detail. To ensure comparability across the different campaigns, we selected only those flux towers which contained the temporally richest EC records at fixed measurement levels.

CASES-99

The CASES-99 experiment was intended as a major field effort aimed at investigating stable ABL flows, as well as revisiting the major tenets on which MOST relies (Poulos et al., 2002). CASES-99 took place during October 1999 in the Walnut River Watershed near Leon, Kansas (Fig. 6.2a). Here we focused on a 22-day period between 7 October 1999 and 28 October 1999. We used data collected at the main 60-m tall tower (C99). C99 was situated in an area of semi-flat, gently rolling terrain with an average slope angle of 0.5 degrees (Van de Wiel et al., 2003). The land-use around C99 was dominated by short prairie grasses and dry soils, characterized by a displacement height $d = 0.08$ m (Van de Wiel et al., 2003) and an aerodynamic roughness length $z_0 = 0.03$ m (Steeneveld et al.,

2006). Because of prevailing arid conditions, the Bowen ratio Bo ranged between 3 and 4 during CASES-99 (Steeneveld et al., 2005). For the investigation of ramp structures and their scaling laws, we used data of the longitudinal u, lateral v and vertical w wind speed components, together with sonic temperature T_s, sampled at 20 Hz (further downsampled to 10 Hz) at 5, 10, 20 and 30 m AGL (Fig. 6.3). Campbell Scientific Inc. CSAT3 sonic anemometers were deployed at the 5-m and 30-m levels, while ATI-K sonic anemometers were used at the 10-m and 20-m levels. We note that the 5-m CSAT3 was deployed on a separate tower roughly 15 m to the east of C99. For simplicity, we will assume it was deployed on C99 in the remainder of the study.

MATERHORN

The overarching goal of the field component of MATERHORN, the MATERHORN-X, conducted during Fall 2012 and Spring 2013 at the Granite Mountain Atmospheric Sciences Testbed (GMAST) of the U.S. Army Dugway Proving Ground (DPG) in central Utah, was the investigation of coupling between thermally and dynamically driven flows across a wide range of scales (Fernando et al., 2015). The central point of MATERHORN was Granite Mountain, a 11.8 km long and 6.1 km wide topographical barrier extending 2200 m above mean sea level (MSL) and situated in the middle of the Dugway Valley (Fig. 6.2b). We use data collected during the Spring 2013 campaign. Despite synoptically forced flows, the Spring 2013 campaign was characterized by mainly northerly-northwesterly daytime and southerly nighttime valley flows throughout the Dugway Valley (Jeglum and Hoch, 2016). We used EC data, sampled at 20 Hz and downsampled to final 10 Hz resolution, from two flux towers: the Playa tower and the East Slope 2 tower.

The Playa tower (PL), with CSAT3 sonic anemometers deployed at heights 5, 10, 20 and 32 m AGL (Fig. 6.3), was situated roughly 15 km to the west of Granite Mountain (Fig. 6.2b). The land-use surrounding PL was characterized by vastly flat, horizontally homogeneous salty-clay playa soils, with negligible aerodynamic roughness length and displacement height (Jensen et al., 2016; Table 6.1). We analyzed a total of 37 days of measurements from 25 April 2013 to 31 May 2013. Despite the moist playa soil table and two major rain events during this period (Hang et al., 2016), the Bowen ratio Bo was overall large, ranging between 1 and 5. In this study, PL will serve as a reference flat terrain flux tower.

The East Slope 2 tower (ES2), on the other hand, was instrumented exclusively with RM Young 81000 sonic anemometers at 5, 10, 16, 20, 25 and 32 m AGL (Fig. 6.3). For

simplicity and consistency with other flux towers analyzed in this study, we will note the 16-m and 32-m levels as 15-m and 30-m, respectively, although we will still retain their exact heights in the scaling analyses. ES2 was located at the base of Granite Mountain, near the bottom of a 1.6 degree slope (Lehner et al., 2015). Similar to PL, flows at ES2 were also characterized by northerly daytime along-valley channeled flows, with occasionally synoptically-driven southerly daytime flows. Area around ES2 was covered with sparse, steppe-like vegetation (Jensen et al., 2017), resulting in a displacement height $d = 0.67$ m and an aerodynamic roughness length $z_0 = 0.0153$ m. We analyzed 24 days of data spanning 30 April 2013 to 23 May 2013. Compared to PL, ES2 experienced a greater range of Bowen ratios Bo, between 1 and 10 (Jensen et al., 2017).

T-REX

From 1 March 2006 to 30 April 2006, T-REX took place in Owens Valley, California, with the aim of studying the evolution of the valley boundary layer in the presence of intense mountain wave activities (Grubišić et al., 2008). Bounded by the Inyo and White Mountains to the northeast and the Sierra Nevada mountain range to the southwest, Owens Valley experienced purely bimodally channeled flows throughout T-REX (Babić et al., 2017; Serafin et al., 2017), with southeasterly upvalley flows during the day and northwesterly downvalley flows during the night. Similar to PL and ES2, along-valley flows of opposite direction were a common occurrence during synoptically perturbed conditions.

We included EC data collected from three National Center for Atmospheric Research (NCAR) Integrated Surface Flux Facility (ISFF) towers (Fig. 6.2c). All three towers, namely the central tower (CT), southern tower (ST) and western tower (WT), were deployed with six levels of CSAT3 sonic anemometers at 5, 10, 15, 20, 25 and 30 m AGL (Fig. 6.3). We note that the 5-m CSAT3 at CT, was operated on a secondary 5-m tower located 9 m to the northwest of CT. Similar to C99, for the sake of simplicity we will assume that the 5-m level was deployed at CT. CT and ST, with a separation of approximately 8 km along the valley's main axis, were sited on the valley floor dominated by low grasslands and shrubs. On the other hand, WT was located at the less vegetated eastern aluvial slope of Sierra Nevada, approximately 9 km to the southwest of CT. Data from all eighteen sonic anemometers, collected initially at 60 samples per second, have been downsampled to 10 Hz for consistency with the other three flux towers presented earlier. Surface conditions in Owens Valley were slightly aerodynamically rougher compared to C99, PL and ES2, owing to taller vegetation (Table 6.1). The three T-REX sites were in a more arid envi-

ronment than the CASES-99 and MATERHORN sites, and characterized by Bowen ratios Bo ranging from 6 to 9 at CT and ST, and between 3 and 7 at WT (Babi et al, 2019, to be submitted).

6.3.2 Post-processing and methodology

30-min turbulence characteristics

All the 10 Hz data sets were split into non-overlapping blocks 30 min in duration, yielding a total of 1056 (C99), 1776 (PL), 1152 (ES2) and 2928 (CT, ST, WT) available 30-min samples. Due to pronounced aridity at all six sites, we assumed equality between T_s and virtual potential temperature θ_v, which we will denote as θ for simplicity. In all of the analyses to follow, we evaluated integral turbulence characteristics (means, variances, covariances) for each of these 30-min samples. With the exception of the three T-REX flux towers, we rotated the three wind speed components into the mean wind using the double rotation method (Stiperski and Rotach, 2016), while turbulent perturbations u', v', w' and θ' were derived using linear detrending. For the T-REX towers, we adopted the planar fit rotation algorithm, and defined the turbulent perturbations using running means of location-dependent time scales (Babić et al., 2017). To obtain all the necessary scaling parameters described in Section 4.2, we used local variables at each height.

To obtain vertical gradients of wind speed dU/dz at each available level, necessary for the calculation of the shear production P, we fitted second order polynomials of the form $U(z) = a \ln(z-d) + b[\ln(z-d)]^2 + c$ (Johansson et al., 2001; Babić and Rotach, 2018) to the 30-min velocity profiles at all six sites. To discard non-stationary 30-min samples, we adopted the Foken and Wichura (1996) (FW96) criterion, which was previously shown by Večenaj and De Wekker (2015) and Babić et al. (2016a) to outperform other common criteria. The FW96 method relies on a ratio FW, defined as the absolute value of the ratio of the difference of the flux averaged over six 5-min sub-samples and the flux averaged over the total 30-min sample, to the flux obtained over the total 30-min sample. If the FW ratio exceeds a critical value $FW_c = 30\%$, the 30-min sample was declared non-stationary.

Viscous dissipation determination

The inertial dissipation method (IDM) was used to obtain ϵ for each 30-min sample. The underlying tenet of IDM is the existence of a -5/3 spectral slope in the inertial subrange of the longitudinal velocity wavenumber spectrum $F_{1,1}$ (Kolmogorov, 1941; Kaimal and

Finnigan, 1994):

$$F_{1,1}(k_1) = \alpha_u \epsilon^{2/3} k_1^{-5/3}, \tag{6.6}$$

where $k_1 = 2\pi f/\overline{U}$ is the longitudinal wavenumber, f is frequency, $\overline{U}$ is the 30-min mean wind speed, $F_{1,1}$ is the longitudinal power spectral density, and α_u is the Kolmogorov constant for the u wind speed component, here taken as 0.53 (Večenaj et al., 2011; Babić, 2016). Alternately, Eq. (6.6) can be rewritten as:

$$\epsilon = \left(\frac{k_1^{5/3} F_{1,1}(k_1)}{\alpha_u} \right)^{3/2}. \tag{6.7}$$

Invoking Taylor's frozen turbulence hypothesis (Stull, 1988) to convert from wavenumber to frequency domain, one finally obtains for the viscous dissipation ϵ:

$$\epsilon = \frac{2\pi}{\overline{U}} \left(\frac{f^{5/3} S_u(f)}{\alpha_u} \right)^{3/2}, \tag{6.8}$$

where $S_{1,1}(f)$ is the longitudinal power spectral density in the frequency domain.

For each 30-min sample, $S_{1,1}$ was obtained from windows consisting of 2^{14} data points, set at the beginning of the sample. Resulting power spectral densities were logarithmically binned and smoothed, after which the portion of $S_{1,1}$ within the inertial subrange was computed similar to Grachev et al. (2013) and Babić and Rotach (2018). Namely, by considering six overlapping segments within the frequency range 0.52-2.55 Hz, associated six values of the spectral slopes were obtained. The deviation of the median of all six slopes from the -5/3 slope, will be used as an additional quality assurance measure for ϵ. The final ϵ value was then obtained within this frequency range using Eq. (6.8).

Wavelet algorithm for ramp structure detection

Following Barthlott et al. (2007), we adopted the wavelet covariance transform for ramp structure detection. The procedure is outlined in Fig. 6.4. To reduce computational time, we low-pass filtered the unprocessed 30-min θ signal with a 2 Hz Butterworth filter, downsampled the time series from 10 Hz to 1 Hz, which we finally linearly detrended to obtain θ' (Fig. 6.4a). We then calculated the wavelet covariance transform $W_n(s)$ of θ':

$$W_n(s) = \frac{1}{\sqrt{s}} \int_{-\infty}^{\infty} \theta'(t)\, \psi \left(\frac{t-n}{s} \right) \mathrm{d}t, \tag{6.9}$$

where t is time, s is a scale dilation, n is a position translation along θ' and ψ is a mother wavelet (Torrence and Compo, 1998). Here, we used the Mexican Hat (MHAT) mother wavelet, best suited for ramp structure detection (Collineau and Brunet, 1993). By performing the convolution (in the frequency domain) between θ' and ψ across the (s, t) parameter space (Fig. 6.4b), we can obtain the exact timing and dominant scale of the major variance-carrying patterns in θ'. To obtain a single global wavelet spectrum $\overline{W(s)}$, we squared and integrated Eq. (6.9):

$$\overline{W(s)} = \frac{1}{\sqrt{s}} \int_{-\infty}^{\infty} |\, W_n(s) \,|^2 \; \mathrm{d}n. \tag{6.10}$$

Traditionally, locating the time scale at which a local maximum in $\overline{W(s)}$ occurs, should ideally represent the dominant ramp structure time scale (Barthlott et al., 2007). However, similar to Litt et al. (2015), we were oftentimes unable to detect a clear local maximum. When this occurred, we detected the first major slope break in $\overline{W(s)}$ instead (Fig. 6.4c), following Litt et al. (2015). In turn, the time scale corresponding to this slope break s_b then corresponds to the time scale of the most energetic ramp structures in θ' (Barthlott et al., 2007). To detect the most energetic ramp structures in θ', the wavelet coefficients corresponding to the time scale of the slope break $W_n(s_b)$ were used to pinpoint the starting and ending points of each ramp structure during a 30 min sample (cyan lines in Fig. 6.4). A local minimum in $W_n(s_b)$ denotes the ramp's starting point, while the following zero-crossing of $W_n(s_b)$ denotes the ramp's ending point (Fig. 6.4a). Finally, we note that we only took into account those ramp structures whose maximum $W_n(s)$ values exceeded 40% of $W_n(s_b)$ (Barthlott et al., 2007).

As one of the main goals of this study is to establish the main similarities and differences in ramp structural properties between flat and complex terrain, we reported several properties of interest: 1) total number of ramp structures within a 30-min sample N; 2) average duration of all ramp structures within 30 min D; 3) average ramp structure length $\ell = D \times \overline{U}$, where $\overline{U}$ is average 30-min wind speed; 4) average ram structure intensity R; 5) momentum F_{uw} and heat flux $F_{w\theta}$ contributions due to ramp structures. To determine F_{uw} and $F_{w\theta}$, we followed Litt et al. (2015) by first determining the flux $\overline{x'w'}_i$ associated with the ith ramp structure:

$$\overline{x'w'}_i = (x_i - \overline{x})\,(w_i - \overline{w})\,, \tag{6.11}$$

where x represents either u or θ. Since ramp structures are typically not of equal duration, we weigh each ramp structure flux with its corresponding duration D_i to obtain the final

flux contribution due to ramp structures F_{xw}:

$$F_{xw} = \left(\sum_{i=1}^{N} \overline{x'w'}_i \, D_i \right) \Big/ \left(\overline{x'w'} \, T \right), \tag{6.12}$$

where $\overline{x'w'}$ is the ensemble EC flux and $T = 30$ min.

Two-point autocorrelation algorithm

To obtain the ramp inclination angle γ, we adopted the method implemented by Marusic and Heuer (2007). This method relies on cross-correlating longitudinal wind speed perturbations u' at multiple levels with the surface shear stress velocity perturbations u_τ. In situations when the wall shear stress is not measured as in our case, the longitudinal velocity perturbations at the lowest level can be used instead (Chauhan et al., 2013). The cross-correlation R_{uu} between the two levels of measurements was performed by means of two-point autocorrelations:

$$R_{uu}(\Delta x, \Delta z) = \frac{\langle u(x,y,z)\, u(x+\Delta x, y, z+\Delta z) \rangle}{\sigma_{u(x,y,z)} \sigma_{u(x+\Delta x, y, z+\Delta z)}}, \tag{6.13}$$

where Δx and Δz are the longitudinal and vertical displacements, respectively. We obtained Δx by utilizing Taylor's frozen turbulence hypothesis (Stull, 1988). At each measurement level relative to the lowest one, R_{uu} peaks at a certain Δx. As Δz increases, the corresponding peak R_{uu} decreases, resulting in an increasing shift in Δx as well, now noted as Δx^*. The linear relationship between Δz and Δx^* can be used to define γ:

$$\gamma = \arctan\left(\langle \Delta z / \Delta x^* \rangle \right). \tag{6.14}$$

To obtain reliable γ estimates, flux towers with as many levels of measurements as possible, are preferred. Hence, we applied the above algorithm only to ST, WT and ES2, having exactly six levels at nearly equal heights AGL. Although CT satisfied this criterion as well, the horizontally displaced 5-m CSAT3 precluded a straightforward Δx^* determination.

Overview of final quality control criteria

The following is a summary of all the criteria simultaneously imposed on every 30-min sample across all 32 sonic anemometers (Table 6.1 shows the final number of 30-min samples at each measurement level satisfying all the requirements):

- Following data quality assurance and control (Vickers and Mahrt, 1997), if the 10 Hz time series contained more than 1% of missing values, it was discarded. Otherwise the missing values were linearly interpolated;
- MO stability parameter $-(z-d)/L > 0$, to disregard stable conditions;
- Kinematic sensible heat flux $\rho c_p \overline{w'\theta'} > 10$ Wm^{-2}, to further reinforce the demand for unstable conditions only;
- Friction velocity $u_* > 0.02$ ms^{-1}, to ensure only conditions with well resolved momentum fluxes, following Li and Bou-Zeid (2011) and Babić et al. (2016a);
- Taylor's frozen turbulence hypothesis $\sigma_u/\overline{U} < 0.3$, to ensure that corrections for $F_{1,1}$ due to distortions caused by converting from wavenumber to frequency domain (Wyngaard and Clifford, 1977), are not needed (Salesky, 2014; Ghannam et al., 2018). Among all the criteria, the necessary rigorousness of this criterion has discarded the largest percentage of 30-min samples;
- Potential temperature standard deviation $\sigma_\theta > 0.2\,^\circ$C (following Katul et al., 1995) to ensure sufficiently thermally excited conditions and thus more reliable ramp structure detection;
- Inertial subrange slopes within $\pm 10\%$ of the theoretical -5/3 value (Stiperski and Calaf, 2017), given the great reliance of this work on the quality of ϵ estimates;
- FW96 ratios simultaneously for both momentum ($FW_{uw} < 30\%$) and sensible heat ($FW_{w\theta} < 30\%$) fluxes (Stiperski and Calaf, 2017).

6.4 Results and Discussion

6.4.1 Governing turbulence production sources

To establish common grounds across all six sites in terms of turbulence production, we first inspected the relative contributions of shear and buoyancy to TKE production (Fig. 6.5).

The most obvious feature of Fig. 6.5 is the dominant prevalence of shear at the three T-REX sites (Fig. 6.5d,e,f) compared to C99, PL and ES2 (Fig. 6.5a,b,c), as revealed by the concentration of 30-min samples near P/ϵ close to unity. In turn, buoyancy was the primary contributor to TKE production at the latter three sites, particularly PL (Fig.

6.5b), where B/ϵ converged to unity with increasingly smaller values of P/ϵ. In other words, during near-neutral conditions ($-(z-d)/L \ll 1$) such as those encountered in Owens Valley (Fig. 6.5d,e,f), the role of buoyancy was negligible. As free-convection conditions prevailed ($-(z-d)/L > 1$), turbulent mixing became driven solely by buoyancy forces.

An additional feature of Fig. 6.5 worth noting, is the closure of the reduced TKE budget (Section 6.2.3). Given the more pronounced flat terrain nature surrounding C99, PL and ES2 to some degree, it is not surprising that the budget was better closed at these sites compared to the T-REX ones. This is evident from the close scattering of 30-min data points around the dashed line in Fig. 6.5 which indicates R/ϵ equal to zero. Here we found the poorest closure at WT, which has already been established previously by Večenaj et al. (2011) for a mountain wave event during T-REX. The main reason for worse closure in Owens Valley stems from poorer applicability of assumptions underlying the reduced TKE budget (Stull, 1988), namely horizontal homogeneity.

6.4.2 Ramp structural properties in the unstable ASL

Site-wide comparison

Ramp structures were a common occurrence in the unstable ASL at all six sites (Fig. 6.6a). Ramp structures were slightly more frequent in Owens Valley compared to other sites, especially below 15 m. Furthermore, the number of ramp structures decreased with height above ground at all sites, a manifestation of the well-known merging mechanism. According to Wilczak and Tillman (1980) and Shaw and Businger (1985), ramp structures merge with height to form the bases of the ML convective thermals near the top or slightly above the SL. In terms of the bottom-up mechanism (Section 6.2.1), the growing TEAL cascade would manifest as fewer ramp structures at upper tower levels. Finally, the rate of merging with height was slightly greater in Owens Valley than at the other sites, given the greater difference in N between 5-m and 30-m.

On average, ramp structures lasted between 60 and 100 s (Fig. 6.6b), in agreement with the range of previously reported values (Barthlott et al., 2007). Ramp structure duration D was negatively correlated with the number of ramp structures N. Interestingly, ramp structures at PL and ES2, the two sites with greatest buoyancy contributions to TKE, tended to be of slightly briefer duration compared to the more shear-prevalent sites (C99, CT, ST, WT). As contributions of shear to TKE diminish, ramp structures exhibit more meandering (Wilczak and Tillman, 1980), equivalent to more lateral than longitudinal elongation, thus helping explain the briefer durations at PL and ES2.

Concerning ramp structure longitudinal lengths ℓ (Fig. 6.6c), it is not surprising to find a positive correlation with D, given that ℓ is derived from D. Ramp structures were more elongated in shear-driven environments (C99, CT, ST, WT) compared to the buoyancy-driven ones (PL, ES2), with values ranging from 350 m near the surface to nearly 1000 m at the highest measurement levels. The overall longest ramp structure lengths found in Owens Valley, could also be explained by laterally constrained roll and cellular convection in the Owens Valley (Babi and De Wekker, 2019, submitted). This additional imposed linearity would also help focus near-surface convection into the mean wind via more pronounced elongation.

As with the other ramp structural properties described above, ramp structure intensities R also showed distinct differences among the six sites. Common to all of them was a decrease of R with height, similar to the decrease of the dimensionless temperature variance with height often observed in the lower half of the CBL (Kaimal and Finnigan, 1994). On average, ramp structures were most intense at the floor of Owens Valley (CT, ST). On the other hand, ramp structures were least intense over the flat sites, C99 and PL. Unlike earlier properties, R seems to have been insensitive to the type of turbulence production source. Specifically, the previously established greatest buoyancy drivers of turbulence at PL (Fig. 6.5b), did not generate the most intense ramp structures there. Instead, R was apparently best correlated with the magnitude of surface heating Q, or similarly, larger Bowen ratios Bo (Table 6.1).

Ramp structure momentum F_{uw} and heat $F_{w\theta}$ flux contributions (Fig. 6.6e,f) also fell within the range of previous studies that relied on MHAT for ramp structure detection (Barthlott et al., 2007; Starkenburg et al., 2013). Similar to these studies, we also found ramp structures contributing slightly more to sensible heat fluxes at all sites, as well as to contribute more to turbulent exchange with increasing distance from the ground. Interestingly, for the sites with smallest buoyancy contributions to TKE (C99, CT, ST, WT), the corresponding ramp structure flux contributions near the ground were lower compared to sites with greater buoyancy effects (PL, ES2). As the height increased, however, this discrepancy diminished and both flux contributions became the largest at the three T-REX sites. This is similar to N earlier, since we found the three T-REX sites to have exhibited greatest amplitude of flux contributions between 5-m and 30-m levels.

To summarize, all of the ramp structural properties reported here agreed well with past observations. We emphasize that the consistent variability between sites driven with shear (C99, CT, ST, WT) as opposed to those driven by buoyancy (PL, ES2), was unlikely to

be influenced by measurement errors, different sonic anemometers used, or the strictness of our QC criteria. The amount of scatter observed in this study, would stem mainly from sampling ramp structures with stationary sensors. However, this deficiency exists at all six sites. As pointed out by Ting and Hay (1977), a stationary sensor samples ramp structures at unknown and randomly distributed sections, thus introducing scatter in the recorded ramp structural properties.

Impact of ramp structures on flux intermittency

Previously, Večenaj and De Wekker (2015) found significant discrepancies among different methods of detecting non-stationarity in turbulent means and (co)variances. They found FW96, one of the most commonly applied criteria, to declare samples contaminated with substantial intermittency, as stationary during unstable situations. We hypothesize that ramp structures were responsible for this weakness of the FW96 criterion. To prove this hypothesis, we considered only those 30-min samples that have passed all the QC criteria (Section 6.3.2), with the exception of FW96 which we did not yet apply for the sake of proving this hypothesis.

When plotting the FW ratios versus the ramp structure number N (Fig. 6.7a), it is evident that application of the FW96 criterion to just $\overline{u'w'}$ would have been redundant. The rigorousness of all the other QC criteria (Section 6.3.2) did an excellent job of filtering out even the non-stationary 30-min samples. However, the same did not apply to the sensible heat flux $\overline{w'\theta'}$ (Fig. 6.7b), where FW96 would have helped filter out a non-negligible amount of 30-min samples characterized by a few weak intermittent ramp structures. This contrasting degree to which the two fluxes experienced ramp structure intermittency has been reported elsewhere (Phong-Anant et al., 1980; Schols, 1984; Katul et al., 1994; Feigenwinter and Vogt, 2005), and ultimately points to the importance of simultaneously demanding stationarity of both momentum and sensible heat fluxes when, for instance, evaluating MOST (Babić et al., 2016a).

Slope effects on ramp structure inclination angle

Among all the ramp structural properties investigated in this study (N, D, ℓ, R, F_{uw}, $F_{w\theta}$, γ), the ramp structure inclination angle γ is the only parameter for which a reference, flat-terrain stability parameterization currently exists (Chauhan et al., 2013). Thus, we can investigate the effects of complex terrain on γ in more detail. This parameterization, given as $\gamma = 12 + 7.3 \ln\left[1 - 70\,(z-d)/L\right]$, was obtained from data collected over the Utah playa

salt flats during May and June 2005 at the Surface Layer Turbulence and Environmental Science Test (SLTEST) main flux tower (Metzger and Holmes, 2008). This flux tower was located about 100 m away from the location of PL during MATERHORN, hence we can assume that such a stability parameterization was representative for PL.

At ST, WT and ES2, the range of γ agreed well with past observations (Antonia et al., 1979, their Table 2; Wilczak and Tillman, 1980; Chauhan et al., 2013; Lotfy and Harun, 2018). The variation of γ with height at ST, can be adequately modelled with the PL parameterization (Fig. 6.8a). This is not surprising, given that ST was located on an essentially flat Owens Valley floor. At WT (Fig. 6.8b), relatively larger departures of γ from the PL parameterization did exist, although the bin-averages still scattered around the reference fit. At ES2 (Fig. 6.8c), however, a consistent departure of γ from the reference fit was obvious. Specifically, with increasing instability, γ at the base of Granite Mountain tended to be consistently greater than the PL parameterization by up to 5 degrees. Since the local terrain slope was smaller at ES2 than at WT (Table 6.1), something else must have driven these larger γ departures at ES2 compared to WT. We hypothesize that greater contribution of buoyancy to TKE at ES2 (Fig. 6.5c), facilitated more upright ramp structures. This is not the case at WT, where buoyancy effects were weaker (Fig. 6.5f). According to McNaughton (2004b), greater buoyancy acts to provide an additional upwards force to ejections of warm, ascending air, as well as an additional downwards force to sweeps of colder, descending air, thus making ramp structures more upright. Of course, local terrain slope also played a role, otherwise the departures of ES2 from PL could not have been explained by buoyancy effects alone, these being significant at both (Fig. 6.5b,c).

Since we found slope angle to have impacted γ, it is instructive to explore if γ also depended on the direction with which ramp structures approached the slope (Fig. 6.8d,e,f). The Owens (ST, WT) and Dugway (ES2) Valleys were best suited for this, as they channeled the flow primarily in the along-valley direction. Purely upslope flows were almost never observed at all three sites, due to along-valley flows overpowering them (Babić et al., 2017). Three interesting features are worth noting here. First, compared to ST (Fig. 6.8d), a tendency for slightly larger γ at WT was noticeable, given the greater bunching of data points closer to the upslope sector. Second, the few downslope 30-min samples (Fig. 6.8e) that have passed the rigorous QC (Section 6.3.2) corresponded to the near-surface streaks that have occurred during westerly downslope windstorms (De Wekker and Mayor, 2009, their Fig. 15). Third, there was essentially no difference in γ between the upvalley and

downvalley sectors at all three sites. This is in agreement with Fesquet et al. (2009), who found ramp structural properties to be independent of upstream land-use heterogeneities. We observed similar insensitivity of other ramp structural properties to wind direction as well (not shown).

6.4.3 Ramp structure scaling in the unstable ASL

To investigate the suitability of different generation mechanisms, we focused on scaling ramp structure lengths ℓ, intensities R and their momentum F_{uw} and sensible heat $F_{w\theta}$ flux contributions. Rather than formulating an exact empirical parameterization for each of these structural parameters, we restricted our investigation to the degree to which scaling parameters of each generation mechanism (Section 4.2) best collapsed the data among all the six sites. We will rely on this collapse as a qualitative measure of which mechanism was overall better suited for scaling ramp structural properties.

Scaling ramp structure length ℓ

Among the four ramp structural properties considered in this section, we first focused on ramp structure length ℓ, as we can directly relate it to the governing scale lengths of all three scaling frameworks. To investigate the degree of collapse among the six sites, we scaled ℓ with the six main length scales (z_s, $z-d$, L, ℓ_P, ℓ_B, ℓ_ϵ) which we plotted as a function of the flux Richardson number $Rf = -P/B$, our choice of the common stability parameter (Fig. 6.9). The issue of self-correlation cannot be entirely avoided, particularly in the case of L, ℓ_P and ℓ_B which share common variables with Rf. Although self-correlation imposes an artificial functional dependency, it does not alter the site-wide collapse we are interested in.

When contrasting the bottom-up (Fig. 6.9a) versus the top-down (Fig. 6.9b,c) frameworks, a considerable amount of scatter was evident. This scatter indicated that, irrespective of the scaling framework, none of the three length scales z_s, $z-d$, L can completely collapse ℓ among all sites. Still, a certain degree of ordering can be attained, particularly between the three T-REX sites and C99, in the case of z_s and $z-d$. We note that, remarkably, such a representation of scaling ℓ reflected the contrasting roles of shear and buoyancy contributions to TKE (Section 6.4.1). Namely, the two sites with the strongest buoyancy contributions, PL and ES2, cannot be collapsed together with the more shear prevalent sites (C99, CT, ST, WT). This motivates us to scale ℓ with the TKE-based scales next.

Scaling ℓ with ℓ_P (Fig. 6.9d) and ℓ_B (Fig. 6.9e) yielded by far the most consistent amount of collapse among all sites. This was especially true for ℓ_P, which nearly fully collapsed even the elusive PL. Despite using ℓ_B to scale ℓ (Fig. 6.9e), the two buoyancy driven sites, ES2 and PL, surprisingly did not collapse, even among each other. This indicates that, although buoyancy effects tended to cause deviations from sites driven by shear, scaling ramp structure lengths with a shear-based scale ℓ_P captured the global ramp structure dynamics far better compared to a buoyancy-based scale ℓ_B. Finally, scaling ℓ with ℓ_ϵ (Fig. 6.9f) did not collapse the six sites, moreso it achieved a similar degree of collapse to scaling with $z-d$. Although Chamecki et al. (2017) have shown the superiority of ℓ_ϵ to z when collapsing the second-order longitudinal structure function in the inertial subrange, this did not seem to be the case when attempting to collapse individually-extracted ramp structures in the unstable ASL.

In conclusion, the fact that the ramp structure lengths ℓ were best scaled with the shear-based length scale ℓ_P, strongly coincided with the theme of the study so far, where the differing contributions of shear and buoyancy seem to have been important to consider in the study of ramp structures. The importance of shear in ramp structure generation has been proposed by many authors (Antonia et al., 1979; Gao et al., 1992; Khanna and Brasseur, 1998), providing additional corroboration of the length scaling results shown here.

Scaling ramp structure intensity R

In the previous section, we found the TKE-based length scales to better collapse ramp structure lengths across all sites, leaving open questions regarding the suitability of the bottom-up and top-down frameworks. To contrast these two mechanisms further, we turned to establishing the degree of collapse among all sites when scaling ramp structure intensity R with the bottom-up θ_ϵ and the top-down θ_* temperature scales (Fig. 6.10). In both cases, near-linear dependencies were observed at all sites, with the exception of PL which tended to deviate more with increasing R. These near-linear dependencies were especially prominent for weak ramps structures, i.e. those corresponding to less unstable conditions. As instability increased, the bin averages deviated more from the apparent near-linear relationship. This deviation was positively correlated with the amount of surface heating (Table 6.1), which we have already established to have been the dominant driver of R (Section 6.4.2).

Regardless of the choice of the temperature scale, the deviations of bin averages from the

near-linear dependency cannot be entirely *scaled away*. Even so, it is clear that, compared to θ_* scaling (Fig. 6.10b), the θ_ϵ scaling (Fig. 6.10a) collapsed the sites significantly better, including the elusive PL (ignoring the one outlying bin average at $\theta_\epsilon \approx 0.75$ K). As shown by Laubach and McNaughton (2009), the only difference between the two temperature scales stems from the dissimilarities in u_ϵ and u_*. Specifically, they tend to diverge more for unstable than for near-neutral conditions, a manifestation of the bottom-up approach better representing the influence of the outer layer on the ASL (McNaughton et al., 2007). The better site-wide collapse in (Fig. 6.10a) indicates that u_ϵ indeed represented this influence better. Furthermore, the ramp structure intensities R scaled with θ_ϵ exhibited significantly less scatter (shorter errobars) in contrast to θ_* scaling. This leads us to conclude that, if the goal is the parameterization of ramp structure intensities with known flow parameters, the bottom-up framework would be a better choice given tighter site-wide collapse and narrower scatter.

Scaling ramp structure flux contributions F_{uw} and $F_{w\theta}$

Finally, we assessed the degree of collapse of the two flux contributions F_{uw} and $F_{w\theta}$ across all six sites, when visualized versus the stability parameters of the bottom-up and top-down generation mechanisms (Fig. 6.11). Common to both flux contributions and irrespective of the invoked scaling framework, was the consistent increase in F_{uw} and $F_{w\theta}$ from near-neutral to progressively more unstable conditions. This increase in F_{uw} and $F_{w\theta}$ with more pronounced instability was also in agreement with past studies (e.g. Barthlott et al., 2007, their Table 6). On average, slightly larger $F_{w\theta}$ were found across the entire stability range, in agreement with the site-wide comparison (Fig. 6.6e,f). Interestingly, both F_{uw} and $F_{w\theta}$ tended to level off at stabilities corresponding to moderately and strongly unstable conditions ($-(z-d)/L > 0.3$ and $(z-d)/z_s > 0.2$). It is known from observations (Wilczak, 1984) and high-resolution simulations (Li et al., 2018) of near-surface ramp structures, that with increasing instability the transport asymmetry between momentum and heat becomes more pronounced. We observed similar behaviour at all six sites, namely where F_{uw} and $F_{w\theta}$ began to taper off. Although mostly PL data were representative of strongly unstable conditions, the discrepancy between F_{uw} and $F_{w\theta}$ was nonetheless much larger there compared to less unstable conditions.

Unlike the preference for the bottom-up scaling framework we found for ramp structure intensity R, the choice of the scaling framework was not as clear-cut in the case of F_{uw} and $F_{w\theta}$. Similar scattering around the bin averages further complicated a preference for a

more suitable scaling framework. Although both F_{uw} and $F_{w\theta}$ exhibited similar trends with increasing instabilities, slightly tighter site-wide collapse was achieved when top-down, MO scaling was used (Fig. 6.11b,d) compared to the bottom-up, SFL scaling (Fig. 6.11a,c).

6.5 Conclusions and Implications

We conducted an investigation of near-surface ramp structures in the unstable ASL over several different terrain types. In doing so, we have analyzed data from 32 sonic anemometers, making our study the most unparalleled in-situ analysis of ramp structures to date. The sites ranged from an extremely smooth and horizontally homogeneous playa to gently rolling grassland, base of a lone mountain, and a deep valley. By contrasting ramp structures over such complex terrain relative to those over the reference playa, we have obviated the representativity shortcoming of past studies.

Shear was the dominant TKE contributor in Kansas and Owens Valley, while buoyancy effects dominated the reduced TKE budget near Granite Mountain. Even though all structural properties were in agreement with previous studies, some stark differences have arisen. Ramp structures in Owens Valley were found to be more numerous, last longer, be more elongated and more intense compared to those over the gently rolling Kansas prairie and in the vicinity of Granite Mountain. Accordingly, ramp structures contributed slightly more to turbulent exchange in Owens Valley, moreso heat than momentum. The contrasting contributions of shear and buoyancy in Owens Valley compared to the other sites, helped explain the observed differences in the structure of ramp structures. Furthermore, ramp structures were found to be an important source of intermittency not detected by the FW96 stationarity criterion, thus explaining its occasional failure in completely filtering out unstable non-stationary periods.

Analysis of ramp structures in Owens Valley and over the eastern slope of Granite Mountain helped us explain the deviations of the ramp structure inclination angle from its flat terrain stability parameterization. This type of investigation is a first of its kind, as ramp structures have not yet been systematically studied over complex terrain. Here, the compounding effects of buoyancy and sloping terrain generated ramp structures that were more upright compared to those over flat terrain. This conjecture holds for the predominantly along-valley flows encountered in Owens and Dugway Valleys, where a purely upslope flow was often masked by a more intense along-valley flow. The presence of sloping terrain undoubtedly modified ramp structures in the unstable ASL, suggesting the need for the development of SGS parameterizations capable of taking into account

local terrain angle. Mountain slopes become increasingly better resolved with increasing computing power (Lehner and Rotach, 2018), thus calling into question the suitability of current LES SGS parameterizations which assume level terrain.

Lastly, we investigated the plausibility of different ramp structure generation mechanisms. We postulated the three frameworks, specifically the bottom-up scaling, top-down scaling, and the TKE-based scaling, with specific length, temperature and stability scaling parameters. We evaluated the performance of each framework by determining the degree of site-wide collapse obtained when normalizing ramp structure length ℓ, intensity R, and flux contributions F_{uw}, $F_{w\theta}$, with relevant scales. Our findings suggest that none of the three ramp structural parameters are best scaled with a single framework. While ramp structure lengths were best collapsed using the shear-based length scale ℓ_P, ramp structure intensities were best collapsed when invoking the bottom-up framework. Regarding the flux contributions, no definitive consensus on the most appropriate scaling framework has emerged. The implications of such disparate scalings, depending on the ramp structural parameter studied, remain elusive and require further investigation.

This study has revealed the importance of ramp structures and their impacts on turbulent exchange, flow intermittency, and in the case of complex terrain, deviations from their relatively better known flat-terrain behavior. The results presented here suggest several research venues worth exploring next. Focusing solely on arid terrains covered with low vegetation (or none at all), we have not addressed ramp structures over rougher, forested slopes. Presence of canopy introduces additional length scales into the problem, thus affecting flow and ramp structure anisotropy to a different extent compared to grasslands (Ghannam et al., 2018). We hypothesize the more pronounced inflexion in the velocity profile across the canopy top, combined with large aerodynamic roughness, to make shear-based length scales a much more obvious scaling choice compared to smoother surfaces studied here. Unfortunately, we were unable to provide any evidence of ramp structure evolution in case of purely upslope flows. The flux tower array ES1-ES5 (Lehner et al., 2015) has the potential for a unique investigation of ramp structure propagation up the eastern slope of Granite Mountain, given that sustained upslope flows were often observed during the Fall 2012 portion of MATERHORN (Hocut et al., 2015). Additionally, the flux tower array deployed during the SELF-2010 experiment in the Swiss Alps (Nadeau et al., 2013), could serve a similar purpose over a much steeper slope. Finally, recent sub-dekameter LES (Sullivan et al., 2016; Inagaki et al., 2017) and DNS (McColl et al., 2017; Li et al., 2018) have shown considerable promise in adequately resolving turbulent exchange

in the ASL, including ramp structures. Validated against rich empirical data sets obtained over a number of terrain and land-use heterogeneities such as in our study, we envisage such simulation tools to spearhead the development of new SGS closures with improved representation of the effects ramp structures impose on near-neutral and unstable ASL flows.

Table 6.1: Site characteristics of the six flux towers analyzed in this study. The columns correspond to: the flux tower designation, altitude H (above mean sea level), slope angle α, aerodynamic roughness length z_0, displacement height d, instrument level h (above ground level), 10-m mean wind speed $\overline{U_{10}}$, 10-m friction velocity $u_{*,10}$, 10-m surface sensible heat flux Q_0, and Bowen ratio $Bo = H/LE$, the ratio of the sensible to latent heat flux. Comma-delimited value pairs for $\overline{U_{10}}$, $u_{*,10}$, Q_{10} represent, respectively, the 25th and 75th percentiles based on all 30-min samples that have satisfied all the QC criteria. The Bowen ratio value ranges were compiled based on previous publications.

Tower	H (m)	α (deg)	z_0 (m)	d (m)	h (m)	30-min samples	$\overline{U_{10}}$ (m/s)	$u_{*,10}$ (m/s)	Q_{10} (Km/s)	Bo
C99	434	0.5	0.03	0.08	5/10/ /20/ /30	163/156/ /102/ /112	4.7, 7.5	0.36, 0.57	0.09, 0.16	3-4
PL	1296	0.002	0.00011	0	5/10/ /20/ /32	229/183/ /110/ / 94	4.6, 8.5	0.20, 0.33	0.05, 0.14	1-5
ES2	1338	1.6	0.0153	0.67	5/10/16/20/25/32	129/116/ 97/ 97/ 98/ 80	5.9, 9.1	0.40, 0.54	0.10, 0.22	1-10
CT	1155	0.2	0.16	0.53	5/10/15/20/25/30	433/493/428/459/428/392	6.4, 9.6	0.60, 0.88	0.14, 0.35	6-9
ST	1141	0.2	0.12	0.53	5/10/15/20/25/30	538/544/519/497/467/437	6.6, 10.7	0.57, 0.86	0.13, 0.30	6-9
WT	1529	3.25	0.06	0.07	5/10/15/20/25/30	295/337/350/313/310/273	5.5, 8.4	0.45, 0.68	0.09, 0.26	3-7

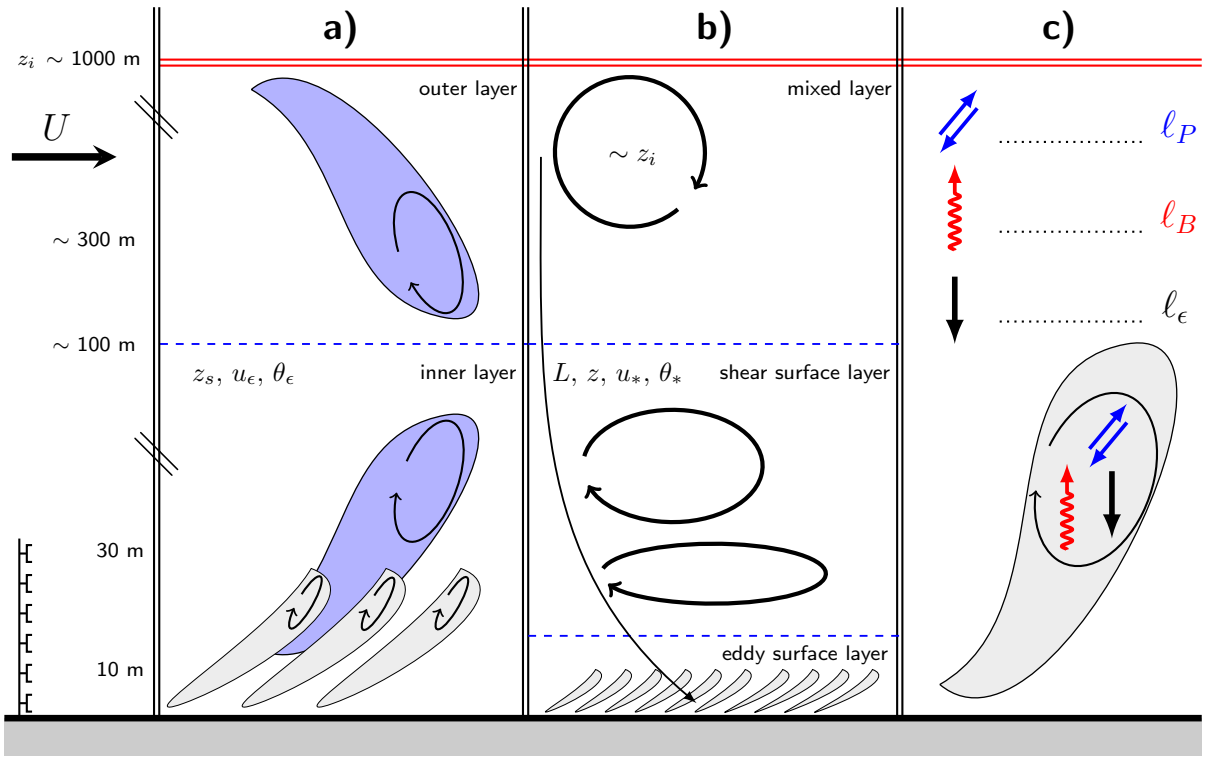

FIGURE 6.1: Conceptual schematic used to illustrate the **(a)** bottom-up ramp scaling framework, **(b)** top-down ramp scaling framework (adopted from Hunt and Carlotti (2001) and Drobinski et al. (2004)), and **(c)** TKE-based scaling framework in terms of dominant production/destruction mechanisms (shear P, buoyancy B, dissipation ϵ). Relevant length, velocity, temperature and stability scales are described in Section 4.2.

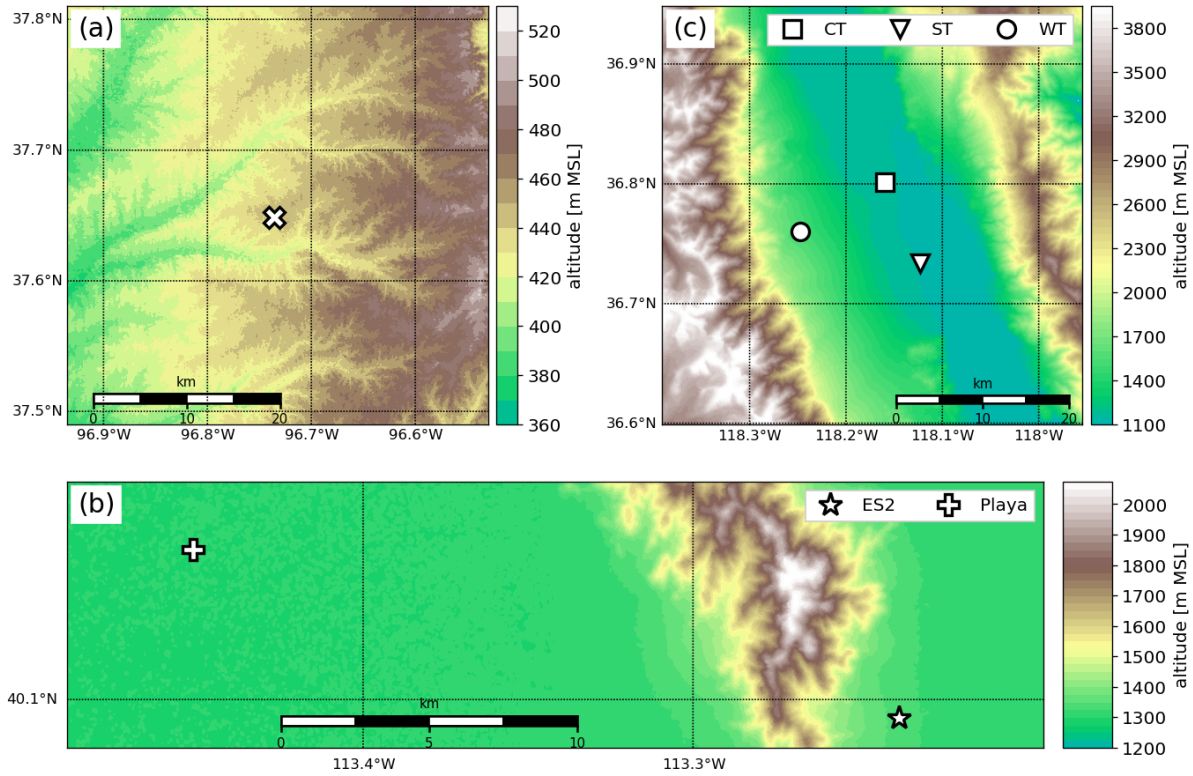

FIGURE 6.2: 1-arc-second Shuttle Radar Topography Mission (Farr et al., 2007) topographical representations of **(a)** CASES-99 experimental area near Leon, Kansas; **(b)** MATERHORN experimental area near Granite Mountain, Utah, and **(c)** T-REX experimental area near Independence, California.

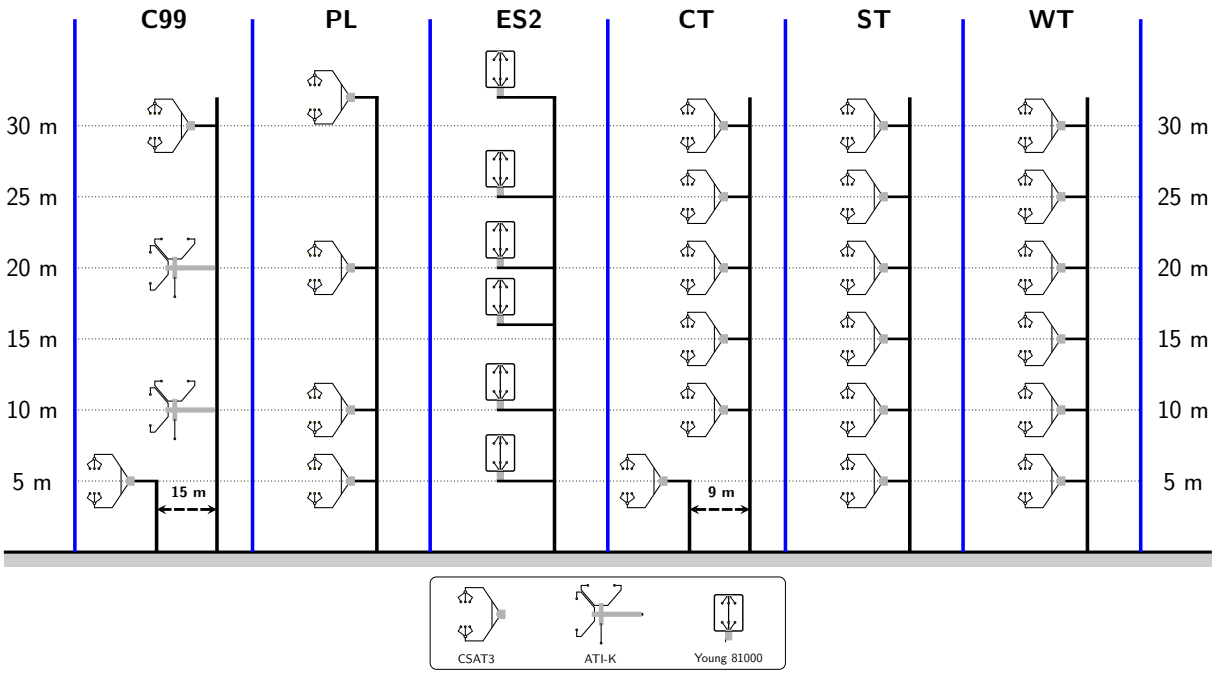

FIGURE 6.3: Conceptual diagram depicting the type of 32 sonic anemometers analyzed in this study. Distances and anemometer sizes are not to scale. Note that the 5-m CSAT3 at C99 and CT, were deployed on two smaller towers 15 m to the east and 9 m to the northwest of C99 and CT, respectively.

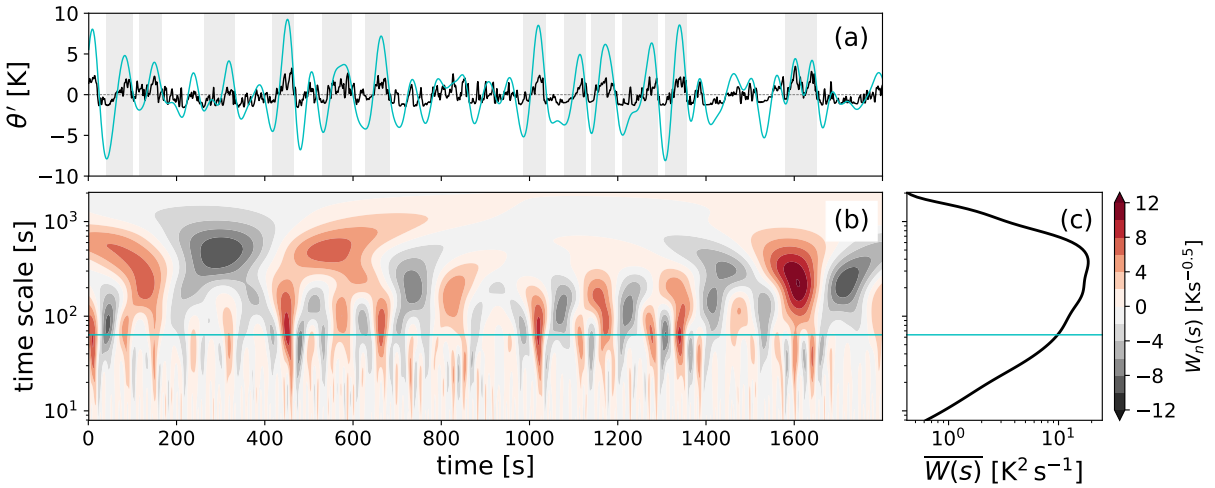

FIGURE 6.4: MHAT ramp detection routine: **(a)** Sample 30-min potential temperature perturbation time series θ' (black). Gray shaded rectangles depict the detected temperature ramps. **(b)** Corresponding scalogram of wavelet covariance coefficients $W_n(s)$ resulting from the convolution of the MHAT mother wavelet with θ'. **(c)** Global wavelet spectrum $\overline{W(s)}$ for the entire 30-min sample. The cyan lines in **(b)** and **(c)** depict the time scale s_b at which a slope break in $\overline{W(s)}$ is registered, determining the corresponding $W_n(s_b)$ coefficients (cyan line in **(a)**) that are used for ramp detection.

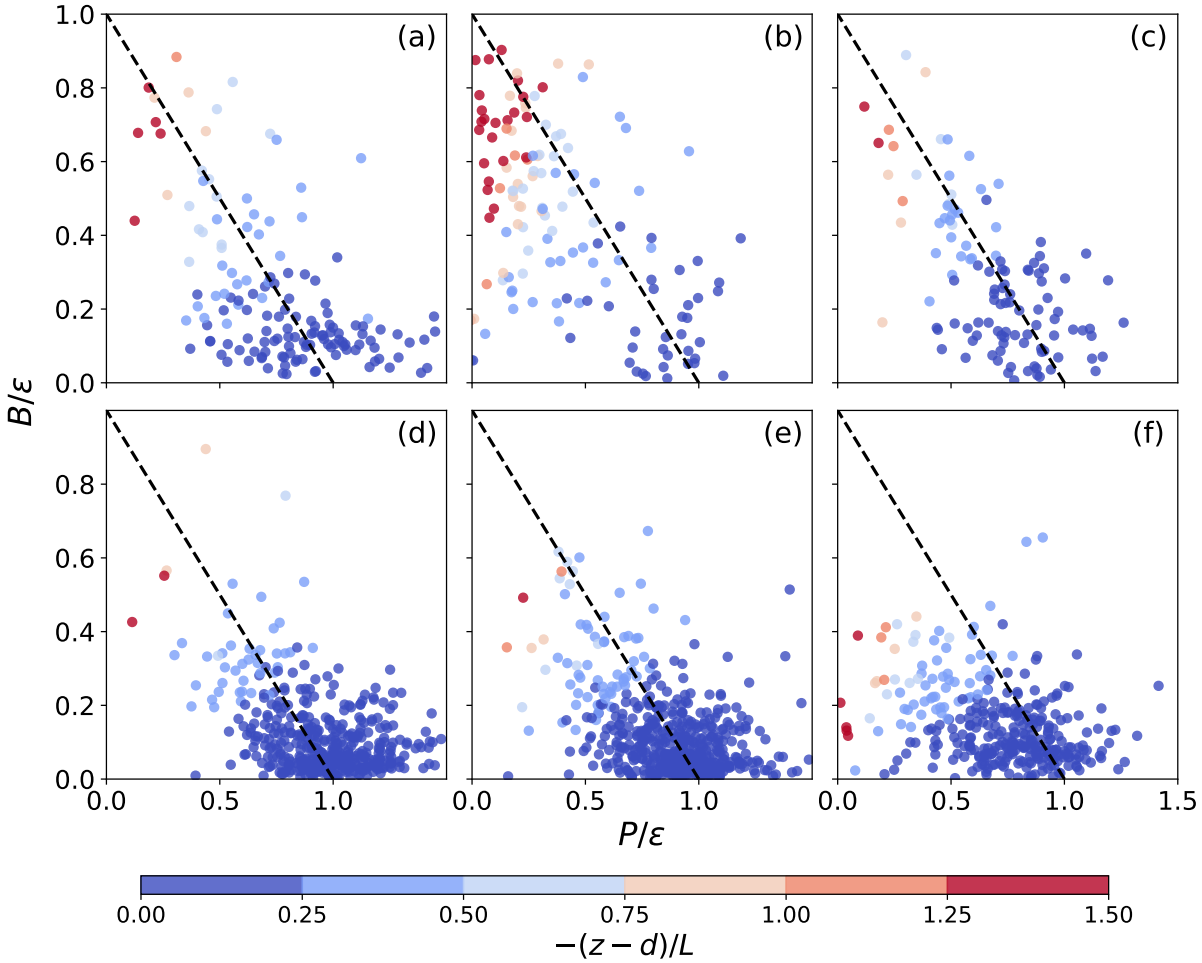

FIGURE 6.5: Two-dimensional phase space bounded by the dissipation-normalized shear production P/ϵ and buoyant production B/ϵ, for the 10-m level at **(a)** C99, **(b)** PL, **(c)** ES2, **(d)** CT, **(e)** ST, and **(f)** WT. Each marker is color-coded with its respective local MO stability parameter $-(z-d)/L$. The black dashed line denotes local balance between production (P, B) and dissipation (ϵ).

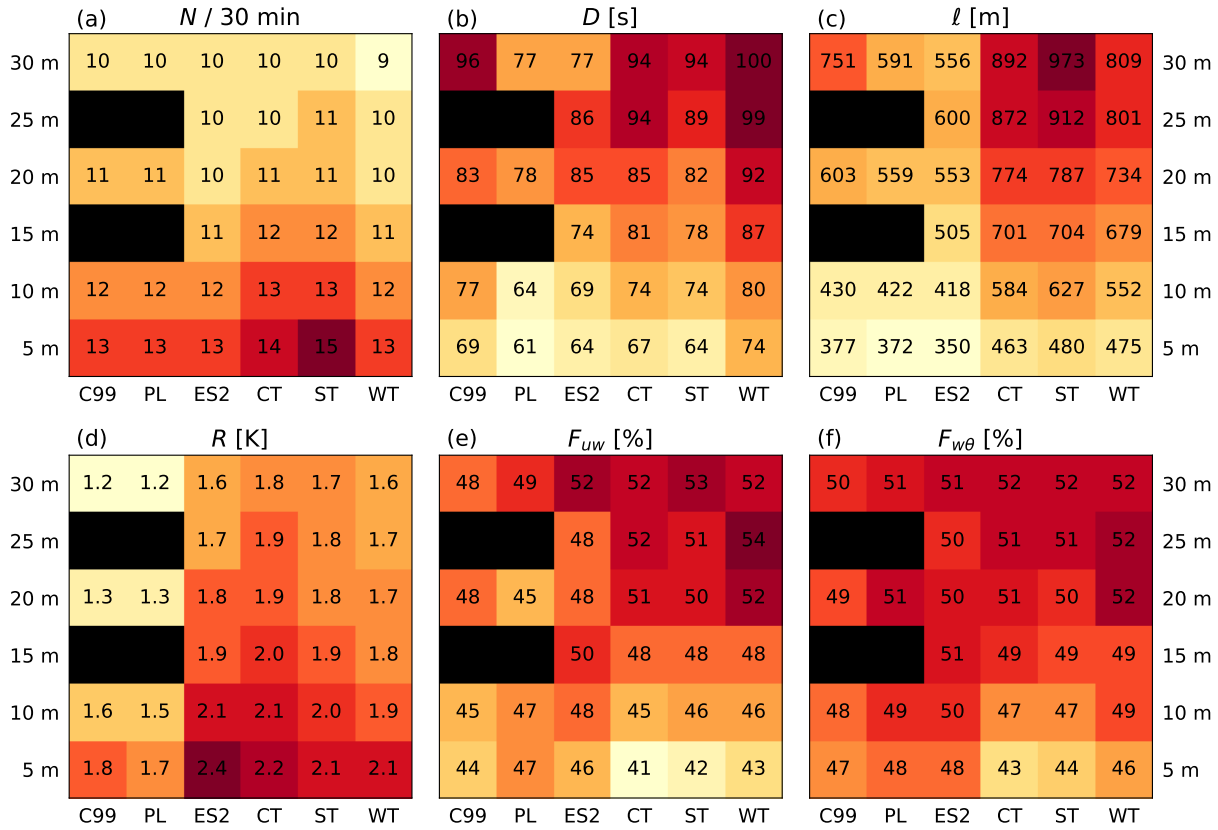

FIGURE 6.6: Ramp structural properties: **(a)** frequency of ramp occurrence within 30 min N, **(b)** duration D, **(c)** ramp length ℓ, **(d)** ramp intensity R, **(e)** momentum flux contribution F_{uw}, and **(f)** sensible heat flux contribution $F_{w\theta}$. Shown are averages of all 30-min samples that have satisfied all the QC criteria (Section 6.3.2). Black squares indicate lack of 15-m and 25-m sonic anemometers on C99 and PL.

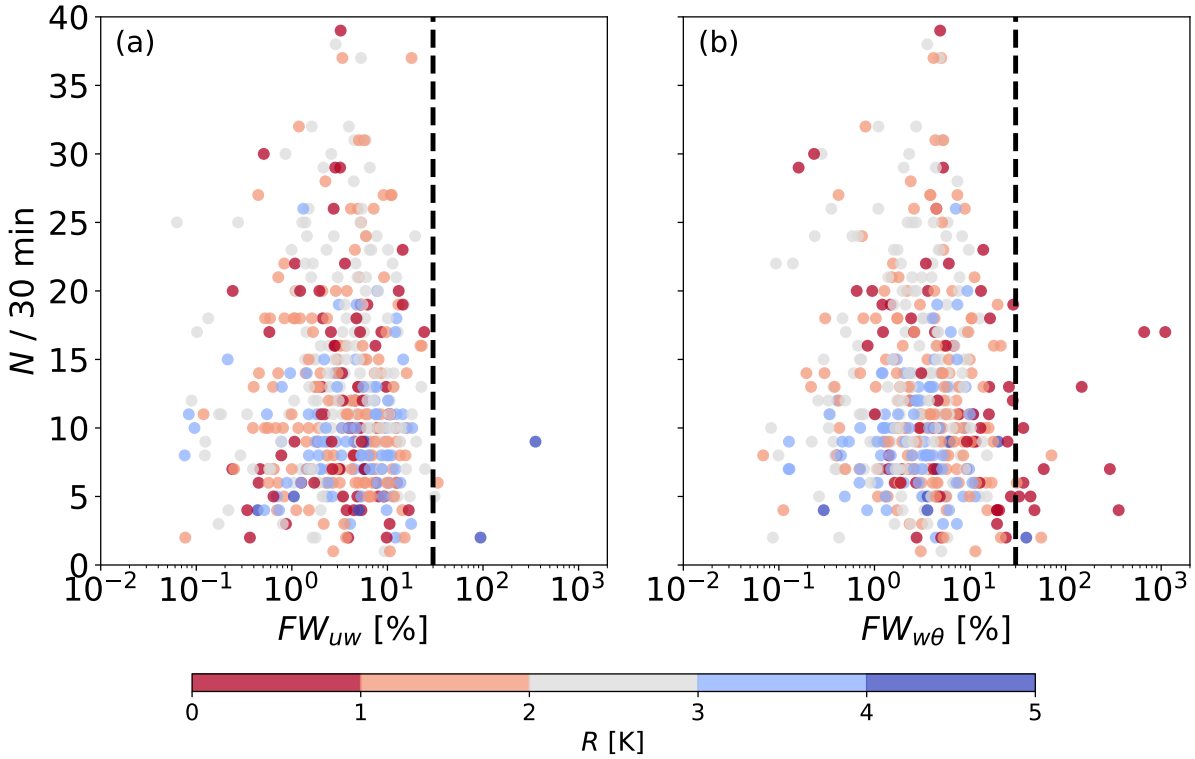

FIGURE 6.7: Frequency of ramp occurrence within 30 min N as a function of **(a)** the FW96 ratio for momentum flux FW_{uw} and **(b)** the FW96 ratio for sensible heat flux $FW_{w\theta}$. Shown are data only for the 10-m level at CT. Each marker is color-coded with its respective ramp intensity R. Vertical dashed line denotes the critical value $FW_c = 30$ %.

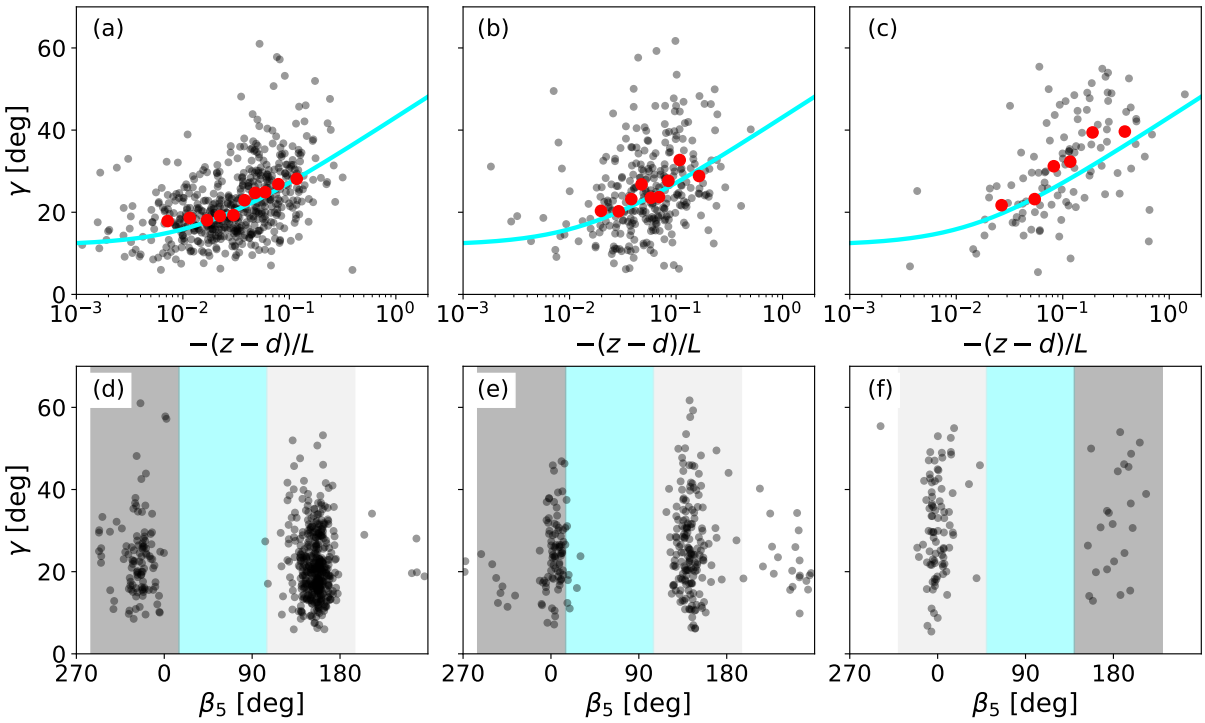

FIGURE 6.8: Ramp inclination angle γ plotted as a function of (**a, b, c**) the 5-m MO stability parameter and (**d, e, f**) 5-m wind direction β_5, at (**a, d**) ST, (**b, e**) WT and (**c, f**) ES2. Cyan line in (**a, b, c**) denotes the Chauhan et al. (2013) SLTEST parameterization, while red markers denote bin averages composed of 50 (ST), 30 (WT) and 20 (ES2) individual 30-min samples. Light blue, white, light gray and dark gray areas in (**d, e, f**) denote the upslope, downslope, upvalley and downvalley wind direction sectors, respectively.

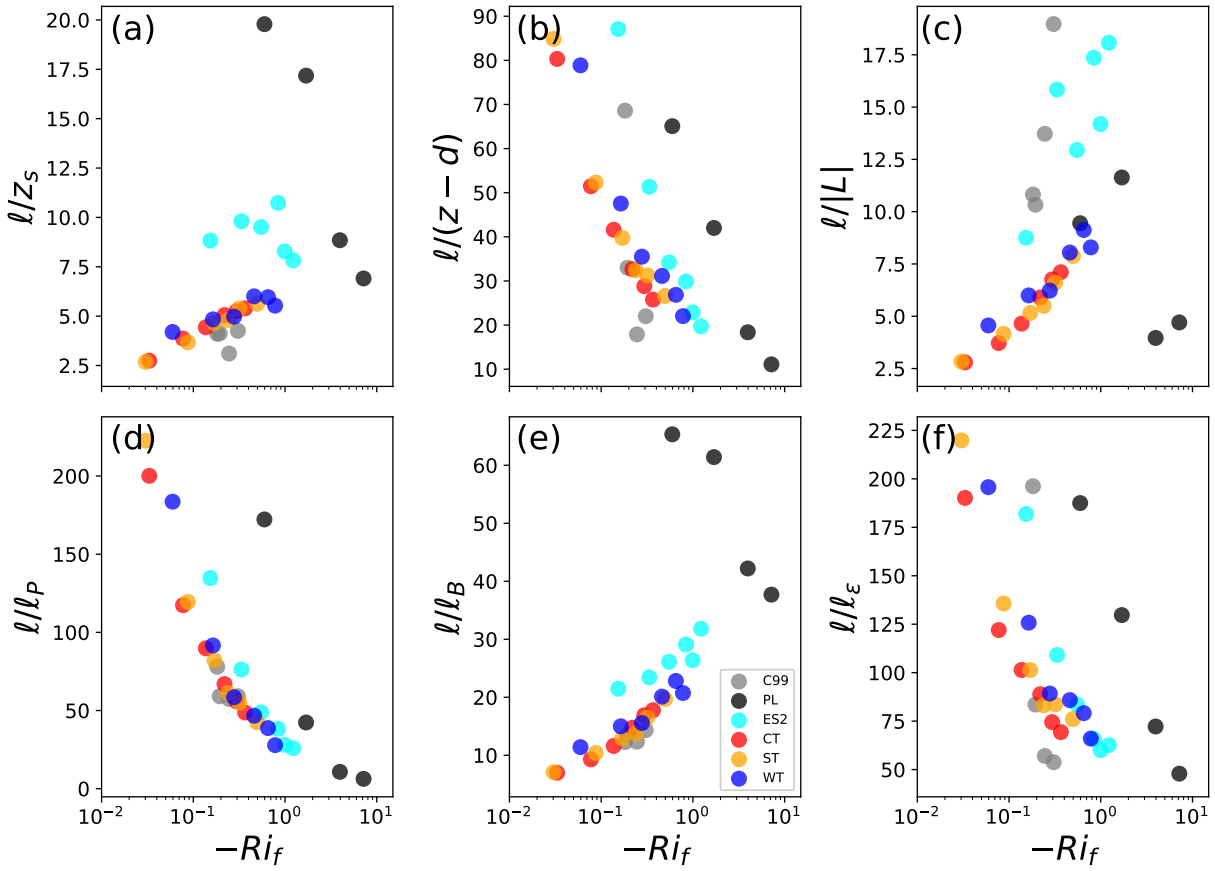

FIGURE 6.9: Ramp length ℓ normalized by **(a)** SFL depth z_s, **(b)** the height above ground $z-d$, **(c)**, Obukhov length $|L|$, **(d)** shear length scale ℓ_P, **(e)** buoyancy length scale ℓ_B, and **(f)** dissipation-based length scale ℓ_ϵ, as a function of the flux Richardson number $-Ri_f$, for all six towers. Each marker represents a bin median of all 30-min samples at a particular level that have satisfied all the QC criteria.

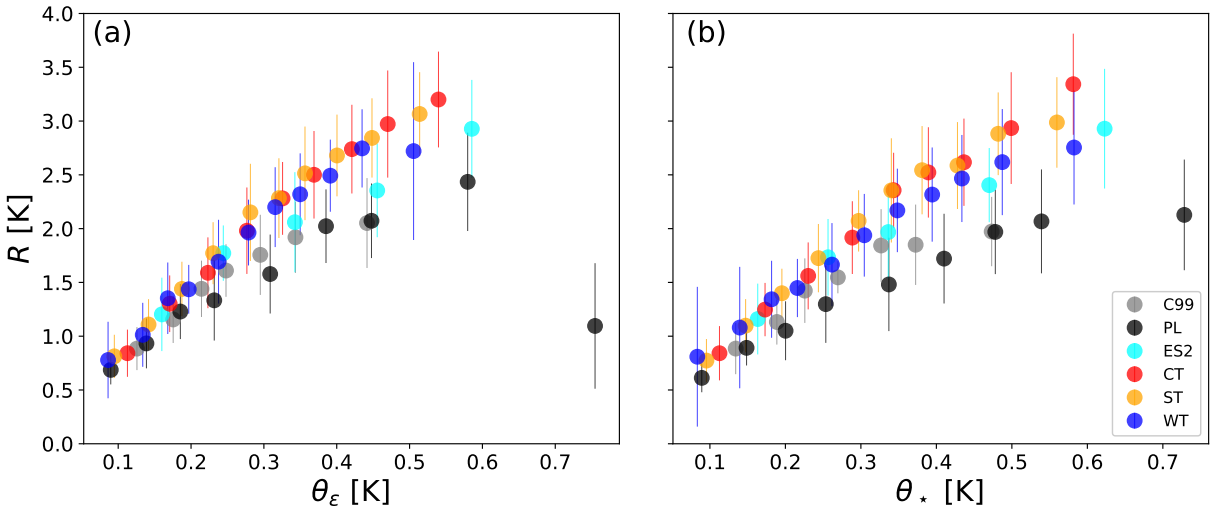

FIGURE 6.10: Ramp intensity R as a function of **(a)** the SFL temperature scale θ_ϵ, and **(b)** the MO temperature scale θ_*, for all six sites at the 10-m level. Each marker denotes a bin average composed of 20 (C99, PL, ES2), 50 (CT, ST) and 30 (WT) individual 30-min samples. Error bars denote $\pm$ one standard deviation.

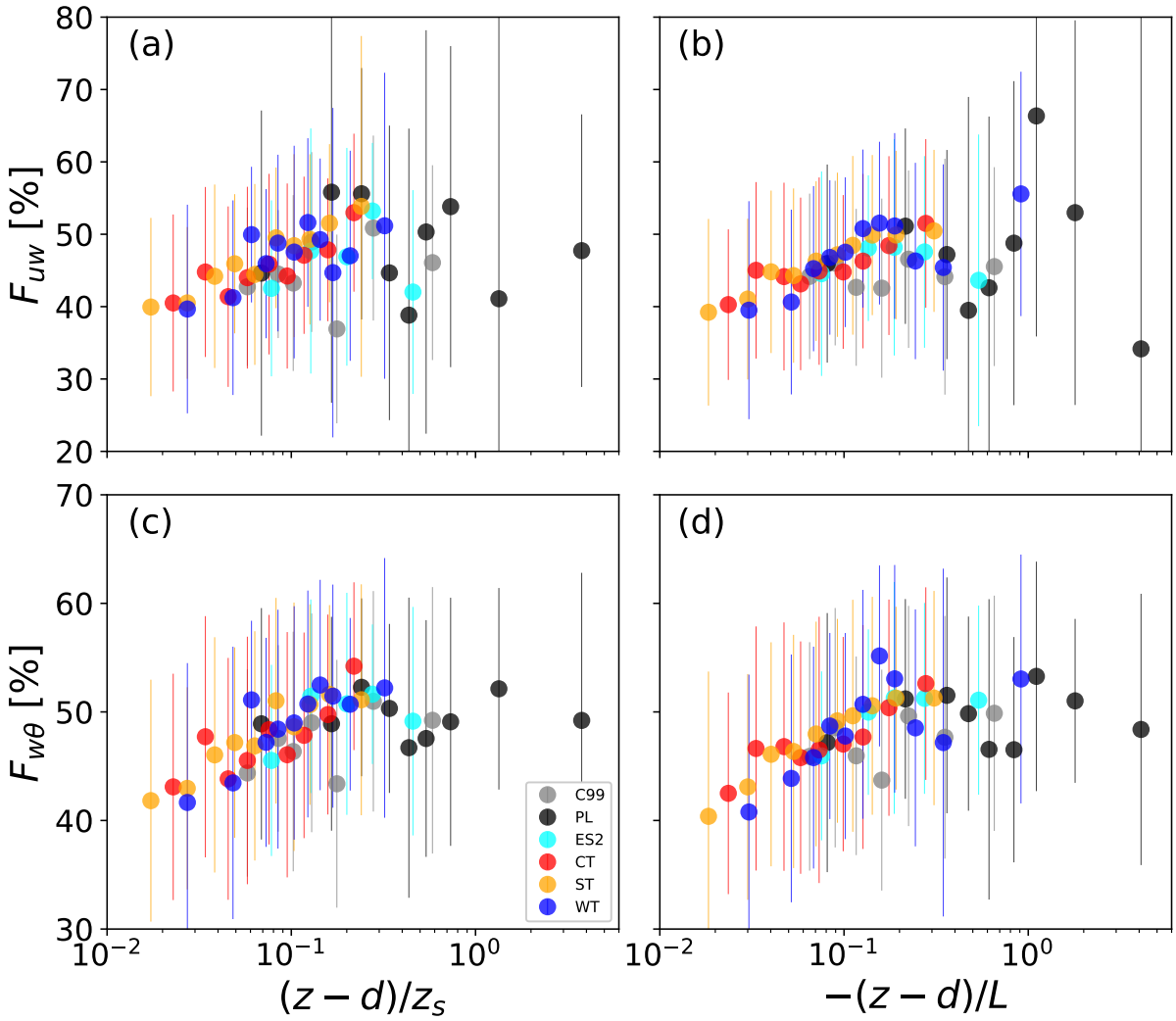

FIGURE 6.11: Ramp momentum flux F_{uw} (**a, b**) and sensible heat flux $F_{w\theta}$ (**c, d**) contribution as functions of (**a, c**) SFL stability parameter $(z-d)/z_s$ and (**b, d**) MO stability parameter $-(z-d)/L$, for all six sites at the 10-m level. Each marker denotes a bin average composed of 20 (C99, PL, ES2), 50 (CT, ST) and 30 (WT) individual 30-min samples. Error bars denote $\pm$ one standard deviation.

7

Conclusions

7.1 Summary of main findings

The overarching goal of this dissertation was to study coherent structures in the CBL over the complex terrain of Owens Valley. The dissertation stressed the importance of simultaneously considering all scales of motion, given their extensive overlap in complex terrain. By utilizing a number of in situ and remote sensing instruments, as well as large-eddy simulations, the dissertation arrived at several novel aspects pertaining to the evolution of CBL and coherent structures in a mountain valley. Following is a summary of the most salient findings of each chapter:

- In Chapter 2, Owens Valley was found to introduce stark deviations from the assumptions underlying flux-variance Monin-Obukhov similarity theory (MOST). The horizontally heterogeneous valley floor and western Owens Valley slope enhanced dimensionless standard deviations of horizontal velocity components at the expense of the vertical velocity component, in agreement with past studies. Different regression approaches were contrasted, revealing inadequacies in the traditionally employed least squares regression when treating outliers. The constant-flux layer hypothesis, which assumes fluxes of momentum and heat to not deviate by more than 10% from their surface layer averages, was challenged in Owens Valley. Specifically, while the heat flux was nearly constant with height in the lowest 30 metres above ground, the momentum flux exhibited significant divergence across the entire stability range. Non-stationarity was determined to detrimentally impact the applicability of MOST

in Owens Valley, however these effects were obviated once stationarity criteria were applied. Among these, the FW96 criterion performed the best in decreasing the scatter around the fitted similarity functions. Such violations of fundamental MOST tenets revealed the need for local scaling in the atmospheric surface layer;

- Chapter 3 investigated the extent and variability of the mesoscale spectral gap throughout Owens Valley, based on a suite of 16 propeller-vane and 12 sonic anemometers. The gap exhibited significant variability in a cross-valley sense, largely dependent on the type of synoptic forcing aloft. The type of synoptic forcing (or lack thereof) was determined by defining three categories based on wind direction. By identifying the gap time scale using MRFD, the dissertation introduced a novel approach of mapping gap scales, thus revealing their spatial variability for the first time. Parameterizations of the gap scales as a function of wind speed and synoptic forcing were proposed. Additionally, upslope flow periodicity was determined using wind profiler data, which we have successfully modelled with a simple model of oscillating anabatic flows. Here, a second novel approach was introduced, by extending MRFD to directional shear (lateral momentum flux) to identify and track weak upslope flows overpowered by stronger upvalley flows;

- By circumventing the *terra incognita*, a two-domain LES nested within three-domain mesoscale WRF was used to investigate the impact of Owens Valley on horizontal convective rolls and open cells in Chapter 4. As such, Chapter 4 represents the first numerical investigation of rolls and cells in a valley. Three case study simulations were performed, one for each of the three categories defined in Chapter 3. Compared to flat terrain, Owens Valley was found to narrow these two most energetic coherent structures, expressed via smaller aspect ratios, smaller wavelengths, larger roll organization factors, and a lack of roll orientation preference relative to the along-valley wind. The transition between rolls and cells occurred over a slightly broader range of the bulk CBL stabilities, compared to the idealized, flat-terrain transition. Furthermore, extending the novel MRFD approach of studying upslope flows from Chapter 3 to LES output, revealed excellent qualitative agreement with the observational climatology from Chapter 3. Additionally, this analysis revealed weak correlation between upslope flows, specifically their strength, and the prevalence of either rolls or cells;

- The aim of Chapter 5 was to investigate the impact of rolls and cells on near-surface

turbulent exchange. The common daytime SEB underclosure, also observed in Owens Valley, has been hypothesized to be impacted by entrainment-driven violation of scalar similarity between temperature and humidity. This chapter presented, for the first time, a direct quantification of this violation, by utilizing MRFD to obtain a scale-dependent measure of entrainment-induced scalar dissimilarity on SEB closure. SEB became fully closed as the entrainment effects weakened, particularly during late afternoon and early evening. Rolls and cells, expressed in this chapter via the magnitude of the bulk CBL stability parameter, were found to be uncorrelated with such scalar dissimilarity, indicating ubiquity of entrainment effects on surface-layer scalar fluxes regardless of the prevalence of these two coherent structures. Additionally, applying the categorization from Chapter 3, revealed a negative correlation between SEB closure and friction velocity during synoptically-driven daytime down-valley flows, otherwise known to be highly correlated. This finding highlighted the importance of differentiating direction of along-valley flows in the presence of synoptic forcing aloft;

- Finally, Chapter 6 examined near-surface ramp structures in complex terrain. First of its kind, this investigation of ramp structures focused on contrasting ramp structural properties between the purely flat playa, gently rolling Kansas prairie, base of the isolated Granite Mountain, and the deep and wide Owens Valley, by utilizing a total of 32 sonic anemometers. We first found that the FW96 stationarity criterion, previously found to be the supreme criterion in Chapter 2, is not always capable of identifying 30-min samples characterized by weak and sporadic ramp structure intermittency. All sites, although characterized by relatively aerodynamically smooth surfaces and overall arid conditions, exhibited various degrees to which shear and buoyancy contributed to TKE. Roles of shear and buoyancy helped explain the observed differences in ramp structural properties, as well as the applicability of three ramp structure scaling frameworks: the bottom-up, top-down, and TKE-based scalings. While a shear-based length scale was found most suitable for scaling ramp structure length, the ramp structure intensity was better parameterized using the bottom-up temperature scale. However, no conclusive preference could be made for ramp structure momentum and heat flux contributions, given both bottom-up and top-down frameworks parameterized the increase of flux contributions with instability in a similar way.

7.2 Implications

These findings demonstrate the importance of CBL coherent structures over complex, mountainous terrain. By taking a synergistic point-of-view that simultaneously considered scales ranging from an entire mountain range down to the very few meters above a floor of a single valley, this dissertation has advanced the knowledge of mechanisms through which complex terrain modulates coherent structures. As advancements in computing power are gradual in time, it is unlikely that the *terra incognita* can be bridged entirely at once. Instead, advancing the knowledge of coherent structure generation, evolution, and final decay, will be crucial in interpreting the resulting numerical artifacts that operational NWP will begin to face significantly more in the years to come. Improved knowledge and appreciation of coherent structures in the *terra incognita*, will benefit not only atmospheric science communities. Environmental communities and policy makers may benefit from improved forecasting of dust storms, air pollution episodes, wildfire as well as ground-level turbulence forecasting over complex terrain. The major societal impact of expanding our knowledge of CBL coherent structures, lies in reducing uncertainties in climate change projections over mountains.

7.3 Recommendations for future research

The synergistic approach to studying CBL coherent structures over complex terrain has teased out a number of research topics worth pursuing. Outlined below is a selection of topics most beneficial to boundary-layer and mountain meteorology:

- While Chapter 2 focused on the flux-variance MOST formulations, it has left open questions regarding the flux-profile formulations, in other words those relating mean velocity and temperature gradients directly to corresponding turbulent fluxes. Future work should explore the impact of different stationarity criteria on flux-profile similarity functions in Owens Valley, as all three NCAR-ISFF flux towers contained an adequate number of levels for obtaining the necessary gradients;

- Findings presented in Chapter 2 are limited to Owens Valley. Since the FW96 and IFC criteria were found most optimal for reducing scatter around flux-variance similarity functions, a potentially useful course of research would be to explore the impact of contrasting complex terrain settings on the performance of just these two criteria. These settings may include valleys of different widths and depths, low and tall

mountaintops, undulating terrain, basins, or canyons;

- In Chapter 3, a spatial dependence of gap scales on wind speed U, synoptic forcing, and elevation, could have been established only for τ_{uu}. This weakness of Chapter 3 raises open questions as to the representativity of such spatial dependencies on gap scales for other variances (τ_{vv}, τ_{ww}, $\tau_{\theta\theta}$) and covariances (τ_{uw}, $\tau_{w\theta}$). Future work should investigate not only the extendability of the established $\tau_{uu} - U$ parameterizations to other valleys, but also the extent to which other gap scales listed above, may depend on wind speed and location in a valley, differently than τ_{uu} does;

- Chapter 3 focused on a climatology of daytime gap scales. Such an approach masked the influence of discrete terrain-forced flow disturbances, such as rotors and downslope windstorms (Strauss et al., 2016), on the short-term gap scale variability. A next step would involve focusing on selected IOP/EOP events during T-REX, when such flow perturbations were sampled with great detail. The short-term impact of these perturbations on gap scales could be investigated by, for instance, sliding the temporal window to which MRFD is applied, forward in time by a small time increment (Viana et al., 2010). This would yield a high-resolution gap scale time series, which can then be brought into relation with the temporal evolution of these terrain-forced flow disturbances;

- The novel approach of tracking anabatic, upslope flows by spectrally decomposing the directional shear $v'w'$ with MRFD, reveals potential for many interesting applications. First, the approach should be extended to other valleys, specifically those characterized by steeper sidewalls where the magnitude of directional shear is larger than in Owens Valley (Van Gorsel et al., 2003). Second, extracting the scale at which the low-frequency portion of $\sum D_{vw}$ begins exhibiting the expected rising or decreasing tendency, may be correlated with the dominant length and time scales of the upslope flow circulation. This scale would have to be validated with, for instance, the depth of the upslope flow layer obtained from tethered balloon soundings or vertical LIDAR scans (Range-Height Indicator, dual-Doppler conical scans). Third, the approach could be extended to nighttime, katabatic, downslope flows. In this case, we hypothesize the low-frequency tendencies in $\sum D_{vw}$ would be clearly visible, with a greater resolution compared to daytime too, since MRFD resolution improves with decreasing time scale. As downslope flow layers are usually shallower than their upslope counterparts, a single tall flux tower might suffice for this purpose;

- In addition to adopting the cell perturbation method to achieve resolved turbulence more rapidly in the nested LES approach, Chapter 4 also revealed the importance of investigating the coherent structures falling into the *terra incognita* in different complex terrain settings. Here, both idealized and nested real-world LES will prove extremely useful, particularly with appropriate observations for validation. Such observations include horizontal dual-Doppler conical scans, which can be used to quantify the structure of prevailing form of convection (Eder et al., 2015a; Träumner et al., 2015);

- Despite the fine horizontal grid spacing in the innermost LES domain used in this dissertation ($\Delta x = 54$ m) in Chapter 4, future nested LES studies should adopt even finer resolutions, on the order of 20 m and less. Only in those cases do second and third order statistical turbulent moments become fully resolved (Sullivan and Patton, 2011). Little is known about spatial variability of such higher-order statistics over complex terrain, namely whether rolls and open cells modify their characteristics differently compared to flat terrain (Salesky et al., 2017);

- Although Chapter 5 confirmed the ubiquity of entrainment effects violating scalar similarity and SEB, the conclusions are still largely specific to the arid nature of Owens Valley. Future research should extend this approach of extracting TOS effects from spectrally decomposed $r_{\theta q}$, to sites characterized with a more pronounced effect of vegetation on the heat flux partitioning, or equivalently, to sites where Bowen ratio does not exceed unity. These include irrigated terrain and forests. Particularly in forests, the degree of heterogeneity of the canopy cover both pre-senescence and post-senescence, will have a large impact on the mid-frequency band (Williams et al., 2007). This fact should be taken into account with special care when isolating the TOS entrainment effect. Nonetheless, this points to another useful research direction of isolating the amplitude of $D_{r_{\theta q}}$ in the mid-frequency band only, to better quantify the seasonal character of canopy patchiness and its influence on flow dynamics in the roughness sublayer;

- Upcoming field efforts, where the aim is a detailed quantification of the effects of advection terms on the SEB closure, should take special care of instrumentation siting (Cuxart et al., 2016). The site setup should recognize the dominant temperature and humidity gradients that may contribute greatly to the advection terms. Valleys with a clear scalar along-valley gradient, such as Owens Valley, are excellent for

this purpose, as the channeling of the valley flow decreases the degrees of freedom of the problem. Furthermore, the site deployment should respect the orientation of this gradient, and if possible, form a line with constant spatial distances along the direction of the gradient. This would enable the quantification of the effect incremental change in separation has on the advection term. Ideally, all sites should contain EC instrumentation, thus enabling the determination of flux densities due to horizontal heat flux divergence which is known to bias SEB closure as well (Moderow et al., 2007; Roo and Mauder, 2018);

- Inclusion of several sites into the study of ramp structures, along with a reference flat terrain site, was one of the main strengths of Chapter 6. Given that ramp structural properties exhibited similar qualitative behavior across all six considered sites, future studies should focus on contrasting ramp structural properties among a much larger number of sites, however only for a single nominal measurement level, for instance 10 m AGL. Majority of experiments conducted in the ASL deploy EC instrumentation at this height, being the standard measurement height according to the World Meteorological Organization (WMO), Environmental Protection Agency (EPA), and the American Association of State Climatologists (AASC). Simultaneous consideration of several tens of easily accessible data sets collected from sites representative of different terrain complexities, land-use characteristics, Bowen ratios and surface roughnesses, will help tease out the dominant controls on ramp structure variability in the unstable ASL;

- Surprisingly, very few studies have brought the CBL depth z_i into relation with ramp structural properties obtained using the MHAT wavelet detection algorithm. Future studies of ramp structures in the unstable ASL should include this elusive yet highly important scaling parameter, as it may help further clarify the disparity and disagreements between the bottom-up and top-down generation mechanisms.

Appendix A

Description of five stationarity criteria

Here we present brief, qualitative descriptions of each of the five stationarity criteria:

Reverse Arrangement Test (RAT)

Presence of a trend is a clear indication of nonstationarity in a time series. According to BP86, one way of detrending a time series is to divide a particular time series into a number of subrecords and make reverse arrangement pairs which are then assigned a certain value (0 or 1) based on relation of each pairs' subrecords. Accumulating each of these values throughout the entire series, one obtains a statistical variable A, represented by an expectation μ_A and standard deviation σ_A. Based on these two values and a significance level (e.g. 95%), the null hypothesis (no trend in the observed time series) is tested. VD15 applied this criterion to all first (means of wind velocity components u, v, w and temperature T) and second order (variances of u, v, w, T and covariances uw, vw, wT) statistical moments.

Running Test (RUT)

Another way of detrending a time series suggested by BP86 is to count the number of groups of consecutive values of the time series being either above (positive runs) or below (negative runs) the median. Similarly to RAT, based on the statistical variable R (number of groups), the null hypothesis (no trend in the time series) is either accepted or rejected. VD15 applied this criterion to all first and second order moments.

M98 criterion

According to M98, standard deviations of second order statistical moments (variances and covariances) of smaller segments can predict those based on larger segments. Final statistical measure obtained is the nonstationarity ratio (NR) of the between-record standard deviation to the random error (obtained from the within-record standard deviation). If this ratio exceeds a critical value (= 2), the observed time series is declared to be non-stationary. VD15 applied this criterion to all first and second order statistical moments.

FW96 criterion

The stationarity test proposed by FW96 relates second order moments to averaging times by dividing the observed time series (typically 30-min intervals) into six 5-min subrecords. If the relative contribution of increasing the averaging time in this manner is above a threshold value (= 30%), the observed time series is declared as non-stationary. VD15 applied this criterion to the second order moments (variances and covariances).

Intermittency Fraction Criterion

According to VD15, even though a number of 30-min intervals were deemed stationary by all four criteria mentioned above, visual inspection revealed occasional occurence of intermittent turbulence. In order to assess and quantify this kind of behaviour, they adopted the approach of Coulter and Doran (2002) and introduced one additional criterion - Intermittency Fraction Criterion (hereafter IFC). If the value of the intermittency fraction (IF) was below a threshold value (=30%), the observed time series was declared as non-stationary. VD15 applied this criterion to the second order moments.

Appendix B

Performance comparison between LSQ and LAD

To enable performing LAD to estimate $\alpha_{i,\theta}$ and $\beta_{i,\theta}$ for our various data sets, reducing 2.5 and 2.6 to a linear functional form $y = ax + b$ is needed. For example, for the wind speed components during unstable stratification, we get:

$$\frac{\sigma_i}{u_*} = \alpha_i \left(1 - \beta_i \zeta\right)^{1/3} \Big/ ()^3 \tag{B.1}$$

$$\underbrace{\left(\frac{\sigma_i}{u_*}\right)^3}_{y} = \underbrace{-\alpha_i^3 \beta_i}_{a} \underbrace{\zeta}_{x} + \underbrace{\alpha_i^3}_{b} \Rightarrow \alpha_i = b^{1/3},\ \beta_i = -a/b \tag{B.2}$$

Table B.1 shows the resulting fitting parameters for other variables and stabilities, while a comparison of α parameters obtained using LSQ and LAD is shown in Fig. B.1. One immediately notices how all six sets of LAD calculated $\alpha_{i,\theta}$ parameters (one for the non-filtered and five for stationary data sets) show a much smaller range of values compared to those calculated using non-linear LSQ. This is especially evident for α_u and α_v parameters. α_w, calculated using both regression methods, show slightly more comparable values and ranges. Further improvement of LAD over LSQ can be observed in the range of α_θ, where LSQ seems to perform quite poor due to giving undue weight to outliers.

Table B.1: Relationship between the LAD fitting parameters (a, b) and the flux-variance parameters $(\alpha_{i,\theta}, \beta_{i,\theta})$.

variable	parameter	$\zeta < 0$	$\zeta > 0$
$i = u, v, w$	α	$b^{1/3}$	$b^{1/3}$
	β	$-a/b$	a/b
θ	α	$b^{-1/3}$	b^{-1}
	β	$-a/b$	a/b

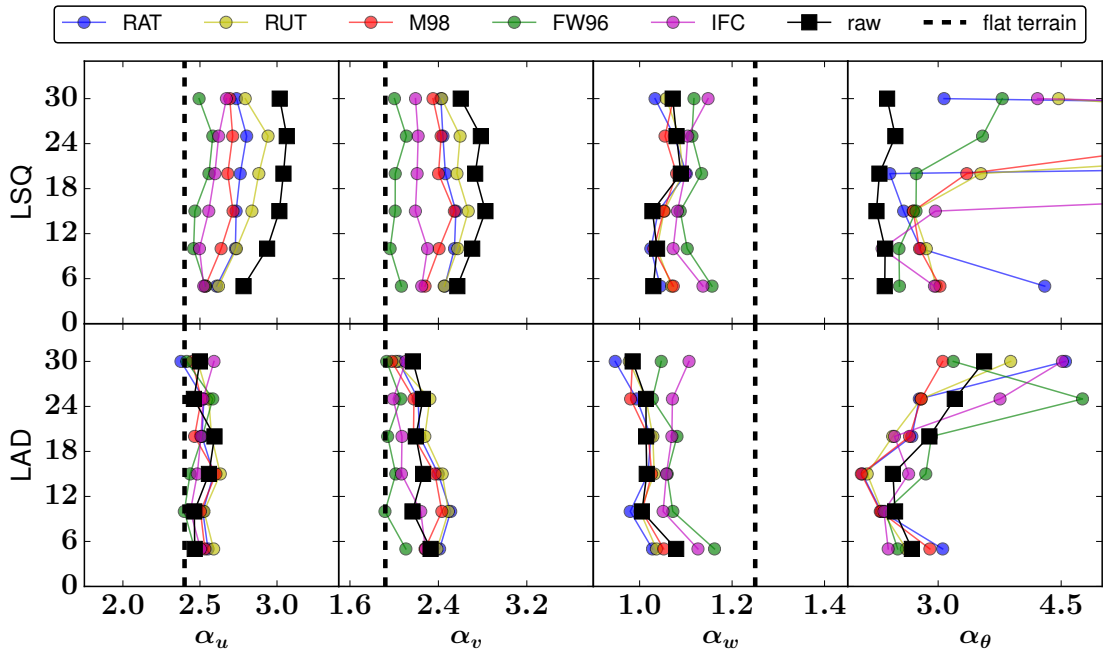

FIGURE B.1: Fitting coefficients α for the unstable regime ($\zeta < 0$), plotted as a function of height at CT. First row is for parameters obtained using non-linear LSQ, while the second row for those obtained using LAD. Color associated with each of the stationarity method is given in the upper legend, together with black dashed lines, which denote the flat terrain values given in Panofsky and Dutton (1984). The black squares denote the parameters obtained based on non-filtered data sets.

Appendix C

Weakness in self-correlation determination

As the β parameter approaches zero (for example, $\beta_{w,\theta}$ for stable stratification, Fig. 2.6), the coefficient of determination becomes ill-defined since both the mean of the data set and its best-fit curve tend to a single constant, i.e. the α parameter. This renders the coefficient of determination R^2_{data} useless since both the numerator and denominator in its definition nearly cancel each other out:

$$R^2_{data} = 1 - \frac{\sum_{i=1}^{n} (y_i - \hat{y}_i)^2}{\sum_{i=1}^{n} (y_i - \overline{y})^2}. \tag{C.1}$$

In the above equation, $\hat{y}_i$ represents the best-fit curve (found using LAD), while $\overline{y}$ denotes the mean of the data set in question. Although R^2_{data} tends to zero when this occurs, R^2_{rand} may not necessarily exhibit the same tendency, resulting in a negative R^2_{diff} (Fig. 2.7b).

Plotting R^2_{data} as a function of β (not shown) revealed that, as β decreases, so does the coefficient of determination R^2_{data}. This can also be shown by plotting R^2 as a function of the extreme value of the stability parameter ζ on either side of the stability range, termed stationary by each of the stationarity criterion (Fig. C.1). On the stable side, there is a slight increase of R^2_w with increasing ζ_{max}. RAT, RUT and M98 extend considerably further into the strongly stable regime, compared to FW96 and IFC. This ultimately has an impact on their β parameters (Fig. 2.6) and R^2_{diff} values, which complicates proper quantification of self-correlation. Slight dependence of R^2_w on ζ_{max} is present also on the

unstable side ($0.6 < R_w^2 < 0.9$), although not nearly as severe as for the stable case ($0 < R_w^2 < 0.6$).

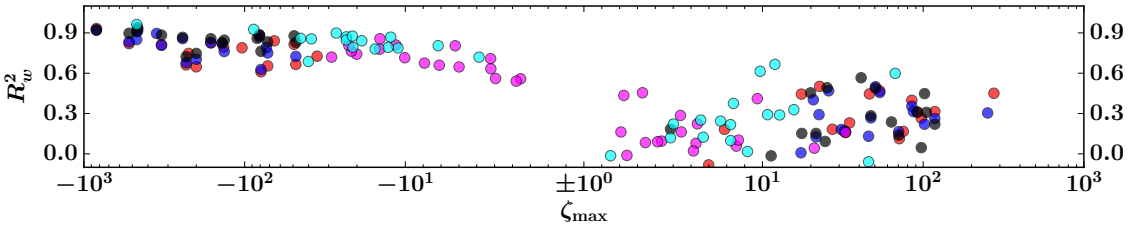

FIGURE C.1: Dependency of R^2_{data} for σ_w/u_{*l} on ζ_{max}. ζ_{max} is obtained as the value of ζ which extends farthest to the left (unstable stratification) and farthest to the right (stable stratification). RAT is represented by red, RUT by blue, M98 by black, FW96 by magenta and IFC by cyan dots, respectively.

Appendix D

WS, SU, SD categorization algorithm

The 30-s data from AWS-10 are used to define the three categories. Wind direction data from this station show the clearest bimodal distribution at the centre of the valley floor (Babić et al., 2016a), thus reducing ambiguity in defining the transitional wind shifts. We define the morning transition as 05:00-09:00 LST, the daytime as 10:00-15:00 LST, and the evening transition as 16:00-20:00 LST. The determination then proceeds as follows:

1. if the circular mean wind direction for the daytime period falls inside the interval [100°, 200°] azimuth (light gray region in Fig. 3.1a), and if the circular standard deviation of wind direction for this daytime period is less than 30°, the day is assigned to the SU category;

2. An additional check is performed upon assigning this day to the SU category: if the circular standard deviation of wind direction during both the morning and evening transition periods is greater than 30° (thus marking a twice daily shift to and from upvalley winds), it is reassigned to the WS category;

3. if the circular mean wind direction for the daytime period falls inside the interval [280°, 20°] azimuth (dark gray region in Fig. 3.1a), and if the circular standard deviation of wind direction for this daytime period is less than 30°, the day is assigned to the SD category.

The above procedure yielded a total of 9 WS days, 22 SU days and 7 SD days, summarized in Table 3.1. We note here that, even though IOP-11 occurred on one of the WS

days (April 9 2006), we are still considering it since the observed rotor event was very rapid and short-lived. The remaining 23 days of the campaign were not assigned to any category, due to insufficiently stationary wind direction during the daytime. We note here that such a robust algorithm is not able to discern between synoptically driven days during which mesoscale phenomena such as rotors and mountain waves might have occurred. The aim is to isolate strong synoptic influence which is known to disturb quiescent valley CBL evolution as a whole, with the expected manifestation of such influence on the overall along-valley flow. For instance, we do not treat rotors as turbulent perturbation flow, but simply consider their overall influence on the variability of the spectra and the resulting gap scales. The categorization introduced above is a compromise between having a statistically rich enough sample and a sufficiently strict conditioning of wind direction variability: the criteria used here are more restrictive than the criteria adopted in e.g. Larsén et al. (2016), thus increasing our confidence in the remainder of the analyses. Finally, we note that our classification does not correspond to the initial classification of Intensive Observing Periods (IOP), which were focused on rotor activity, nor to the Enhanced Observing Periods (EOP), which were focused on quiescent nighttime rather than daytime conditions (Grubišić et al., 2008); filtering only the highest clearness indices (Whiteman and Allwine, 1986) revealed that such indices were not necessarily tied with weakest synoptic influence (Table 3.1).

Appendix E

Multiresolution flux decomposition (MRFD)

MRFD partitions time series of any two variables x and y (each of length 2^M data points) into segments containing 1, 2, 4, ..., 2^M consecutive data points. For each subsequent scale, the segment mean average is subtracted and the MR cospectrum for that segment is calculated. This procedure can be thought of as a highpass filter (Vickers and Mahrt, 2003). The equations neccesary for the calculation of the MR cospectrum associated with a scale $m+1$ are as follows:

$$\hat{x}_n(m) = \frac{1}{2^m} \sum_{i=1}^{n2^m} x_{r_i}(m), \tag{E.1}$$

$$\hat{y}_n(m) = \frac{1}{2^m} \sum_{i=1}^{n2^m} y_{r_i}(m), \tag{E.2}$$

$$D_{xy}(m+1) = \frac{1}{2^{M-m}} \sum_{n=1}^{2^{M-m}} \hat{x}_n(m)\hat{y}_n(m), \tag{E.3}$$

where $x_{r_i}(m)$ and $y_{r_i}(m)$ denote the residual time series (following successive removal of segment means on windows with preceding widths greater than 2^m points), while the $\hat{}$ notation denotes the average at a local scale n (Metzger and Holmes, 2008). The cumulative MR cospectrum is calculated by summing over all averaging scales 1, ..., S in a Reynold's averaging fashion:

$$\sum_{m=1}^{S} D_{xy}(m) = \left[\left(x - \hat{x}^S\right)\left(y - \hat{y}^S\right)\right]. \tag{E.4}$$

Appendix F

VK07 gap scale algorithm

To each individual MR (co)spectrum obtained previously by applying MRFD to propeller-vane or sonic data, we fit fifth order polynomials P by a least squares technique, following VK07. The gap scale retrieval is then accomplished by the following set of rules:

1. P is checked for a local extremum at the turbulent scales, i.e. at $\tau = E_0 < 600$ s;
2. P is checked for roots R_i, other extrema E_i and inflection points I_i at $E_0 < \tau < T$, where T equals 2 h 8 min for the propeller-vanes and 1 h 49 min for the sonics;
3. To check whether P levels off, the derivative at $\tau = I_2$ was checked to be sufficiently small, i.e. $|P'(I_2)/P'(I_1)| < 0.5$;
4. the gap scale τ_g is finally estimated as: $P(\tau_g) = P(\tau_m) + 0.02\,(P(E_0) - P(\tau_m))$, where $\tau_m = \min\{E_1, R_1, I_2\}$.

To ensure that the estimated gap scales are based on accurate fifth order fits while still retaining large enough samples, we filter out gap scales for which the fit error ϵ satisfies the following condition:

$$\epsilon = \frac{\sum_{i=1}^{M} [P(i) - D_{xy}(i)]^2}{\sum_{i=1}^{M} [D_{xy}(i) - \langle D_{xy} \rangle]^2} \leqslant 15\%, \tag{F.1}$$

where $\langle D_{xy} \rangle$ is the average MRFD (co)variance, while M is equal to 8 for propeller-vanes and 16 for the sonics. Although the choices for the order of the polynomial fit and the error

value are arbitrary to a certain extent, they are deemed by VK07 to be the most optimal choice for gap scale determination, both for variances and covariances. As for the value of 0.02 in the 4th step of the algorithm, we suspect it was selected by VK07 to nudge the obtained gap scale slightly away from the spectral gap (by a couple of seconds at most), which has a negligible impact on the rest of the analyses presented in this study. We note that shifting the maximum value of E_0, the first extremum of the fit, from 400 s (VK07) to 600 s proved to be crucial in increasing the number of successful τ_{uu} retrievals. By doing so, we have taken into account the intensification of convective thermals whose spectral signature is located at increasingly longer periods as the CBL deepens throughout the day.

Appendix G

Double rotation versus planar-fit

While double rotation (DR, Kaimal and Finnigan, 1994) is traditionally applied to individual 30-min records collected over flat terrain, resulting in $\overline{v} = \overline{w} = 0$ and the x axis oriented along the mean wind, planar-fit (PF, Wilczak et al., 2001) is typically found more suitable over uneven, complex terrain, resulting in the x axis oriented along the mean wind and $\overline{v} = 0$, based on climatological flow streamlines. However, Stiperski and Rotach (2016) have recently found that, in a valley, PF may underestimate daytime heat fluxes compared to DR, indicating that this choice may not be straightforward.

As heat fluxes represent key variables in SEB, we investigate whether this choice is important for Owens Valley by determining if H and LE at 5-m, are statistically significantly different when DR and PF are applied, at a 95% significance level using the Student t-test. We found statistically insignificant differences at all three sites and for both heat fluxes, when comparing their 2-month average daytime values (CT: $p_H = 0.35$, $p_{LE} = 0.17$; ST: $p_H = 0.81$, $p_{LE} = 0.52$; WT: $p_H = 0.45$, $p_{LE} = 0.57$), enabling us to apply PF at all three sites.

Appendix H

R_{net} sensitivity on terrain aspect and inclination

Over sloping terrain, magnitude of R_{net} may substantially differ when obtained using a gravity-vertical as opposed to a slope-normal instrumentation. Since radiation instrumentation at all three sites was deployed in a gravity-vertical configuration, we need to determine whether this had a potential to degrade R_{net} and thus SEB. We apply the method adopted in Serrano-Ortiz et al. (2016) to model the slope-normal R_{net} based on measured vertical R_{net} at all three sites. Differences between 2-month daytime average measured and modelled R_{net} were found to be statistically insignificant, even over the gentle western slope ($p_{CT} = 0.32$, $p_{ST} = 0.31$, $p_{WT} = 0.09$). Hence, for consistency among all three sites, we do not apply this correction to R_{net}.

Bibliography

Adler, B. and Kalthoff, N. (2014), "Multi-scale transport processes observed in the boundary layer over a mountainous island," *Boundary-Layer Meteorol.*, 153, 515–537.

Adrian, R. J. (2007), "Hairpin vortex organization in wall turbulence)," *Phys. Fluids (1994-present)*, 19, 041301.

Adrian, R. J., Meinhart, C. D., and Tomkins, C. D. (2000), "Vortex organization in the outer region of the turbulent boundary layer," *J. Fluid Mech.*, 422, 1–54.

Agee, E. and Gluhovsky, A. (1999), "LES model sensitivities to domains, grids, and large-eddy timescales," *J. Atmos. Sci.*, 56, 599–604.

Aksamit, N. O. and Pomeroy, J. W. (2018), "The effect of coherent structures in the atmospheric surface layer on blowing-snow transport," *Boundary-Layer Meteorol.*, 167, 211–233.

Al-Jiboori, M., Xu, Y., and Qian, Y. (2002), "Local similarity relationships in the urban boundary layer," *Boundary-Layer Meteorol.*, 102, 63–82.

Anderson, R. G. and Wang, D. (2014), "Energy budget closure observed in paired Eddy Covariance towers with increased and continuous daily turbulence," *Agr. Forest Meteorol.*, 184, 204–209.

Andreas, E. L., Hill, R. J., Gosz, J. R., Moore, D. I., Otto, W. D., and Sarma, A. D. (1998), "Statistics of surface-layer turbulence over terrain with metre-scale heterogeneity," *Boundary-Layer Meteorol.*, 86, 379–408.

Andreas, E. L., Geiger, C. A., Treviño, G., and Claffey, K. J. (2008), "Identifying nonstationarity in turbulence series," *Boundary-Layer Meteorol.*, 127, 37–56.

Angevine, W. M., White, A. B., and Avery, S. K. (1994), "Boundary-layer depth and entrainment zone characterization with a boundary-layer profiler," *Boundary-Layer Meteorol.*, 68, 375–385.

Angevine, W. M., Bazile, E., Legain, D., and Pino, D. (2014), "Land surface spinup for episodic modeling," *Atmos. Chem. Phys.*, 14, 8165–8172.

Antonia, R., Chambers, A., Friehe, C., and Van Atta, C. (1979), "Temperature ramps in the atmospheric surface layer," *J. Atmos. Sci.*, 36, 99–108.

Antonia, R., Chambers, A., and Bradley, E. F. (1982), "Relationships between structure functions and temperature ramps in the atmospheric surface layer," *Boundary-Layer Meteorol.*, 23, 395–403.

Asanuma, J., Tamagawa, I., Ishikawa, H., Ma, Y., Hayashi, T., Qi, Y., and Wang, J. (2007), "Spectral similarity between scalars at very low frequencies in the unstable atmospheric surface layer over the Tibetan plateau," *Boundary-Layer Meteorol.*, 122, 85–103.

Atkinson, B. and Zhang, J. (1996), "Mesoscale shallow convection in the atmosphere," *Rev. Geophys.*, 34, 403–431.

Baas, P., Steeneveld, G., Van De Wiel, B., and Holtslag, A. (2006), "Exploring self-correlation in flux-gradient relationships for stably stratified conditions," *J. Atmos. Sci.*, 63, 3045–3054.

Babić, K. (2016), "Low-level turbulence characteristics over inhomogeneous surface during wintertime," Ph.D. thesis, Faculty of Science, University of Zagreb.

Babić, K. and Rotach, M. (2018), "Turbulence kinetic energy budget in the stable boundary layer over a heterogeneous surface," *Q. J. R. Meteorol. Soc.*

Babić, N., Večenaj, Ž., and De Wekker, S. F. (2016a), "Flux–variance similarity in complex terrain and its sensitivity to different methods of treating non-stationarity," *Boundary-Layer Meteorol.*, 159, 123–145.

Babić, N., Večenaj, Ž., Kozmar, H., Horvath, K., De Wekker, S. F., and Grisogono, B. (2016b), "On turbulent fluxes during strong winter bora wind events," *Boundary-Layer Meteorol.*, 158, 331–350.

Babić, N., Večenaj, Ž., and De Wekker, S. F. (2017), "Spectral gap characteristics in a daytime valley boundary layer," *Q. J. R. Meteorol. Soc.*, 143, 2509–2523.

Baldocchi, D., Falge, E., Gu, L., Olson, R., Hollinger, D., Running, S., Anthoni, P., Bernhofer, C., Davis, K., Evans, R., et al. (2001), "FLUXNET: A new tool to study the temporal and spatial variability of ecosystem–scale carbon dioxide, water vapor, and energy flux densities," *Bull. Am. Meteorol. Soc.*, 82, 2415–2434.

Baldocchi, D. D. and Meyers, T. P. (1988), "Turbulence structure in a deciduous forest," *Boundary-Layer Meteorol.*, 43, 345–364.

Barnhart, B., Eichinger, W., and Prueger, J. (2012), "A new eddy-covariance method using empirical mode decomposition," *Boundary-Layer Meteorol.*, pp. 1–14.

Barthlott, C., Drobinski, P., Fesquet, C., Dubos, T., and Pietras, C. (2007), "Long-term study of coherent structures in the atmospheric surface layer," *Boundary-Layer Meteorol.*, 125, 1–24.

Bastin, S. and Drobinski, P. (2005), "Temperature and wind velocity oscillations along a gentle slope during sea-breeze events," *Boundary-Layer Meteorol.*, 114, 573–594.

Beljaars, A. (1987), "On the memory of wind standard deviation for upstream roughness," *Boundary-Layer Meteorol.*, 38, 95–101.

Belušić, D. and Mahrt, L. (2012), "Is geometry more universal than physics in atmospheric boundary layer flow?" *J. Geophys. Res. Atmos.*, 117.

Belušić, D., Žagar, M., and Grisogono, B. (2007), "Numerical simulation of pulsations in the bora wind," *Q. J. R. Meteorol. Soc.*, 133, 1371–1388.

Belušić, D., Večenaj, Ž., and LeMone, M. A. (2015), "Possible observation of horizontal roll vortices over the Adriatic Sea during bora," *Front. Earth Sci.*, 3, 23.

Bendat, J. S. and Piersol, A. G. (1986), *Random Data: Analysis and Measurement Procedures*, John Wiley & Sons.

Brötz, B., Eigenmann, R., Dörnbrack, A., Foken, T., and Wirth, V. (2014), "Early-morning flow transition in a valley in low-mountain terrain under clear-sky conditions," *Boundary-Layer Meteorol.*, 152, 45–63.

Burns, S. P., Sun, J., Lenschow, D. H., Oncley, S. P., Stephens, B. B., Yi, C., Anderson, D. E., Hu, J., and Monson, R. K. (2011), "Atmospheric stability effects on wind fields and scalar mixing within and just above a subalpine forest in sloping terrain," *Boundary-Layer Meteorol.*, 138, 231–262.

Calaf, M., Hultmark, M., Oldroyd, H., Simeonov, V., and Parlange, M. (2013), "Coherent structures and the k-1 spectral behaviour," *Phys. Fluids*, 25, 125107.

Cancelli, D. M., Chamecki, M., and Dias, N. L. (2014), "A large-eddy simulation study of scalar dissimilarity in the convective atmospheric boundary layer," *J. Atmos. Sci.*, 71, 3–15.

Carper, M. A. and Porté-Agel, F. (2004), "The role of coherent structures in subfilter-scale dissipation of turbulence measured in the atmospheric surface layer," *J. Turbul.*, 5, 32–32.

Castelli, S. T. and Falabino, S. (2013), "Analysis of the parameterization for the wind-velocity fluctuation standard deviations in the surface layer in low-wind conditions," *Meteorol. Atmos. Phys.*, 119, 91–107.

Catalano, F. and Moeng, C.-H. (2010), "Large-eddy simulation of the daytime boundary layer in an idealized valley using the Weather Research and Forecasting numerical model," *Boundary-Layer Meteorol.*, 137, 49–75.

Caughey, S. (1977), "Boundary-layer turbulence spectra in stable conditions," *Boundary-Layer Meteorol.*, 11, 3–14.

Cava, D., Contini, D., Donateo, A., and Martano, P. (2008), "Analysis of short-term closure of the surface energy balance above short vegetation," *Agr. Forest. Meteorol.*, 148, 82–93.

Chamecki, M., Dias, N. L., Salesky, S. T., and Pan, Y. (2017), "Scaling laws for the longitudinal structure function in the atmospheric surface layer," *J. Atmos. Sci.*, 74, 1127–1147.

Chamecki, M., Dias, N. L., and Freire, L. S. (2018), "A TKE-based framework for studying disturbed atmospheric surface layer flows and application to vertical velocity variance over canopies," *Geophys. Res. Lett.*, 45, 6734–6740.

Charuchittipan, D., Babel, W., Mauder, M., Leps, J.-P., and Foken, T. (2014), "Extension of the averaging time in eddy-covariance measurements and its effect on the energy balance closure," *Boundary-Layer Meteorol.*, 152, 303–327.

Chauhan, K., Hutchins, N., Monty, J., and Marusic, I. (2013), "Structure inclination angles in the convective atmospheric surface layer," *Boundary-Layer Meteorol.*, 147, 41–50.

Chen, F. and Dudhia, J. (2001), "Coupling an advanced land surface–hydrology model with the Penn State–NCAR MM5 modeling system. Part I: Model implementation and sensitivity," *Mon. Weather Rev.*, 129, 569–585.

Cheng, Y., Parlange, M. B., and Brutsaert, W. (2005), "Pathology of Monin-Obukhov similarity in the stable boundary layer," *J. Geophys. Res. - Atmos.*, 110.

Ching, J., Rotunno, R., LeMone, M., Martilli, A., Kosovic, B., Jimenez, P., and Dudhia, J. (2014), "Convectively induced secondary circulations in fine-grid mesoscale numerical weather prediction models," *Mon. Weather Rev.*, 142, 3284–3302.

Chow, F. K., Weigel, A. P., Street, R. L., Rotach, M. W., and Xue, M. (2006), "High-resolution large-eddy simulations of flow in a steep Alpine valley. Part I: Methodology, verification, and sensitivity experiments," *J. Appl. Meteorol. Climatol.*, 45, 63–86.

Christen, A., van Gorsel, E., and Vogt, R. (2007), "Coherent structures in urban roughness sublayer turbulence," *Intl. J. Climatol.*, 27, 1955–1968.

Collineau, S. and Brunet, Y. (1993), "Detection of turbulent coherent motions in a forest canopy part I: Wavelet analysis," *Boundary-Layer Meteorol.*, 65, 357–379.

Cotton, W. R., Alexander, G. D., Hertenstein, R., Walko, R. L., McAnelly, R. L., and Nicholls, M. (1995), "Cloud ventingA review and some new global annual estimates," *Earth-Sci. Rev.*, 39, 169–206.

Coulter, R. L. and Doran, J. (2002), "Spatial and temporal occurrences of intermittent turbulence during CASES-99," *Boundary-Layer Meteorol.*, 105, 329–349.

Crosman, E. T. and Horel, J. D. (2017), "Large-eddy simulations of a Salt Lake Valley cold-air pool," *Atmos. Res.*, 193, 10–25.

Cullen, N. J., Steffen, K., and Blanken, P. D. (2007), "Nonstationarity of turbulent heat fluxes at Summit, Greenland," *Boundary-Layer Meteorol.*, 122, 439–455.

Cuxart, J. (2015), "When can a high-resolution simulation over complex terrain be called LES?" *Front. Earth Sci.*, 3, 87.

Cuxart, J., Wrenger, B., Martínez Villagrasa, D., Reuder, J., Jonassen, M. O., Jiménez Cortés, M. A., Lothon, M., Lohou, F., Hartogensis, O., Dünnermann, J., et al. (2016), "Estimation of the advection effects induced by surface heterogeneities in the surface energy budget," *Atmos. Chem. Phys.*, 16, 9489–9504.

Daniels, M. H. (2010), *Soil moisture in complex terrain: quantifying effects on atmospheric boundary layer flow and providing improved surface boundary conditions for mesoscale models*, PhD Dissertation, University of California, Berkeley.

Daniels, M. H., Lundquist, K. A., Mirocha, J. D., Wiersema, D. J., and Chow, F. K. (2016), "A new vertical grid nesting capability in the Weather Research and Forecasting (WRF) Model," *Mon. Weather Rev.*, 144, 3725–3747.

Darby, L. S. and Poulos, G. S. (2006), "The evolution of lee-wave-rotor activity in the lee of Pike's Peak under the influence of a cold frontal passage: Implications for aircraft safety," *Mon. Weather Rev.*, 134, 2857–2876.

De Bruin, H. and Verhoef, A. (1997), "A new method to determine the zero-plane displacement," *Boundary-Layer Meteorol.*, 82, 159–164.

De Bruin, H., Hartogensis, O., Allen, R., and Kramer, J. (2005), "Regional advection perturbations in an irrigated desert (RAPID) experiment," *Theor. Appl. Climatol.*, 80, 143–152.

De Franceschi, M., Zardi, D., Tagliazucca, M., and Tampieri, F. (2009), "Analysis of second-order moments in surface layer turbulence in an Alpine valley," *Q. J. R. Meteorol. Soc.*, 135, 1750–1765.

de Roode, S. R., Duynkerke, P. G., and Jonker, H. J. (2004), "Large-eddy simulation: How large is large enough?" *J. Atmos. Sci.*, 61, 403–421.

De Wekker, S., Kossmann, M., Knievel, J., Giovannini, L., Gutmann, E., and Zardi, D. (2018), "Meteorological applications benefiting from an improved understanding of atmospheric exchange processes over mountains," *Atmosphere*, 9, 371.

De Wekker, S. F. (2008), "Observational and numerical evidence of depressed convective boundary layer heights near a mountain base," *J. Appl. Meteorol. Climatol.*, 47, 1017–1026.

De Wekker, S. F. and Kossmann, M. (2015), "Convective boundary layer heights over mountainous terraina review of concepts," *Front. Earth Sci.*, 3, 77.

De Wekker, S. F. and Mayor, S. D. (2009), "Observations of atmospheric structure and dynamics in the Owens Valley of California with a ground-based, eye-safe, scanning aerosol lidar," *J. Appl. Meteorol. Clim.*, 48, 1483–1499.

De Wekker, S. F., Steyn, D., Fast, J. D., Rotach, M. W., and Zhong, S. (2005), "The performance of RAMS in representing the convective boundary layer structure in a very steep valley," *Environ. Fluid Mech*, 5, 35–62.

Deardorff, J. W. (1972), "Numerical investigation of neutral and unstable planetary boundary layers," *J. Atmos. Sci.*, 29, 91–115.

Detto, M., Katul, G., Mancini, M., Montaldo, N., and Albertson, J. (2008), "Surface heterogeneity and its signature in higher-order scalar similarity relationships," *Agr. Forest Meteorol.*, 148, 902–916.

Dias, N., Gonçalves, J., Freire, L., Hasegawa, T., and Malheiros, A. (2012), "Obtaining potential virtual temperature profiles, entrainment fluxes, and spectra from mini unmanned aerial vehicle data," *Boundary-Layer Meteorol.*, 145, 93–111.

Doyle, J. D., Grubišić, V., Brown, W. O., De Wekker, S. F., Dörnbrack, A., Jiang, Q., Mayor, S. D., and Weissmann, M. (2009), "Observations and numerical simulations of subrotor vortices during T-REX," *J. Atmos. Sci.*, 66, 1229–1249.

Drobinski, P., Carlotti, P., Newsom, R. K., Banta, R. M., Foster, R. C., and Redelsperger, J.-L. (2004), "The structure of the near-neutral atmospheric surface layer," *J. Atmos. Sci.*, 61, 699–714.

Drobinski, P., Carlotti, P., Redelsperger, J.-L., Masson, V., Banta, R. M., and Newsom, R. K. (2007a), "Numerical and experimental investigation of the neutral atmospheric surface layer," *J. Atmos. Sci.*, 64, 137–156.

Drobinski, P., Said, F., Ancellet, G., Arteta, J., Augustin, P., Bastin, S., Brut, A., Caccia, J., Campistron, B., Cautenet, S., et al. (2007b), "Regional transport and dilution during high-pollution episodes in southern France: Summary of findings from the Field Experiment to Constraint Models of Atmospheric Pollution and Emissions Transport (ESCOMPTE)," *J. Geophys. Res. - Atmos.*, 112.

Dudhia, J. (1989), "Numerical study of convection observed during the winter monsoon experiment using a mesoscale two-dimensional model," *J. Atmos. Sci.*, 46, 3077–3107.

Dudhia, J. (1995), "A nonhydrostatic version of the Penn State–NCAR mesoscale model: Validation tests and simulation of an Atlantic cyclone and cold front - Reply," *Mon. Weather Rev.*, 123, 2573–2575.

Duine, G.-J. and De Wekker, S. F. (2017), "The effects of horizontal grid spacing on simulated daytime boundary layer depths in an area of complex terrain in Utah," *Environ. Fluid Mech.*, pp. 1–19.

DOdorico, P., Bhattachan, A., Davis, K. F., Ravi, S., and Runyan, C. W. (2013), "Global desertification: drivers and feedbacks," *Adv. Water Resour.*, 51, 326–344.

Eder, F., Schmidt, M., Damian, T., Träumner, K., and Mauder, M. (2015a), "Mesoscale eddies affect near-surface turbulent exchange: evidence from lidar and tower measurements," *J. Appl. Meteorol. Clim.*, 54, 189–206.

Eder, F., De Roo, F., Rotenberg, E., Yakir, D., Schmid, H. P., and Mauder, M. (2015b), "Secondary circulations at a solitary forest surrounded by semi-arid shrubland and their impact on eddy-covariance measurements," *Agr. Forest Meteorol.*, 211, 115–127.

Etling, D. and Brown, R. (1993), "Roll vortices in the planetary boundary layer: A review," *Boundary-Layer Meteorol.*, 65, 215–248.

Eymard, L. and Weill, A. (1982), "Investigation of clear air convective structures in the PBL using a dual Doppler radar and a Doppler sodar," *J. Appl. Meteor.*, 21, 1891–1906.

Farr, T. G., Rosen, P. A., Caro, E., Crippen, R., Duren, R., Hensley, S., Kobrick, M., Paller, M., Rodriguez, E., Roth, L., et al. (2007), "The shuttle radar topography mission," *Rev. Geophys.*, 45.

Feigenwinter, C. and Vogt, R. (2005), "Detection and analysis of coherent structures in urban turbulence," *Theor. Appl. Climatol.*, 81, 219–230.

Fernando, H., Pardyjak, E., Di Sabatino, S., Chow, F., De Wekker, S., Hoch, S., Hacker, J., Pace, J., Pratt, T., Pu, Z., et al. (2015), "The MATERHORN: Unraveling the intricacies of mountain weather," *Bull. Am. Meteorol. Soc.*, 96, 1945–1967.

Fesquet, C., Drobinski, P., Barthlott, C., and Dubos, T. (2009), "Impact of terrain heterogeneity on near-surface turbulence structure," *Atmos. Res.*, 94, 254–269.

Fiedler, F. and Panofsky, H. A. (1970), "Atmospheric scales and spectral gaps," *Bull. Am. Meteorol. Soc.*, 51, 1114–1120.

Figueroa-Espinoza, B. and Salles, P. (2014), "Local Monin–Obukhov similarity in heterogeneous terrain," *Atmos. Sci. Lett.*, 15, 299–306.

Finnigan, J., Clement, R., Malhi, Y., Leuning, R., and Cleugh, H. (2003), "A re-evaluation of long-term flux measurement techniques part I: averaging and coordinate rotation," *Boundary-Layer Meteorol.*, 107, 1–48.

Foken, T. (2006), "50 years of the Monin–Obukhov similarity theory," *Boundary-Layer Meteorol.*, 119, 431–447.

Foken, T. (2008), "The energy balance closure problem: an overview," *Ecol. Appl.*, 18, 1351–1367.

Foken, T. and Wichura, B. (1996), "Tools for quality assessment of surface-based flux measurements," *Agr. Forest Meteorol.*, 78, 83–105.

Foken, T., Aubinet, M., Finnigan, J. J., Leclerc, M. Y., Mauder, M., and Paw U, K. T. (2011), "Results of a panel discussion about the energy balance closure correction for trace gases," *Bull. Am. Meteorol. Soc.*, 92, ES13–ES18.

Fortuniak, K., Pawlak, W., and Siedlecki, M. (2013), "Integral turbulence statistics over a central European city centre," *Boundary-Layer Meteorol.*, 146, 257–276.

Franssen, H. H., Stöckli, R., Lehner, I., Rotenberg, E., and Seneviratne, S. (2010), "Energy balance closure of eddy-covariance data: A multisite analysis for European FLUXNET stations," *Agr. Forest Meteorol.*, 150, 1553–1567.

Fuhrer, O. and Schär, C. (2007), "Dynamics of orographically triggered banded convection in sheared moist orographic flows," *J. Atmos. Sci.*, 64, 3542–3561.

Gao, W., Shaw, R., and Paw, K. U. (1992), "Conditional analysis of temperature and humidity microfronts and ejection/sweep motions within and above a deciduous forest," *Boundary-Layer Meteorol.*, 59, 35–57.

Gao, Z., Liu, H., Russell, E. S., Huang, J., Foken, T., and Oncley, S. P. (2016), "Large eddies modulating flux convergence and divergence in a disturbed unstable atmospheric surface layer," *J. Geophys. Res. Atmos.*, 121, 1475–1492.

Gao, Z., Liu, H., Katul, G. G., and Foken, T. (2017), "Non-closure of the surface energy balance explained by phase difference between vertical velocity and scalars of large atmospheric eddies," *Environ. Res. Lett.*, 12, 034025.

Gao, Z., Liu, H., Li, D., Katul, G. G., and Blanken, P. D. (2018), "Enhanced temperature-humidity similarity caused by entrainment processes with increased wind shear," *J. Geophys. Res. Atmos.*

Garai, A. and Kleissl, J. (2011), "Air and surface temperature coupling in the convective atmospheric boundary layer," *J. Atmos. Sci.*, 68, 2945–2954.

Garai, A., Pardyjak, E., Steeneveld, G.-J., and Kleissl, J. (2013), "Surface temperature and surface-layer turbulence in a convective boundary layer," *Boundary-Layer Meteorol.*, 148, 51–72.

Georg, W., Albin, H., Georg, N., Katharina, S., Enrico, T., and Peng, Z. (2016), "On the energy balance closure and net radiation in complex terrain," *Agr. Forest Meteorol.*, 226, 37–49.

Ghannam, K., Katul, G. G., Bou-Zeid, E., Gerken, T., and Chamecki, M. (2018), "Scaling and similarity of the anisotropic coherent eddies in near-surface atmospheric turbulence," *J. Atmos. Sci.*, 75, 943–964.

Gibbs, J. A. and Fedorovich, E. (2014), "Comparison of convective boundary layer velocity spectra retrieved from large-eddy-simulation and weather research and forecasting model data," *J. Appl. Meteorol. Climatol.*, 53, 377–394.

Gibbs, J. A., Fedorovich, E., and Van Eijk, A. M. (2011), "Evaluating Weather Research and Forecasting (WRF) model predictions of turbulent flow parameters in a dry convective boundary layer," *J. Appl. Meteorol. Climatol.*, 50, 2429–2444.

Gobiet, A., Kotlarski, S., Beniston, M., Heinrich, G., Rajczak, J., and Stoffel, M. (2014), "21st century climate change in the European Alps - A review," *Sci. Total Environ.*, 493, 1138–1151.

Grachev, A. and Fairall, C. (1997), "Dependence of the Monin-Obukhov stability parameter on the bulk Richardson number over the ocean," *J. Appl. Meteorol.*, 36, 406–414.

Grachev, A. A., Fairall, C. W., Persson, P. O. G., Andreas, E. L., and Guest, P. S. (2005), "Stable boundary-layer scaling regimes: The SHEBA data," *Boundary-Layer Meteorol.*, 116, 201–235.

Grachev, A. A., Andreas, E. L., Fairall, C. W., Guest, P. S., and Persson, P. O. G. (2007a), "On the turbulent Prandtl number in the stable atmospheric boundary layer," *Boundary-Layer Meteorol.*, 125, 329–341.

Grachev, A. A., Andreas, E. L., Fairall, C. W., Guest, P. S., and Persson, P. O. G. (2007b), "SHEBA flux–profile relationships in the stable atmospheric boundary layer," *Boundary-Layer Meteorol.*, 124, 315–333.

Grachev, A. A., Andreas, E. L., Fairall, C. W., Guest, P. S., and Persson, P. O. G. (2013), "The critical Richardson number and limits of applicability of local similarity theory in the stable boundary layer," *Boundary-Layer Meteorol.*, 147, 51–82.

Gray, W. M., Landsea, C. W., Mielke Jr, P. W., and Berry, K. J. (1993), "Predicting Atlantic basin seasonal tropical cyclone activity by 1 August," *Weather Forecast.*, 8, 73–86.

Grisogono, B. and Belušić, D. (2009), "A review of recent advances in understanding the meso- and microscale properties of the severe Bora wind," *Tellus A*, 61, 1–16.

Grubišić, V., Doyle, J. D., Kuettner, J., Mobbs, S., Smith, R. B., Whiteman, C. D., Dirks, R., Czyzyk, S., Cohn, S. A., Vosper, S., et al. (2008), "The Terrain-Induced Rotor Experiment: A field campaign overview including observational highlights," *Bull. Am. Meteorol. Soc.*, 89, 1513–1534.

Hahnenberger, M. and Nicoll, K. (2012), "Meteorological characteristics of dust storm events in the eastern Great Basin of Utah, USA," *Atmos. Environ.*, 60, 601–612.

Hammerle, A., Haslwanter, A., Schmitt, M., Bahn, M., Tappeiner, U., Cernusca, A., and Wohlfahrt, G. (2007), "Eddy covariance measurements of carbon dioxide, latent and sensible energy fluxes above a meadow on a mountain slope," *Boundary-Layer Meteorol.*, 122, 397–416.

Hang, C., Nadeau, D. F., Jensen, D. D., Hoch, S. W., and Pardyjak, E. R. (2016), "Playa soil moisture and evaporation dynamics during the MATERHORN field program," *Boundary-Layer Meteorol.*, 159, 521–538.

Head, M. and Bandyopadhyay, P. (1981), "New aspects of turbulent boundary-layer structure," *J. Fluid Mech.*, 107, 297–338.

Heath, N. K., Fuelberg, H. E., Tanelli, S., Turk, F. J., Lawson, R. P., Woods, S., and Freeman, S. (2017), "WRF nested large-eddy simulations of deep convection during SEAC4RS," *J. Geophys. Res. Atmos.*, 122, 3953–3974.

Heinze, R., Dipankar, A., Henken, C. C., Moseley, C., Sourdeval, O., Trömel, S., Xie, X., Adamidis, P., Ament, F., Baars, H., et al. (2017), "Large-eddy simulations over Germany using ICON: a comprehensive evaluation," *Q. J. R. Meteorol. Soc.*, 143, 69–100.

Henne, S., Furger, M., and Prévôt, A. H. (2005), "Climatology of mountain venting-induced elevated moisture layers in the lee of the Alps," *J. Appl. Meteorol.*, 44, 620–633.

Heo, B.-H., Jacoby-Koaly, S., Kim, K.-E., Campistron, B., Benech, B., and Jung, E.-S. (2003), "Use of the Doppler spectral width to improve the estimation of the convective boundary layer height from UHF wind profiler observations," *J. Atmos. Ocean. Tech.*, 20, 408–424.

Hertenstein, R. F. and Kuettner, J. P. (2005), "Rotor types associated with steep lee topography: Influence of the wind profile," *Tellus A*, 57, 117–135.

Heusinkveld, B., Jacobs, A., Holtslag, A., and Berkowicz, S. (2004), "Surface energy balance closure in an arid region: role of soil heat flux," *Agr. Forest Meteorol.*, 122, 21–37.

Hiller, R., Zeeman, M. J., and Eugster, W. (2008), "Eddy-covariance flux measurements in the complex terrain of an Alpine valley in Switzerland," *Boundary-Layer Meteorol.*, 127, 449–467.

Hocut, C., Liberzon, D., and Fernando, H. (2015), "Separation of upslope flow over a uniform slope," *J. Fluid Mech.*, 775, 266–287.

Högström, U. (1996), "Review of some basic characteristics of the atmospheric surface layer," *Boundary-Layer Meteorol.*, 78, 215–246.

Holzworth, G. C. (1964), "Estimates of mean maximum mixing depths in the contiguous United States," *Mon. Weather Rev.*, 92, 235–242.

Hong, S.-Y., Noh, Y., and Dudhia, J. (2006), "A new vertical diffusion package with an explicit treatment of entrainment processes," *Mon. Weather Rev.*, 134, 2318–2341.

Horst, T. and Oncley, S. (2006), "Corrections to inertial-range power spectra measured by CSAT3 and Solent sonic anemometers, 1. Path-averaging errors," *Boundary-Layer Meteorol.*, 119, 375–395.

Horst, T., Semmer, S., and Maclean, G. (2015), "Correction of a non-orthogonal, three-component sonic anemometer for flow distortion by transducer shadowing," *Boundary-Layer Meteorol.*, 155, 371–395.

Howell, J. and Mahrt, L. (1997), "Multiresolution flux decomposition," *Boundary-Layer Meteorol.*, 83, 117–137.

Huang, N. E., Shen, Z., Long, S. R., Wu, M. C., Shih, H. H., Zheng, Q., Yen, N.-C., Tung, C. C., and Liu, H. H. (1998), "The empirical mode decomposition and the Hilbert spectrum for nonlinear and non-stationary time series analysis," *P. Roy. Soc. Lond. A Mat.*, 454, 903–995.

Huang, Q., Marsham, J. H., Parker, D. J., Tian, W., and Weckwerth, T. (2009), "A comparison of roll and nonroll convection and the subsequent deepening moist convection: An LEM case study based on SCMS data," *Mon. Weather Rev.*, 137, 350–365.

Hunt, J. and Carlotti, P. (2001), "Statistical structure at the wall of the high Reynolds number turbulent boundary layer," *Flow Turbul. Combust.*, 66, 453–475.

Hunt, J. C. and Morrison, J. F. (2000), "Eddy structure in turbulent boundary layers," *Eur. J. Mech. B-Fluid.*, 19, 673–694.

Hutchins, N. and Marusic, I. (2007), "Evidence of very long meandering features in the logarithmic region of turbulent boundary layers," *J. Fluid Mech.*, 579, 1–28.

Inagaki, A., Kanda, M., Ahmad, N. H., Yagi, A., Onodera, N., and Aoki, T. (2017), "A numerical study of turbulence statistics and the structure of a spatially-developing boundary layer over a realistic urban geometry," *Boundary-Layer Meteorol.*, 164, 161–181.

Jeglum, M. E. and Hoch, S. W. (2016), "Multiscale characteristics of surface winds in an area of complex terrain in northwest Utah," *J. Appl. Meteorol. Clim.*, 55, 1549–1563.

Jensen, D. D., Nadeau, D. F., Hoch, S. W., and Pardyjak, E. R. (2016), "Observations of near-surface heat-flux and temperature profiles through the early evening transition over contrasting surfaces," *Boundary-Layer Meteorol.*, 159, 567–587.

Jensen, D. D., Nadeau, D. F., Hoch, S. W., and Pardyjak, E. R. (2017), "The evolution and sensitivity of katabatic flow dynamics to external influences through the evening transition," *Q. J. R. Meteorol. Soc.*, 143, 423–438.

Jiang, Q., Doyle, J. D., and Smith, R. B. (2006), "Interaction between trapped waves and boundary layers," *J. Atmos. Sci.*, 63, 617–633.

Jiménez, P. A., Dudhia, J., González-Rouco, J. F., Navarro, J., Montávez, J. P., and García-Bustamante, E. (2012), "A revised scheme for the WRF surface layer formulation," *Mon. Weather Rev.*, 140, 898–918.

Jirak, I. L. and Cotton, W. R. (2006), "Effect of air pollution on precipitation along the Front Range of the Rocky Mountains," *J. Appl. Meteorol. Clim.*, 45, 236–245.

Johansson, C., Smedman, A.-S., Högström, U., Brasseur, J. G., and Khanna, S. (2001), "Critical test of the validity of Monin–Obukhov similarity during convective conditions," *J. Atmos. Sci.*, 58, 1549–1566.

Kaimal, J. and Businger, J. (1970), "Case studies of a convective plume and a dust devil," *J. Appl. Meteorol.*, 9, 612–620.

Kaimal, J., Wyngaard, J., Izumi, Y., and Coté, O. (1972), "Spectral characteristics of surface-layer turbulence," *Q. J. R. Meteorol. Soc.*, 98, 563–589.

Kaimal, J., Eversole, R., Lenschow, D., Stankov, B., Kahn, P., and Businger, J. (1982), "Spectral characteristics of the convective boundary layer over uneven terrain," *J. Atmos. Sci.*, 39, 1098–1114.

Kaimal, J. C. and Finnigan, J. J. (1994), *Atmospheric boundary layer flows: their structure and measurement*, Oxford university press.

Kain, J. S. (2004), "The Kain–Fritsch convective parameterization: an update," *J. Appl. Meteor.*, 43, 170–181.

Kalverla, P. C., Duine, G.-J., Steeneveld, G.-J., and Hedde, T. (2016), "Evaluation of the Weather Research and Forecasting model in the Durance Valley complex terrain during the KASCADE field campaign," *J. Appl. Meteorol. Climatol.*, 55, 861–882.

Kanda, M., Inagaki, A., Letzel, M. O., Raasch, S., and Watanabe, T. (2004), "LES study of the energy imbalance problem with eddy covariance fluxes," *Boundary-Layer Meteorol.*, 110, 381–404.

Kanda, M., Moriwaki, R., and Kasamatsu, F. (2006), "Spatial variability of both turbulent fluxes and temperature profiles in an urban roughness layer," *Boundary-Layer Meteorol.*, 121, 339–350.

Kang, S.-L. (2009), "Temporal oscillations in the convective boundary layer forced by mesoscale surface heat-flux variations," *Boundary-Layer Meteorol.*, 132, 59–81.

Katul, G., Hsieh, C.-I., Bowling, D., Clark, K., Shurpali, N., Turnipseed, A., Albertson, J., Tu, K., Hollinger, D., Evans, B., et al. (1999), "Spatial variability of turbulent fluxes in the roughness sublayer of an even-aged pine forest," *Boundary-Layer Meteorol.*, 93, 1–28.

Katul, G. G., Albertson, J., Parlange, M., Chu, C.-R., and Stricker, H. (1994), "Conditional sampling, bursting, and the intermittent structure of sensible heat flux," *J. Geophys. Res. Atmos.*, 99, 22869–22876.

Katul, G. G., Parlange, M. B., Albertson, J. D., and Chu, C. R. (1995), "Local isotropy and anisotropy in the sheared and heated atmospheric surface layer," *Boundary-Layer Meteorol.*, 72, 123–148.

Katul, G. G., Schieldge, J., Hsieh, C.-I., and Vidakovic, B. (1998), "Skin temperature perturbations induced by surface layer turbulence above a grass surface," *Water Resour. Res.*, 34, 1265–1274.

Kelly, R. D. (1984), "Horizontal roll and boundary-layer interrelationships observed over Lake Michigan," *J. Atmos. Sci.*, 41, 1816–1826.

Khanna, S. and Brasseur, J. G. (1998), "Three-dimensional buoyancy-and shear-induced local structure of the atmospheric boundary layer," *J. Atmos. Sci.*, 55, 710–743.

Kirschbaum, D., Adler, R., Adler, D., Peters-Lidard, C., and Huffman, G. (2012), "Global distribution of extreme precipitation and high-impact landslides in 2010 relative to previous years," *J. Hydrometeorol.*, 13, 1536–1551.

Kline, S. J., Reynolds, W. C., Schraub, F., and Runstadler, P. (1967), "The structure of turbulent boundary layers," *J. Fluid Mech.*, 30, 741–773.

Klipp, C. (2014), "Turbulence Anisotropy in the Near-Surface Atmosphere and the Evaluation of Multiple Outer Length Scales," *Boundary-Layer Meteorol.*, 151, 57–77.

Klipp, C. L. and Mahrt, L. (2004), "Flux–gradient relationship, self-correlation and intermittency in the stable boundary layer," *Q J R Meteorol Soc*, 130, 2087–2103.

Kolmogorov, A. N. (1941), "The local structure of turbulence in incompressible viscous fluid for very large Reynolds numbers," *Dokl. Akad. Nauk SSSR*, 30, 299–303.

Kral, S. T., Sjöblom, A., and Nygård, T. (2014), "Observations of summer turbulent surface fluxes in a High Arctic fjord," *Q. J. R. Meteorol. Soc.*, 140, 666–675.

Kristensen, L. (2000), "Measuring higher-order moments with a cup anemometer," *J. Atmos. Ocean. Tech.*, 17, 1139–1148.

Krusche, N. and De Oliveira, A. P. (2004), "Characterization of coherent structures in the atmospheric surface layer," *Boundary-Layer Meteorol.*, 110, 191–211.

Kuettner, J. P. (1971), "Cloud bands in the earth's atmosphere: Observations and theory," *Tellus*, 23, 404–426.

Lamaud, E. and Irvine, M. (2006), "Temperature–humidity dissimilarity and heat-to-water-vapour transport efficiency above and within a pine forest canopy: the role of the Bowen ratio," *Boundary-Layer Meteorol.*, 120, 87–109.

Lareau, N. P., Crosman, E., Whiteman, C. D., Horel, J. D., Hoch, S. W., Brown, W. O., and Horst, T. W. (2013), "The persistent cold-air pool study," *Bull. Am. Meteorol. Soc.*, 94, 51–63.

Larsén, X. G., Larsen, S. E., and Petersen, E. L. (2016), "Full-scale spectrum of boundary-layer winds," *Boundary-Layer Meteorol.*, 159, 349–371.

Laubach, J. and McNaughton, K. G. (2009), "Scaling properties of temperature spectra and heat-flux cospectra in the surface friction layer beneath an unstable outer layer," *Boundary-Layer Meteorol.*, 133, 219–252.

Lee, T. R. and De Wekker, S. F. (2016), "Estimating daytime planetary boundary layer heights over a valley from rawinsonde observations at a nearby airport: an application to the Page Valley in Virginia, United States," *J. Appl. Meteorol. Climatol.*, 55, 791–809.

Lee, X., Massman, W., and Law, B. E. (2006), *Handbook of micrometeorology: a guide for surface flux measurement and analysis*, vol. 29, Springer Science & Business Media.

Lehner, M. and Rotach, M. (2018), "Current challenges in understanding and predicting transport and exchange in the atmosphere over mountainous terrain," *Atmosphere*, 9, 276.

Lehner, M., Whiteman, C. D., Hoch, S. W., Jensen, D., Pardyjak, E. R., Leo, L. S., Di Sabatino, S., and Fernando, H. J. (2015), "A case study of the nocturnal boundary layer evolution on a slope at the foot of a desert mountain," *J. Appl. Meteorol. Clim.*, 54, 732–751.

Lemone, M. A. (1973), "The structure and dynamics of horizontal roll vortices in the planetary boundary layer," *J. Atmos. Sci.*, 30, 1077–1091.

Lemone, M. A. (1976), "Modulation of turbulence energy by longitudinal rolls in an unstable planetary boundary layer," *J. Atmos. Sci.*, 33, 1308–1320.

LeMone, M. A., Chen, F., Tewari, M., Dudhia, J., Geerts, B., Miao, Q., Coulter, R. L., and Grossman, R. L. (2010), "Simulating the IHOP_2002 fair-weather CBL with the WRF-ARW–Noah modeling system. Part II: Structures from a few kilometers to 100 km across," *Mon. Weather Rev.*, 138, 745–764.

LeMone, M. A., Tewari, M., Chen, F., and Dudhia, J. (2013), "Objectively determined fair-weather CBL depths in the ARW-WRF model and their comparison to CASES-97 observations," *Mon. Weather Rev.*, 141, 30–54.

Lenschow, D., Mann, J., and Kristensen, L. (1994), "How long is long enough when measuring fluxes and other turbulence statistics?" *J. Atmos. Ocean. Tech.*, 11, 661–673.

Leukauf, D., Gohm, A., and Rotach, M. W. (2016), "Quantifying horizontal and vertical tracer mass fluxes in an idealized valley during daytime," *Atmos. Chem. Phys.*, 16, 13049–13066.

Leuning, R., Van Gorsel, E., Massman, W. J., and Isaac, P. R. (2012), "Reflections on the surface energy imbalance problem," *Agr. Forest Meteorol.*, 156, 65–74.

Li, D. and Bou-Zeid, E. (2011), "Coherent structures and the dissimilarity of turbulent transport of momentum and scalars in the unstable atmospheric surface layer," *Boundary-Layer Meteorol.*, 140, 243–262.

Li, D., Bou-Zeid, E., and De Bruin, H. A. (2012), "Monin–Obukhov similarity functions for the structure parameters of temperature and humidity," *Boundary-Layer Meteorol.*, 145, 45–67.

Li, Q., Gentine, P., Mellado, J. P., and McColl, K. A. (2018), "Implications of Nonlocal Transport and Conditionally Averaged Statistics on Monin–Obukhov Similarity Theory and Townsends Attached Eddy Hypothesis," *J. Atmos. Sci.*, 75, 3403–3431.

Liang, J., Zhang, L., Wang, Y., Cao, X., Zhang, Q., Wang, H., and Zhang, B. (2014), "Turbulence regimes and the validity of similarity theory in the stable boundary layer over complex terrain of the Loess Plateau, China," *J. Geophys. Res. - Atmos.*, 119, 6009–6021.

Liang, J., Zhang, L., Cao, X., Wen, J., Wang, J., and Wang, G. (2017), "Energy balance in the semiarid area of the Loess Plateau, China," *J. Geophys. Res. Atmos.*, 122, 2155–2168.

Litt, M., Sicart, J.-E., Helgason, W. D., and Wagnon, P. (2015), "Turbulence Characteristics in the Atmospheric Surface Layer for Different Wind Regimes over the Tropical Zongo Glacier (Bolivia, 16 deg S)," *Boundary-Layer Meteorol.*, 154, 471–495.

Liu, L., Hu, F., and Cheng, X.-L. (2011), "Probability density functions of turbulent velocity and temperature fluctuations in the unstable atmospheric surface layer," *J. Geophys. Res. - Atmos.*, 116.

Lohou, F., Druilhet, A., and Campistron, B. (1998), "Spatial and temporal characteristics of horizontal rolls and cells in the atmospheric boundary layer based on radar and in situ observations," *Boundary-Layer Meteorol.*, 89, 407–444.

Long, D. and Singh, V. P. (2010), "Integration of the GG model with SEBAL to produce time series of evapotranspiration of high spatial resolution at watershed scales," *J. Geophys. Res. Atmos.*, 115.

Lotfy, E. R. and Harun, Z. (2018), "Effect of atmospheric boundary layer stability on the inclination angle of turbulence coherent structures," *Environ. Fluid Mech.*, 18, 637–659.

Lumley, J. L. and Panofsky, H. A. (1964), "The structure of atmospheric turbulence," *Boundary-Layer Meteorol.*

Lundquist, J. K. (2003), "Intermittent and elliptical inertial oscillations in the atmospheric boundary layer," *J. Atmos. Sci.*, 60, 2661–2673.

Maestre, F. T., Eldridge, D. J., Soliveres, S., Kéfi, S., Delgado-Baquerizo, M., Bowker, M. A., García-Palacios, P., Gaitán, J., Gallardo, A., Lázaro, R., et al. (2016), "Structure and functioning of dryland ecosystems in a changing world," *Annu. Rev. Ecol. Evol. S.*, 47, 215–237.

Magnago, R., Moraes, O., and Acevedo, O. (2009), "Turbulence velocity spectra dependence on the mean wind at the bottom of a valley," *Physica A*, 388, 1908–1916.

Mahrt, L. (1991), "Boundary-layer moisture regimes," *Q. J. R. Meteorol. Soc.*, 117, 151–176.

Mahrt, L. (1998), "Flux sampling errors for aircraft and towers," *J. Atmos. Ocean. Tech.*, 15, 416–429.

Mahrt, L. (2007), "The influence of nonstationarity on the turbulent flux–gradient relationship for stable stratification," *Boundary-Layer Meteorol.*, 125, 245–264.

Mahrt, L. and Howell, J. (1994), "The influence of coherent structures and microfronts on scaling laws using global and local transforms," *J. Fluid Mech.*, 260, 247–270.

Mahrt, L., Sun, J., Blumen, W., Delany, T., and Oncley, S. (1998), "Nocturnal boundary-layer regimes," *Boundary-Layer Meteorol.*, 88, 255–278.

Marques Filho, E. P., Sa, L. D. A., Karam, H., Alvala, R., Souza, A., and Pereira, M. (2008), "Atmospheric surface layer characteristics of turbulence above the Pantanal wetland regarding the similarity theory," *Agr. Forest Meteorol.*, 148, 883–892.

Martins, C. A., Moraes, O. L., Acevedo, O. C., and Degrazia, G. A. (2009), "Turbulence intensity parameters over a very complex terrain," *Boundary-Layer Meteorol.*, 133, 35–45.

Marusic, I. and Heuer, W. D. (2007), "Reynolds number invariance of the structure inclination angle in wall turbulence," *Phys. Rev. Lett.*, 99, 114504.

Mason, R. A., Shirer, H. N., Wells, R., and Young, G. S. (2002), "Vertical transports by plumes within the moderately convective marine atmospheric surface layer," *J. Atmos. Sci.*, 59, 1337–1355.

Massey, J. D., Steenburgh, W. J., Hoch, S. W., and Knievel, J. C. (2014), "Sensitivity of near-surface temperature forecasts to soil properties over a sparsely vegetated dryland region," *J. Appl. Meteorol. Climatol.*, 53, 1976–1995.

Massey, J. D., Steenburgh, W. J., Knievel, J. C., and Cheng, W. Y. (2016), "Regional soil moisture biases and their influence on WRF model temperature forecasts over the Intermountain West," *Weather Forecast.*, 31, 197–216.

Massman, W. J. (2000), "A simple method for estimating frequency response corrections for eddy covariance systems," *Agr. Forest Meteorol.*, 104, 185–198.

Massman, W. J. (2001), "Reply to comment by Rannik on "A simple method for estimating frequency response corrections for eddy covariance systems"," *Agr. Forest Meteorol.*, 107, 247–251.

Matzinger, N., Andretta, M., Gorsel, E. V., Vogt, R., Ohmura, A., and Rotach, M. (2003), "Surface radiation budget in an Alpine valley," *Q. J. R. Meteorol. Soc.*, 129, 877–895.

Mazzaro, L. J., Muñoz-Esparza, D., Lundquist, J. K., and Linn, R. R. (2017), "Nested mesoscale-to-LES modeling of the atmospheric boundary layer in the presence of underresolved convective structures," *J. Adv. Model. Earth Syst.*

McColl, K. A., van Heerwaarden, C. C., Katul, G. G., Gentine, P., and Entekhabi, D. (2017), "Role of large eddies in the breakdown of the Reynolds analogy in an idealized mildly unstable atmospheric surface layer," *Q. J. R. Meteorol. Soc.*, 143, 2182–2197.

McGloin, R., Šigut, L., Havránková, K., Dušek, J., Pavelka, M., and Sedlák, P. (2018), "Energy balance closure at a variety of ecosystems in Central Europe with contrasting topographies," *Agr. Forest Meteorol.*, 248, 418–431.

McNaughton, K. (2004a), "Attached eddies and production spectra in the atmospheric logarithmic layer," *Boundary-Layer Meteorol.*, 111, 1–18.

McNaughton, K. (2004b), "Turbulence structure of the unstable atmospheric surface layer and transition to the outer layer," *Boundary-Layer Meteorol.*, 112, 199–221.

McNaughton, K., Clement, R., and Moncrieff, J. (2007), "Scaling properties of velocity and temperature spectra above the surface friction layer in a convective atmospheric boundary layer," *Nonlinear Proc. Geoph.*, 14, 257–271.

Melfi, S. and Palm, S. P. (2012), "Estimating the orientation and spacing of midlatitude linear convective boundary layer features: Cloud streets," *J. Atmos. Sci.*, 69, 352–364.

Metzger, M. and Holmes, H. (2008), "Time scales in the unstable atmospheric surface layer," *Boundary-Layer Meteorol.*, 126, 29–50.

Metzger, M., McKeon, B., and Holmes, H. (2007), "The near-neutral atmospheric surface layer: turbulence and non-stationarity," *Proc. Roy. Soc. London A*, 365, 859–876.

Meybeck, M., Green, P., and Vörösmarty, C. (2001), "A new typology for mountains and other relief classes: an application to global continental water resources and population distribution," *Mt. Res. Dev.*, 21, 34–45.

Meyers, M. P. and Steenburgh, W. J. (2013), "Mountain weather prediction: phenomenological challenges and forecast methodology," in *Mountain Weather Research and Forecasting*, pp. 1–34, Springer.

Miao, S. and Chen, F. (2008), "Formation of horizontal convective rolls in urban areas," *Atmos. Res.*, 89, 298–304.

Michioka, T. and Chow, F. K. (2008), "High-resolution large-eddy simulations of scalar transport in atmospheric boundary layer flow over complex terrain," *J. Appl. Meteorol. Climatol.*, 47, 3150–3169.

Miura, Y. (1986), "Aspect ratios of longitudinal rolls and convection cells observed during cold air outbreaks," *J. Atmos. Sci.*, 43, 26–39.

Mlawer, E. J., Taubman, S. J., Brown, P. D., Iacono, M. J., and Clough, S. A. (1997), "Radiative transfer for inhomogeneous atmospheres: RRTM, a validated correlated-k model for the longwave," *J. Geophys. Res. Atmos.*, 102, 16663–16682.

Moderow, U., Feigenwinter, C., and Bernhofer, C. (2007), "Estimating the components of the sensible heat budget of a tall forest canopy in complex terrain," *Boundary-Layer Meteorol.*, 123, 99–120.

Moeng, C.-H. (1984), "A large-eddy-simulation model for the study of planetary boundary-layer turbulence," *J. Atmos. Sci.*, 41, 2052–2062.

Moeng, C.-H. and Sullivan, P. P. (1994), "A comparison of shear-and buoyancy-driven planetary boundary layer flows," *J. Atmos. Sci.*, 51, 999–1022.

Monin, A. and Obukhov, A. (1954), "Basic laws of turbulent mixing in the surface layer of the atmosphere," *Contrib. Geophys. Inst. Acad. Sci. USSR*, 151, 163–187.

Monin, A. and Yaglom, A. (1975), "Statistical fluid mechanics: Mechanics of turbulence, 874 pp," .

Moraes, O. L., Acevedo, O. C., Degrazia, G. A., Anfossi, D., da Silva, R., and Anabor, V. (2005), "Surface layer turbulence parameters over a complex terrain," *Atmos. Environ.*, 39, 3103–3112.

Morrison, H., Thompson, G., and Tatarskii, V. (2009), "Impact of cloud microphysics on the development of trailing stratiform precipitation in a simulated squall line: Comparison of one- and two-moment schemes," *Mon. Weather Rev.*, 137, 991–1007.

Müller, G. and Chlond, A. (1996), "Three-dimensional numerical study of cell broadening during cold-air outbreaks," *Boundary-Layer Meteorol.*, 81, 289–323.

Muñoz-Esparza, D. and Kosović, B. (2018), "Generation of inflow turbulence in large-eddy simulations of non-neutral atmospheric boundary layers with the cell perturbation method," *Mon. Weather Rev.*, 146, 1889–1909.

Muñoz-Esparza, D., Kosović, B., Mirocha, J., and van Beeck, J. (2014), "Bridging the transition from mesoscale to microscale turbulence in numerical weather prediction models," *Boundary-Layer Meteorol.*, 153, 409–440.

Muñoz-Esparza, D., Lundquist, J. K., Sauer, J. A., Kosović, B., and Linn, R. R. (2017), "Coupled mesoscale-LES modeling of a diurnal cycle during the CWEX-13 field campaign: From weather to boundary-layer eddies," *J. Adv. Model. Earth Syst.*, 9, 1572–1594.

Nadeau, D. F., Pardyjak, E. R., Higgins, C. W., and Parlange, M. B. (2013), "Similarity scaling over a steep alpine slope," *Boundary-Layer Meteorol.*, 147, 401–419.

Nadeau, D. F., Oldroyd, H. J., Pardyjak, E. R., Sommer, N., Hoch, S. W., and Parlange, M. B. (2018), "Field observations of the morning transition over a steep slope in a narrow alpine valley," *Environ. Fluid Mech.*, pp. 1–22.

Nakamura, R. and Mahrt, L. (2001), "Similarity theory for local and spatially averaged momentum fluxes," *Agr. Forest Meteorol.*, 108, 265–279.

Nieuwstadt, F. T. (1984), "The turbulent structure of the stable, nocturnal boundary layer," *J. Atmos Sci.*, 41, 2202–2216.

Nogués-Bravo, D., Araújo, M. B., Errea, M., and Martinez-Rica, J. (2007), "Exposure of global mountain systems to climate warming during the 21st Century," *Global Environ. Chang.*, 17, 420–428.

Nordbo, A., Järvi, L., Haapanala, S., Moilanen, J., and Vesala, T. (2013), "Intra-city variation in urban morphology and turbulence structure in Helsinki, Finland," *Boundary-Layer Meteorol.*, 146, 469–496.

Nuissier, O., Ducrocq, V., Ricard, D., Lebeaupin, C., and Anquetin, S. (2008), "A numerical study of three catastrophic precipitating events over southern France. I: Numerical framework and synoptic ingredients," *Q. J. R. Meteorol. Soc.*, 134, 111–130.

Obukhov, A. (1946), "Turbulence in an atmosphere with a non-uniform temperature," *Trudy Inst. Theor. Geofiz. AN SSSR*, 1, 95–115.

Oldroyd, H. J., Pardyjak, E. R., Huwald, H., and Parlange, M. B. (2016), "Adapting tilt corrections and the governing flow equations for steep, fully three-dimensional, mountainous terrain," *Boundary-Layer Meteorol.*, 159, 539–565.

Oncley, S. P., Friehe, C. A., Larue, J. C., Businger, J. A., Itsweire, E. C., and Chang, S. S. (1996), "Surface-layer fluxes, profiles, and turbulence measurements over uniform terrain under near-neutral conditions," *J. Atmos. Sci.*, 53, 1029–1044.

Oncley, S. P., Foken, T., Vogt, R., Kohsiek, W., DeBruin, H., Bernhofer, C., Christen, A., Van Gorsel, E., Grantz, D., Feigenwinter, C., et al. (2007), "The energy balance experiment EBEX-2000. Part I: overview and energy balance," *Boundary-Layer Meteorol.*, 123, 1–28.

Oncley, S. P., Hartogensis, O., and Tong, C. (2016), "Whirlwinds and Hairpins in the Atmospheric Surface Layer," *J. Atmos. Sci.*, 73, 4927–4943.

Pahlow, M., Parlange, M. B., and Porté-Agel, F. (2001), "On Monin–Obukhov similarity in the stable atmospheric boundary layer," *Boundary-Layer Meteorol.*, 99, 225–248.

Panofsky, H., Larko, D., Lipschutz, R., Stone, G., Bradley, E., Bowen, A. J., and Højstrup, J. (1982), "Spectra of velocity components over complex terrain," *Q. J. R. Meteorol. Soc.*, 108, 215–230.

Panofsky, H. A. and Dutton, J. A. (1984), "Atmospheric turbulence: models and methods for engineering aplications," in *Atmospheric turbulence: models and methods for engineering aplications*, John Wiley & Sons.

Parsons, D., Dabberdt, W., Cole, H., Hock, T., Martin, C., Barrett, A.-L., Miller, E., Spowart, M., Howard, M., Ecklund, W., et al. (1994), "The integrated sounding system: Description and preliminary observations from TOGA COARE," *Bull. Am. Meteorol. Soc.*, 75, 553–567.

Patton, E. G., Sullivan, P. P., and Moeng, C.-H. (2005), "The influence of idealized heterogeneity on wet and dry planetary boundary layers coupled to the land surface," *J. Atmos. Sci.*, 62, 2078–2097.

Pegahfar, N. and Bidokhti, A. (2013), "Similarity relations in a stable and relatively neutral surface layer in an urban area with complex topography (Tehran)," *Environ. Fluid Mech.*, 13, 1–31.

Pepin, N., Bradley, R., Diaz, H., Baraër, M., Caceres, E., Forsythe, N., Fowler, H., Greenwood, G., Hashmi, M., Liu, X., et al. (2015), "Elevation-dependent warming in mountain regions of the world," *Nat. Clim. Change*, 5, 424–430.

Phong-Anant, D., Antonia, R., Chambers, A., and Rajagopalan, S. (1980), "Features of the organized motion in the atmospheric surface layer," *J. Geophys. Res. Oceans*, 85, 424–432.

Piper, M. and Lundquist, J. K. (2004), "Surface layer turbulence measurements during a frontal passage," *J. Atmos. Sci.*, 61, 1768–1780.

Potužníková, K., Sedlák, P., and Knížová, P. K. (2015), "Detection of low-frequency organized structures in night-time air flow within a spruce canopy on the upwind and downwind sides of a mountain ridge," *Atmos. Sci. Lett.*, 16, 432–437.

Poulos, G. S., Blumen, W., Fritts, D. C., Lundquist, J. K., Sun, J., Burns, S. P., Nappo, C., Banta, R., Newsom, R., Cuxart, J., et al. (2002), "CASES-99: A comprehensive investigation of the stable nocturnal boundary layer," *Bull. Am. Meteorol. Soc.*, 83, 555–582.

Powers, J. G., Klemp, J. B., Skamarock, W. C., Davis, C. A., Dudhia, J., Gill, D. O., Coen, J. L., Gochis, D. J., Ahmadov, R., Peckham, S. E., et al. (2017), "The Weather Research and Forecasting model: Overview, system efforts, and future directions," *Bull. Am. Meteorol. Soc.*, 98, 1717–1737.

Prandtl, L. (1942), "Bemerkungen zur Theorie der freien Turbulenz." *ZAMM-Journal of Applied Mathematics and Mechanics/Zeitschrift für Angewandte Mathematik und Mechanik*, 22, 241–243.

Quan, L. and Hu, F. (2009), "Relationship between turbulent flux and variance in the urban canopy," *Meteorol. Atmos. Phys.*, 104, 29–36.

Rai, R. K., Berg, L. K., Kosović, B., Mirocha, J. D., Pekour, M. S., and Shaw, W. J. (2017a), "Comparison of measured and numerically simulated turbulence statistics in a convective boundary layer over complex terrain," *Boundary-Layer Meteorol.*, 163, 69–89.

Rai, R. K., Berg, L. K., Pekour, M., Shaw, W. J., Kosovic, B., Mirocha, J. D., and Ennis, B. L. (2017b), "Spatiotemporal Variability of Turbulence Kinetic Energy Budgets in the Convective Boundary Layer over Both Simple and Complex Terrain," *J. Appl. Meteorol. Climatol.*, 56, 3285–3302.

Reuten, C., Steyn, D., Strawbridge, K., and Bovis, P. (2005), "Observations of the relation between upslope flows and the convective boundary layer in steep terrain," *Boundary-Layer Meteorol.*, 116, 37–61.

Reynolds, O. (1894), "On the dynamical theory of incompressible viscous fluids and the determination of the criterion." *P. Roy. Soc. London*, 56, 40–45.

Robinson, S. K. (1991), "Coherent motions in the turbulent boundary layer," *Annu. Rev. Fluid Mech.*, 23, 601–639.

Rodrigo, J. S. and Anderson, P. S. (2013), "Investigation of the stable atmospheric boundary layer at Halley Antarctica," *Boundary-Layer Meteorol.*, 148, 517–539.

Roo, F. D. and Mauder, M. (2018), "The influence of idealized surface heterogeneity on virtual turbulent flux measurements," *Atmos. Chem. Phys.*, 18, 5059–5074.

Rotach, M., Andretta, M., Calanca, P., Weigel, A., and Weiss, A. (2008), "Boundary layer characteristics and turbulent exchange mechanisms in highly complex terrain," *Acta Geophys.*, 56, 194–219.

Rotach, M. W., Wohlfahrt, G., Hansel, A., Reif, M., Wagner, J., and Gohm, A. (2014), "The world is not flat: implications for the global carbon balance," *Bull. Am. Meteorol. Soc.*, 95, 1021–1028.

Rotach, M. W., Gohm, A., Lang, M. N., Leukauf, D., Stiperski, I., and Wagner, J. S. (2015), "On the vertical exchange of heat, mass, and momentum over complex, mountainous terrain," *Front. Earth Sci.*, 3, 76.

Roth, M. (2000), "Review of atmospheric turbulence over cities," *Q. J. R. Meteorol. Soc.*, 126, 941–990.

Ryu, Y.-H., Baik, J.-J., and Han, J.-Y. (2013), "Daytime urban breeze circulation and its interaction with convective cells," *Q. J. R. Meteorol. Soc.*, 139, 401–413.

Sakai, R. K., Fitzjarrald, D. R., and Moore, K. E. (2001), "Importance of low-frequency contributions to eddy fluxes observed over rough surfaces," *J. Appl. Meteorol.*, 40, 2178–2192.

Salesky, S. T. (2014), "Monin-Obukhov similarity and convective organization in the unstable atmospheric boundary layer," Ph.D. thesis, Pennsylvania State University.

Salesky, S. T., Chamecki, M., and Bou-Zeid, E. (2017), "On the nature of the transition between roll and cellular organization in the convective boundary layer," *Boundary-Layer Meteorol.*, 163, 41–68.

Scanlon, T. M. and Albertson, J. D. (2001), "Turbulent transport of carbon dioxide and water vapor within a vegetation canopy during unstable conditions: identification of episodes using wavelet analysis," *J. Geophys. Res. Atmos.*, 106, 7251–7262.

Scanlon, T. M. and Sahu, P. (2008), "On the correlation structure of water vapor and carbon dioxide in the atmospheric surface layer: a basis for flux partitioning," *Water Resour. Res.*, 44.

Schalkwijk, J., Jonker, H. J., Siebesma, A. P., and Van Meijgaard, E. (2015), "Weather forecasting using GPU-based large-eddy simulations," *Bull. Am. Meteorol. Soc.*, 96, 715–723.

Schicker, I., Arias, D. A., and Seibert, P. (2016), "Influences of updated land-use datasets on WRF simulations for two Austrian regions," *Meteorol. Atmos. Phys.*, 128, 279–301.

Schmidli, J. (2013), "Daytime heat transfer processes over mountainous terrain," *J. Atmos. Sci.*, 70, 4041–4066.

Schmidli, J., Poulos, G. S., Daniels, M. H., and Chow, F. K. (2009), "External influences on nocturnal thermally driven flows in a deep valley," *J. Appl. Meteorol. Climatol.*, 48, 3–23.

Schmidli, J., Billings, B., Chow, F. K., de Wekker, S. F., Doyle, J., Grubišić, V., Holt, T., Jiang, Q., Lundquist, K. A., Sheridan, P., et al. (2011), "Intercomparison of mesoscale model simulations of the daytime valley wind system," *Mon. Weather Rev.*, 139, 1389–1409.

Schmidli, J., Böing, S., and Fuhrer, O. (2018), "Accuracy of Simulated Diurnal Valley Winds in the Swiss Alps: Influence of Grid Resolution, Topography Filtering, and Land Surface Datasets," *Atmosphere*, 9, 196.

Schmidt, H. and Schumann, U. (1989), "Coherent structure of the convective boundary layer derived from large-eddy simulations," *J. Fluid Mech.*, 200, 511–562.

Schols, J. (1984), "The detection and measurement of turbulent structures in the atmospheric surface layer," *Boundary-Layer Meteorol.*, 29, 39–58.

Schols, J. and Wartena, L. (1986), "A dynamical description of turbulent structures in the near neutral atmospheric surface layer: the role of static pressure fluctuations," *Boundary-Layer Meteorol.*, 34, 1–15.

Schotanus, P., Nieuwstadt, F., and De Bruin, H. (1983), "Temperature measurement with a sonic anemometer and its application to heat and moisture fluxes," *Boundary-Layer Meteorol.*, 26, 81–93.

Schumann, U. (1990), "Large-eddy simulation of the up-slope boundary layer," *Q. J. R. Meteorol. Soc.*, 116, 637–670.

Schüttemeyer, D., Moene, A., Holtslag, A., De Bruin, H., and Van De Giesen, N. (2006), "Surface fluxes and characteristics of drying semi-arid terrain in West Africa," *Boundary-Layer Meteorol.*, 118, 583–612.

Serafimovich, A., Thomas, C., and Foken, T. (2011), "Vertical and horizontal transport of energy and matter by coherent motions in a tall spruce canopy," *Boundary-Layer Meteorol.*, 140, 429–451.

Serafin, S., Strauss, L., and Grubišić, V. (2017), "Climatology of westerly wind events in the Lee of the Sierra Nevada," *J. Appl. Meteorol. Clim.*, 56, 1003–1023.

Serafin, S., Adler, B., Cuxart, J., De Wekker, S. F., Gohm, A., Grisogono, B., Kalthoff, N., Kirshbaum, D. J., Rotach, M. W., Schmidli, J., et al. (2018), "Exchange Processes in the Atmospheric Boundary Layer Over Mountainous Terrain," *Atmosphere*, 9, 102.

Serrano-Ortiz, P., Sánchez-Cañete, E., Olmo, F., Metzger, S., Pérez-Priego, O., Carrara, A., Alados-Arboledas, L., and Kowalski, A. (2016), "Surface-parallel sensor orientation for assessing energy balance components on mountain slopes," *Boundary-Layer Meteorol.*, 158, 489–499.

Shao, Y. and Hacker, J. M. (1990), "Local similarity relationships in a horizontally inhomogeneous boundary layer," *Boundary-Layer Meteorol.*, 52, 17–40.

Shaw, W. J. and Businger, J. A. (1985), "Intermittency and the organization of turbulence in the near-neutral marine atmospheric boundary layer," *J. Atmos. Sci.*, 42, 2563–2584.

Shimizu, T. (2015), "Effect of coordinate rotation systems on calculated fluxes over a forest in complex terrain: a comprehensive comparison," *Boundary-Layer Meteorol.*, 156, 277–301.

Sievers, J., Papakyriakou, T., Larsen, S. E., Jammet, M. M., Rysgaard, S., Sejr, M. K., and Sørensen, L. (2015), "Estimating surface fluxes using eddy covariance and numerical ogive optimization," *Atmos. Chem. Phys.*, 15, 2081–2103.

Singha, A. and Sadr, R. (2012), "Characteristics of surface layer turbulence in coastal area of Qatar," *Environ. Fluid Mech.*, 12, 515–531.

Sreenivasan, K., Antonia, R., and Britz, D. (1979), "Local isotropy and large structures in a heated turbulent jet," *J. Fluid Mech.*, 94, 745–775.

Starkenburg, D., Fochesatto, G. J., Prakash, A., Cristóbal, J., Gens, R., and Kane, D. L. (2013), "The role of coherent flow structures in the sensible heat fluxes of an Alaskan boreal forest," *J. Geophys. Res. Atmos.*, 118, 8140–8155.

Steenburgh, W. J., Mass, C. F., and Ferguson, S. A. (1997), "The influence of terrain-induced circulations on wintertime temperature and snow level in the Washington Cascades," *Weather Forecast.*, 12, 208–227.

Steeneveld, G., Holtslag, A., and DeBruin, H. (2005), "Fluxes and gradients in the convective surface layer and the possible role of boundary-layer depth and entrainment flux," *Boundary-Layer Meteorol.*, 116, 237–252.

Steeneveld, G., Van de Wiel, B., and Holtslag, A. (2006), "Modeling the evolution of the atmospheric boundary layer coupled to the land surface for three contrasting nights in CASES-99," *J. Atmos. Sci.*, 63, 920–935.

Stiperski, I. and Calaf, M. (2017), "Dependence of near-surface similarity scaling on the anisotropy of atmospheric turbulence," *Q. J. R. Meteorol. Soc.*

Stiperski, I. and Rotach, M. W. (2016), "On the measurement of turbulence over complex mountainous terrain," *Boundary-Layer Meteorol.*, 159, 97–121.

Strauss, L., Serafin, S., and Grubišić, V. (2016), "Atmospheric rotors and severe turbulence in a long deep valley," *J. Atmos. Sci.*, 73, 1481–1506.

Strobach, K. (1991), "Unser Planet Erde: Ursprung und Dynamik," *Berlin: Gebruder Borntraeger, 1991.*, 1.

Stull, R. (1988), *An Introduction to Boundary Layer Meteorology*, Kluwer Academic Publishers Dordrecht.

Sullivan, P. P. and Patton, E. G. (2011), "The effect of mesh resolution on convective boundary layer statistics and structures generated by large-eddy simulation," *J. Atmos. Sci.*, 68, 2395–2415.

Sullivan, P. P., Moeng, C.-H., Stevens, B., Lenschow, D. H., and Mayor, S. D. (1998), "Structure of the entrainment zone capping the convective atmospheric boundary layer," *J. Atmos. Sci.*, 55, 3042–3064.

Sullivan, P. P., Weil, J. C., Patton, E. G., Jonker, H. J., and Mironov, D. V. (2016), "Turbulent winds and temperature fronts in large-eddy simulations of the stable atmospheric boundary layer," *J. Atmos. Sci.*, 73, 1815–1840.

Swinbank, W. (1951), "The measurement of vertical transfer of heat and water vapor by eddies in the lower atmosphere," *J. Meteorol.*, 8, 135–145.

Talbot, C., Bou-Zeid, E., and Smith, J. (2012), "Nested mesoscale large-eddy simulations with WRF: performance in real test cases," *J. Hydrometeorol.*, 13, 1421–1441.

Tampieri, F., Maurizi, A., and Viola, A. (2009), "An investigation on temperature variance scaling in the atmospheric surface layer," *Boundary-Layer Meteorol.*, 132, 31–42.

Tang, Y., Lean, H. W., and Bornemann, J. (2013), "The benefits of the Met Office variable resolution NWP model for forecasting convection," *Meteorol. Appl.*, 20, 417–426.

Tanner, B., Swiatek, E., and Greene, J. (1993), "Density fluctuations and use of the krypton hygrometer in surface flux measurements," *Management of irrigation and drainage systems: integrated perspectives. American Society of Civil Engineers, New York, NY*, pp. 945–952.

Taylor, R. (1958), "Thermal structures in the lowest layers of the atmosphere," *Aust. J. Phys.*, 11, 168–176.

Tennekes, H. (1973), "A model for the dynamics of the inversion above a convective boundary layer," *J. Atmos. Sci.*, 30, 558–567.

Thurston, W., Fawcett, R. J., Tory, K. J., and Kepert, J. D. (2016), "Simulating boundary-layer rolls with a numerical weather prediction model," *Q. J. R. Meteorol. Soc.*, 142, 211–223.

Tian, W. and Parker, D. J. (2003), "A modeling study and scaling analysis of orographic effects on boundary layer shallow convection," *J. Atmos. Sci.*, 60, 1981–1991.

Tian, W., Parker, D. J., and Kilburn, C. A. (2003), "Observations and numerical simulation of atmospheric cellular convection over mesoscale topography," *Mon. Weather Rev.*, 131, 222–235.

Tian, W.-S. and Parker, D. J. (2002), "Two-dimensional simulation of orographic effects on mesoscale boundary-layer convection," *Q. J. R. Meteorol. Soc.*, 128, 1929–1952.

Ting, C. and Hay, D. (1977), "Thermal plumes and turbulence spectra in the atmospheric boundary layer," *Boundary-Layer Meteorol.*, 11, 243–263.

Torrence, C. and Compo, G. P. (1998), "A practical guide to wavelet analysis," *Bull. Am. Meteorol. Soc.*, 79, 61–78.

Townsend, A. (1961), "Equilibrium layers and wall turbulence," *J. Fluid Mech.*, 11, 97–120.

Träumner, K., Kottmeier, C., Corsmeier, U., and Wieser, A. (2011), "Convective boundary-layer entrainment: Short review and progress using Doppler lidar," *Boundary-Layer Meteorol.*, 141, 369–391.

Träumner, K., Damian, T., Stawiarski, C., and Wieser, A. (2015), "Turbulent structures and coherence in the atmospheric surface layer," *Boundary-Layer Meteorol.*, 154, 1–25.

Trini Castelli, S., Falabino, S., Mortarini, L., Ferrero, E., Richiardone, R., and Anfossi, D. (2014), "Experimental investigation of surface-layer parameters in low wind-speed conditions in a suburban area," *Q. J. R. Meteorol. Soc.*, 140, 2023–2036.

Twine, T. E., Kustas, W., Norman, J., Cook, D., Houser, P., Meyers, T., Prueger, J., Starks, P., and Wesely, M. (2000), "Correcting eddy-covariance flux underestimates over a grassland," *Agr. Forest Meteorol.*, 103, 279–300.

Van de Boer, A., Moene, A., Graf, A., Schüttemeyer, D., and Simmer, C. (2014), "Detection of entrainment influences on surface-layer measurements and extension of Monin–Obukhov similarity theory," *Boundary-Layer Meteorol.*, 152, 19–44.

Van de Wiel, B., Moene, A., Hartogensis, O., De Bruin, H., and Holtslag, A. (2003), "Intermittent turbulence in the stable boundary layer over land. Part III: A classification for observations during CASES-99," *J. Atmos. Sci.*, 60, 2509–2522.

Van der Hoven, I. (1957), "Power spectrum of horizontal wind speed in the frequency range from 0.0007 to 900 cycles per hour," *J. Met.*, 14, 160–164.

Van Gorsel, E., Christen, A., Feigenwinter, C., Parlow, E., and Vogt, R. (2003), "Daytime turbulence statistics above a steep forested slope," *Boundary-Layer Meteorol.*, 109, 311–329.

Večenaj, Ž. and De Wekker, S. F. (2015), "Determination of non-stationarity in the surface layer during the T-REX experiment," *Q. J. R. Meteorol. Soc.*, 141, 1560–1571.

Večenaj, Ž., Belušić, D., and Grisogono, B. (2010), "Characteristics of the near-surface turbulence during a bora event," *Ann. Geophys.*, 28, 155–163.

Večenaj, Ž., De Wekker, S. F., and Grubišić, V. (2011), "Near-surface characteristics of the turbulence structure during a mountain-wave event," *J. Appl. Meteorol. Clim.*, 50, 1088–1106.

Večenaj, Ž., Belušić, D., Grubišić, V., and Grisogono, B. (2012), "Along-coast features of bora-related turbulence," *Boundary-Layer Meteorol.*, 143, 527–545.

Vesala, T., Järvi, L., Launiainen, S., Sogachev, A., Rannik, Ü., Mammarella, I., Siivola, E., Keronen, P., Rinne, J., Riikonen, A., et al. (2008), "Surface–atmosphere interactions over complex urban terrain in Helsinki, Finland," *Tellus B*, 60, 188–199.

Viana, S., Terradellas, E., and Yagüe, C. (2010), "Analysis of gravity waves generated at the top of a drainage flow," *J. Atmos. Sci.*, 67, 3949–3966.

Vickers, D. and Mahrt, L. (1997), "Quality control and flux sampling problems for tower and aircraft data," *J. Atmos. Ocean. Tech.*, 14, 512–526.

Vickers, D. and Mahrt, L. (2003), "The cospectral gap and turbulent flux calculations," *J. Atmos. Ocean. Tech.*, 20, 660–672.

Vido, J., Tadesse, T., Šustek, Z., Kandrík, R., Hanzelová, M., Škvarenina, J., Škvareninová, J., and Hayes, M. (2015), "Drought Occurrence in Central European Mountainous Region (Tatra National Park, Slovakia) within the Period 1961–2010," *Adv. Meteorol.*, 2015.

Vinnichenko, N. (1970), "The kinetic energy spectrum in the free atmosphere1 second to 5 years," *Tellus*, 22, 158–166.

von Randow, C., Kruijt, B., and Holtslag, A. A. (2006), "Low-frequency modulation of the atmospheric surface layer over Amazonian rain forest and its implication for similarity relationships," *Agr. Forest Meteorol.*, 141, 192–207.

Voronovich, V. and Kiely, G. (2007), "On the gap in the spectra of surface-layer atmospheric turbulence," *Boundary-Layer Meteorol.*, 122, 67–83.

Wagner, J., Gohm, A., and Rotach, M. (2014a), "The impact of valley geometry on daytime thermally driven flows and vertical transport processes," *Q. J. R. Meteorol. Soc.*

Wagner, J. S., Gohm, A., and Rotach, M. W. (2014b), "The impact of horizontal model grid resolution on the boundary layer structure over an idealized valley," *Mon. Weather Rev.*, 142, 3446–3465.

Wang, L., Li, D., Gao, Z., Sun, T., Guo, X., and Bou-Zeid, E. (2014), "Turbulent transport of momentum and scalars above an urban canopy," *Boundary-Layer Meteorol.*, 150, 485–511.

Webb, E. K., Pearman, G. I., and Leuning, R. (1980), "Correction of flux measurements for density effects due to heat and water vapour transfer," *Q. J. R. Meteorol. Soc.*, 106, 85–100.

Weckwerth, T. M. (2000), "The effect of small-scale moisture variability on thunderstorm initiation," *Mon. Weather Rev.*, 128, 4017–4030.

Weckwerth, T. M., Wilson, J. W., Wakimoto, R. M., and Crook, N. A. (1997), "Horizontal convective rolls: Determining the environmental conditions supporting their existence and characteristics," *Mon. Weather Rev.*, 125, 505–526.

Weckwerth, T. M., Horst, T. W., and Wilson, J. W. (1999), "An observational study of the evolution of horizontal convective rolls," *Mon. Weather Rev.*, 127, 2160–2179.

Weigel, A. P. and Rotach, M. W. (2004), "Flow structure and turbulence characteristics of the daytime atmosphere in a steep and narrow Alpine valley," *Q. J. R. Meteorol. Soc.*, 130, 2605–2627.

Weston, K. (1980), "An observational study of convective cloud streets," *Tellus*, 32, 433–438.

Whiteman, C. D. (2000), *Mountain meteorology: fundamentals and applications*, Oxford University Press.

Whiteman, C. D. and Allwine, K. J. (1986), "Extraterrestrial solar radiation on inclined surfaces," *Environ. Softw.*, 1, 164–169.

Wilczak, J. (1984), "Large-scale eddies in the unstably stratified atmospheric surface layer. Part I: Velocity and temperature structure," *J. Atmos. Sci.*, 41, 3537–3550.

Wilczak, J. and Businger, J. A. (1984), "Large-scale eddies in the unstably stratified atmospheric surface layer. Part II: Turbulent pressure fluctuations and the budgets of heat flux, stress and turbulent kinetic energy," *J. Atmos. Sci.*, 41, 3551–3567.

Wilczak, J. M. and Tillman, J. (1980), "The three-dimensional structure of convection in the atmospheric surface layer," *J. Atmos. Sci.*, 37, 2424–2443.

Wilczak, J. M., Oncley, S. P., and Stage, S. A. (2001), "Sonic anemometer tilt correction algorithms," *Boundary-Layer Meteorol.*, 99, 127–150.

Williams, C. A., Scanlon, T. M., and Albertson, J. D. (2007), "Influence of surface heterogeneity on scalar dissimilarity in the roughness sublayer," *Boundary-Layer Meteorol.*, 122, 149.

Williams, M., Richardson, A., Reichstein, M., Stoy, P., Peylin, P., Verbeeck, H., Carvalhais, N., Jung, M., Hollinger, D., Kattge, J., et al. (2009), "Improving land surface models with FLUXNET data," *Biogeosciences*, 6, 1341–1359.

Wilson, J. (2008), "Monin-Obukhov functions for standard deviations of velocity," *Boundary-Layer Meteorol.*, 129, 353–369.

Wilson, K., Goldstein, A., Falge, E., Aubinet, M., Baldocchi, D., Berbigier, P., Bernhofer, C., Ceulemans, R., Dolman, H., Field, C., et al. (2002), "Energy balance closure at FLUXNET sites," *Agr. Forest Meteorol.*, 113, 223–243.

Wood, C., Lacser, A., Barlow, J. F., Padhra, A., Belcher, S. E., Nemitz, E., Helfter, C., Famulari, D., and Grimmond, C. (2010), "Turbulent flow at 190 m height above London during 2006–2008: A climatology and the applicability of similarity theory," *Boundary-Layer Meteorol.*, 137, 77–96.

Wood, R. (2012), "Stratocumulus clouds," *Mon. Weather Rev.*, 140, 2373–2423.

Worthington, R. (2006), "Diurnal variation of mountain waves," *Ann. Geophys.*, 24, 2891–2900.

Worthington, R. and Thomas, L. (1998), "The frequency spectrum of mountain waves," *Q. J. R. Meteorol. Soc.*, 124, 687–703.

Wyngaard, J. and Clifford, S. (1977), "Taylor's hypothesis and high–frequency turbulence spectra," *J. Atmos. Sci.*, 34, 922–929.

Wyngaard, J., Coté, O., and Izumi, Y. (1971), "Local free convection, similarity, and the budgets of shear stress and heat flux," *J. Atmos. Sci.*, 28, 1171–1182.

Wyngaard, J., Pennell, W., Lenschow, D., and LeMone, M. (1978), "The temperature-humidity covariance budget in the convective boundary layer," *J. Atmos. Sci.*, 35, 47–58.

Wyngaard, J. C. (2004), "Toward numerical modeling in the Terra Incognita," *J. Atmos. Sci.*, 61, 1816–1826.

Xu, Z., Ma, Y., Liu, S., Shi, W., and Wang, J. (2017), "Assessment of the Energy Balance Closure under Advective Conditions and Its Impact Using Remote Sensing Data," *J. Appl. Meteorol. Clim.*, 56, 127–140.

Xue, L., Chu, X., Rasmussen, R., Breed, D., Boe, B., and Geerts, B. (2014), "The dispersion of silver iodide particles from ground-based generators over complex terrain. Part II: WRF large-eddy simulations versus observations," *J. Appl. Meteorol. Climatol.*, 53, 1342–1361.

Yagi, A., Inagaki, A., Kanda, M., Fujiwara, C., and Fujiyoshi, Y. (2017), "Nature of streaky structures observed with a Doppler lidar," *Boundary-Layer Meteorol.*, 163, 19–40.

Yahaya, S. and Frangi, J. (2004), "Cup anemometer response to the wind turbulence-measurement of the horizontal wind variance," *Ann. Geophys.*, 22, 3363–3374.

Ye, Z., Segal, M., and Pielke, R. (1987), "Effects of atmospheric thermal stability and slope steepness on the development of daytime thermally induced upslope flow," *J. Atmos. Sci.*, 44, 3341–3354.

Young, G. S., Kristovich, D. A., Hjelmfelt, M. R., and Foster, R. C. (2002), "Supplement to rolls, streets, waves, and more," *Bull. Am. Meteorol. Soc.*, 83, 1001–1001.

Yue, X., Mickley, L. J., and Logan, J. A. (2014), "Projection of wildfire activity in southern California in the mid-twenty-first century," *Clim. Dynam.*, 43, 1973–1991.

Yusup, Y. and Lim, J.-F. (2014), "Turbulence variances in the convective urban roughness sublayer: an application of similarity theory using local scales," *Meteorol. Appl.*, 21, 149–160.

Zardi, D. and Whiteman, C. D. (2013), "Diurnal mountain wind systems," in *Mountain Weather Research and Forecasting*, pp. 35–119, Springer.

Zhang, J. A., Katsaros, K. B., Black, P. G., Lehner, S., French, J. R., and Drennan, W. M. (2008), "Effects of roll vortices on turbulent fluxes in the hurricane boundary layer," *Boundary-Layer Meteorol.*, 128, 173–189.

Zhang, Y., Liu, H., Foken, T., Williams, Q. L., Mauder, M., and Thomas, C. (2011), "Coherent structures and flux contribution over an inhomogeneously irrigated cotton field," *Theor. Appl. Climatol.*, 103, 119–131.

Zhao, Z., Gao, Z., Li, D., Bi, X., Liu, C., and Liao, F. (2013), "Scalar flux–gradient relationships under unstable conditions over water in coastal rEgions," *Boundary-Layer Meteorol.*, 148, 495–516.

Zhong, S. and Chow, F. K. (2013), "Meso-and fine-scale modeling over complex terrain: parameterizations and applications," in *Mountain Weather Research and Forecasting*, pp. 591–653, Springer.

Zhong, S., Li, J., Whiteman, C. D., Bian, X., and Yao, W. (2008), "Climatology of high wind events in the Owens Valley, California," *Mon. Weather Rev.*, 136, 3536–3552.

Zhou, B. and Chow, F. K. (2013), "Nighttime turbulent events in a steep valley: a nested large-eddy simulation study," *J. Atmos. Sci.*, 70, 3262–3276.

Zhou, B., Simon, J. S., and Chow, F. K. (2014), "The convective boundary layer in the terra incognita," *J. Atmos. Sci.*, 71, 2545–2563.

Zhuang, Y. (1995), "Dynamics and energetics of convective plumes in the atmospheric surface layer," *J. Atmos. Sci.*, 52, 1712–1722.